

Herbert Oertel

Introduction to Fluid Mechanics

**Fundamentals and
Applications**



universitätsverlag karlsruhe

Introduction to Fluid Mechanics

Fundamentals and Applications

by
Herbert Oertel

Translated by Katherine Mayes



universitätsverlag karlsruhe

Autor

Prof. Prof. e.h. Dr.-Ing.habil. Herbert Oertel, Ordinarius
Institut für Strömungslehre, Universität Karlsruhe (TH)
Kaiserstr. 12, 76128 Karlsruhe

Übersetzung

Katherine Mayes
Institut für Festkörperphysik, TU Darmstadt,
Hochschulstr. 8, 64289 Darmstadt

Originalveröffentlichung im Verlag
Friedr. Vieweg & Sohn, Verlagsgesellschaft mbH,
Braunschweig/Wiesbaden, 2001

Impressum

Universitätsverlag Karlsruhe
c/o Universitätsbibliothek
Straße am Forum 2
D-76131 Karlsruhe
www.uvka.de



Dieses Werk ist unter folgender Creative Commons-Lizenz
lizenziert: <http://creativecommons.org/licenses/by-nc-nd/2.0/de/>

Universitätsverlag Karlsruhe 2005
Print on Demand

ISBN 3-937300-81-3

1 Introduction

This textbook on fluid mechanics is aimed at engineering students at Bachelor's degree level. In Chapter 2 the fundamentals of fluid mechanics, needed for the description and analysis of flows in technology, are presented. One-dimensional stream filament theory, along with the momentum integral and angular momentum integral equations, already present us with one method of constructing fluid technological appliances and experiments. For example, the dimensions of a machine can be determined quite accurately in one first step and predictions made about the flow losses which occur.

However, these methods fail when machines are to be optimized, or when appliances are to be developed to operate under extreme conditions, such as silent operation, high efficiency, small dimensions, greatly damped oscillatory behavior, etc. In addition to this, even for most simple cases of application, simple fluid mechanical fundamentals cannot determine the operating behavior of a machine accurately enough. This requires extensive experiments to be carried out and these can be very costly and time consuming.

At this point we refer to more detailed textbooks which progress systematically from the fundamental fluid mechanical equations and their methods of solution to the application of fluid mechanical software.

The methods used in fluid mechanics are analytical, numerical and experimental. Although numerical methods are increasingly used to replace experimental methods, all three are still needed to solve fluid mechanical problems. This book is restricted to theoretical, that is analytical, methods. After working through this book, students are qualified to understand the basics and phenomena of fluid mechanics, and will have obtained an initial insight into fluid mechanical software, even if further studies into the fundamental equations of fluid mechanics and numerical methods are necessary for the application of this software.

The composition of this book is partly very theoretical. In order not to lose sight of the connection to technical applications during the extensive derivations, we have selected flows past airplane wings, flows past vehicles and flows in pipes of process engineering systems as representative examples to illustrate the basics of one-dimensional fluid mechanics.

We now introduce the student to the great variety of fluid mechanical applications, demonstrating that flows are all around us in our technological environment, by describing selected examples of flows in the following introductory sections.

1.1 Flows in Technology

Flows are responsible for most transport and mixing processes, such as those which occur in the transport of pollutants in our environment, in industrial processes, and in living organisms. The combustion of the limited fossil fuels currently produces the majority of electrical and heat energy. Optimizing the flows in these combustion processes serves to reduce oil and pollutant emissions. Flows are also of interest in the propulsion of airplanes, ships and vehicles, in pumping oil and gas through pipelines, and in the production and coating of materials. It is the flow of oxygen and carbon dioxide in organisms which permits life. Flows are of importance in the construction of low drag automobiles and airplanes;

in the development of booster rockets and space craft for transport to space stations; in energy and environmental technology; from process engineering to the simulation of entire production plants; in geophysics and astrophysics; and from meteorology and climatology to medicine, where innovations frequently go hand in hand with fluid mechanical optimization of artificial heart valves, hearts and artificial vessels.

We now turn to **examples of technical flows**. Our environment is characterized by flow phenomena in many different ways. The optimization of flows leads to a decrease in the drag of airplanes, trains and vehicles and thus to savings in fuel. In drive assemblies it leads to an increase in efficiency and a reduction in polluting emissions. When materials are constructed from a melt, flow optimization determines the inner structure and thus the strength and load capacity of the material. In chemical production plants and pipelines, the optimization of flows reduces losses, and thus also the pump power needed to manufacture and transport liquids and gases.

The development of airplanes and trains over the last decades is shown in Figure 1.1. The aim here has been to find low drag body shapes corresponding to the transport velocity, in order to keep the engine fuel or the electrical power of the driving motors as low as possible. The development of **civil air travel** began in the 1930's with the legendary Ju 52. It transported 17 passengers with a velocity of 250 km/h and was driven by three piston air motors. The endeavor to fly as fast as possible from one place to another led to the development of the jet engine, which currently makes it possible to fly at an altitude of 10 km , at a speed of 950 km/h . Jumbo jets can transport up to 450 passengers, with the next generation carrying up to 650 passengers. The first member of this aerodynamic new generation of airplane was the Boeing 707 (center Figure 1.1). The decisive aerodynamic discovery was the swept wing in the early 1940's at the aerodynamic laboratory in Göttingen. This only allowed low drag flight at so-called transonic velocities. The Airbus A310 is a representative of the new generation of civil aircraft. Here the body of the plane is much larger, in order to transport as many passengers as possible. And still a considerable saving of fuel is attained compared to the Boeing 707. As well as the improved aerodynamics of transonic airfoils, it is the lighter materials and improved production engineering, together with new fan engines and the automated two-pilot cockpit, which have led to this saving in fuel and thus to the reduction in polluting emissions. Fan engines have a considerably larger diameter than jet engines. One part of the cold air condensed by the fan is guided past the hot propulsion jet as an air coating. This has the additional useful effect of reducing the noise emissions of jet engines drastically while simultaneously increasing their efficiency.

A similar course of development has also been seen in **trains** over the past decades. Because the power required increases with the cube of the velocity and the drag with the square, at velocities over 100 km/h it is necessary to adapt the aerodynamic shaping suitably. Whereas in the case of conventional steam engines, the flow optimization merely shielded the driver's cab from smoke using side-mounted wind deflectors, in the case of Inter-City (IC) trains, a better low drag design of the locomotive and the air deflectors close to the carriage wheels were realized. It is only in the case of Inter-City-Express (ICE) trains, where speeds of 330 km/h are reached, that a thorough aerodynamic shaping has been technically implemented, although even here the current collectors, for example, could use an aerodynamic covering. The fluid mechanical development of trains is also not yet completed. At present there are projects planned for travel in pipes at speeds of up to 500 km/h .

In the past, the aerodynamics of airplanes and trains were developed entirely in wind tunnels. Figure 1.2 shows the wind tunnel model of the Airbus A340 in its take-off phase. Scales integrated into the mounting support of the model measure six components of the aerodynamic forces. Because the model, at rest in the wind tunnel, is in an air flow with a wind speed of about 300 km/h, the floor of the wind tunnel has to be moved with the same speed. These are very thorough experiments and are a key factor in determining the time needed to develop an airplane, a process which can take up to eight years, from the definition of requirements (flight speed, payload), through the design phase, to the introduction of the product. These very long and expensive development processes have now been reduced considerably with the use of fluid mechanical simulation on large-scale computers. Flow simulation permits reasonably simple variations in the geometry and flow parameters, without the need to build new wind tunnel models each time. In future projects, both fluid mechanical software on large-scale computers and the wind tunnel will be tools of develop-



Fig. 1.1 : Development of airplanes and trains

ment for design engineers. Wind tunnel experiments will increasingly be used to verify the computer results.

The low drag aerodynamic shaping of an **automobile** was already resolved technically in 1938. The Mercedes-Benz racing car built in 1937 to beat the world land-speed record is shown in Figure 1.3. The present-day usual drag coefficient c_W (dimensionless drag force) is 0.365, but by lowering the driver in the racing car and covering the wheels, a so-called streamline body (Chapter 2.3.2) was achieved, with the drastic reduction in drag to a c_W value of 0.17. Figure 1.4 demonstrates that the optimal obtainable aerodynamic value is 0.15, indicating just how remarkable was the achievement of those Mercedes-Benz engineers. These findings on motor vehicles were really only taken into account in the 1980's, after the oil crisis made fuel savings necessary. At present, the automobile industry has reached a compromise in the drag coefficient with a value of about 0.26. This permits a comfortable passenger area with the necessary all-round view.

This introduction to technical examples can be supplemented with an anecdote. In 1952, the only wind tunnel for the aerodynamic development of motor vehicles in Germany which was operational and equipped with the appropriate scales was in Schlichting's institute in Braunschweig. So it stood to reason that the neighboring Wolfsburg factory should use the Braunschweig wind tunnel to measure the aerodynamic drag of the Volkswagen VW11 and VWX_2 models. The wind tunnel results are shown in Figure 1.5. The prototype VWX_2 showed a considerably better drag coefficient of 0.22, while the VW Beetle which was finally produced had a very poor drag coefficient of 0.4. Schlichting was so annoyed by the lack of attention paid to his work, that he presented the results in Figure 1.5 at the next

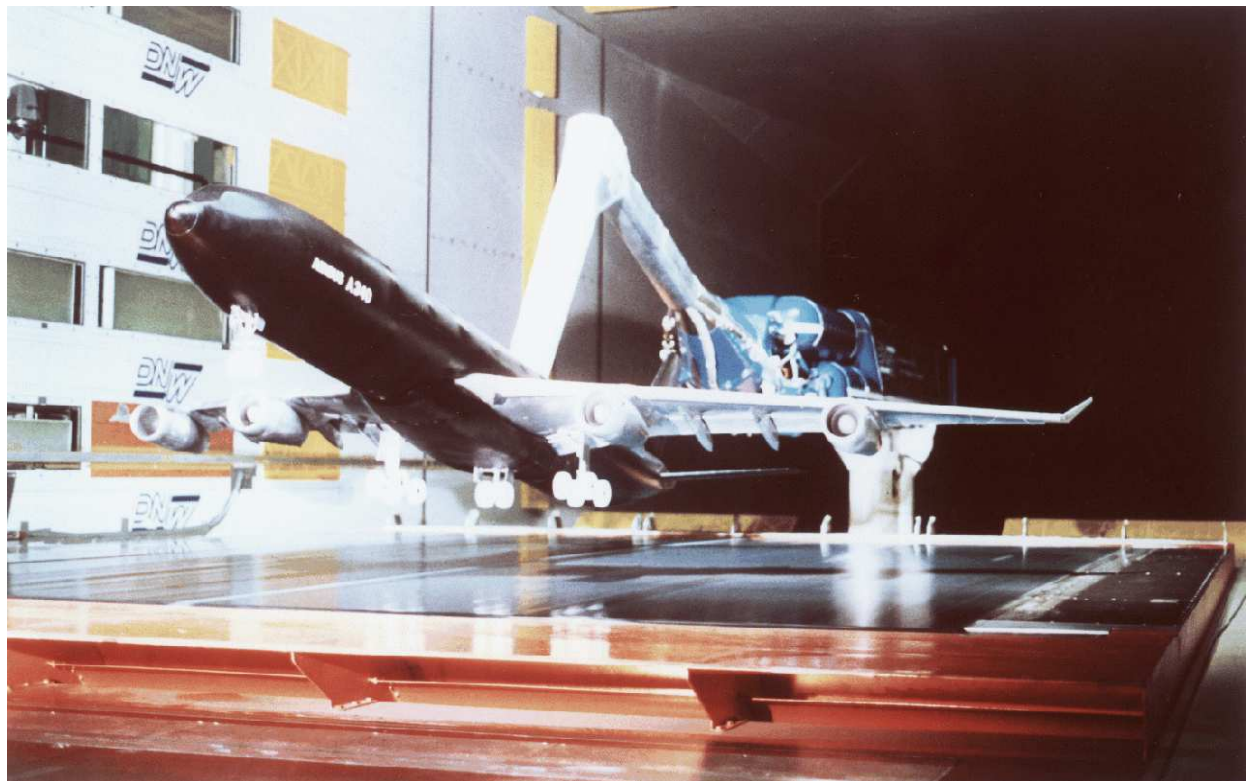


Fig. 1.2 : Model of an Airbus A 340 in a wind tunnel

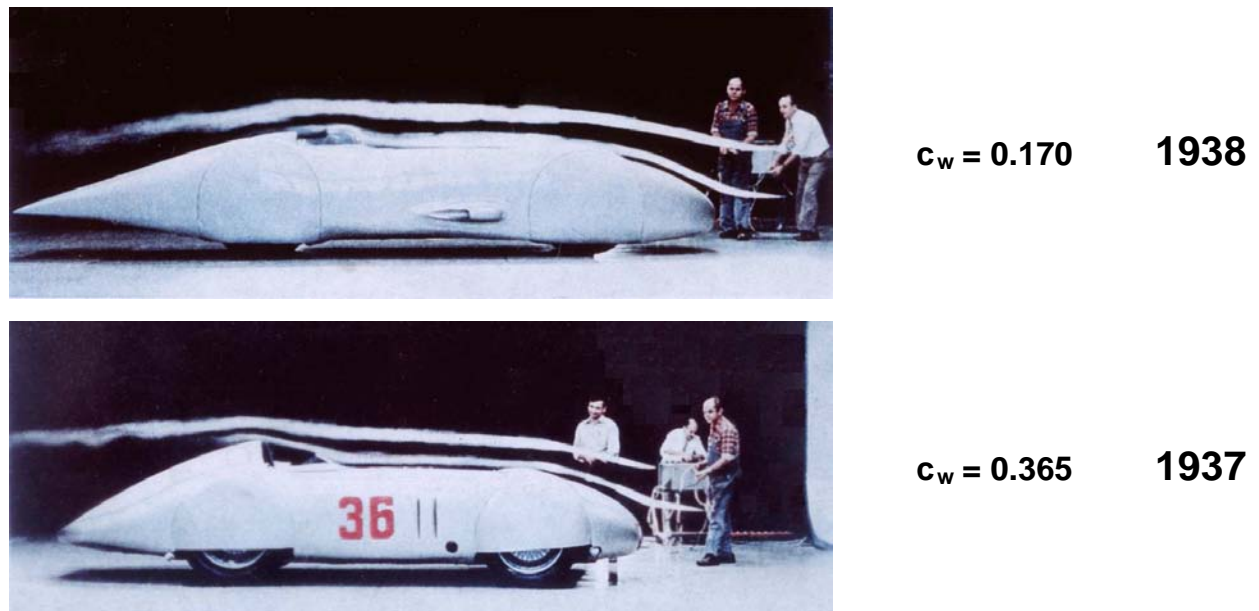


Fig. 1.3 : Mercedes-Benz W125 in a wind tunnel

international conference, much to the infuriation of the company involved.

A further technical example of **building aerodynamics** is shown in Figure 1.6. The Tacoma Narrows bridge, which has now become famous for its erroneous aerodynamic construction, extends 1.81 km over the narrows of Puget Sound in Washington State. On the 7th of November 1940, the wind was blowing with a speed of about 68 km/h at right-angles to the bridge. This caused a periodic separation of the air, known as a Kármán vortex street, to form at the opposite side of the bridge. Unfortunately, the eigenfrequency of the bridge was the same as the frequency of the periodic flow separation, so that mechanical eigen-oscillations were stimulated, leading to the bridge's collapse.

The optimization of flows is also important in the construction of **internal combustion engines**. The well-known cycle of an Otto engine is shown in Figure 1.7. The fuel-air mixture is sucked in through the open intake valve by the backward motion of the piston. In order to attain a mixture which is as homogeneous as possible, a rotating flow, called a

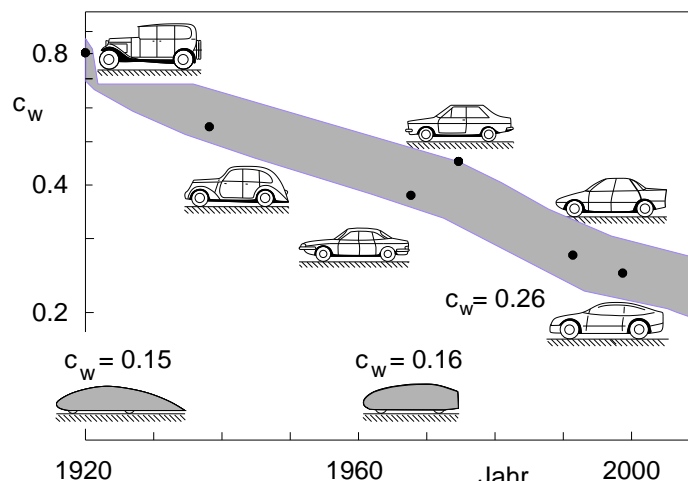


Fig. 1.4 : Development of the c_w value of motor vehicles

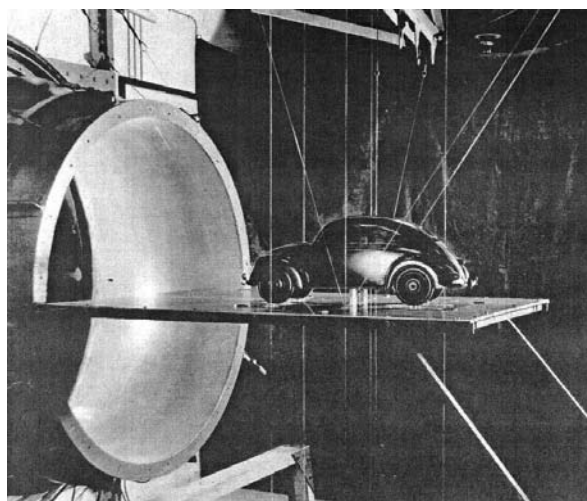
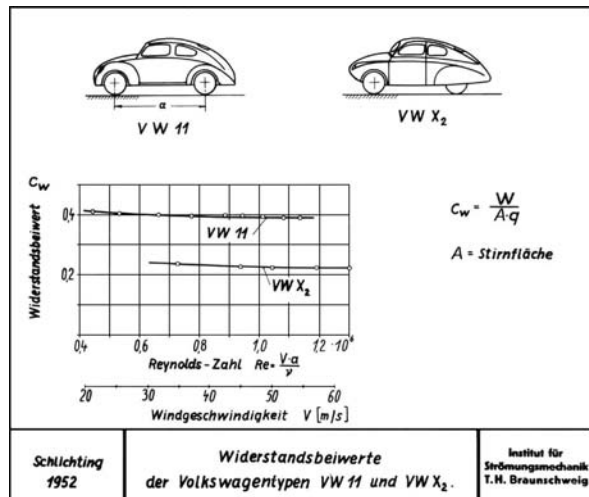


Fig. 1.5 : Measurement of automobile drag coefficients in the wind tunnel

tumble, is superimposed on the flow. In the second step, the valve is closed and the fuel-air mixture is compressed, so that, after igniting the combustion, the expanding hot gas moves the piston for the mechanical propulsion downwards. When the combustion cycle is completed, the exhaust is expelled through the outlet valve (step 4). It might be expected after more than 100 years of development of combustion engines that the flow processes



Fig. 1.6 : Aerodynamically excited oscillations of Tacoma Bridge

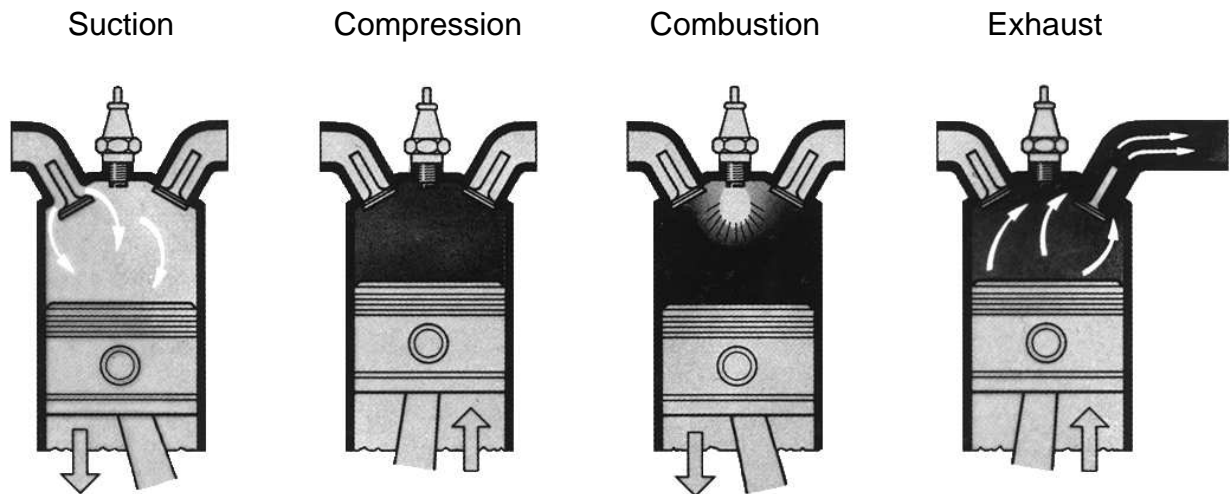


Fig. 1.7 : Cycle of an Otto engine

of intake, compression, combustion and exhaust expulsion would already be optimized; yet the need for an additional catalyst to reduce emission of pollutants shows that this is still not the case. For example, intensive efforts are being made to realize the direct injection of fuel, usual in diesel engines, in Otto engines too. This is expected to yield a fuel saving of about 10%, with a simultaneous increase in efficiency. Figure 1.8 shows a direct fuel-injection Otto engine. In the compression phase, the combustible gas mixture introduced through the injection valve is ignited directly at the spark plug via the bend in the cavity. However, the fluid mechanical problem of optimizing the combustion with respect to pollutant emissions remains.

Flows with **chemical reactions** are very important for many applications in energy, chemical and combustion technology. Figure 1.9 shows an example of a flame, whose structure is due to a flow. Flames are characterized by a wide spectrum of time and length scales. Typical length scales of the flow vary from the size of the combustion chamber right down to

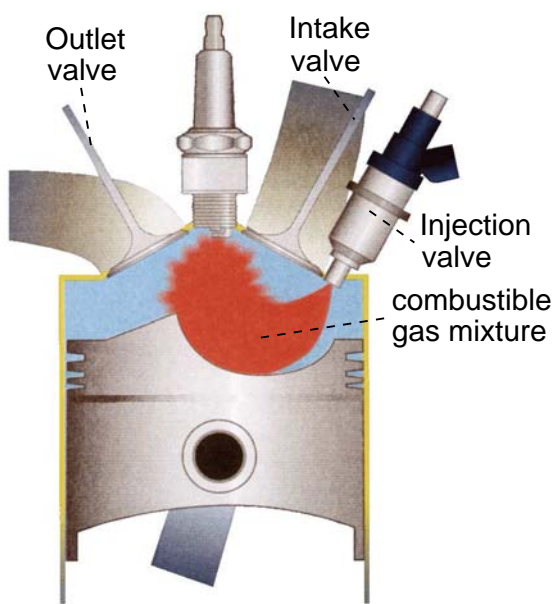


Fig. 1.8 : Otto engine with direct fuel injection

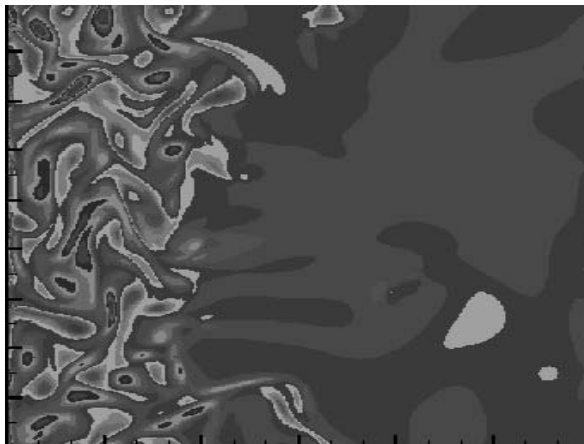


Fig. 1.9 : Flow structure of a flame

the smallest vortex in which kinetic energy is dissipated. The chemical reactions occurring in combustion determine the wide spectrum of time scales. Knowledge of the interaction of these combustion time scales with the spatial structure of the flow is required to predict the pollutants in combustion processes.

Flows are also involved in the **production of materials** such as in the microscopic structure of solidified steel in Figure 1.10. We see convection cells which have formed at the solidification front as the hot molten metal becomes rigid. They are due to lift flows and determine the material properties of steel, such as its strength.

In **process engineering** and chemical production plants (Figure 1.11), it is pipe flows in bends and junctions which introduce losses. If there are liquid separators in use, as in refineries, multi-phase flows with drops and bubbles have to be taken into account, as they can complicate matters considerably in optimizing the flow processes.

There are many more examples of flow in technology. If you have followed the text so far, your interest will be awakened to move on to the basics and methods of fluid mechanics in the following chapters, so that you too will be able to solve fluid mechanical problems in engineering.

We conclude this introduction by referring to **additional literature**. To supplement this

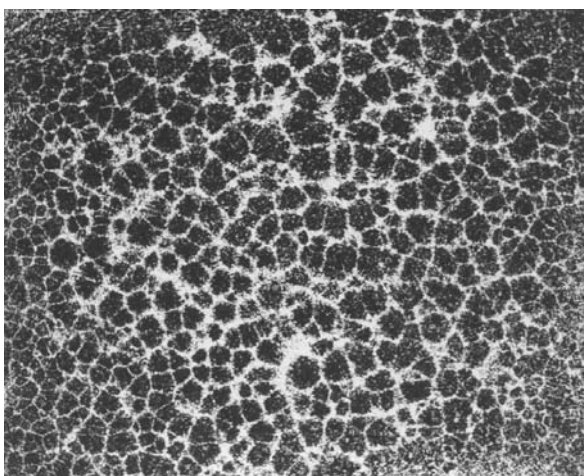


Fig. 1.10 : Microscopic structure of solidified steel



Fig. 1.11 : Production plant in chemical process engineering

text on fluid mechanics, we recommend PRANDTL–Guide of Fluid Mechanics 2001 for additional material on the fundamentals of fluid mechanics. This text describes further areas of fluid mechanics, such as aerodynamics, turbulent flows, fluid mechanical instabilities, flows with heat and material transfer, two phase flows and flows with chemical reactions, flows in the atmosphere and in the ocean, biological flows, as well as flow machinery. The fluid mechanical phenomena derived from technical problems are to be found in our textbook H. OERTEL jr., M. BOEHLE 1999. Further information on analytical and numerical methods is to be found in the textbooks H. OERTEL jr., E. LAURIEN 2002, H. OERTEL jr., J. DELFS 1996, H. OERTEL jr. 1994. Analytical descriptions of the fluid mechanics basics and methods are to be found in G. K. BATCHELOR 1994, K. GERSTEN, H. HERWIG 1992, W. SCHNEIDER 1978, J. H. SPURK 1997, F.M. WHITE 1974 and the technical application of boundary layer theory in H. SCHLICHTING, K. GERSTEN 1999. The mathematical basics may be found in more detail in the books by K. MEYBERG, P. VACHENAUER 1997,1998.

1.2 Flow Regimes

The first contact one makes with a flow might be at a water faucet. If you hold your finger in the stream of water, you will feel a **force \vec{F}** which the flow exerts on the finger. This force is called the drag, and is experienced by a body in a flow. The drag is dependent on the geometry of the body in the flow, the properties of its surface, the flowing medium and the flow variables. The drag has a different value for a stream of gas than for the water stream we have considered. In order not to constantly have to distinguish between gases and liquids, we will use the generic term **fluid**.

The moving fluid is considered to be a **continuum**. This means that we neglect the molecular structure of the fluid, since the mean free path of the molecules is small compared to the characteristic macroscopic dimensions of the flow field. The characteristic physical quantities of the flow field of Figure 1.12, such as the velocity vector \vec{v} with components in three directions u, v, w , the pressure p , the density ρ and the temperature T , are assumed to be continuous functions of position $\vec{x} = (x, y, z)$ and time t .

Let the finger in the stream of water which we considered initially be replaced by a horizontal plate, as in Figure 1.12. The **unperturbed flow** w_∞ points in the vertical direction and has the index ∞ . In order to describe the flow, the three scalar field quantities p, ρ and T , as well as the three components (u, v, w) of the vector velocity \vec{v} have to be calculated as functions of the coordinates (x, y, z) and the time t :

$$p(x, y, z, t) , \quad \rho(x, y, z, t) , \quad T(x, y, z, t) , \quad \vec{v}(x, y, z, t) = \begin{pmatrix} u(x, y, z, t) \\ v(x, y, z, t) \\ w(x, y, z, t) \end{pmatrix} \quad (1.1)$$

In order to calculate these six flow quantities, we have the continuum mechanical fundamental equations of **mass, momentum and energy conservation** as well as the thermodynamic equations of state at our disposal.

In Figure 1.13, the example of a horizontal plate in a flow is considered further, in order to introduce some fundamental terms needed for the description of flows. The left-hand picture shows flow paths made visible with small aluminum particles. One particular point is noticeable in the middle of the plate. This is called the **stagnation point**, where the streamlines branch to the left and right. In the stagnation point of a flow field, the velocity vector \vec{v} is equal to zero, and the pressure p is at a maximum.

The right-hand illustration in Figure 1.13 is a sketch of the flow. The **no-slip condition** holds at the surface of the plate. Here again the velocity is equal to zero, but the pressure generally varies along the coordinate x . The velocity perpendicular to the plate at the position under consideration varies from the value zero to the constant velocity of the outer

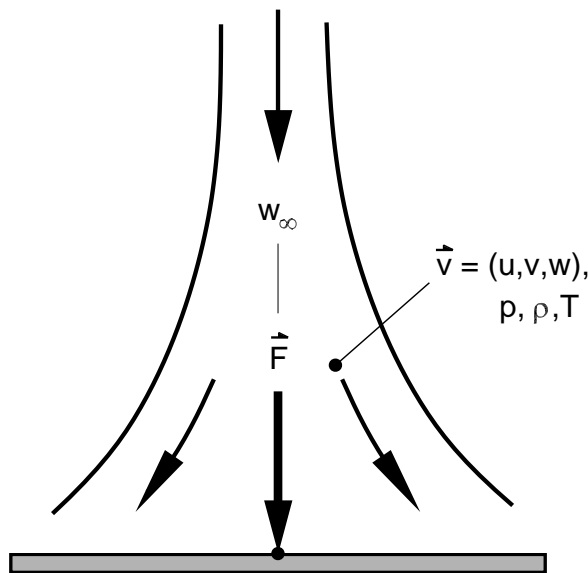


Fig. 1.12 : Forces acting in a flow

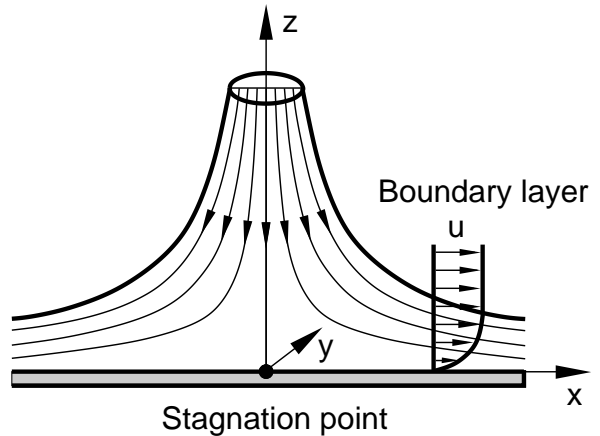
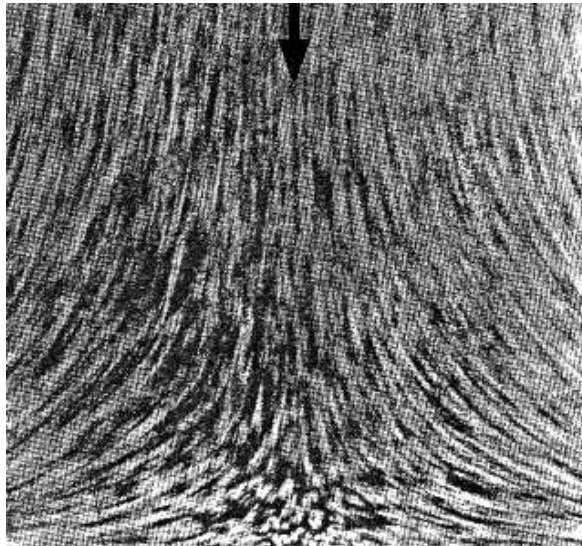


Fig. 1.13 : Liquid jet at a horizontal plate

flow. This presents us with an initial division into different flow regimes: the **boundary layer flow** and the **outer flow**. If we take into consideration the flow properties, such as the viscosity μ (see Chap. 2.1), responsible for the friction in the flow, the boundary layer flow is the **viscous** part of the flow field, and the outer flow is the **inviscid** part.

The origin of the internal friction is the inter-molecular interaction forces of the fluid. Whereas two elastic spheres (Figure 1.14) exchange momentum and energy completely and instantaneously, and thus have the infinitely large interaction force sketched in Figure 1.14, the interaction between molecules of a moving fluid is characterized by repulsive or attractive interaction forces (see Chap. 2.1), depending on their distance apart r . These interaction forces between the molecules determine the **transport properties** of the fluid, such as the viscosity (friction), heat conduction (energy transport) and diffusion (mass transport).

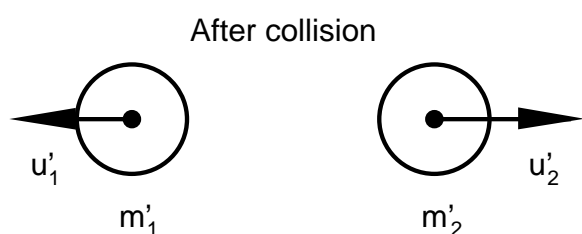
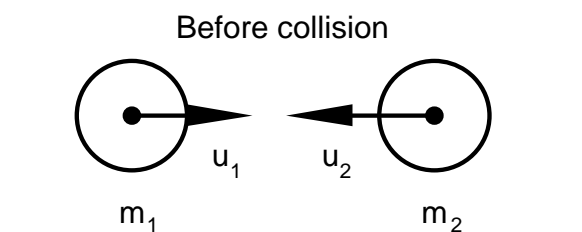


Fig. 1.14 : Collision between two spheres (point mechanics)

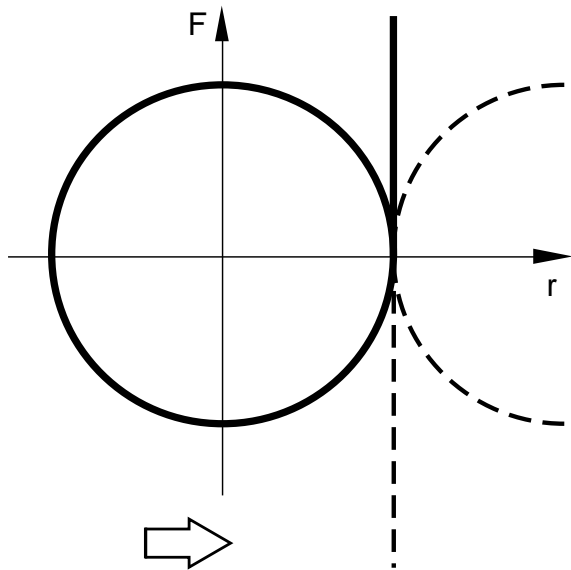


Fig. 1.15 : Interaction force in the collision of hard spheres

For the different regimes of the moving fluid we have the corresponding fundamental equations of continuum mechanics: mass, momentum and energy conservation. These are valid for both viscous boundary layers flows, as well as for inviscid outer flows.

If we consider the flow quantities velocity \vec{v} and density ρ , we are led to a completely different division of the flow regimes. We speak of an **incompressible** flow if the density ρ in the flow field is constant for a given temperature, e.g. in water flows. The flow is **compressible** if the density varies in the flow field, e.g. in air flows. If the velocity vector \vec{v} is equal to zero, the medium at rest is called **hydrostatic** ($\rho = \text{const.}$) or **aerostatic** (ρ variable). Similarly regimes where the fluid is in motion are called **hydrodynamic** or **aerodynamic**.

	Material at rest		Flow	
	Hydrostatic	Aerostatic	Hydrodynamic	Aerodynamic
	incompressible	compressible	incompressible	compressible
Examples	standing column of water	Atmosphere at rest	moving liquid	moving gas

Fig. 1.16 : Division of flow regimes

Examples are shown in Figure 1.16. For example, hydrostatics treats the linear pressure distribution in a standing column of water, aerostatics the pressure and temperature (or density) distributions in the atmosphere at rest, hydrodynamics the water flow past a plate, and aerodynamics the flow past a wing.

Flow Past a Wing

Let us consider the first technical flow problem, the flow past the wing of an airplane. This was already introduced in Chapter 1.1. Figure 1.17 shows the wing of an Airbus A310. The flow is from the left of the wing, with **Mach number** M_∞ (ratio of the free stream velocity u_∞ to the speed of sound a_∞ , velocity of propagation of small perturbations). The free stream here has a subsonic Mach number of $M_\infty \approx 0.8$. A further dimensionless characteristic number which describes the viscous boundary layer regime of the flow past a wing is the **Reynolds number**, Re_L , which is made up of the free stream velocity u_∞ , the depth of the wing L and the kinematic viscosity ν ($\nu = \mu/\rho$): $Re_L = u_\infty \cdot L/\nu$. For civil airplanes it has a value of about $Re_L \approx 7 \cdot 10^7$.

In flights, the flow losses must be kept low, so that the ratio between lift and drag attains as high a value as possible. In order to achieve this, the engineer must be aware of the different flow phenomena, so that the computational methods can be applied appropriately.

However, it is not only the flow past a wing at altitude which is of interest. The design of the wing must be such that it generates enough lift at take-off and landing, with the use of additional high lift flaps. In addition, the development of an airplane must take into

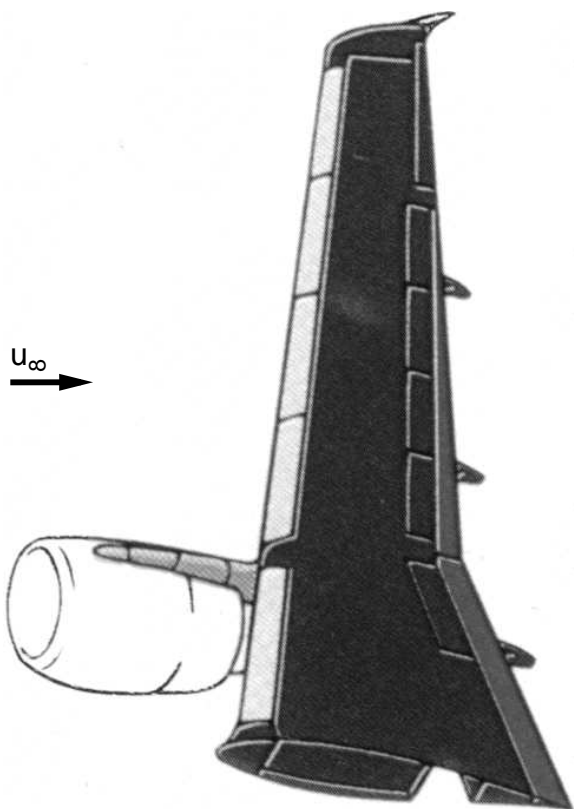


Fig. 1.17 : Wing of a civil airplane

account how the fuselage and engines of the plane affect the flow past the wing, and what, for example, the best position is for the engines.

Analytical and, to an even greater extent, numerical methods are used to answer all these questions. During the design phase, the engineer endeavors, with the help of a few wind tunnel experiments, to keep the development costs and time as low as possible. In addition, the optimization of an Airbus wing and the investigation of the lift and drag behavior at different angles of attack, for example, would be inconceivable without modern fluid mechanical methods.

The flow regimes at a section of a wing are shown in Figure 1.18, both with the dimensionless pressure distribution indicated, as well as the flow made visible with small particles. For the discussion that follows, we need the dimensionless **pressure coefficient** c_p , which is defined as follows:

$$c_p = \frac{p - p_\infty}{\frac{1}{2} \cdot \rho_\infty \cdot u_\infty^2} . \quad (1.2)$$

p is the pressure at an arbitrary position in the flow field, with p_∞ , ρ_∞ and u_∞ denoting the pressure, density and velocity respectively in the free stream. Figure 1.18 shows the values of $-c_p$ on the wing, indicating the negative pressure on the upper side (suction side) and the over-pressure on the lower side (pressure side) compared to the free stream. The free stream with the velocity u_∞ is decelerated along the stagnation line. At the leading edge of the wing, the flow comes to rest, reaching its maximum pressure coefficient of c_p ($-c_p$ minimum). This point on the wing is called the stagnation point.

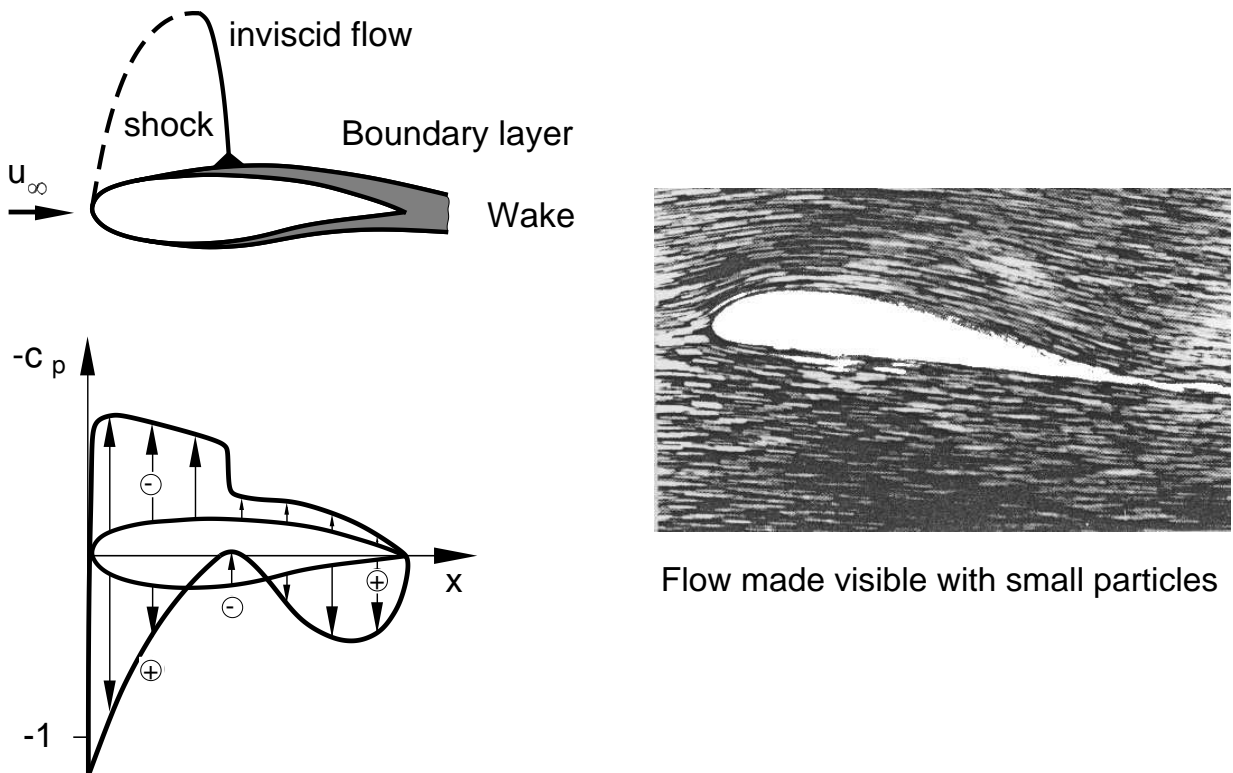


Fig. 1.18 : Flow regimes and pressure distribution on a wing

Moving away from the stagnation point, the stagnation line branches towards the suction and pressure sides. We will first look at $-c_p$ along the suction side. The flow is greatly accelerated from the stagnation point along the upper side (the $-c_p$ value becomes larger) and on the front part of the wing it reaches supersonic velocities. Further downstream, the flow is decelerated through a jump in pressure, called a **shock wave**, to subsonic velocities again (there is a sharp drop in the $-c_p$ value). The flow is then further decelerated towards the trailing edge.

On the pressure side, the flow is also accelerated away from the stagnation point. However the acceleration close to the nose is not as great as that on the suction side, so that no supersonic velocities occur on the entire pressure side. At about the middle of the wing, the flow is again decelerated, and the $-c_p$ value approaches the $-c_p$ value on the suction side downstream. At the trailing edge, the pressure coefficients of the pressure and suction sides are approximately the same.

A thin **boundary layer** forms on the suction and pressure sides. The suction and pressure side boundary layers meet at the trailing edge and form the **wake flow** further downstream. Both the flow in the boundary layer and the flow in the wake are **viscous**. Outside these regions, the flow is essentially **inviscid**.

The different properties of the different flow regions result in different equations to compute each flow. In boundary layer flows it is the boundary layer equations which hold, to good approximation. On the other hand, calculating the wake flow and the flow close to the trailing edge is more difficult. In these regions the Navier-Stokes equations have to be solved. The inviscid flow in the region in front of the shock may be tackled with comparatively less difficulty using the inviscid equation.



Fig. 1.19 : Flow traces on the surface of a wing in a wind tunnel

Figure 1.19 shows traces of color indicating the flows on a wing in a wind tunnel experiment. It is seen that the color follows straight lines in a large area of the width of the wing. The statements made above are valid in these regions. Close to the body of the plane, the flow lines are no longer straight, and they form a vortex on the rear surface of the wing. In the following chapters, this concept will be used together with the idea of **flow separation**, which has a considerable influence on the behavior of an airplane.

As we conclude the example of a wing, we consider the question of why the wing of a civil airplane, in contrast to that of a glider, is swept. This is because of the Mach number dependence of the dimensionless drag coefficient c_w at high Mach numbers of 0.8. We introduce the **drag coefficient** c_w with

$$c_w = \frac{W}{\frac{1}{2} \cdot \rho_\infty \cdot u_\infty^2 \cdot A} \quad (1.3)$$

where W is the drag and A the cross-sectional area of the wing. The drag increases greatly for transonic flows. Since the aim in civil aircraft is to fly as fast as possible (high Mach number), but with as low a drag as possible to keep the fuel consumption down, the wing is swept to about $\phi = 30^\circ$. The geometric relation

$$M = M_\infty \cdot \cos(\phi)$$

lowers the local Mach number at that section in the profile of the wing by the value $\cos(\phi)$, reducing the drag coefficient by the corresponding amount. This means a civil aircraft can fly at Mach number $M_\infty = 0.8$ at an altitude of 10 km with a velocity of 950 km/h.

Flow Past an Automobile

One of the first steps in developing an automobile is to decide on its contour. This is determined more by the designer than by the aerodynamic engineer. The limits within which the engineer determines the possible variations in the contour (Figure 1.20) are small compared to the length or width of the automobile to be developed.

Taking these guidelines into account, the aerodynamic engineer optimizes the contour so that the flow drag is as small as possible. In recent years vehicles have been developed whose drag coefficients c_w are smaller than 0.3.

However, minimizing the drag is certainly not the only job of the aerodynamic engineer at the design stage. At the same time, all the forces and moments which arise in an air flow have to be taken into account in optimizing the contour. In particular, the lift force, the side-wind force and the moment about the main axis of the vehicle are important, since these influence the driving stability to the greatest degree. In addition, the aerodynamic engineer has to ensure that the wind noises are minimal, that the windows do not become dirty during travel, that the side mirrors do not vibrate at high speeds, and so on.

In contrast to the flow past the wing of an airplane, the flow past an automobile can be described as **incompressible** to good approximation. This is because the variations in density are small. As in the case of the wing, in Figure 1.21 we differentiate between different **flow regimes**: **inviscid flow**, **boundary layer flow** and **viscous wake flow**.

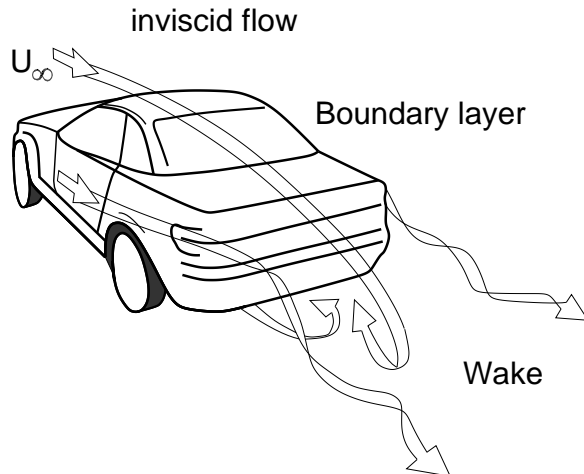
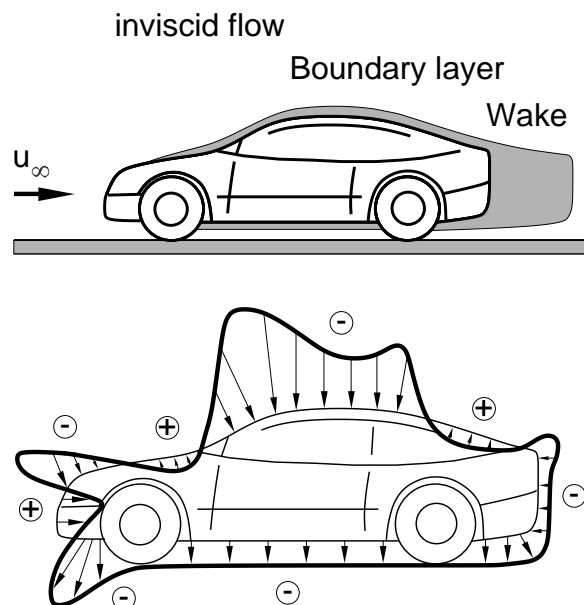


Fig. 1.20 : Flow past an automobile

The pressure distribution has a stagnation point at the radiator. The flow is accelerated along the hood, leading to a pressure drop. At the windshield, the flow is again blocked, leading to an increase in pressure. After the pressure minimum has been reached on the roof, the flow is decelerated, with a pressure rise. Downstream of the trunk the boundary layer flow turns into the wake flow.

The flow in the wind tunnel experiment is made visible with smoke, and this shows that downstream from the back of the automobile, a backflow region forms. This is shown as the dark region into which no flow indicators (white smoke particles) can penetrate.

If we consider the flow under the automobile we see that the lower ground flow can be considered to be a gap flow whose upper boundary is rough. The average height of the roughness is about $\approx 10 \text{ cm}$ for an automobile. This means that the flow directly at the upper wall has to be assumed to be swirled.



wake flow

Fig. 1.21 : Flow regions and pressure force on an automobile

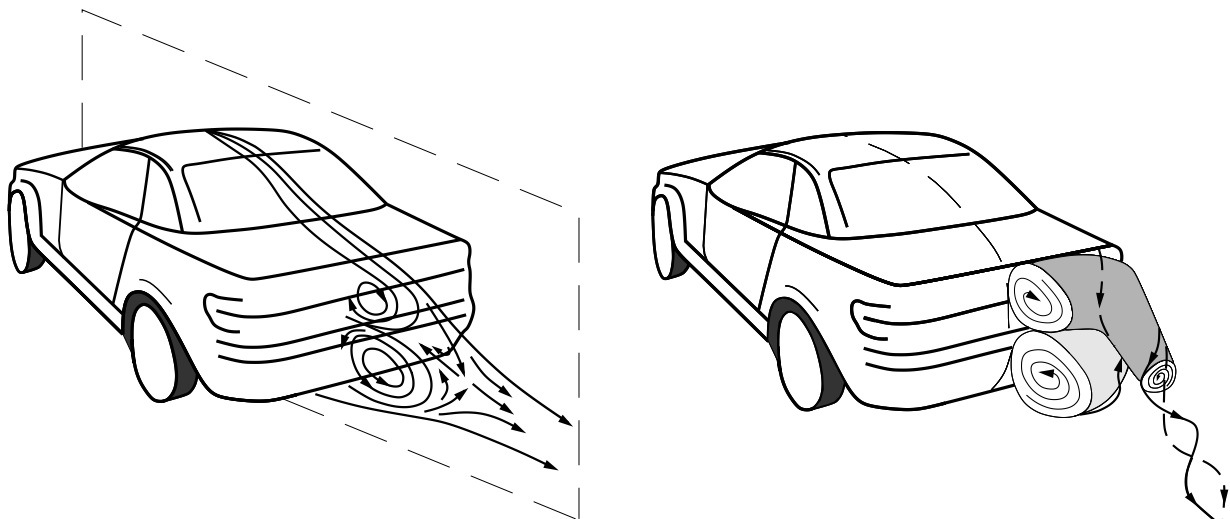


Fig. 1.22 : Structure of the wake flow of a vehicle

In order to avoid the flow being swirled like this, front spoilers are placed on many automobiles in the lower region of the vehicle, in front of the entrance to the gap. The result of this is that a large part of the flow does not pass under the vehicle, where the swirling would lead to an increase in the drag. The savings made in this way are greater than the losses due to the extra drag of the spoiler.

The pressure force on the upper contour is considerably smaller in most regions than that under the vehicle, and this pressure difference leads to a lift. In the aerodynamic design, one attempts to keep both the lift and the drag small. As already mentioned in the discussion of the flow below the automobile, in many cases of application, changes are made to the contour and spoilers are introduced, which divert the flow so that the vehicle experiences a reduction in lift.

Let us come back to the wake flow downstream of the vehicle. In Figure 1.22 the structure of the flow in a cross-section through the vehicle is considered. We recognise the backflow region with a stagnation point on the surface of the vehicle, together with a saddle point downstream in the the flow field, where the flow lines branch into the wake flow and the backflow region. Completing the three-dimensional structure of the wake flow, as in the right-hand picture in Figure 1.22, we see that in the upper region of the roof of the trunk a so-called horseshoe vortex forms, seen when snow is driven together at the rear of a vehicle.

Liquid-Steam Separator

In **chemical production plants** quite different **flow regimes** have to be taken into consideration. If we take the example of a liquid-steam separator, we have to differentiate between liquid flows in pipes and bubble flows, drop flows and steam flows. Liquid-steam separators are to be found, for example, in refineries for the extraction of heavy hydrocarbons from crude oil gas.

Figure 1.23 shows a basic sketch of such a set-up. It consists of a throttle valve, the separator (demister), the steam compressor and the pump which produces a pressure drop and undercooling of the liquid.

An incompressible liquid is present in flow region **1**. This is guided via a throttle valve into flow region **2**, a two-phase flow (liquid and steam). By means of an adiabatic throttle process, an obstacle such as a shut-off valve or a test diaphragm is used to produce a pressure drop $\Delta p = p_1 - p_2$ with $p_2 < p_1$, with the temperature T , or the enthalpy h of the liquid remaining constant (log(p)- h diagram). The two-phase flow in **2** is then directed to a separator or demister, where isobaric separation of liquid and steam takes place.

After separation, a compressible steam flow is present in region **3**, and an incompressible liquid flow in region **5**. These processes can be discussed by means of a thermodynamic log(p)- h diagram. Here the pressure p is plotted on a logarithmic scale against the enthalpy h of the medium.

A mixture of liquid and steam is present in the two-phase or wet steam regime. This regime is defined to the left by the lower limiting curve and to the right by the upper limiting curve. Both curves meet at the critical point K . The lower limiting curve is the connecting line of all points at the start of evaporation, and separates the liquid from the two-phase regime. The upper limiting curve is the connection of all points at the end of evaporation and separates the two-phase regime from the steam. As is usual in thermodynamics, the variable X denotes the amount of steam in the vapor, so that the lower limiting curve is denoted by $X = 0$ and the upper by $X = 1$.

By choosing different pressure differences Δp in the throttle, different flow regions **2** in the two-phase regime can be attained. This is indicated on the log(p)- h diagram by the thin lines. The steam flow **2** is compressed, leading to a compressible gas flow in flow region **4**. In general, steam is any gas-like substance close to the limiting curve. The compressor ensures that the thermodynamical state of the medium in region **4** in the log(p)- h diagram is at a greater distance from the limiting curve than the steam in region **3**. That is why the flow downstream from the compressor is called a gas flow rather than a steam flow.

Inside the pump, where the incompressible liquid flow passes over from flow region **5** to flow region **6**, the accelerating moving liquid can produce large pressure drops. Therefore it has

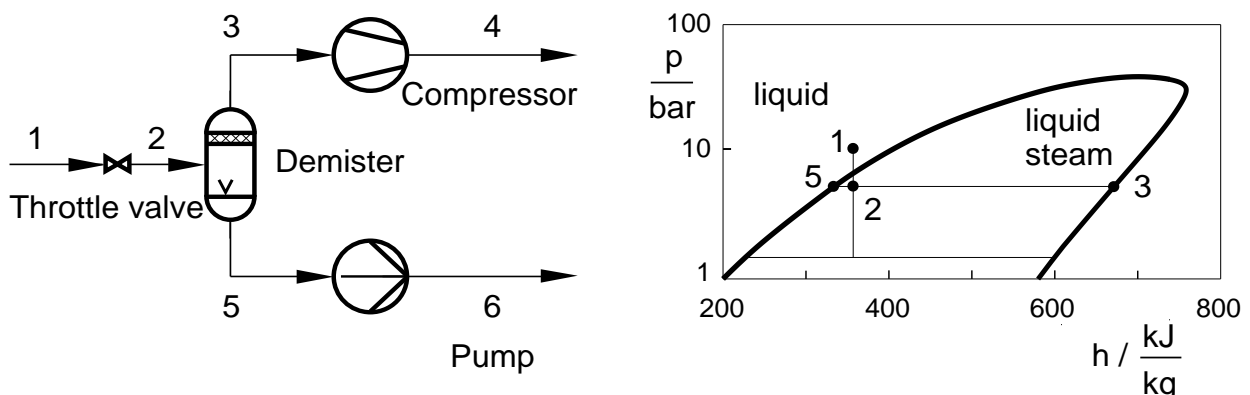


Fig. 1.23 : Sketch and pressure-enthalpy diagram of a liquid-steam separator

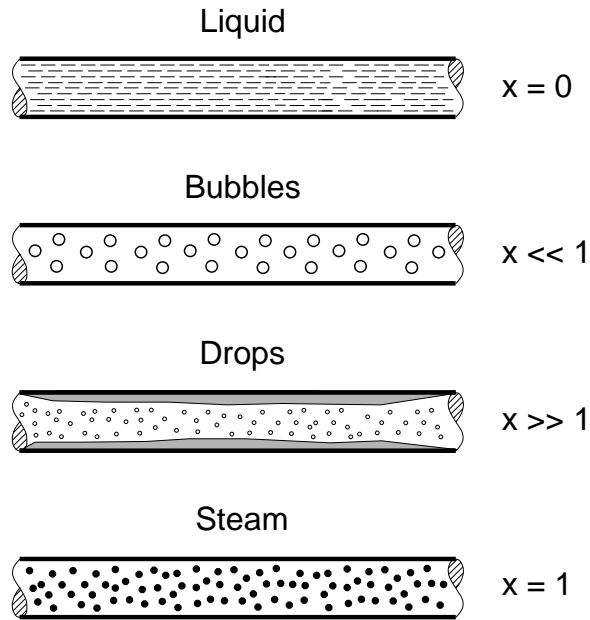


Fig. 1.24 : Flow regions in a two-phase flow

to be ensured that the minimum static pressure p_{min} does not fall below the steam pressure p_D . This would lead to damaging cavitation effects which could destroy the pump.

The flow regime **1** as well as the regions **5** and **6** are typical examples of the incompressible flows through straight or curved pipes which frequently appear in technical applications. As a fluid flows through such pipes, friction effects lead to pressure losses Δp_V which have to be determined. For example, knowledge of these pressure losses is necessary in order to choose suitable pumps with appropriate efficiency. The flow region **2** of the two-phase flow, where the fluid is present in two aggregate states, is a typical example from process engineering. Flow regions **3** and **4** are examples of compressible flows, where, as well as the variations in pressure and velocity, the variation in the state variables density ρ and temperature T also have to be taken into account.

Figure 1.24 shows the flow regimes of the two-phase flow. In the different pipe systems of the liquid-steam separator we distinguish between the liquid flow with $X = 0$, the bubble flow in liquid with $0 < X << 1$, the drop flow with fluid film at the walls of the pipe with $0 << X < 1$, and the steam flow with $X = 1$.

1.3 Product Development

Whereas the aim of a scientist is to determine the mathematical and physical descriptions of flow processes, and thus derive the continuum mechanical fundamental equations, the engineer must implement this scientific knowledge in new products. The fundamentals of fluid mechanics described in Chapter 2 are necessary to do this, but so too are the analytical and numerical methods of solution and the fluid mechanical software of Chapter 3 needed to solve the fundamental equations. The formal development process of a new product is therefore always the same.

If we follow the development of a wing of an airplane, we first have to set out the **requirements**. The airplane has to convey, for example, 250 passengers at an altitude of 10 km over a distance of 7,500 km at Mach number $M_\infty = 0.8$. The requirements which, for example, the Airbus A300 satisfies lead to the following lift coefficient required for transport of the payload:

$$c_a = \frac{A}{\frac{1}{2} \cdot \rho_\infty \cdot u_\infty^2 \cdot A_F} \quad (1.4)$$

with lift force A , free stream velocity u_∞ and wing surface area A_F . It also has to be taken into consideration that the airplane will take off and land with a speed of about 250 km/h. This necessitates the integration of high-lift flaps into the wings, to increase the surface area of the wing at take-off and landing in correspondence to the lower velocity, so as to reach the required lift.

The development engineer must design a wing which will have as low a drag as possible, in order to minimize the engine's fuel consumption. The flight Mach number of $M_\infty = 0.8$ leads to a sweep angle of $\phi = 30^\circ$. In addition, the integration of the wing into the cylindrical body of the airplane must be carried out, and the number of engines necessary for propulsion determined.

The first job for the development engineer is the **preliminary design**, as shown in Figure 1.25. The curvature of the wing profile is provisionally determined, using simple methods which we will meet in Chapter 2. The pressure distribution c_p sketched in Figure 1.26 has to satisfy the required lift coefficient c_a and simultaneously have a drag coefficient c_w

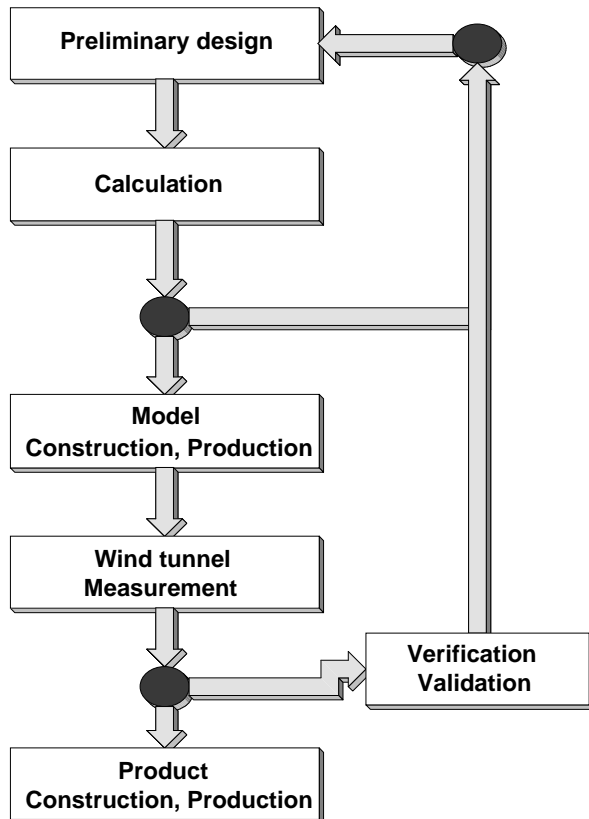
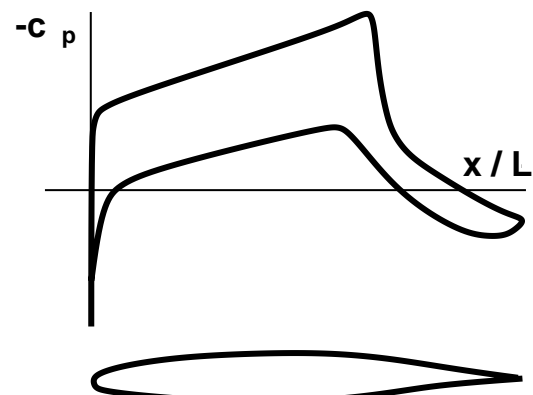


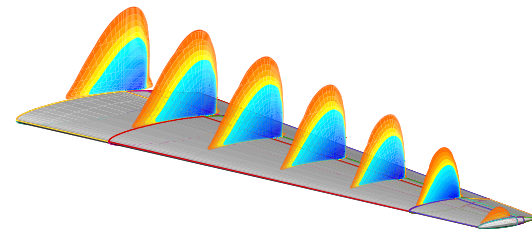
Fig. 1.25 : Product development

which is as low as possible. In the second step, the **calculation** of the swept wing designed with this profile is carried out. At this stage, the warping of the wing and its integration into the body of the plane also have to be taken into account. To do this we require the fluid mechanical software as presented in Chapter 3, as well as the simplifications of the fundamental equations in the different flow regions. These equations form a system of partial differential equations which have to be solved approximately using numerical methods. The first calculation of the wing generally will not attain the required lift coefficient c_a , or the computed drag coefficient c_w will still be too large. A further iteration step is then necessary to get an improved preliminary design with the computed data. This design iteration is carried out in 2 to 3 steps.

Preliminary design



Calculation



Wind tunnel experiment



Fig. 1.26 : Wing design: preliminary design, calculation, wind tunnel experiment, verification and validation

If the required aerodynamic coefficients are satisfied, the second step of the design process takes place, the **construction** and the **building** of the **wind tunnel model**. This generally consists of stainless steel, and has numerous pressure holes to allow the measurement of the pressure distribution at different cross-sections of the wing.

In Chapter 2 we will learn that the integral of this pressure distribution permits the calculation of the required forces. As shown in Figure 1.26, the wing model is fitted out with model engines, so that the airplane model in the wind tunnel is geometrically similar to the original.

Extensive measurements are now carried out in different wind tunnels. The wing is investigated at the free stream Mach number $M_\infty = 0.8$ (950 km/h , 10 km altitude) and at different angles of attack, as well as in the take-off and landing phases with extended landing flaps, that is, with a larger wing surface and a lower speed of 250 to 300 km/h .

The results of the calculation may not initially agree with the wind tunnel results. This is because of the mathematical and physical difficulty of the numerical solutions, and because of experimental errors and disturbances in the wind tunnel.

The next important step in the design process is **verification** and **validation**. These require all the engineering skills of the developer. Verification is the comparison of the experimental results with the numerical results, as well as the adaptation of the numerical methods of solution and the instrumentation in the wind tunnel. Validation requires the further development of the physical models in the fundamental equations of the different flow regimes. This is a very time-consuming process which has a great influence on the development time of an airplane.

As shown in Figure 1.26, in the verification and validation phases, the calculation, or the preliminary design, are corrected in 3 to 4 iteration steps, until the initial requirements are satisfied. In each iteration step, a new wind tunnel model has to be built, and the time-consuming measurements in the wind tunnels repeated. The fewer the number of iteration steps which have to be carried out, the more successful the design process.

We have described the development steps of an airplane using the example of the aerodynamics of the wing. Similar development processes are also carried out for the structure of the plane, the development of the engines, the flight mechanics and the system integration in the cockpit. Therefore different disciplines are interconnected in the different design processes. If we consider how many different companies in different countries are involved in the European project Airbus (Figure 1.27), for example, we can see how complex the development of an airplane is. The same is true of the development of an automobile, a flow engine or a process engineering production plant. For each of these, the development process described, using the example of a wing, has to be carried out for each of the disciplines involved.

At the end of the development process comes the **verification** of the **finished product**. In the case of an airplane, this is its first flight and consequent registration. The airplane has to prove itself in certain extreme flight conditions. Only minimal changes to the airplane can now be carried out. Any development errors which were discovered during the design cycle can now only be corrected up to a point. For example, when developing the Airbus A320, the interaction between the relatively large engines and the body of the plane was

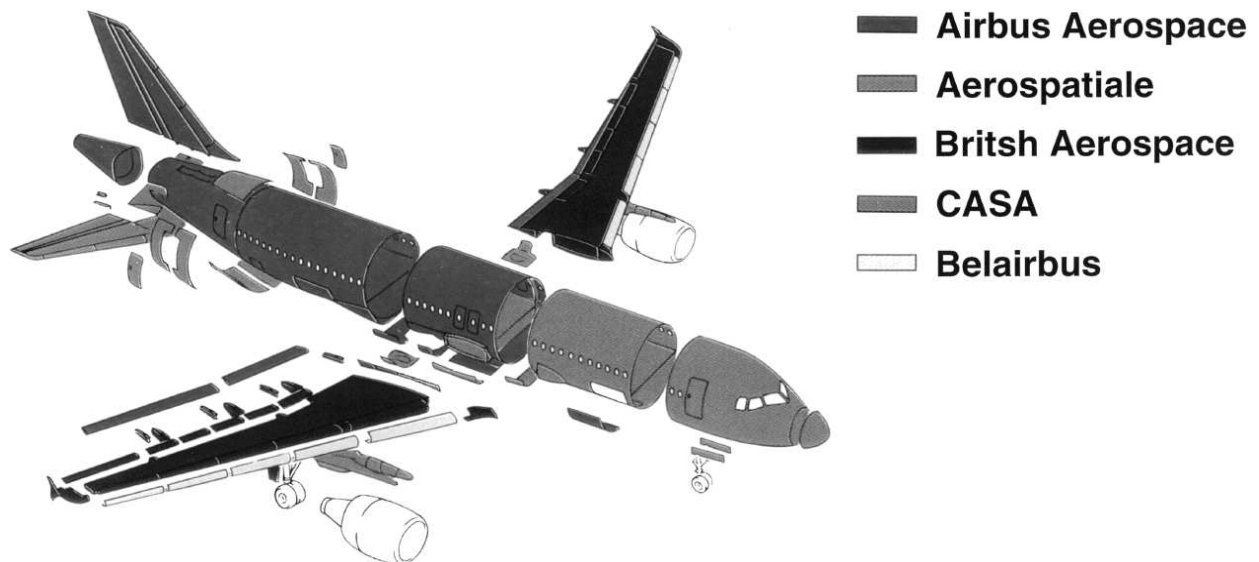


Fig. 1.27 : Construction elements of an Airbus A320

not given enough attention. This manifests itself in an unpleasant drone in the body of the plane during take-off. The experiences gained in the final verification are retained in the databases of the airplane manufacturers and can be taken into account right at the start of the preliminary design of the next project.

2 Fundamentals of Fluid Mechanics

2.1 Flow Properties

We distinguish between the **kinematic properties** of the flow, and the **transport properties** and **thermodynamic properties** of the fluid. While the kinematic properties velocity \vec{v} , angular velocity $\vec{\omega}$, acceleration \vec{b} , and vortex strength $\vec{\omega}_R$ are properties of the flow field and not of the fluid itself, we will see in Chapter 2.3.1 that the transport properties viscosity, heat conduction and mass diffusion, as well as the thermodynamic properties pressure p , density ρ , temperature T , enthalpy h , entropy s , the specific heats c_p, c_v , and the expansion coefficient α are properties of the fluid. First of all we present the definitions of the fundamental concepts. For further details we recommend PRANDTL-Guide of Fluid Mechanics 2001, and BIRD, STEWART, LIGHTFOOT 1960.

2.1.1 Transport Properties

One transport property which we have already met is the **friction**. It determines the **momentum transport** in the viscous flow regimes and is linked to the gradient of the velocity vector \vec{v} . For example, heavy oil or tar need a long time to flow out of a container, whereas light oil flows faster.

In order to introduce the **shear stress** τ , we look at the one-dimensional flow problem in Figure 2.1. Between a lower plate at rest and an upper plate moving with constant velocity U , there is a constant shear rate with linear velocity profile $u(z)$. This is called **Couette flow**. The boundary condition on the surfaces of the plates is the **no-slip condition**, which on the lower plate leads to $u = 0$ and on the upper plate $u = U$. In order to maintain the constant velocity U in the presence of the friction, a constant force F is required. The applied force is proportional to the drag velocity $F \sim U$, proportional to the plate surface area A , $F \sim A$ and inversely proportional to the height of the gap H , $F \sim 1/H$.

Thus the force is

$$F \sim \frac{U \cdot A}{H}$$

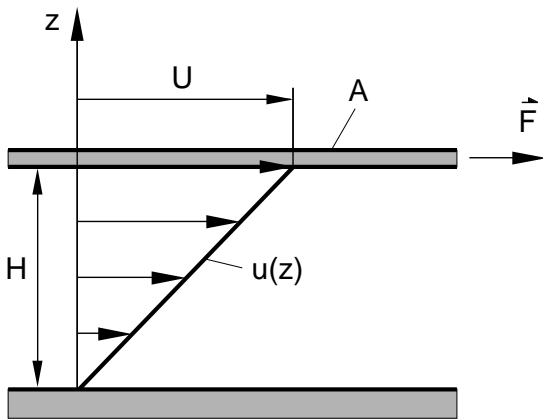


Fig. 2.1 : Couette flow, definition of shear stress τ

or with the constant of proportionality μ

$$F = \mu \cdot \frac{U \cdot A}{H} .$$

μ is a material constant of the fluid which is called the dynamic viscosity. It has the dimensions $[F \cdot T / L^2]$ with the force F , the characteristic time T and the characteristic length L , in our example the gap height H , and the units $\{Ns/m^2\}$.

The shear stress τ (shear rate) is

$$\tau = \frac{F}{A} = \mu \cdot \frac{U}{H}$$

with the units $\{N/m^2\}$. For Couette flow we have the linear velocity profile

$$\frac{U}{H} = \frac{du}{dz} .$$

This yields

$$\boxed{\tau = \mu \cdot \frac{du}{dz}} .$$

(2.1)

If this linear relationship between the shear stress τ and the velocity gradient du/dz holds, the fluid is a **Newtonian fluid**. Examples of Newtonian media are water, smoothly flowing oil and gases.

Using the relationship already derived, we can already discuss an important technical application. Air bearings have a particularly small friction drag. If, for example, we move a glass plate on a 0.1 mm thick air cushion with a constant velocity of 0.1 m/s , we have

$$\frac{du}{dz} = \frac{U}{H} = 10^3 \left\{ \frac{1}{s} \right\} ,$$

for air at $20^\circ C$, $\mu = 1.71 \cdot 10^{-5}\text{ Ns/m}^2$, and so

$$\tau = \mu \frac{du}{dz} = 1.71 \cdot 10^{-2} \left\{ \frac{N}{m^2} \right\} .$$

With a plate surface area of $A = 0.01\text{ m}^2$ we obtain the very small force

$$F = \tau \cdot A = 1.71 \cdot 10^{-4}\{N\} .$$

In general flows are not, as assumed until now, one-dimensional. There are three shear stress components for each spatial direction, that is 9 components of the shear stress tensor τ_{ij} . These characterize the friction in the three-dimensional flow field. In this terminology, the shear stress component τ_{xz} in Couette flow determines the velocity profile $u(z)$, with x the direction of flow and z the vertical coordinate

$$\tau_{xz} = \mu \left(\frac{\partial u}{\partial z} + \frac{\partial w}{\partial x} \right) .$$

For the one-dimensional theory, to be treated in Chapter 2.3, with w and $\partial w/\partial x$ equal to zero, it suffices to set

$$\tau_{xz} = \tau = \mu \frac{du}{dz} .$$

As well as Newtonian fluids, we also have **non-Newtonian fluids**. In this case the functional relation in equation (2.1) is non-linear. Some examples of non-Newtonian fluids are shown in Figure 2.2. The curves for fluids which cannot withstand a shear rate must go through the origin. So-called yielding fluids have a finite shear stress even for vanishing velocity gradients. These fluids behave partly as rigid bodies and partly as fluids. The slope of the curves for pseudo-elastic fluids such as molten metal or high polymers decrease as the shear stress increases. In contrast to this, dilatant fluids, such as suspensions, have an increase in the slope. Toothpaste and mortar are examples of ideal Bingham materials. The finite value of τ at $du/dz = 0$ follows the linear progression of a Newtonian fluid. In addition to this, the shear stress of some non-Newtonian media is time dependent. Even if the shear rate is kept constant, the shear stress changes. An ansatz frequently used for non-Newtonian media is

$$\tau_{xz} \approx K \cdot \tau_{xz}^n , \quad (2.2)$$

where K and n are material constants. For $n < 1$ we have a pseudo-elastic fluid, $n = 1$ with $K = \mu$ is a Newtonian fluid, and for $n > 1$ a dilatant fluid. Note that the ansatz (2.2) yields unrealistic values for the root in Figure 2.2.

Numerous other laws have been derived for non-Newtonian media, mainly from experimental results. In what follows we will no longer consider these and will restrict ourselves to Newtonian fluids.

The viscosity μ of a Newtonian fluid is directly related to the interaction forces between the molecules of the flowing medium. If we consider the interaction force between two molecules in the air (nitrogen, oxygen) in Figure 2.3, we see that at large distances r the molecules have a negative attraction, and at small distances they have a positive repulsion. The attractive force between the molecules results from the Van der Waals interaction, whose

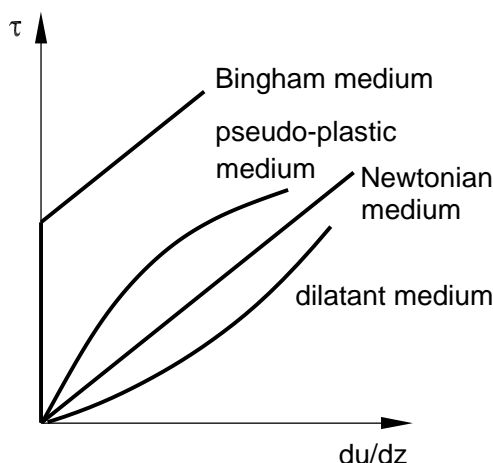


Fig. 2.2 : Shear stress τ for Newtonian and non-Newtonian fluids

origin lies in the dipole moment produced by the deformation of the electron shells. The almost exponential repulsion is due to the electrostatic repulsion of shells with like charge. In a collision between molecules due to their eigen-motion, this interaction will first act to attract the molecules and then to repel them strongly. This interaction of the 10^{23} molecules per mole in the air causes not only friction, but also heat conduction and diffusion. Since the eigen-motion of the molecules, and thus also their collision probability, depends on the temperature T and pressure p , the viscosity μ is also temperature and pressure dependent.

Figure 2.4 shows the qualitative temperature dependence for liquids and gases at constant pressure. In liquids, the kinematic viscosity μ decreases with increasing temperature, whereas in gases it increases. The viscosity of liquids and gases increases with increasing pressure.

Following this brief digression into molecular physics, we look at the reason for the boundary conditions at fixed walls. The no-slip conditions $\vec{v} = 0$ is due to the fact that the interaction between the molecules of the fluid and the crystal lattice at the fixed surface is considerably larger than that between the fluid molecules themselves. In continuum mechanical conditions, to which we will restrict ourselves in this textbook, each fluid molecule sticks to a fixed wall on collision.

The energy transport through **heat conduction** can be developed analogously to the friction. In Figure 2.5 the linear temperature profile $T(z)$ in a fluid layer at rest between two horizontal plates with the temperature T_1 and T_2 corresponds to the linear velocity profile $u(z)$ of Couette flow. The heat flux q , which is the amount of heat transferred per unit time Q per area A , corresponds to the shear stress τ .

$$\tau = \frac{F}{A} = \mu \cdot \frac{du}{dz} ; \quad q = \frac{Q}{A} = -k \cdot \frac{dT}{dz} . \quad (2.3)$$

The heat flux q can be written as the Fourier law

$$q = -k \cdot \nabla T . \quad (2.4)$$

For the one-dimensional case under consideration, dT/dz corresponds to the velocity gradient du/dz . This analogy is only valid for the one-dimensional case. For three-dimensional flow, we have already stated that the shear stress τ_{ij} is a tensor with 9 components, while \vec{q} is a vector.

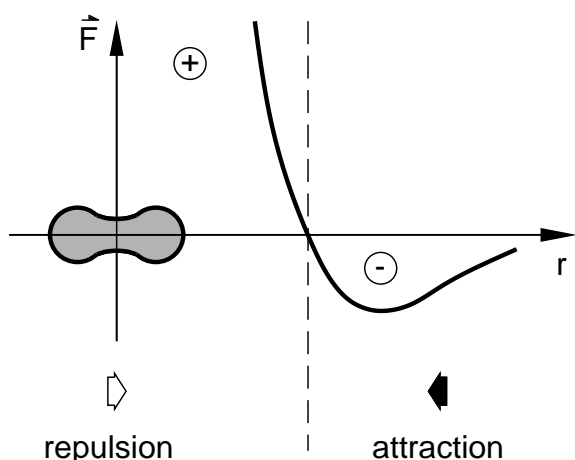


Fig. 2.3 : Inter-molecular interaction force \vec{F}

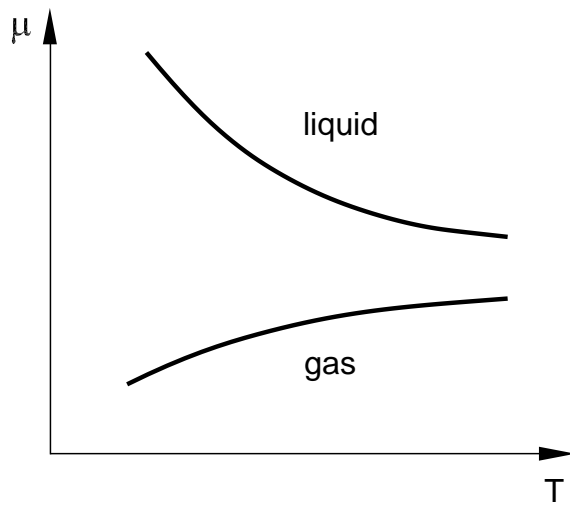


Fig. 2.4 : Temperature dependence of the dynamic viscosity μ

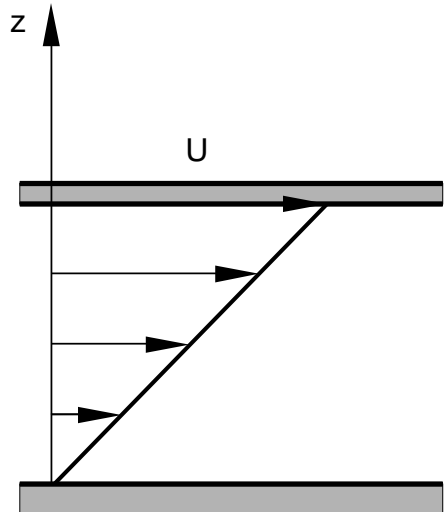
Introducing the kinematic viscosity with

$$\nu = \frac{\mu}{\rho} \left[\frac{L^2}{T} \right] \left\{ \frac{m^2}{s} \right\} ,$$

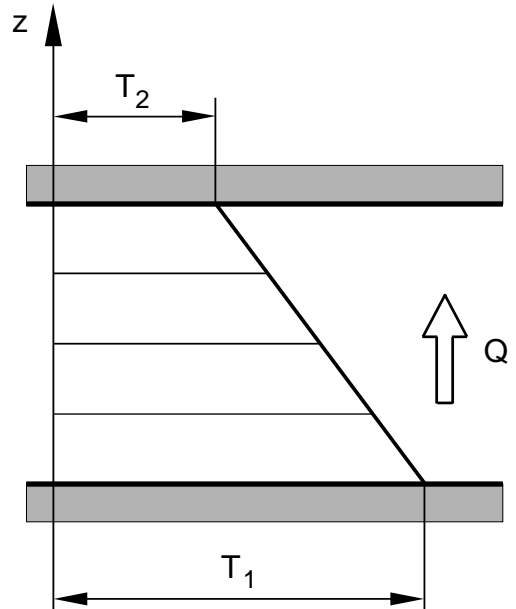
the thermal diffusivity $a = k/(\rho \cdot c_p)$, which has the same dimensions as ν , can be used to form a dimensionless characteristic number

$$Pr = \frac{\nu}{a} .$$

The **Prandtl number Pr** describes the ratio of momentum transport (friction) to energy



Couette flow



heat conduction

Fig. 2.5 : Analogy between friction and heat conduction

transport (heat conduction) in the fluid under consideration. Gases have the Prandtl number 0.71, water 6.7, oils several thousand.

The mass diffusion (mass transport) in the fluid may be treated equivalently if two media with partial densities ρ_i ($i = 1, 2$) mix together due to a concentration gradient. The concentrations of the two components are $C_i = \rho_i/\rho$, with the total density of the mixture ρ . In analogy to friction and heat conduction, we postulate that the mass flux per unit time m_i for the substance i is written as

$$\frac{m_i}{A} = -D \cdot \nabla(\rho_i) \quad ,$$

with the diffusion coefficient $D[L^2/T]\{m^2/s\}$. For mass concentrations C_i , Fick's law is written

$$\frac{m_i}{A} = -D \cdot \nabla(\rho \cdot C_i) \quad .$$

In analogy to the Prandtl number, the dimensionless Schmidt number Sc and the Lewis number Le for the mass diffusion can be defined as follows:

$$Sc = \frac{\nu}{D} \quad , \quad Le = \frac{D}{a}$$

The Schmidt number describes the ratio of momentum transport to mass diffusion, the Lewis number the ratio of mass diffusion to energy transport.

2.1.2 Thermodynamic Properties

Classical thermodynamics, as taught in freshman courses, cannot be directly applied to fluid mechanics, since a viscous flow is not in thermodynamic equilibrium. However, in most technical applications, the deviation from **local thermodynamic equilibrium** is so small that it may be neglected. There are two exceptions: flows with chemical reactions and sudden changes in the thermodynamic variables of state, such as can occur in strong shock waves, to be treated in Chapter 2.3.3.

The most important thermodynamic quantities are pressure p , density ρ , temperature T , entropy s , enthalpy h and the internal energy e . Two of these six quantities suffice to determine a thermodynamic state uniquely, as long as these are thermodynamic variables of state. The most important relations which we will need in the following chapters will now be discussed briefly.

The **first law of thermodynamics** is written

$$dE = dQ + dW \quad , \tag{2.5}$$

with dE the total energy of the system under consideration, dQ the heat supplied and dW the work done by the system. For a fluid at rest

$$dW = -p \cdot dV \quad , \quad dQ = T \cdot ds \quad ,$$

where V is the volume. Thus (2.5) per unit mass becomes

$$de = T \cdot ds + \frac{p}{\rho^2} \cdot d\rho \quad . \quad (2.6)$$

Writing the total differential describing the change in the internal energy as

$$de = \frac{\partial e}{\partial s} \cdot ds + \frac{\partial e}{\partial \rho} \cdot d\rho \quad ,$$

we obtain

$$T = \frac{\partial e}{\partial s}|_{\rho} \quad , \quad p = \rho^2 \cdot \frac{\partial e}{\partial \rho}|_s \quad .$$

The enthalpy is by definition

$$h = e + \frac{p}{\rho} \quad ,$$

and so with (2.6) the first law of thermodynamics can be written in the form

$$dh = T \cdot ds + \frac{1}{\rho} \cdot dp \quad .$$

(2.7)

The temperature T and $1/\rho$ are then

$$T = \frac{\partial h}{\partial s}|_p \quad , \quad \frac{1}{\rho} = \frac{\partial h}{\partial p}|_s.$$

The **thermal equation of state** for the ideal gas is

$$p = R \cdot \rho \cdot T \quad ,$$

(2.8)

with the gas constant R . This yields the speed of sound a

$$a^2 = \frac{\partial p}{\partial \rho}|_s = \kappa \cdot R \cdot T \quad , \quad (2.9)$$

with the dimensionless ratio of the specific heats κ

$$\kappa = \frac{c_p}{c_v} \quad , \quad c_p = \frac{\partial h}{\partial T}|_p \quad , \quad c_v = \frac{\partial e}{\partial T}|_v \quad . \quad (2.10)$$

For flows with heat transport, the thermal expansion coefficient α is required:

$$\alpha = -\frac{1}{\rho} \cdot \frac{\partial \rho}{\partial T}|_p \quad . \quad (2.11)$$

For ideal gases this yields

$$\alpha = \frac{1}{T} \quad .$$

Liquids generally have thermal expansion coefficients which are smaller than $1/T$. Negative values can also occur, such as in the case of water close to the freezing point. The thermal expansion coefficient can be used to write the dependence of the enthalpy on the pressure as

$$dh = c_p \cdot dT + (1 - \alpha \cdot T) \cdot \frac{dp}{\rho} . \quad (2.12)$$

For an ideal gas, the second term vanishes and the enthalpy depends only on the temperature $h = h(T)$.

In multi-phase flows, as met first in Chapter 1.2, the thermodynamic states close to the critical point are of particular interest. Figure 2.6 shows the isothermal lines of a liquid-steam mixture. The different thermodynamic behavior in the liquid and in the steam phase can be explained by considering the different inter-molecular interaction forces. If a gas is compressed isothermally, the mean translational energy of the molecules remains constant and the mean spacing between neighboring molecules decreases. If the specific volume $1/\rho$ of the gas becomes so small that the mean spacing is only a few molecular diameters, the attractive forces between the molecules become significant. If the temperature exceeds a critical value T_c , a further reduction in the specific volume leads to an unstable state where the molecules are beyond the region of the inter-molecular attractive interaction forces and so begin to form molecule clusters.

This intermediate state between the liquid and gas phases is unstable to the smallest disturbance. A minimal increase in the pressure will lead to complete condensation to a homogeneous liquid with consequently large density, or a small drop in pressure will cause the homogeneous steam phase to occur with correspondingly small density. The almost constant pressure in the transition phase is called the saturation steam pressure.

At temperatures above the critical temperature T_c , the translational energy of the molecules becomes so large that the formation of molecule clusters is prevented. A continuous transition occurs along the isothermal lines from the gas phase to the liquid phase, while the specific volume decreases. In this temperature regime, the Van der Waals equation describes

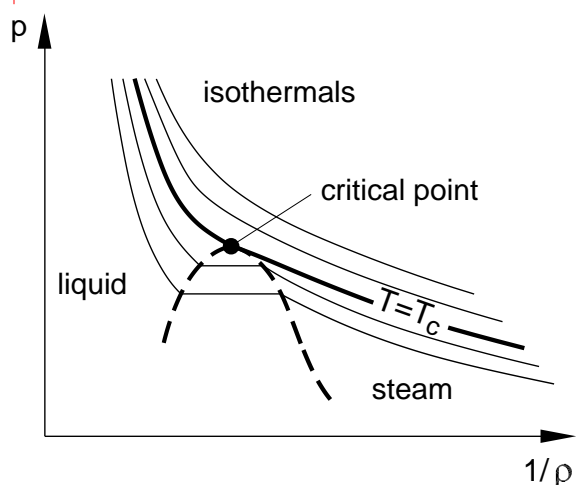


Fig. 2.6 : Isothermal lines of a liquid-steam mixture

the thermodynamic state of real gases:

$$p = \frac{R \cdot \rho \cdot T}{1 - b \cdot \rho} - c \cdot \rho^2 , \quad (2.13)$$

where b and c are constants along the isothermal lines which characterize the attractive force between the molecules.

A further property of fluids is the **surface tension** σ of liquids and the interface tension between different liquids, or between liquids and solids. The temperature dependence of the surface tension can cause flows. Surface and interface tension is also due to the interaction forces between the molecules. Figure 2.7 shows the forces of a molecule in a liquid and of a molecule at the interface between liquid and gas. Within the liquid, the forces on the molecule under consideration balance each other out on average since the molecule is surrounded by the same number of molecules on all sides. At the surface of the liquid, the interaction between the liquid and gas molecules is considerably smaller than that between the liquid molecules. This causes the resulting force \vec{R} , which causes the surface tension σ . By definition this is

$$\sigma = \frac{|\vec{F}|}{L} , \quad (2.14)$$

with the surface force \vec{F} and the length of the surface L . For example, for the interface between water and air $\sigma = 7.1 \cdot 10^{-2} \text{ N/m}$ at a given temperature.

At a doubly curved surface with radii of curvature R_1 and R_2 , the balance of the forces at the surfaces leads to a **pressure jump**

$$\Delta p = \sigma \left(\frac{1}{R_1} + \frac{1}{R_2} \right) . \quad (2.15)$$

This results in a higher pressure on the concave side of the curved surface. For a bubble or drop, with $R_1 = R_2 = r$, the pressure difference across the surface is

$$\Delta p = \frac{2 \cdot \sigma}{r} .$$

A soap bubble with an inner and an outer surface has the following increased pressure inside:

$$\Delta p = \frac{4 \cdot \sigma}{r} .$$

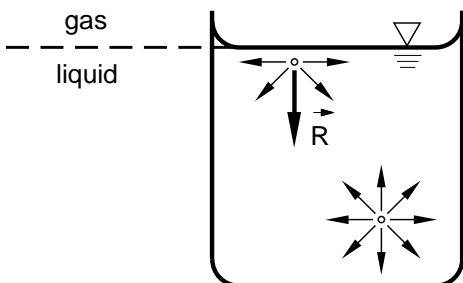


Fig. 2.7 : Surface tension

This pressure difference in a drop causes, for example, a hole in a solid surface to be filled with liquid. The hole is then only filled when the **angle of contact** α between the liquid and the surface is smaller than 90° .

This angle of contact between the liquid and solid surface is determined by the energy of the interfaces. It causes the raising and lowering of a liquid in a capillary.

Let us consider the interfaces between different liquids in Figure 2.8. For example, on a glass surface a mercury droplet will not cause any wetting. The angle of contact α is larger than 90° (about 150°) and the surface tension σ of the mercury is larger than the adhesion force between mercury and glass. For a water droplet on a glass surface, the contact angle α is smaller than 90° and so there is wetting. The surface tension σ of water is smaller than the adhesion force between water and glass. On the other hand, for a water droplet on a wax surface, there is no wetting and the contact angle is thus greater than 90° . The wetting of oil on glass is almost complete, so $\alpha \rightarrow 0$. The surface tension of the oil is vanishingly small compared to the adhesion force between oil and glass.

The angle of contact α between solid surfaces, liquids and gases can be computed using Young's equation

$$\sigma_{solid/gas} = \sigma_{solid/liquid} + \sigma_{gas/liquid} \cdot \cos(\alpha) , \quad (2.16)$$

as long as the individual surface tensions are known.

Because of the surface tension, the liquid tends to form **minimal areas**. This is seen in the experiment shown in Figure 2.9. A thread with a loop is laid onto a surface of soap suds. If the soapy skin inside the loop is burst, a circle forms, so that the remaining liquid surface forms a minimal area. Gradients of the surface tension $\nabla\sigma$ cause **shear forces** τ in the surrounding media A and B , as, for example, at the interface between a liquid and a gas,

$$\nabla\sigma = \tau_A + \tau_B .$$

The surface moves in the direction of greater surface tension, and by means of the shear stresses τ_A and τ_B , causes flows in the different media. Gradients in the surface tension can be caused by concentration gradients along the surface. This causes, for example, pieces of camphor to move back and forth sporadically on a water surface, since the camphor molecules locally reduce the surface tension. Another example are the tears in wine or cocktail glasses. Because of the concentration gradients in the water-alcohol mixture, the liquid at the glass is raised up and then flows back down into the liquid as regular drops. The

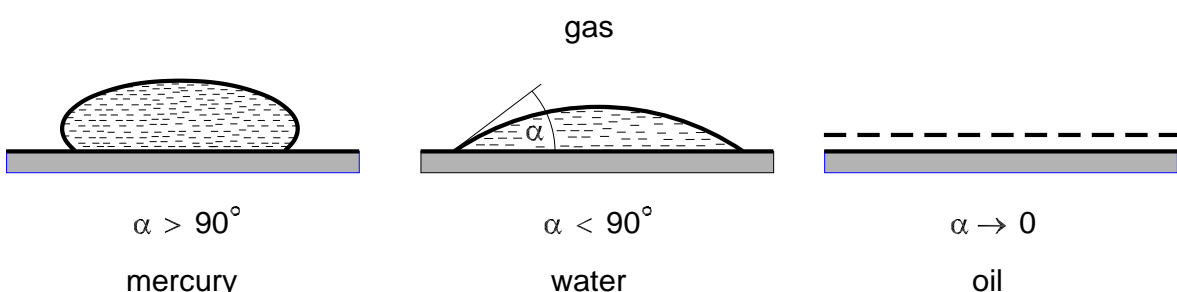


Fig. 2.8 : Angle of contact between solid, mercury, water, oil and air

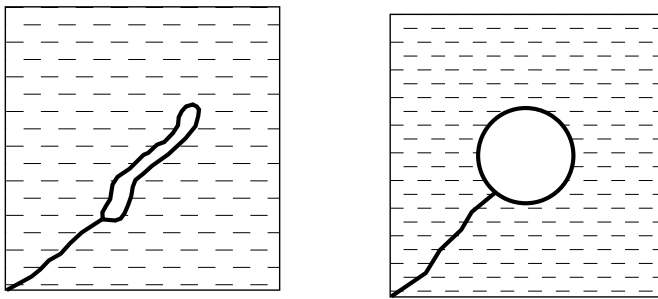


Fig. 2.9 : Minimal areas

evaporation of the alcohol causes a reduction of the alcohol content and thus an increase in the surface tension. The liquid is continually transported from the middle of the glass to the edge.

Temperature gradients also cause gradients in the surface tension, bringing us back again to the thermodynamic properties of fluids. If a thin metal plate wetted with silicon oil is heated from below with a hot rod, a hole in the oil film occurs at the heated point. The increase in the temperature leads to a decrease in the surface tension. The liquid surface moves in the direction of the colder areas with greater surface tension. A piece of ice on the oil surface has the opposite effect. The liquid film causes a swelling in the colder region.

The same effect can be used to transport bubbles in a liquid which is heated from one side. The cold side of the bubble has a higher surface tension than the warm side, and so it pulls the surface from the warm side, setting the bubble into motion.

2.2 Hydro-Aerostatics

In this chapter we will treat the properties and fundamental equations of **fluids at rest**. As in Chapter 1.2, **hydrostatics** describes incompressible fluids at rest and **aerostatics** compressible fluids at rest. When a fluid is at rest no shear stresses occur, so that the forces acting at each point on any volume element are normal to each surface. Therefore these forces can only be pressure or tractive forces. In a liquid, only pressure forces occur. Here pressure force \vec{F}_p on a surface element A increases with the size of the surface element. We introduce the scalar quantity pressure p as the pressure force per unit area.

$$p = \frac{F_p}{A} , \quad \text{with dimensions } \left[\frac{F}{L^2} \right] \quad \text{and units } \left\{ \frac{N}{m^2} \right\} . \quad (2.17)$$

The objective of hydro-aerostatics is to determine the pressure $p(x, y, z)$ at the different points of the fluid at rest.

2.2.1 Hydrostatics

In order to compute the pressure $p(z)$ in a column of water at rest, we consider the balance of forces on some cubic liquid element $dV = dx \cdot dy \cdot dz$ (Figure 2.10). Let the pressure

on the lower side of the liquid element be p , i.e. the pressure force on the surface element $dx \cdot dy$ is $F_p = p \cdot dx \cdot dy$. The pressure changes over the height of the fluid element dz . The pressure change can be written as a Taylor series, up to first order. Thus the pressure on the upper side of the fluid element is $(p + (dp/dz) \cdot dz + \dots)$ and the pressure force $(p + (dp/dz) \cdot dz) \cdot dx \cdot dy$. The pressure forces on the side surfaces of the fluid element cancel each other out, as they are the same all around at any given level and all act normal to the surface element. In addition, we have the gravitation $G = dm \cdot g = \rho \cdot dV \cdot g = \rho \cdot g \cdot dx \cdot dy \cdot dz$ which acts on the center of mass of the fluid element.

The balance of forces on the fluid element at rest is therefore

$$p \cdot dx \cdot dy - (p + \frac{dp}{dz} \cdot dz) dx \cdot dy - \rho \cdot g \cdot dx \cdot dy \cdot dz = 0 \quad .$$

If we divide this equation by the fluid element $dV = dx \cdot dy \cdot dz$ we obtain the **fundamental hydrostatic equation** for the pressure change in a column of water due to gravitation

$$\frac{dp}{dz} = -\rho \cdot g \quad .$$

(2.18)

This is a first order ordinary differential equation which, on integrating once, yields the linear pressure distribution

$$p(z) = -\rho \cdot g \cdot z + c \quad .$$

The constant of integration c can be determined with the boundary condition of the given problem. For the vessel shown in Figure 2.11 with boundary condition $p(z = 0) = p_0$, $c = p_0$ and the linear pressure distribution is

$$p(z) = p_0 - \rho \cdot g \cdot z \quad . \quad (2.19)$$

Two important consequences follow from this relation. Figure 2.12 shown three containers with the same base area and height. The pressure on the base of each container is the same: $p_0 = p_\infty + \rho \cdot g \cdot h$. With the same base area, the pressure force is therefore the same, although

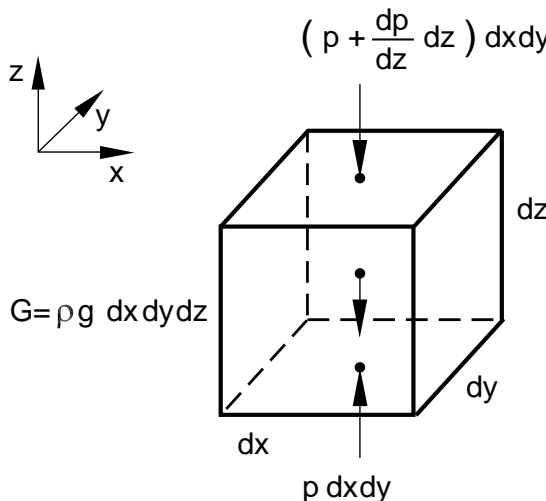


Fig. 2.10 : Balance of forces on a fluid element at rest

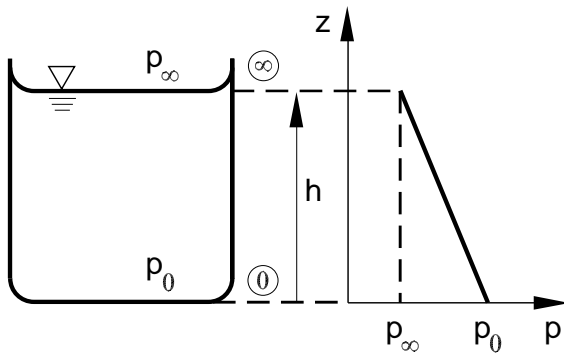


Fig. 2.11 : Linear pressure distribution in a gravitational field

the weight of the fluid in each of the containers is different. This fact is obvious when one considers (2.19) and is called the **hydrostatic paradox**.

In communicating pipes, the pressure in both sides of the pipe is equal to the outer pressure p_∞ . Therefore the surface of the liquid must be at the same height in both, since, according to (2.19), the pressure depends uniquely on the height.

A U-pipe can also be used as a pressure gauge. If a pressure vessel filled with gas is attached to one end of the U-pipe in the right-hand picture in Figure 2.12, an overpressure p_1 occurs, so that there is a height difference Δh in the two sides of the U-pipe. Since the density of the gas ρ_G is considerably smaller than the density of the liquid ρ_F , (2.19) can be written as

$$p_1 = p_\infty + \rho_F \cdot g \cdot \Delta h \quad . \quad (2.20)$$

By measuring Δh , the overpressure p_1 in the gas container can be computed using (2.20).

A further conclusion can be drawn from the hydrostatic fundamental equation. This is known as **Archimedes' principle**. For a body of volume V_K completely submerged in liquid, the upthrust \vec{F}_A is equal to the weight of the fluid displaced \vec{G} . In order to derive this law, we consider a cubic fluid element of base area dA and height Δh , completely submerged in a liquid of density ρ_F , as shown in Figure 2.13.

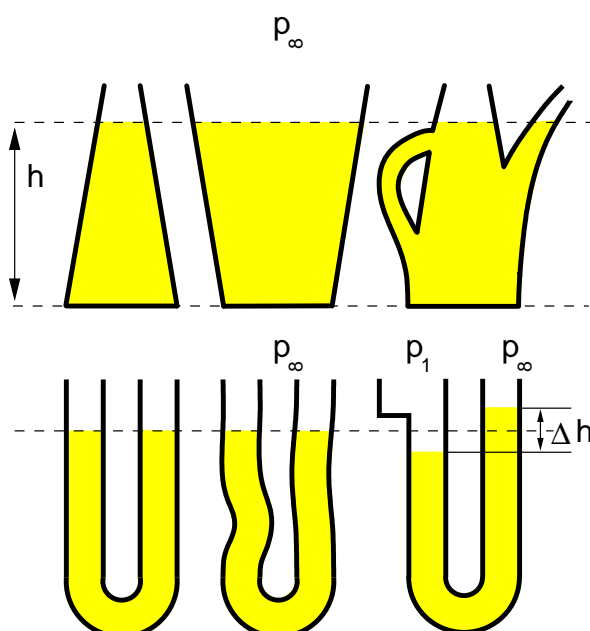


Fig. 2.12 : Hydrostatic paradox, communicating pipes, U-pipe pressure gauge

The pressure p_2 on the lower side of the body is larger than the pressure p_1 on the upper side of the body, due to the hydrostatic pressure distribution. The difference in the pressure forces \vec{F}_2 and \vec{F}_1 results in an upthrust \vec{F}_A , directed vertically upwards. The magnitude of this upthrust is

$$d|\vec{F}_A| = |\vec{F}_2| - |\vec{F}_1| = p_2 \cdot dA - p_1 \cdot dA = (p_2 - p_1) \cdot dA .$$

Using the solution of the hydrostatic fundamental equation (2.19), $p_2 = p_1 + \rho_F \cdot g \cdot \Delta h$, it follows that

$$d|\vec{F}_A| = \rho_F \cdot g \cdot \Delta h \cdot dA = \rho_F \cdot g \cdot dV_K \Rightarrow |\vec{F}_A| = \int_{V_K} \rho_F \cdot g \cdot dV_K = \rho_F \cdot g \cdot V_K ,$$

upthrust $|\vec{F}_A| = \rho_F \cdot g \cdot V_K$

(2.21)

In a **rotating vessel**, moving with constant angular velocity $\vec{\omega}$ (Figure 2.14), as well as the gravitation \vec{G} , there is also the centrifugal force \vec{Z} . This causes a liquid surface which would be horizontal were there no rotation to become deformed to a parabolic surface. The water surface is always perpendicular to the resulting force acting. For an observer rotating with the vessel, the liquid is at rest, so that the hydrostatic fundamental equation (2.18) has to be extended by the radially acting centrifugal force \vec{Z} . The magnitude of the centrifugal force for a fluid element dV is

$$|\vec{Z}| = \rho \cdot dV \cdot \omega^2 \cdot r ,$$

with $r^2 = x^2 + z^2$. Integrating the hydrostatic fundamental equation for a uniformly rotating liquid yields

$$p = p_0 + \frac{1}{2} \cdot \rho_F \cdot \omega^2 \cdot r^2 - \rho_F \cdot g \cdot z . \quad (2.22)$$

In the vertical direction, the pressure decreases linearly with the height z , as in a non-rotating liquid. In the horizontal direction it increases quadratically with the distance from

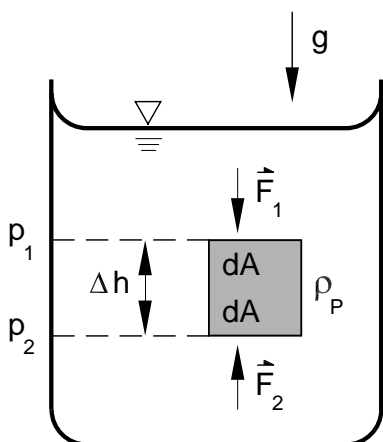
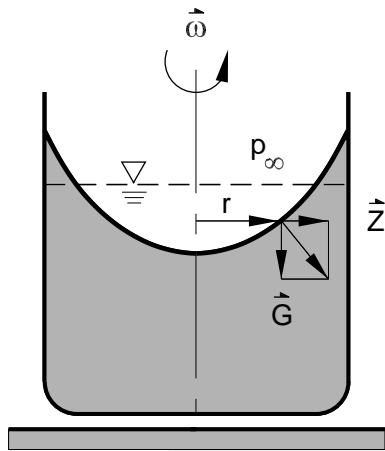


Fig. 2.13 : Determining the upthrust

**Fig. 2.14 :** Pressure in a rotating liquid

the axis of rotation. On the surface of the liquid, with $p = p_0$, we find

$$p_0 = p_0 + \frac{1}{2} \cdot \rho_F \cdot \omega^2 \cdot r^2 - \rho_F \cdot g \cdot z .$$

Therefore the surface of the liquid forms a paraboloid of rotation:

$$z = \frac{\omega^2 \cdot r^2}{2 \cdot g} .$$

2.2.2 Aerostatics

The most important example of aerostatics is the computation of the pressure, density and temperature distributions in the atmosphere. Figure 2.15 shows that the pressure p in the earth's atmosphere decreases continually with increasing height. In the different layers of the atmosphere, the temperature first decreases to about $-56^\circ C$, and then, because of chemical processes in the air, increases again. At higher altitudes, the temperature again drops with height, only to increase again at even greater altitudes with radiation from the sun.

The lower layer of the atmosphere is called the troposphere, and can be between 9 and 11 km thick, depending on the time of year. According to the ideal gas equation for air (2.8), the temperature and pressure decrease is associated with a decrease in density, and so the cold, heavy air is situated above the warm, lighter air. This air layering is thermally unstable, and causes the weather in the troposphere.

The next layer is the stratosphere, at a height of between 11 and 47 km. Here the temperature initially remains constant and then increases again with increasing height. The ozone layer forms in this atmospheric layer. This absorbs the UV-radiation from the sun and thus leads to a temperature increase. The stratosphere is thermally stable, since the warmer lighter air is now layered above the cold, heavy air. This is reason why civil aircraft fly in the stable lower stratosphere whatever the weather.

At altitudes between 47 and 86 km, the air chemistry dominant in the mesosphere again causes a thermally unstable temperature decrease. A small decrease in the density of the air with increasing height is connected with this chemistry. In this somewhat greater air density, small meteors glow and are seen as shooting stars. The dust from volcano eruptions

can also reach these heights, and can influence the chemistry of the air considerably for many decades.

The transition to the ionosphere occurs at heights above 87 km. Here the highly energetic sun and particle radiation leads to the ionization of the air molecules. This again leads to a thermally stable temperature increase with increasing height. The stable temperature and density layering in the ionosphere ensures that the atmosphere of the earth does not escape from the earth. The electrically charged particles lead to electrical flows in the ionosphere which can affect short-wave radio signals considerably.

In this chapter we restrict ourselves to the lower atmosphere (troposphere and lower stratosphere), where 99 % of the mass of the atmosphere is, and whose temperature, density and pressure distributions can be found in the internet as the so-called **US standard atmospheres**.

<http://aero.stanford.edu/StdAtm.html>

The standardized temperature distribution is shown in Figure 2.16. In the troposphere the temperature decreases linearly

$$T(z) = T_0 + a \cdot (z - z_0) \quad , \quad (2.23)$$

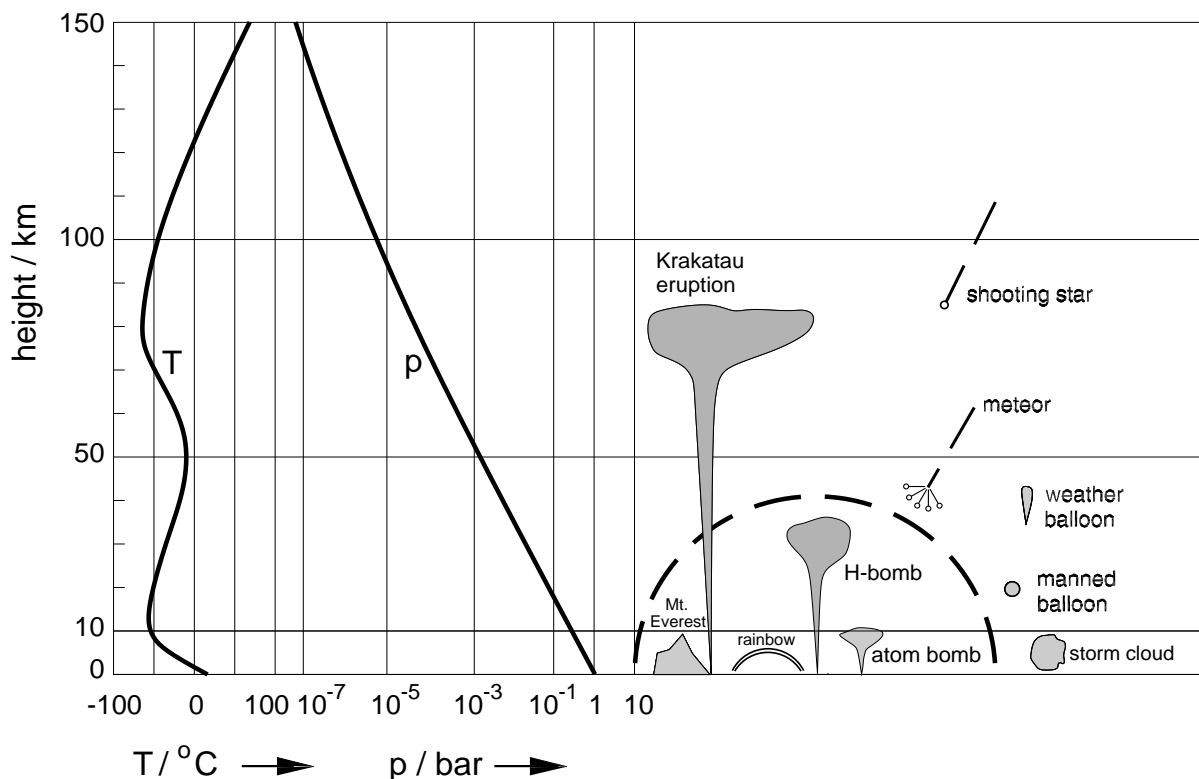


Fig. 2.15 : Temperature and pressure distribution in the atmosphere

with $T_0 = 288.16 \text{ K}$ at the surface of the earth $z_0 = 0$, the constant $a = -6.5 \cdot 10^{-3} \text{ K/m}$ and the air pressure at the surface of the earth $p_0 = 1.013 \cdot 10^5 \text{ N/m}^2$.

In the lower stratosphere, the temperature is assumed to be constant

$$T = T_1 = 216.66 \text{ K} = \text{const.} , \quad \text{with} \quad p(z = z_1 = 11 \text{ km}) = p_1 . \quad (2.24)$$

For the given temperature distribution, the **fundamental aerostatic equation** yields the associated pressure and density distributions $p(z)$, $\rho(z)$. Again the starting point is the fundamental hydrostatic equation (2.18)

$$\frac{dp}{dz} = -\rho(z) \cdot g .$$

However now the density ρ is a function of the height coordinate z . With the thermal equation of state for an ideal gas (2.8)

$$p = R \cdot \rho \cdot T \Rightarrow \rho(z) = \frac{p(z)}{R \cdot T(z)} ,$$

we find the fundamental aerostatic equation

$$\frac{dp}{p} = -\frac{g}{R} \cdot \frac{dz}{T} .$$

(2.25)

This is again a first order differential equation which is uniquely solvable with one boundary condition and a given temperature distribution.

For the temperature distribution in the troposphere (2.23), we obtain

$$dz = \frac{1}{a} \cdot dT .$$

Substituting dz into (2.25) and integrating the aerostatic fundamental equation yields

$$\frac{dp}{p} = -\frac{g}{R \cdot a} \cdot \frac{dT}{T} \Rightarrow \int_{p_0}^p \frac{dp}{p} = -\frac{g}{R \cdot a} \cdot \int_{T_0}^T \frac{dT}{T} \Rightarrow [\ln(p)]_{p_0}^p = -\frac{g}{R \cdot a} [\ln(T)]_{T_0}^T ,$$

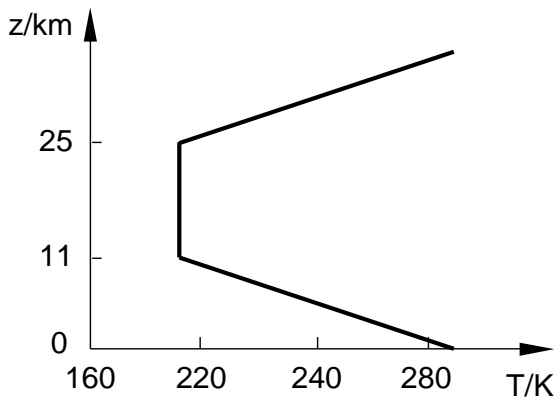


Fig. 2.16 : Standardized temperature distribution in the troposphere and lower stratosphere (US standard atmosphere)

$$\ln\left(\frac{p(z)}{p_0}\right) = -\frac{g}{R \cdot a} \cdot \ln\left(\frac{T(z)}{T_0}\right) \Rightarrow \frac{p(z)}{p_0} = \exp\left[-\frac{g}{R \cdot a} \cdot \ln\left(\frac{T(z)}{T_0}\right)\right] = \left(\frac{T(z)}{T_0}\right)^{-\frac{g}{R \cdot a}},$$

$$p(z) = p_0 \cdot \left(\frac{T(z)}{T_0}\right)^{-\frac{g}{R \cdot a}} , \quad (2.26)$$

$\rho(z)$ follows from $p(z)$, using the equation of state for ideal gases

$$R = \frac{p(z)}{\rho(z) \cdot T(z)} = \frac{p_0}{\rho_0 \cdot T_0} \Rightarrow \frac{p(z)}{p_0} = \frac{\rho(z) \cdot T(z)}{\rho_0 \cdot T_0} \Rightarrow \frac{\rho(z)}{\rho_0} = \frac{T_0}{T(z)} \cdot \left(\frac{T(z)}{T_0}\right)^{-\frac{g}{R \cdot a}} ,$$

$$\frac{\rho(z)}{\rho_0} = \left(\frac{T(z)}{T_0}\right)^{-1} \cdot \left(\frac{T(z)}{T_0}\right)^{-\frac{g}{R \cdot a}} = \left(\frac{T(z)}{T_0}\right)^{-\frac{g}{R \cdot a}-1} ,$$

$$\rho(z) = \rho_0 \cdot \left(\frac{T(z)}{T_0}\right)^{-\left(\frac{g}{R \cdot a}+1\right)} . \quad (2.27)$$

Pressure and density decrease with increasing height in the atmosphere for the given linear temperature distribution, according to the power laws (2.26) and (2.27).

In the lower stratosphere the temperature distribution is isothermal $T = T_1$ (2.24) and there is an exponential decrease in the pressure.

$$\frac{1}{p} \cdot dp = -\frac{g}{R \cdot T_1} \cdot dz \Rightarrow \int_{p_1}^p \frac{1}{p} \cdot dp = -\frac{g}{R \cdot T_1} \int_{z_1}^z dz \Rightarrow [\ln(p)]_{p_1}^p = -\frac{g}{R \cdot T_1} [z]_{z_1}^z ,$$

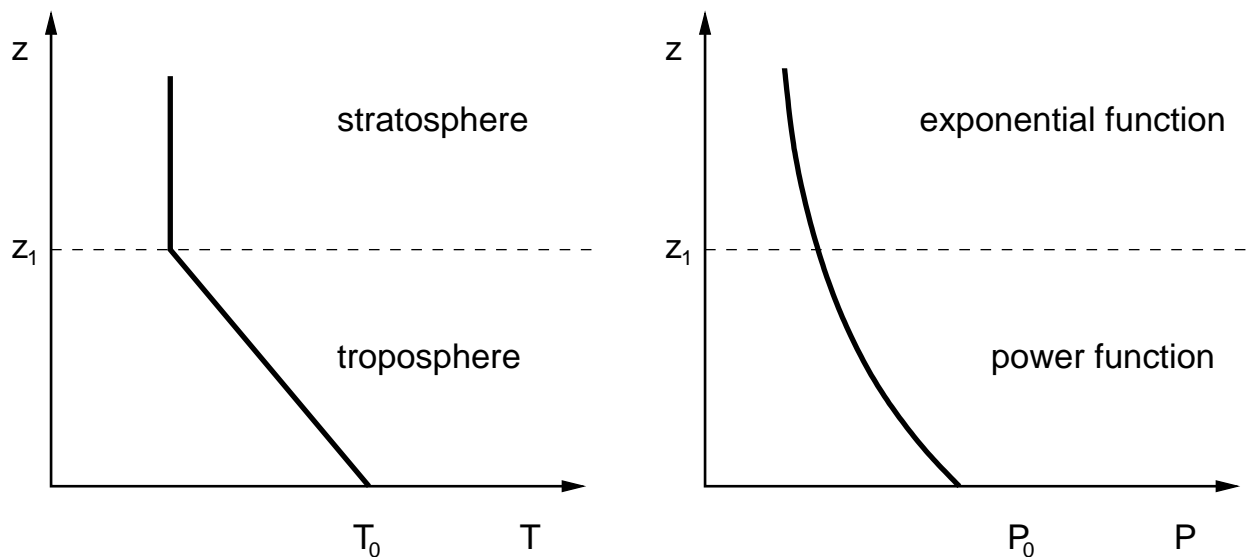


Fig. 2.17 : Temperature and pressure distributions in the US standard atmosphere

$$\ln \left(\frac{p}{p_1} \right) = -\frac{g}{R \cdot T_1} \cdot (z - z_1) \Rightarrow \frac{p}{p_1} = \exp \left(-\frac{g}{R \cdot T_1} \cdot (z - z_1) \right) ,$$

$$p(z) = p_1 \cdot \exp \left(-\frac{g}{R \cdot T_1} \cdot (z - z_1) \right) . \quad (2.28)$$

The results of the pressure distributions are shown in Figure 2.17. $\rho(z)$ follows from $p(z)$ with the ideal equation of state $\rho(z) = p(z)/(R \cdot T_1)$,

$$\rho(z) = \frac{p_1}{R \cdot T_1} \cdot \exp \left(-\frac{g}{R \cdot T_1} \cdot (z - z_1) \right) = \rho_1 \cdot \exp \left(-\frac{g}{R \cdot T_1} \cdot (z - z_1) \right) . \quad (2.29)$$

2.3 Hydro-Aerodynamics, Stream Filament Theory

2.3.1 Basic Kinematic Concepts

Before we turn to the computation of flows within the framework of the simplified **one-dimensional stream filament theory**, we first set out the **basic kinematic concepts** for the mathematical description of flows.

The kinematics of a flow describe the motion of the fluid without taking the forces which cause this motion into account. The aim of kinematics is to compute the position vector $\vec{x}(t)$ of a fluid element and thus the dependence of its motion on the time t with respect to the chosen coordinate system $\vec{x} = (x, y, z)$ for a given velocity field $\vec{v}(u, v, w)$.

As in Figure 2.18, we follow the path of a fluid element or of a particle in the flow in time. The initial position of the particle motion at time $t = 0$ is determined by the position vector $\vec{x}_0 = (x_0, y_0, z_0)$. At the time $t_1 > 0$, the particle has moved along the path sketched to the position $\vec{x}(t_1)$ and at the time $t_2 > t_1$ to the position $\vec{x}(t_2)$ etc. The instantaneous position

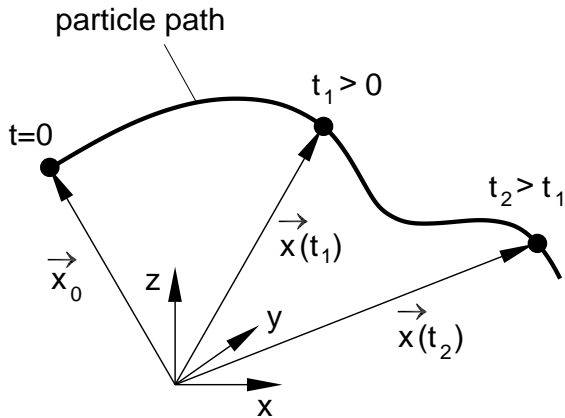


Fig. 2.18 : Particle path

\vec{x} of the particle under consideration is therefore a function of the initial position \vec{x}_0 and the time t . The **particle path** is therefore

$$\vec{x} = \vec{f}(\vec{x}_0, t) .$$

The ordinary differential equation to compute the particle path for a given velocity field $\vec{v}(u, v, w)$ is therefore

$$\frac{d\vec{x}}{dt} = \vec{v}(\vec{x}, t) . \quad (2.30)$$

This is none other than the well-known defining equation of velocity. The differential equations for the individual velocity components read

$$\frac{dx}{dt} = u(x, y, z, t) , \quad \frac{dy}{dt} = v(x, y, z, t) , \quad \frac{dz}{dt} = w(x, y, z, t) . \quad (2.31)$$

This is a system of first order ordinary differential equations. The particle path is computed by integrating these differential equations with the initial conditions $\vec{x}_0 = \vec{x}(t = 0)$.

For a **steady flow**, the system of differential equations is not dependent on the time t and is written as

$$\frac{d\vec{x}}{dt} = \vec{v}(\vec{x}) . \quad (2.32)$$

Here it is to be noted that although $\partial/\partial t \equiv 0$, the total differential $d/dt \neq 0$.

Another way of describing flows is by means of **streamlines**. These indicate the direction field of the velocity vector \vec{v} at a certain time t_n (Figure 2.19). Since the tangents are parallel to the velocity vector at every position and every time, the determining equation for the streamline reads

$$\vec{v} \times d\vec{x} = 0 . \quad (2.33)$$

The velocity components are then

$$\begin{pmatrix} u \\ v \\ w \end{pmatrix} \times \begin{pmatrix} dx \\ dy \\ dz \end{pmatrix} = \begin{pmatrix} v \cdot dz - w \cdot dy \\ w \cdot dx - u \cdot dz \\ u \cdot dy - v \cdot dx \end{pmatrix} = \begin{pmatrix} 0 \\ 0 \\ 0 \end{pmatrix} \Rightarrow \begin{array}{l} v \cdot dz = w \cdot dy \\ w \cdot dx = u \cdot dz \\ u \cdot dy = v \cdot dx \end{array} .$$

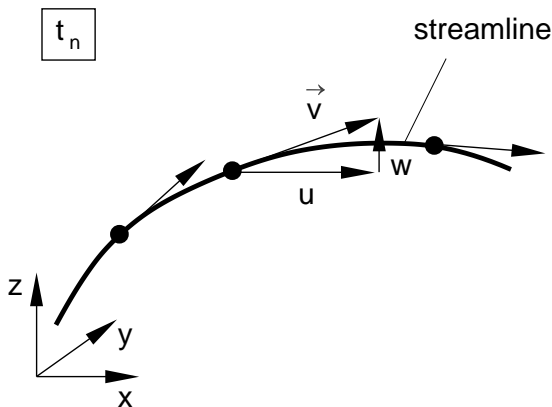


Fig. 2.19 : Streamline

This yields the system of first order differential equations for the streamline:

$$\boxed{\frac{dz}{dy} = \frac{w(x, y, z, t)}{v(x, y, z, t)} , \quad \frac{dz}{dx} = \frac{w(x, y, z, t)}{u(x, y, z, t)} , \quad \frac{dy}{dx} = \frac{v(x, y, z, t)}{u(x, y, z, t)}} . \quad (2.34)$$

The streamlines are again determined by integration, using the method of separation of variables, and so are integral curves of the direction field of the given velocity vector \vec{v} .

In experiment, or even in a computed flow field, the path lines can be made visible by coloring a particle or a fluid element. By photographing the flow region using a long exposure times the particle path is made visible. Similarly a picture of the streamlines is obtained by marking many particles and photographing the flow field with a short exposure time. The picture then shows many short dashes, whose directions indicate the tangent field of the velocity vector at the time of the shot. The lines connecting the individual dashes are the streamlines.

The third important way of describing flows is using **streaklines**. These are shown in Figure 2.20 and, for a given time t_n , are the lines connecting the positions which the path lines of all particles have reached which passed the fixed position \vec{x}_0 at any time $t_0 < t_n$. If color or smoke is added to the flow field at the position \vec{x}_0 , the snapshots of the colored filaments or threads of smoke are streaklines.

The equation of the streakline at the time t_n is

$$\vec{x} = \vec{x}(\vec{x}_0, t_0, t) , \quad (2.35)$$

where t_0 is the curve parameter and \vec{x}_0 the family parameter. A parameterless representation of the streakline is found by eliminating the curve parameter t_0 .

For example, the following equation is known from a computation of a particle path:

$$\vec{x} = \vec{x}(\vec{x}_0, t_0, t) = \begin{pmatrix} (x_0 + t_0 + 1) \cdot e^{(t-t_0)} - t - 1 \\ (y_0 - t_0 + 1) \cdot e^{-(t-t_0)} + t - 1 \end{pmatrix} = \begin{pmatrix} x \\ y \end{pmatrix} .$$

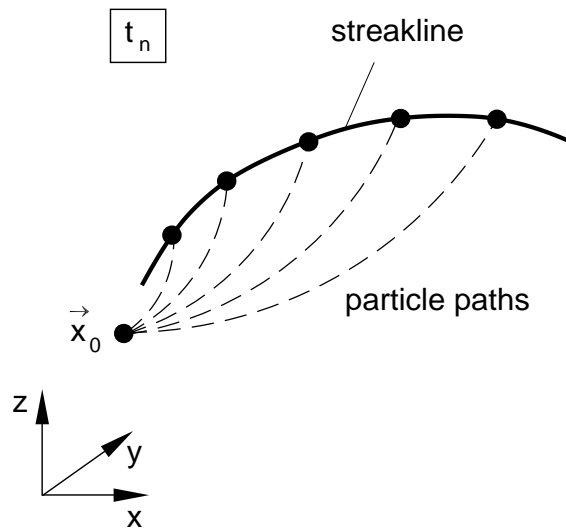


Fig. 2.20 : Streaklines

Let us consider the equation of that streakline in the (x, y) plane which passes through the point $(x_0, y_0) = (-1, -1)$ at the time $t = 0$. If we insert the above ansatz into equation (2.35), we obtain

$$x = t_0 \cdot e^{-t_0} - 1 \quad , \quad y = -t_0 \cdot e^{t_0} - 1 \quad \Rightarrow \quad x + 1 = t_0 \cdot e^{-t_0} \quad , \quad y + 1 = -t_0 \cdot e^{t_0} \quad ,$$

$$(x + 1) \cdot (y + 1) = -t_0^2 \quad \Rightarrow \quad t_0 = \sqrt{-(x + 1) \cdot (y + 1)} \quad .$$

t_0 inserted into $x = t_0 \cdot e^{-t_0} - 1$ yields an implicit equation for the streakline in the (x, y) plane

$$x = \sqrt{-(x + 1) \cdot (y + 1)} \cdot \exp\left(-\sqrt{(x - 1) \cdot (y + 1)}\right) - 1 \quad .$$

In **steady flows**, the particle paths, streamlines and streaklines are the same. In unsteady flows the curves are different.

Let us return to the examples of flows discussed in the introduction in Chapter 1.2. Both the flow past a vertical plate and the flow past a wing and an automobile were presented as steady flow problems. Now we can interpret the flow lines in Figures 1.13 and 1.18 as particle paths and streamlines respectively. Small particles of aluminum are added to each flow in the water channel and a snapshot of these with a long enough exposure time characterizes the structure of the steady flow. In Figure 1.21, the wake flow of an automobile in a wind tunnel was made visible with smoke allowed into the free stream at a fixed position \vec{x}_0 . All smoke particles have passed through the same position, so that it is the streaklines which we see in this shot. Figure 2.21 supplements the sketches of particle paths, streamlines and streaklines, which all lie on the same curve in these three examples of steady flows.

For **unsteady** flows, the particle paths are different from the streamlines and streaklines, making the interpretation of unsteady flows difficult. We will illustrate this using a simple flow example. In Figure 2.22 we move a sphere with constant velocity u_∞ through a fluid at rest. As the sphere is moved along, the particle path forms a loop, while the snapshot of the streamlines indicates closed curves. This is the flow field which we see as an external observer at rest. The streamline picture looks completely different if we move with the sphere. We then see the constant free stream u_∞ coming towards us and the flow becomes time independent. Instead of the closed streamlines, steady streamlines form from left to right, along the same curves as the pathlines and streaklines. Depending on our frame of reference, the flow field looks completely different. Expressed physically, this means that the streamlines and particles paths are **not invariant** when the **inertial frame** is changed (position transformation with constant translation velocity).

Two further examples of shear flows serve to extend these ideas. Let us consider a plane **wave** in a plate boundary layer flow. The u component of the velocity displacement is written as

$$u(x, z, t) = \hat{u}(z) \cdot e^{i \cdot (a \cdot x - \omega \cdot t)} \quad ,$$

with the amplitude function $\hat{u}(z)$, which is a function only of the vertical coordinate z , the wave number a and the angular frequency ω . The phase velocity c of the wave is $c = \omega/a$.

The observer at rest sees circles for the particle paths and streamlines of the wave moving past with the phase velocity c , as sketched in the snapshot in Figure 2.23. The observer moving with the wave sees the plate moving with the phase velocity c and a streamline picture which looks like cat's eyes.

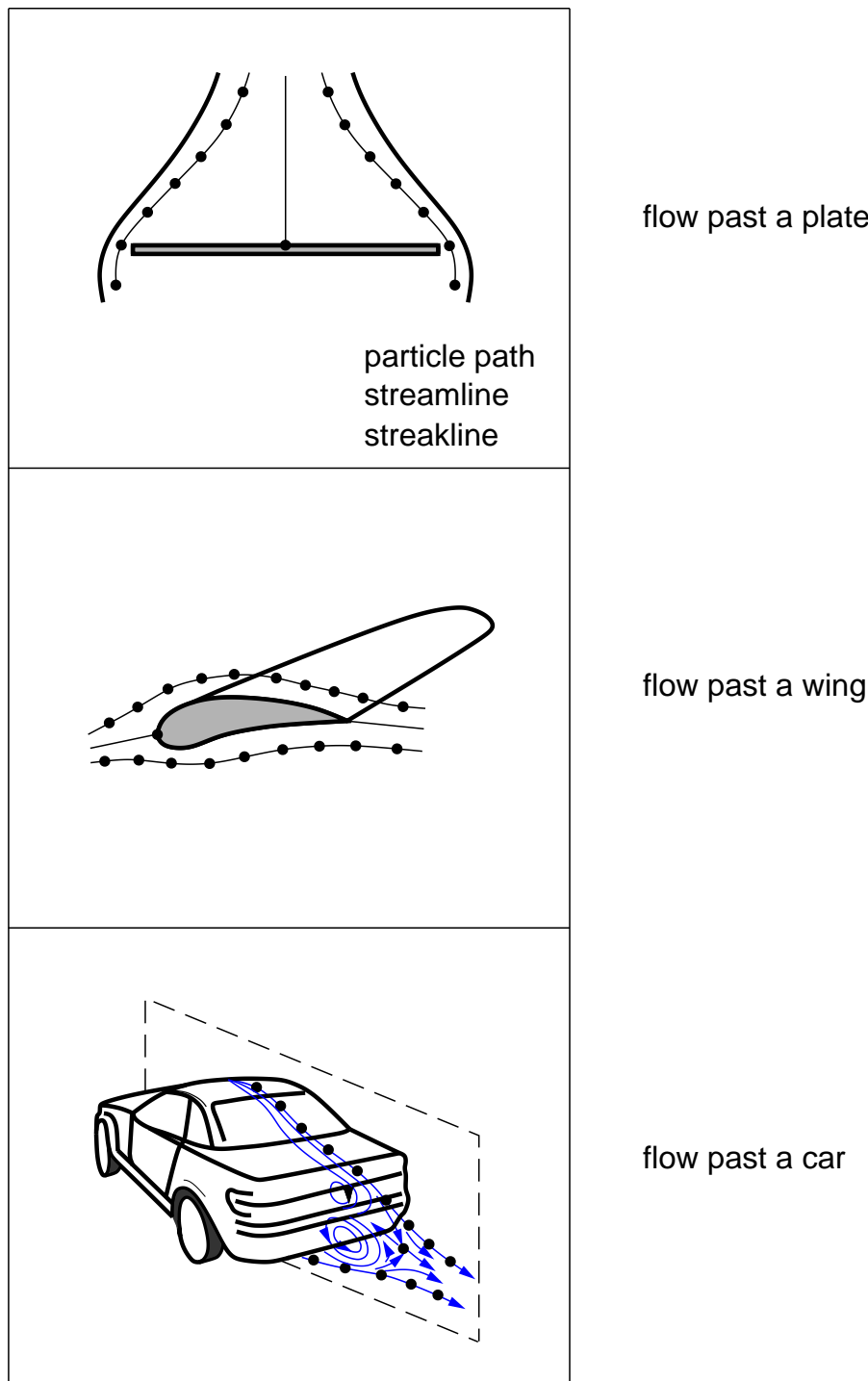


Fig. 2.21 : Particle paths, streamlines, streaklines of the steady flow past a horizontal plate, a wing and an automobile

The third example of shear layer flow is the wake flow of a cylinder, already met in Chapter 1.1 as the Kármán vortex street in connection with the collapse of the Tacoma bridge. The humming of high voltage wires in the wind is also due to the periodic flow separation of the Kármán vortex street at the cylindrical cross-section. Figure 2.24 shows first the streaklines, particle paths and streamlines of a cylinder moving through a fluid at rest with constant velocity u_∞ for an observer at rest. The observer moving with the vortices periodically swimming downstream with phase velocity c again sees the perturbed streamlines as cat's

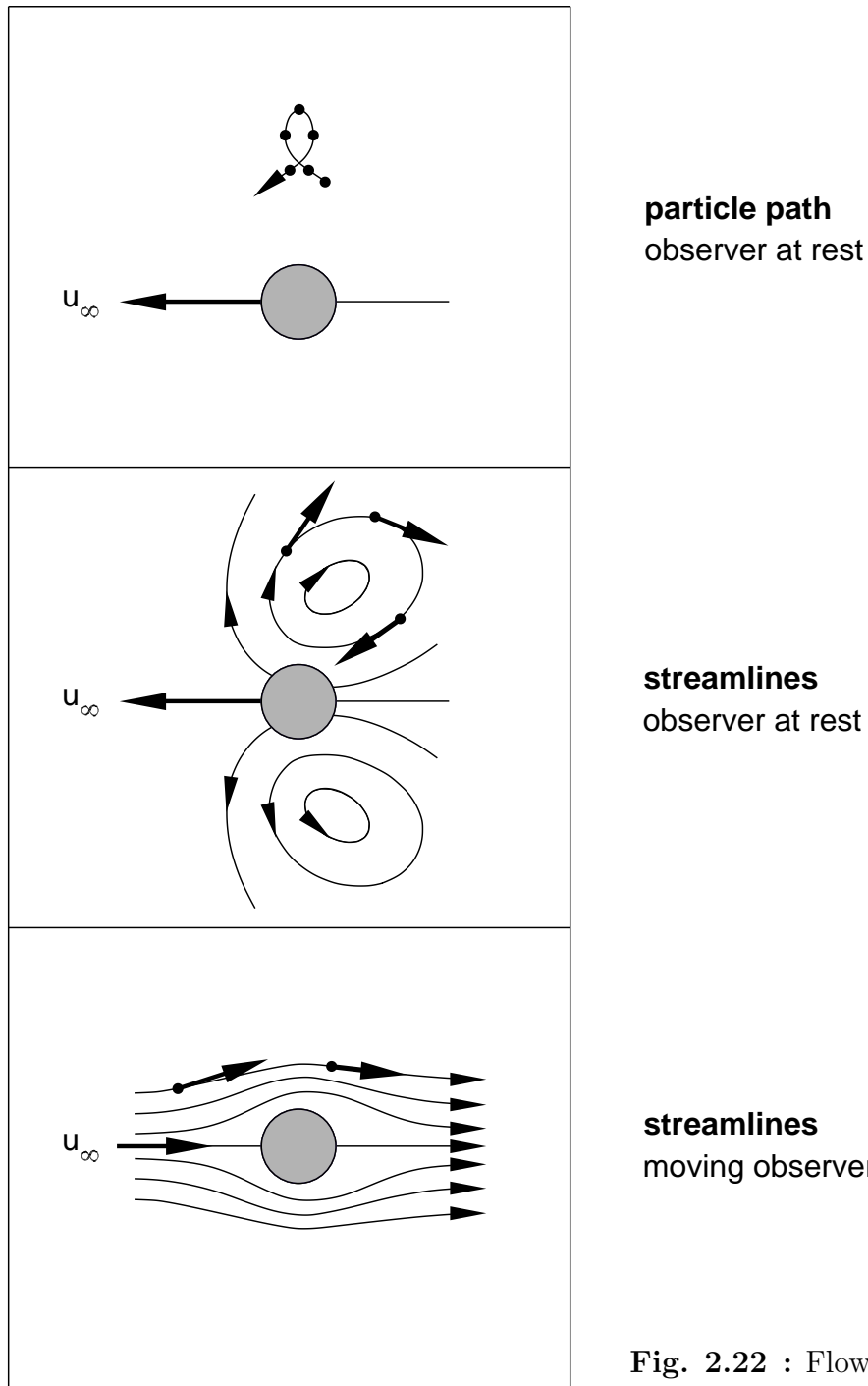


Fig. 2.22 : Flow past a sphere, with observer at rest and moving

eyes. The historical photographs of PRANDTL 1929 and TIMME 1957 in the water channel and the theoretically computed streamlines of VON KÁRMÁN 1912 are shown in Figure 2.25.

As we have already learned from the examples of unsteady flows, the description of the kinematics of unsteady flows in particular is very difficult. Much practice and experience is required to be able to interpret the experimental results in the wind tunnel or the flow simulations on a computer correctly. However it is precisely the kinematic description of the flow which yields important insights into the structure of a flow.

Now that we have seen that the flow picture is dependent on the frame of reference, there are basically two different ways of treating a flow mathematically. In the **Euler picture** we assume a **fixed** observer. This manner of description corresponds to using measuring apparatus which is fixed in position to measure local flow quantities.

The **Lagrange picture** assumes a frame of reference moving with a particle or fluid element. The mathematical relationship between the two picture is, for example for the acceleration of the flow $\vec{b} = d\vec{v}/dt = d^2\vec{x}/dt^2$, the **total differential** of the velocity vector $\vec{v}(u, v, w)$. For the u component $u(x, y, z, t)$ of the velocity vector we have

$$du = \frac{\partial u}{\partial t} \cdot dt + \frac{\partial u}{\partial x} \cdot dx + \frac{\partial u}{\partial y} \cdot dy + \frac{\partial u}{\partial z} \cdot dz \quad .$$

So the total time derivative of u is

$$\frac{du}{dt} = \frac{\partial u}{\partial t} + \frac{\partial u}{\partial x} \cdot \frac{dx}{dt} + \frac{\partial u}{\partial y} \cdot \frac{dy}{dt} + \frac{\partial u}{\partial z} \cdot \frac{dz}{dt} \quad ,$$

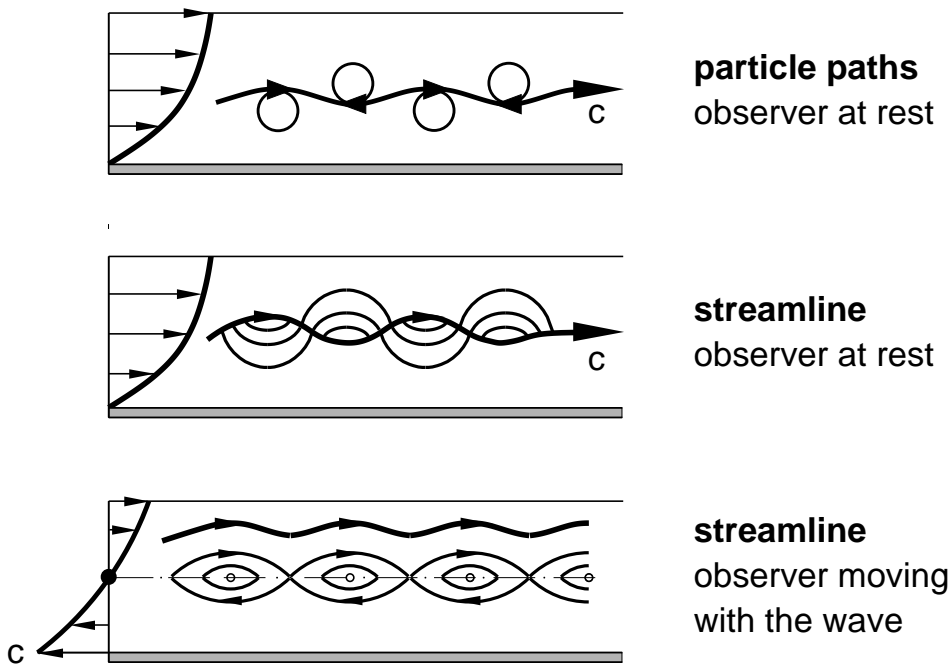


Fig. 2.23 : Wave in a boundary layer, observer at rest and moving

with

$$\frac{dx}{dt} = u \quad , \quad \frac{dy}{dt} = v \quad , \quad \frac{dz}{dt} = w$$

and we have

$$\underbrace{\frac{du}{dt}}_{\mathbf{S}} = \underbrace{\frac{\partial u}{\partial t}}_{\mathbf{L}} + \underbrace{u \cdot \frac{\partial u}{\partial x} + v \cdot \frac{\partial u}{\partial y} + w \cdot \frac{\partial u}{\partial z}}_{\mathbf{C}} . \quad (2.36)$$

In this equation

- S** substantial rate of change, **Lagrange picture**,
- L** local rate of change at a fixed position, **Euler picture**,
- C** convective spatial changes due to convection from place to place, effect of the velocity field $\vec{v} = (u, v, w)$.

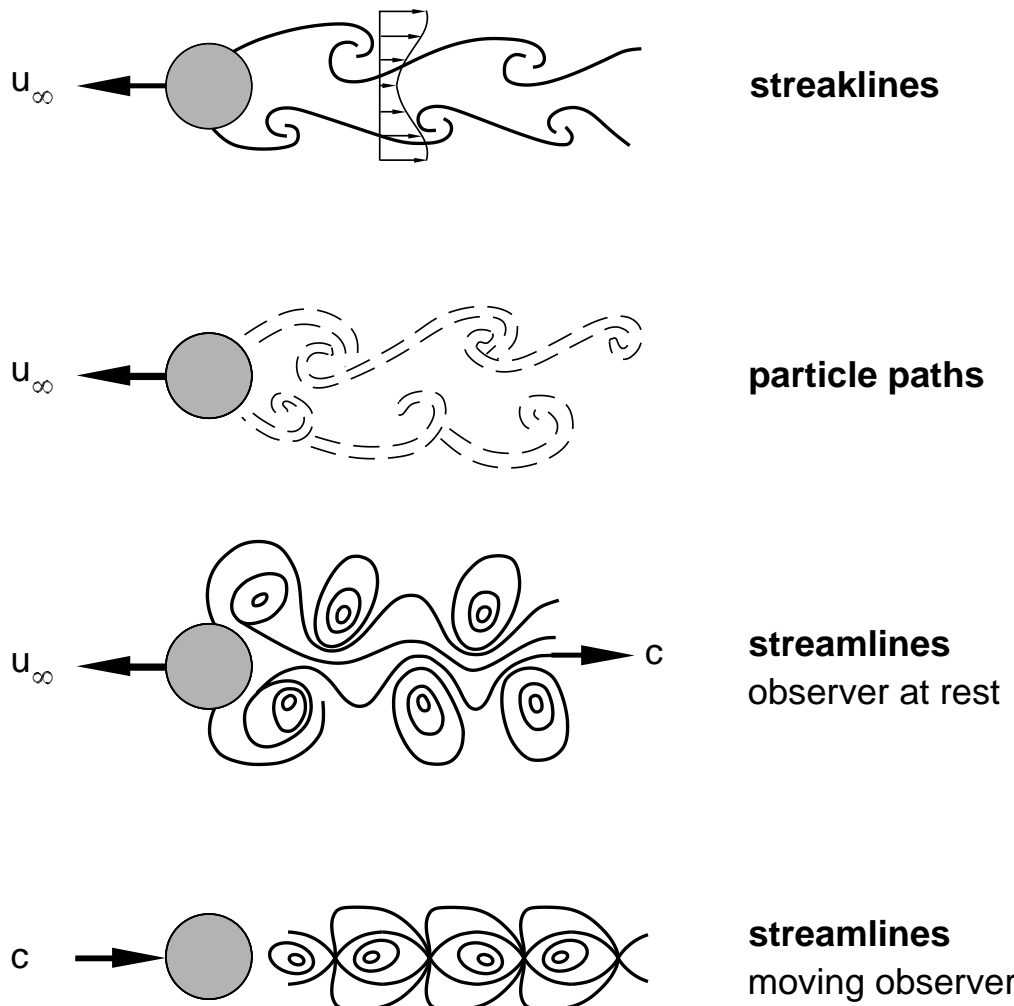


Fig. 2.24 : Kármán vortex street, observer at rest and moving

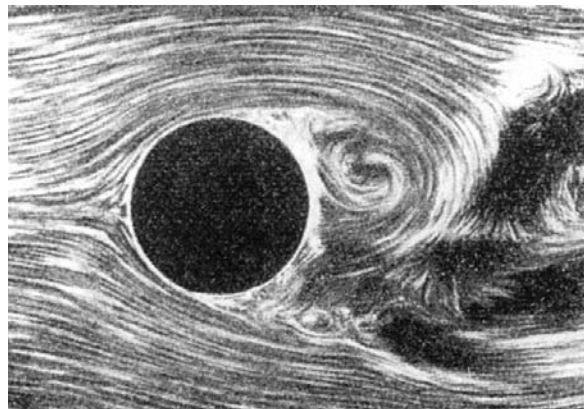
For the acceleration \vec{b} of the flow field which we will need in the following chapters, we obtain

$$\vec{b} = \frac{d\vec{v}}{dt} = \frac{\partial \vec{v}}{\partial t} + u \cdot \frac{\partial \vec{v}}{\partial x} + v \cdot \frac{\partial \vec{v}}{\partial y} + w \cdot \frac{\partial \vec{v}}{\partial z} = \frac{\partial \vec{v}}{\partial t} + (\vec{v} \cdot \nabla) \vec{v} , \quad (2.37)$$

with the nabla operator $\nabla = (\partial/\partial x, \partial/\partial y, \partial/\partial z)$ and $(\vec{v} \cdot \nabla)$ the scalar product of the velocity vector \vec{v} and the nabla operator ∇ .

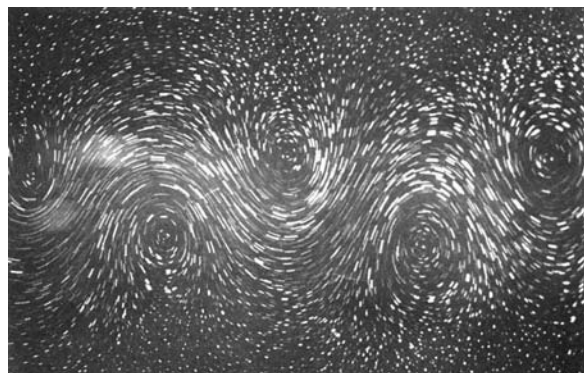
For Cartesian coordinates this yields

$$\vec{b} = \begin{pmatrix} b_x \\ b_y \\ b_z \end{pmatrix} = \begin{pmatrix} \frac{du}{dt} \\ \frac{dv}{dt} \\ \frac{dw}{dt} \end{pmatrix} = \begin{pmatrix} \frac{\partial u}{\partial t} + u \cdot \frac{\partial u}{\partial x} + v \cdot \frac{\partial u}{\partial y} + w \cdot \frac{\partial u}{\partial z} \\ \frac{\partial v}{\partial t} + u \cdot \frac{\partial v}{\partial x} + v \cdot \frac{\partial v}{\partial y} + w \cdot \frac{\partial v}{\partial z} \\ \frac{\partial w}{\partial t} + u \cdot \frac{\partial w}{\partial x} + v \cdot \frac{\partial w}{\partial y} + w \cdot \frac{\partial w}{\partial z} \end{pmatrix} ,$$



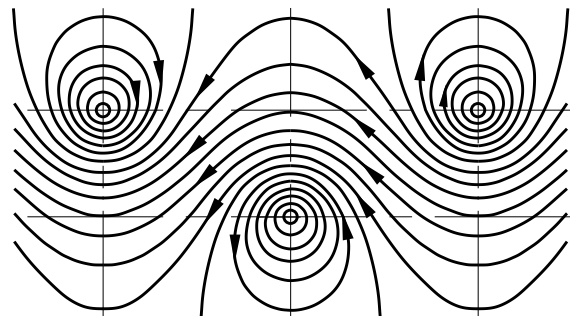
streaklines

PRANDTL 1929



particle paths

TIMME 1975



computed
streamlines

von KARMAN 1912

Fig. 2.25 : Streaklines, particle paths and streamlines of the Kármán vortex street

and for $(\vec{v} \cdot \nabla) \cdot \vec{v}$

$$\vec{v} \cdot \nabla = \begin{pmatrix} u \\ v \\ w \end{pmatrix} \cdot \begin{pmatrix} \frac{\partial}{\partial x} \\ \frac{\partial}{\partial y} \\ \frac{\partial}{\partial z} \end{pmatrix} = u \cdot \frac{\partial}{\partial x} + v \cdot \frac{\partial}{\partial y} + w \cdot \frac{\partial}{\partial z} ,$$

$$(\vec{v} \cdot \nabla) \cdot \vec{v} = \left(u \cdot \frac{\partial}{\partial x} + v \cdot \frac{\partial}{\partial y} + w \cdot \frac{\partial}{\partial z} \right) \cdot \begin{pmatrix} u \\ v \\ w \end{pmatrix} = \begin{pmatrix} u \cdot \frac{\partial u}{\partial x} + v \cdot \frac{\partial u}{\partial y} + w \cdot \frac{\partial u}{\partial z} \\ u \cdot \frac{\partial v}{\partial x} + v \cdot \frac{\partial v}{\partial y} + w \cdot \frac{\partial v}{\partial z} \\ u \cdot \frac{\partial w}{\partial x} + v \cdot \frac{\partial w}{\partial y} + w \cdot \frac{\partial w}{\partial z} \end{pmatrix} .$$

In the case of a steady flow, all partial derivatives with respect to time vanish, so $\partial/\partial t = 0$, while the substantial derivative with respect to time d/dt can indeed be non-zero when convective changes occur. In unsteady flows both $\partial/\partial t \neq 0$ and $d/dt \neq 0$.

2.3.2 Incompressible Flows

The fundamental equations and methods of **one-dimensional stream filament theory** are still used today in industry for the preliminary design of new products. It is for this reason that one-dimensional stream filament theory is a good introduction to the theoretical treatment of flows. The solution software of the algebraic system of equations to be treated will be presented in Chapter 3.1.

We will denote the one-dimensional velocity component with $c(s)$. This is a function of s only, called the stream filament coordinate. In order to introduce this one-dimensional coordinate s it is first of all useful to introduce the concept of the **streamtube**. If the streamlines form a closed surface, this surrounding surface is called a streamtube (Figure 2.26).

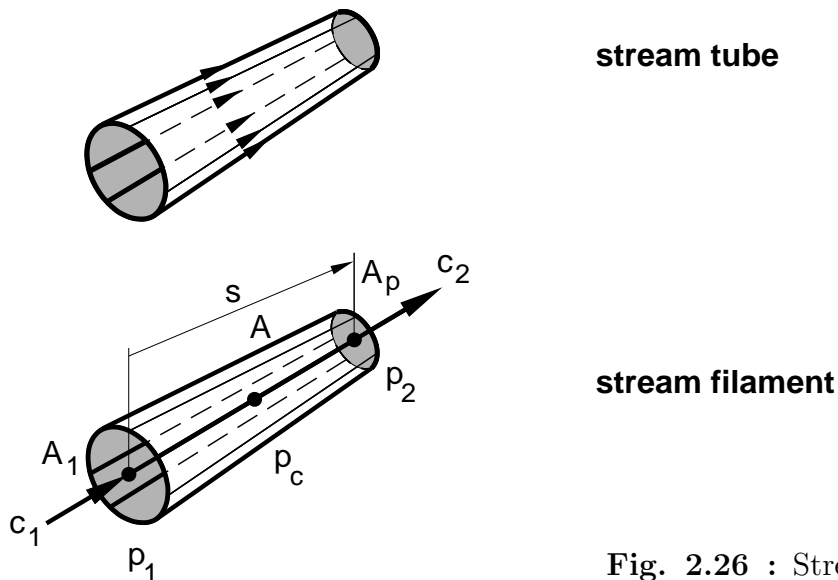


Fig. 2.26 : Streamtube and stream filament

Since the streamlines are by definition the tangents to the velocity vectors, no fluid mass will pass through the walls of the streamtube. This means that channels with fixed walls form streamtubes. If the changes in the flow quantities over the cross-section of the streamtube are small compared to the change along the streamtube, the (approximately) one-dimensional changes in the flow quantities along the hypothetical **stream filament** can be computed. The coordinate along the stream filament is called the stream filament coordinate s . Along a stream filament, for incompressible and steady flows, we have

$$c = c(s) \quad , \quad p = p(s) \quad , \quad A = A(s) \quad .$$

All flow quantities as well as the cross-section A of the streamtube are functions of the stream filament coordinate s only. For the problem of the flow past an automobile, for example, **stream surfaces** can be determined, corresponding to the streamtubes of channel flows. Figure 2.27 shows such a stream surface past an automobile. If the changes perpendicular to the stream surface are small compared to the changes along the streamline, as is the case along the mid-section of the vehicle flow, a stream filament can again be determined, along which the variation in the flow quantities is approximately one-dimensional.

The **fundamental equations for one-dimensional stream filament theory** are as follows:

Conservation of Mass:

The mass flux entering a streamtube \dot{m}_1 is equal to the mass flux exiting the streamtube \dot{m}_2 . Using the volume flux \dot{V}_1 and \dot{V}_2 , we find

$$\dot{m}_1 = \rho_1 \cdot \dot{V}_1 = \rho_1 \cdot c_1 \cdot A_1 = \rho_2 \cdot c_2 \cdot A_2 = \rho_2 \cdot \dot{V}_2 = \dot{m}_2 \quad ,$$

$\dot{m} = \rho \cdot c \cdot A = \text{const.}$

(2.38)

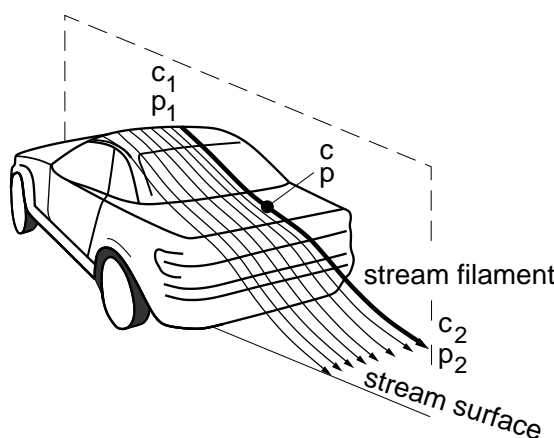


Fig. 2.27 : Stream surface and stream filament

Conservation of Momentum or Equation of Motion:

We first formulate the equation of motion for a stream filament placed in the **inviscid** outer flow or the inviscid core flow of a channel. From the balance of forces along a selected stream filament element dV (Figure 2.28), the variation in cross-section along the stream filament can be neglected to first approximation. The equation of motion reads **mass · acceleration = sum of all external forces acting**. Therefore for the volume element dV we have

$$dm \cdot b = \sum_i F_i . \quad (2.39)$$

We have already considered the acceleration b in Chapter 2.3.1. For a one-dimensional stream filament, equation (2.37) is written as

$$b = \frac{dc}{dt} = \frac{\partial c}{\partial t} + c \cdot \frac{\partial c}{\partial s} ,$$

for this flow which is assumed to be steady $c \cdot (dc/ds)$. The mass of the volume element dV considered in Figure 2.28 is $dm = \rho \cdot dA \cdot ds$. The forces acting on the volume element are the pressure forces and the gravitation, and their components along the stream filament coordinate are in equilibrium. This yields

$$\begin{aligned} \rho \cdot dA \cdot ds \cdot \frac{dc}{dt} &= \rho \cdot dA \cdot ds \cdot \left(\frac{\partial c}{\partial t} + c \cdot \frac{\partial c}{\partial s} \right) = \\ &= p \cdot dA - \left(p + \frac{\partial p}{\partial s} \cdot ds \right) \cdot dA - \rho \cdot g \cdot dA \cdot ds \cdot \cos(\varphi) , \end{aligned}$$

$\cos(\varphi) = dz/ds$ and division by $\rho \cdot dA \cdot ds$ delivers the **Euler equation** for the stream filament

$$\boxed{\frac{dc}{dt} = \frac{\partial c}{\partial t} + c \cdot \frac{\partial c}{\partial s} = -\frac{1}{\rho} \cdot \frac{\partial p}{\partial s} - g \cdot \frac{dz}{ds}} . \quad (2.40)$$

For **steady** flows, all quantities are functions only of s and it follows that

$$c \cdot \frac{dc}{ds} = \frac{d}{ds} \left(\frac{c^2}{2} \right) = -\frac{1}{\rho} \cdot \frac{dp}{ds} - g \cdot \frac{dz}{ds} \Rightarrow d \left(\frac{c^2}{2} \right) + \frac{1}{\rho} \cdot dp + g \cdot dz = 0 .$$

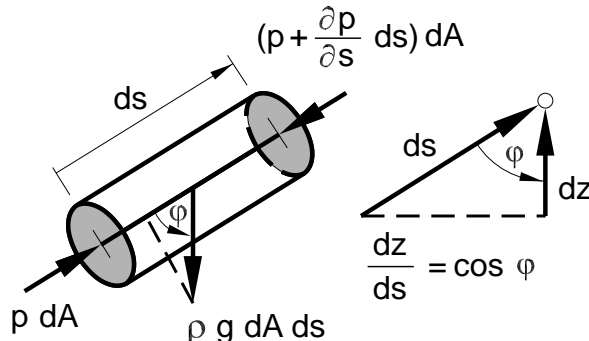


Fig. 2.28 : Balance of forces at a stream filament element dV

Integration along the stream filament s from position 1 with c_1, p_1 and s_1, z_1 to position 2 with c_2, p_2 and s_2, z_2 yields

$$\frac{1}{2} (c_2^2 - c_1^2) + \int_{p_1}^{p_2} \frac{1}{\rho} \cdot dp + g \cdot (z_2 - z_1) = 0 \quad .$$

For the incompressible flow under consideration $\rho = \text{const.}$, so that the factor $1/\rho$ can be written in front of the integral and we obtain the **Bernoulli equation** for incompressible, steady, inviscid flows. The dimensions are energy per unit mass:

$$\frac{c_2^2}{2} + \frac{p_2}{\rho} + g \cdot z_2 = \frac{c_1^2}{2} + \frac{p_1}{\rho} + g \cdot z_1 = \text{const.} \quad .$$

(2.41)

Alternatively, the Bernoulli equation with the dimensions of energy per unit volume is frequently used

$$p_2 + \frac{1}{2} \cdot \rho \cdot c_2^2 + \rho \cdot g \cdot z_2 = p_1 + \frac{1}{2} \cdot \rho \cdot c_1^2 + \rho \cdot g \cdot z_1 = \text{const.} \quad .$$

(2.42)

At some given position, the Bernoulli equation for steady flows reads

$$p + \frac{1}{2} \cdot \rho \cdot c^2 + \rho \cdot g \cdot z = \text{const.} \quad \text{or} \quad \frac{p}{\rho} + \frac{c^2}{2} + g \cdot z = \text{const.} \quad (2.43)$$

Here the constant summarizes the three known terms at an initial state. It has the same value for all points along s of a stream filament, but can vary from one stream filament to the next. The Bernoulli equation is an algebraic equation and yields the relation between velocity and pressure. For **unsteady** flows, the partial time derivative $\partial c / \partial t$ of the Euler equation must also be integrated along the stream filament s . Here the integration is to be carried out at a fixed time t from s_1 to s_2 . The Bernoulli equation for unsteady one-dimensional flows is found:

$$\rho \cdot \int_{s_1}^{s_2} \frac{\partial c}{\partial t} \cdot ds + p_2 + \frac{1}{2} \cdot \rho \cdot c_2^2 + \rho \cdot g \cdot z_2 = \text{const.} \quad ,$$

$$\int_{s_1}^{s_2} \frac{\partial c}{\partial t} \cdot ds + \frac{p_2}{\rho} + \frac{c_2^2}{2} + g \cdot z_2 = \text{const.} \quad .$$

(2.44)

Application of the Bernoulli Equation

There are many examples of application of the Bernoulli equation in the book of solved problems accompanying this textbook. We will look at two examples which are applied in practice. Using the **Venturi pipe** shown in Figure 2.29, the mass flux can be determined by measuring the pressure at the narrowest cross-section and applying the Bernoulli equation (2.41). The narrowing of the cross-section causes an acceleration in the nozzle, and, according to the Bernoulli equation, a pressure drop. A widening in the cross-section causes

a deceleration of the flow with corresponding pressure recovery. If the pressure p is measured at the narrowest cross-section A , and for known values of c_1 and p_1 , the velocity c is determined using

$$\frac{c^2}{2} + \frac{p}{\rho} = \frac{c_1^2}{2} + \frac{p_1}{\rho} = \text{const.} .$$

Since in this example $z_1 = z_2$, the gravitation term is eliminated. For a known cross-sectional area at the narrowest cross-section A , the mass flux is determined to be

$$\dot{m} = \rho \cdot c \cdot A .$$

The application of the Bernoulli equation (2.41) therefore makes it possible to determine the flow velocity c from a measured pressure p . This is used in the case of aircraft, for example, to determine the flight velocity using a **Prandtl tube**. Before we look at the way a Prandtl tube works, we first have to introduce some pressure definitions. We consider the Bernoulli equation (2.42)

$$p + \frac{1}{2} \cdot \rho \cdot c^2 + \rho \cdot g \cdot z = \text{const.} .$$

Here we denote $p = p_{\text{stat}}$ as the static pressure and $(1/2) \cdot \rho \cdot c^2 = p_{\text{dyn}}$ as the dynamic pressure. The static pressure p_{stat} is the pressure measured when one moves with the flow velocity c in the fluid. Therefore the static pressure is that which is responsible for the pressure force which acts on a body in a flow. The dynamic pressure p_{dyn} can be considered to be a measure of the kinetic energy per unit volume of a volume element of the fluid moving with velocity c .

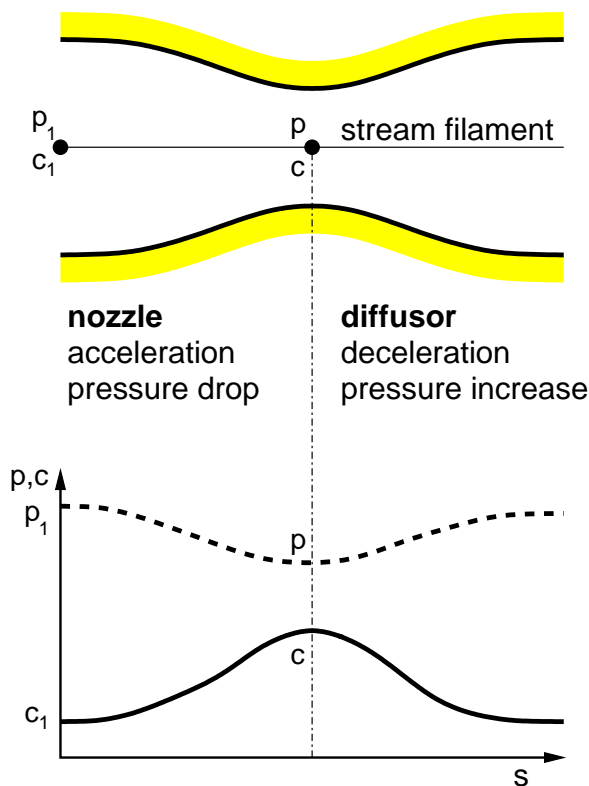


Fig. 2.29 : Venturi pipe

In the case of shear flows, such as the boundary layer flow past a wing, $z_1 = z_2$ and the gravitation term $\rho \cdot g \cdot z$ is eliminated from the equation. The constant on the right-hand side of the Bernoulli equation can vary from one streamline to the next. It is a property of the streamline under consideration and is determined by suitable reference values. Such reference values can be, for example, the known values of the undisturbed free stream, such as p_∞ and c_∞ . In the case of the flow past a wing, the constant on the so-called stagnation streamline can be determined. This stagnation streamline leads from the free stream in infinity, past a variable point 1 to the stagnation point 0 on the wing (Figure 2.30).

The Bernoulli equation on the stagnation streamline reads

$$p_\infty + \frac{1}{2} \cdot \rho \cdot c_\infty^2 = p_1 + \frac{1}{2} \cdot \rho \cdot c_1^2 = p_0 = \text{const.} .$$

In the stagnation point $c = 0$, and so there is no dynamic pressure at this point. The variable p_0 denotes the pressure in the stagnation point. This is also called the reservoir pressure or the total pressure. Therefore we have

$$p_0 = p_{\text{tot}} = p_{\text{res}} = p_{\text{stat}} + p_{\text{dyn}} . \quad (2.45)$$

We have already used the dynamic pressure of the free stream $(1/2) \cdot \rho \cdot c_\infty^2$ in the introductory chapters for the dimensionless pressure coefficient c_p

$$c_p = \frac{p - p_\infty}{\frac{1}{2} \cdot \rho \cdot c_\infty^2} .$$

The different pressure definitions are summarized in Figure 2.31. The pressures can be measured using classical hydrostatic methods.

Measurement of the **static pressure** p_{stat} :

The most simple measurement principle to determine the static pressure p_{stat} consists of bore hole in a wall and the U-pipe pressure gauge introduced in Chapter 2.2.1. The static pressure p_{stat} of the outer flow is imprinted onto the boundary layer, i.e. it is constant within the boundary layer in the direction normal to the wall. The static pressure of the outer flow is measured as follows. The relations in Figure 2.32 between pressure difference Δp and height difference Δh in the pressure gauge are valid, with ρ_a the density of the air, ρ_l the density of the liquid, and p_{ref} the reference pressure.

Figure 2.33 shows the wind tunnel model of a wing. The pressure bore holes, from which the pressure distribution in Figure 1.18 was taken, are so small that they cannot be seen in the

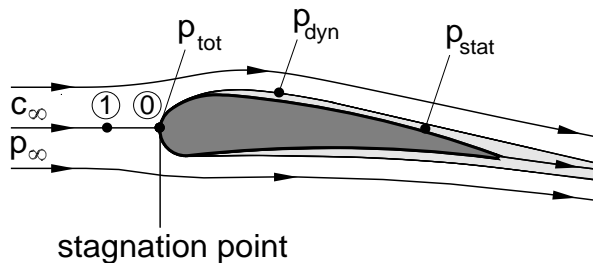


Fig. 2.30 : Pressure definitions in the flow past a wing

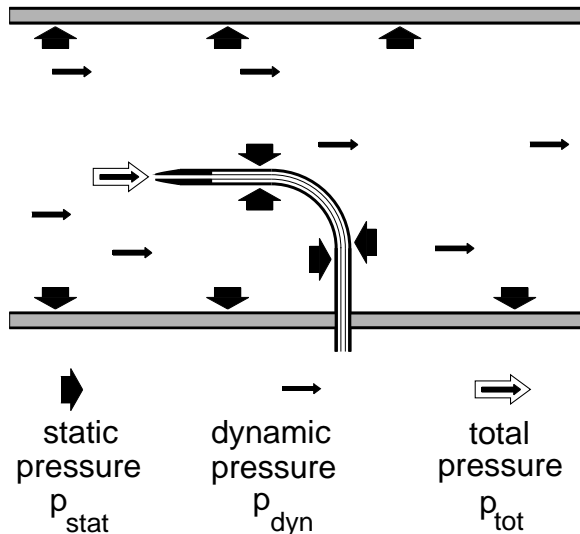
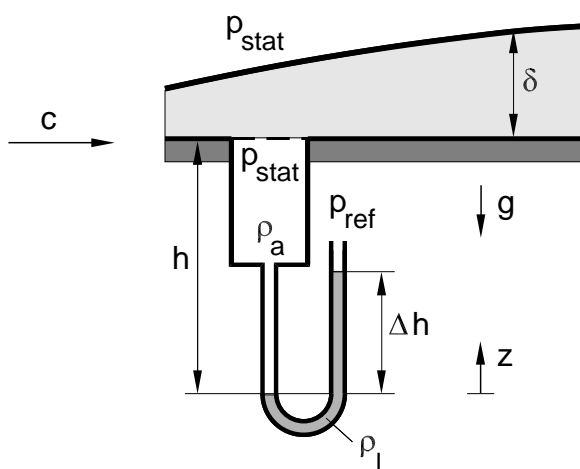


Fig. 2.31 : The different pressure definitions: static pressure p_{stat} , dynamic pressure p_{dyn} , total pressure p_{tot}

figure. It is only the small pressure tubes inside the wing model which can be seen. These measure the pressure, and these days are piezoquartz pressure sensors rather than classical U-pipe pressure gauges.

The static pressure p_{stat} can be measured with a probe held in the flow (Figure 2.34). It works according to the same principle as the wall bore holes, but in this case the bore holes are distributed around the probe to measure the static pressure. Here too a boundary layer forms around the top of the probe and this is imprinted with the static pressure of the outer flow. In order to minimize measurement errors, the bore holes must be at a large enough distance from the top of the probe and the shaft of the probe. This is so that the disturbances caused by the holes die away and are not measured too.



$$\begin{aligned}
 p_{stat} + \rho_a \cdot g \cdot h &= p_{ref} + \rho_l \cdot g \cdot \Delta h \\
 p_{stat} - p_{ref} &= \rho_l \cdot g \cdot \Delta h - \rho_a \cdot g \cdot h \\
 \text{frequently: } \rho_a \cdot g \cdot h &\ll \rho_l \cdot g \cdot \Delta h \\
 \Rightarrow \Delta p &= p_{stat} - p_{ref} = \rho_l \cdot g \cdot \Delta h
 \end{aligned}$$

Fig. 2.32 : Measurement of the static pressure p_{stat}

Measurement of the **total pressure** p_{tot} or reservoir pressure p_0 :

The measurement of the total pressure p_{tot} or the reservoir pressure p_0 is carried out using a Pitot tube. By placing this into the parallel flow, the tube will be filled with air for a few moments, until the air everywhere in the tube has come to rest, since it cannot expand any further. This is also true for the entrance cross-section, where the stagnation point forms with $c = 0$. It then follows that the same total pressure p_{tot} is at hand everywhere in the Pitot tube, and this again is measured by a U-pipe pressure gauge.

Measurement of the **dynamic pressure** p_{dyn} :

In order to measure the dynamic pressure p_{dyn} , a combination of a static probe and a Pitot tube is used, called the **Prandtl stagnation tube**. This determines the dynamic pressure as the difference between the total pressure and the static pressure, and from it the velocity can be determined.

$$c = \sqrt{\frac{2 \cdot p_{dyn}}{\rho_L}} = \sqrt{\frac{2 \cdot \rho_{Fl} \cdot g \cdot \Delta h}{\rho_L}} . \quad (2.46)$$

An example of a Prandtl tube, as can be seen on any aircraft, is shown in Figure 2.35.



Fig. 2.33 : Static pressure bore holes in a wing model

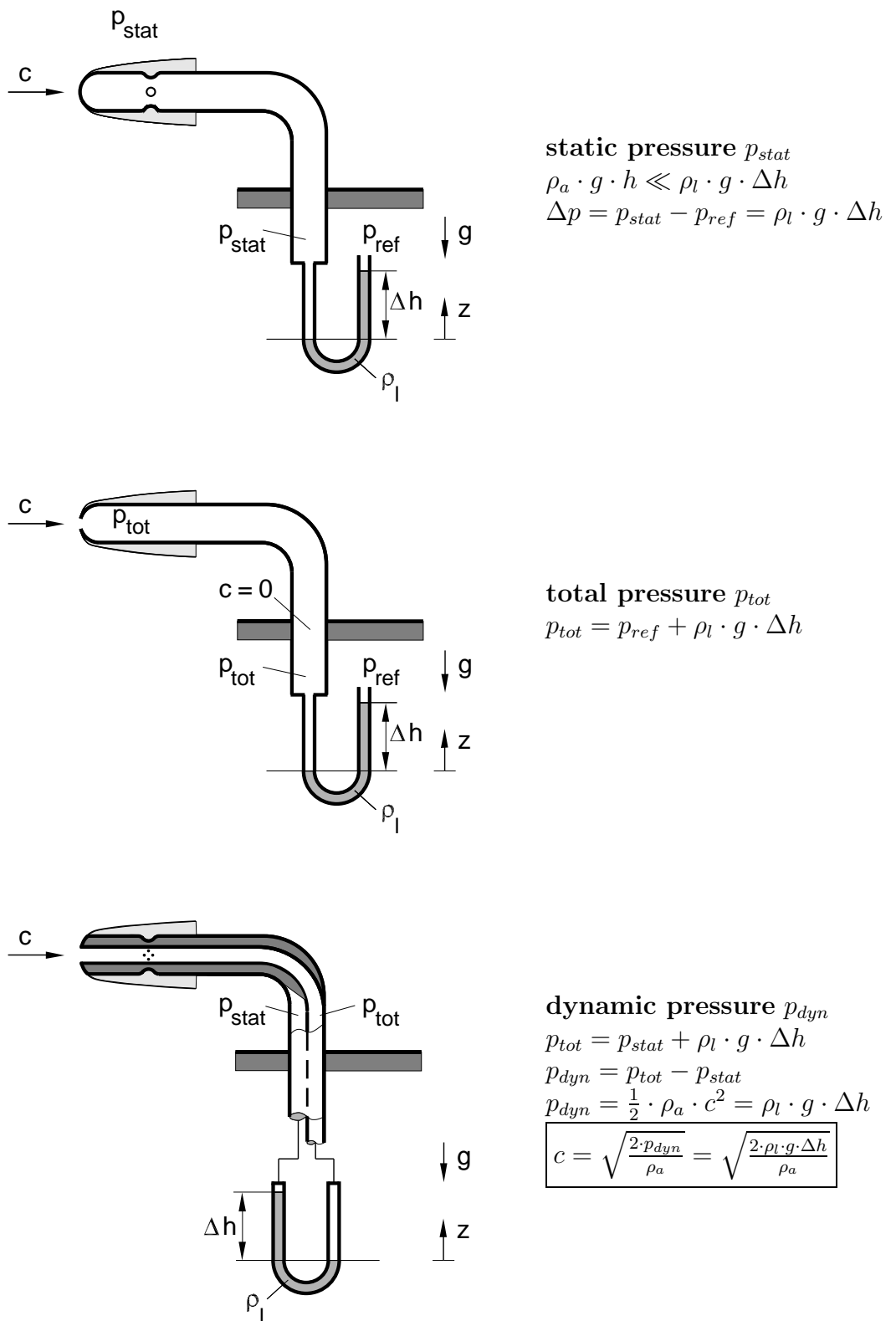


Fig. 2.34 : Measurement of the static pressure p_{stat} , the total pressure p_{tot} and the dynamic pressure p_{dyn}

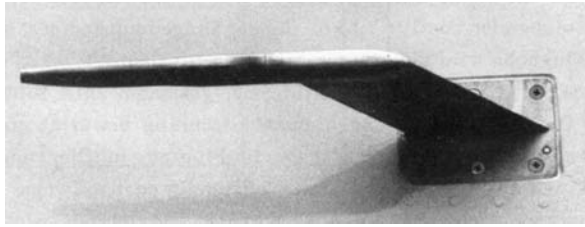


Fig. 2.35 : Prandtl stagnation tube

Balance of Forces Perpendicular to the Stream Filament

Up until now we have discussed examples of flows where the changes along the stream filament have been large compared to the changes perpendicular to the stream filament by definition. If the changes are larger than those along the stream filament, we carry out the balance of forces on the volume element dV perpendicular to the stream filament along the normal direction n . s now denotes the arc length of the stream filament, r is the local radius of curvature. The equation of motion normal to the stream filament reads

$$dm \cdot b_n = \sum_i F_i \quad .$$

The mass element dm is found to be $dm = \rho \cdot dV = \rho \cdot dA \cdot dn$. If c denotes the velocity along the stream filament coordinate s , the magnitude of the acceleration b_n is determined from the ratio of the magnitude of the centripetal force F_z and the mass element dm . Therefore we have

$$F_z = \frac{dm \cdot c^2}{r} \quad \Rightarrow \quad b_n = \frac{F_z}{dm} = \frac{c^2}{r} \quad .$$

This acceleration b_n keeps the mass element on the curved path, and so its direction indicates the local center of curvature, opposite to the direction of n . The external forces are the pressure forces and one component of gravity $\rho \cdot dA \cdot dn \cdot g$ (Figure 2.36). Therefore the equation of motion becomes

$$dm \cdot b_n = \rho \cdot dA \cdot dn \cdot \left(-\frac{c^2}{r} \right) = p \cdot dA - \left(p + \frac{\partial p}{\partial n} \cdot dn \right) \cdot dA + \rho \cdot dA \cdot dn \cdot g \sin(\varphi) \quad ,$$

and after division by $(-\rho \cdot dA \cdot dn)$ and with $\sin(\varphi) = -dz/dn$ it follows that

$$\frac{c^2}{r} = \frac{1}{\rho} \cdot \frac{\partial p}{\partial n} + g \cdot \frac{dz}{dn} \quad . \quad (2.47)$$

For a plane shear flow at $z = const.$, we find using $dz = 0$ that

$$\frac{c^2}{r} = \frac{1}{\rho} \cdot \frac{\partial p}{\partial n} \quad .$$

(2.48)

The pressure increases in the direction of the external normal direction n , or in the case of plane circular flows, in the radial direction r . The pressure force and centripetal force are in equilibrium.

Vortex motions on concentric circular paths can be computed with the ordinary differential equation (2.48). For example, the pressure and velocity distributions of a tornado (Figure

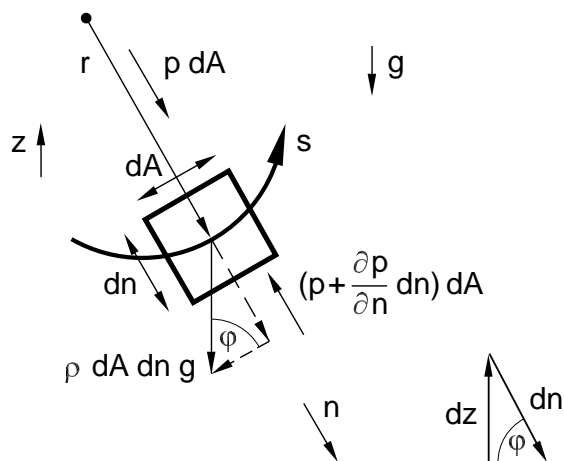


Fig. 2.36 : Balance of forces at a volume element perpendicular to the stream filament

2.37) can be determined approximately using one-dimensional stream filament theory. The streamlines are concentric circles. For a velocity magnitude of c , on circular paths we have $c(r) = c_r/r$ with the circumferential velocity $c(R_0) = c_0$ at a given radius R_0 and the constant $c_r = c_0 \cdot R_0$. With $n = r$, equation (2.48) is written

$$\frac{c_r^2}{r^3} = \frac{1}{\rho} \cdot \frac{dp}{dr} . \quad (2.49)$$

Integration of this first order ordinary differential equation with the boundary condition $p(R_0) = p_0$ at a fixed radius R_0 yields

$$p(r) = p_0 + \frac{\rho \cdot c_r^2}{2} \cdot \left(\frac{1}{R_0^2} - \frac{1}{r^2} \right) . \quad (2.50)$$

This can be written in the following form

$$p(r) + \frac{\rho}{2} \cdot c^2(r) = p_0 + \frac{\rho}{2} \cdot c_0^2 = \text{const.}$$

. (2.51)

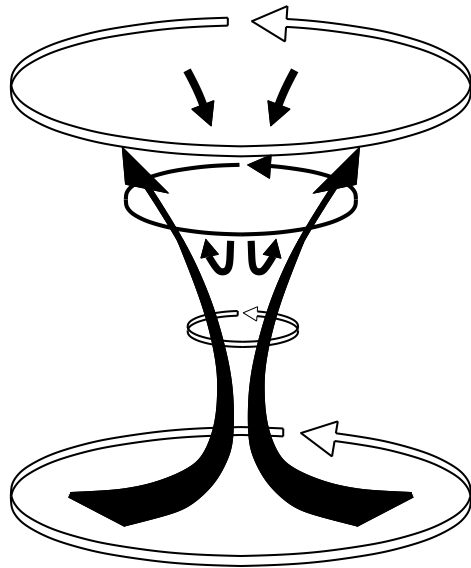


Fig. 2.37 : Circular flow in a tornado

This is the Bernoulli equation for vortex flows on concentric circles, derived from the balance of forces perpendicular to the stream filament. It can be shown that the flow on concentric circles is irrotational, with $\nabla \times \vec{c} = 0$. Figure 2.38, for $r \geq R_0$ shows the pressure distribution computed with equation (2.50) as well as the assumed velocity distribution $c = c_r/r$.

According to the Bernoulli equation (2.51), pressure and velocity behave differently with increasing r . For $r > 0$, the velocity for a potential vortex would increase indefinitely. Since this is not what happens in reality, the differential equation for inviscid vortex flows (2.49) is replaced by the differential equation for viscous flows for $r > R_0$. This equation will be treated at the end of this chapter. Here too the division of flow regimes introduced in Chapter 1.2 is seen. In the core of the vortex the flow corresponds to a frictional rigid body rotation with constant angular velocity ω_r and linear velocity distribution $c = \omega_r \cdot r$. The pressure drops for $r < R_0$ again, and in the case of a tornado, reaches values of between 20 and 200 mbar.

Conservation of Energy

The third fundamental equation needed for the complete mathematical description of flows with heat transport, which is also needed if the work done by flow machinery is to be taken

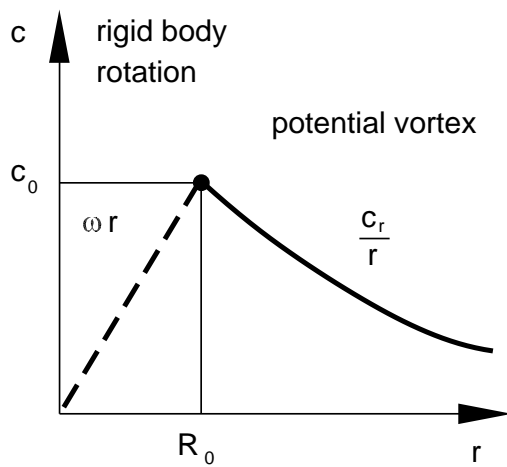
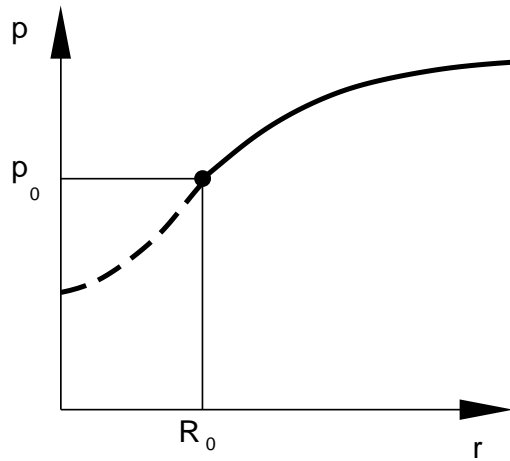


Fig. 2.38 : Pressure and velocity distribution in a potential vortex

into account, is the conservation of energy. In order to derive the balance of energy, we add to the sketches of the streamtube and the stream filament in Figure 2.26 an additional heat flux q (Figure 2.39).

In general the conservation of energy of a steady inviscid flow states that the change in energy flux in a given volume element dV is equal to the work done by the forces acting and by the heat flux. The energy flux \dot{E} written in Watts ($\{W\} = \{J/s\}$) is

$$\dot{E} = \left(e + \frac{c^2}{2} \right) \cdot \dot{m} = \left(e + \frac{c^2}{2} \right) \rho \cdot c \cdot A ,$$

with the internal energy e referred to the mass element $dm = \rho \cdot dV$ and the mass specific kinetic energy $c^2/2$. For both cross-sections A_1 and A_2 of the streamtube considered, and with the continuity equation $\dot{m} = const.$, we have

$$\dot{E}_1 = \left(e_1 + \frac{c_1^2}{2} \right) \cdot \dot{m} = \left(e_1 + \frac{c_1^2}{2} \right) \rho_1 \cdot c_1 \cdot A_1 ,$$

$$\dot{E}_2 = \left(e_2 + \frac{c_2^2}{2} \right) \cdot \dot{m} = \left(e_2 + \frac{c_2^2}{2} \right) \rho_2 \cdot c_2 \cdot A_2 .$$

The work done by the forces acting (pressure forces and gravity), as well as the power of the heat flux $q \cdot \dot{m}$, lead (neglecting the friction) to a change in the energy flux from 1 to 2 according to the following balance equations

$$\dot{E}_2 - \dot{E}_1 = p_1 \cdot A_1 \cdot c_1 - p_2 \cdot A_2 \cdot c_2 + g \cdot (z_1 - z_2) \cdot \dot{m} + q \cdot \dot{m} ,$$

$$\left(e_2 + \frac{c_2^2}{2} \right) \cdot \dot{m} - \left(e_1 + \frac{c_1^2}{2} \right) \cdot \dot{m} = p_1 \cdot A_1 \cdot c_1 - p_2 \cdot A_2 \cdot c_2 + g \cdot (z_1 - z_2) \cdot \dot{m} + q \cdot \dot{m} .$$

After division by $\dot{m} = \rho_1 \cdot c_1 \cdot A_1 = \rho_2 \cdot c_2 \cdot A_2$ it follows that

$$e_2 + \frac{p_2}{\rho_2} + \frac{1}{2} \cdot c_2^2 + g \cdot z_2 = e_1 + \frac{p_1}{\rho_1} + \frac{1}{2} \cdot c_1^2 + g \cdot z_1 + q .$$

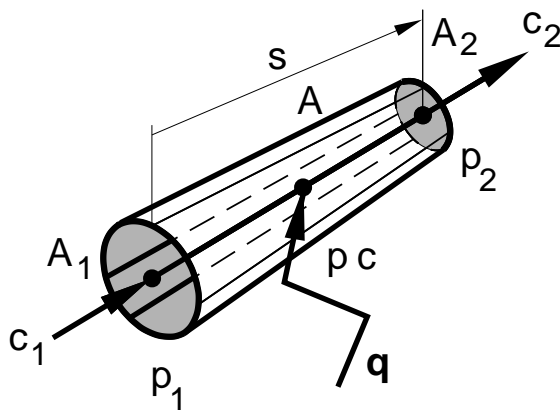


Fig. 2.39 : Streamtube and stream filament with heat flux q

With the definition of the mass specific enthalpy $h = e + p/\rho$ we find

$$h_2 + \frac{1}{2} \cdot c_2^2 + g \cdot z_2 = h_1 + \frac{1}{2} \cdot c_1^2 + g \cdot z_1 + q .$$

The three quantities h_1, c_1 and $g \cdot z_1$ at the cross-section A_1 , which are known quantities according to $h_1 + (1/2) \cdot c_1^2 + g \cdot z_1 = \text{const.}$, can be brought together to one constant. Considering the quantities at the cross-section A , we obtain

$$h + \frac{1}{2} \cdot c^2 + g \cdot z - q = \text{const.} .$$

(2.52)

If no heat is supplied or removed and so the internal energy does not change, the balance of energy and the Bernoulli equation are identical. This is only valid for the incompressible flow considered in this chapter.

For flows with mechanical supply of energy (**pumps**) or mechanical removal of energy (**turbines**), such as are found in the night storage power station in Figure 2.40, the balance of energy (2.52), or, if the heat losses in the pumps and turbines are neglected, the Bernoulli equation (2.42), is extended by a term which describes the specific work done Δl_P by the pump. The same holds for the turbine with specific work done Δl_T (units $\{J/m^3\}$).

During the day, when the load is at its maximum, the water in the storage power station flows from the reservoir at height z_2 along the pressure pipe down to the collection basin at height z_1 , and the flow drives the turbine. At night, when the network load is lower, the water is pumped back up from z_1 to z_2 by the turbine which now acts as a pump. While the water being pumped from positions 1 to 2, energy is being supplied to it. The energy content per unit volume $\{J/m^3\}$ of the fluid is therefore larger at 2 than at 1

$$p_2 + \frac{1}{2} \cdot \rho \cdot c_2^2 + \rho \cdot g \cdot z_2 > p_1 + \frac{1}{2} \cdot \rho \cdot c_1^2 + \rho \cdot g \cdot z_1 .$$

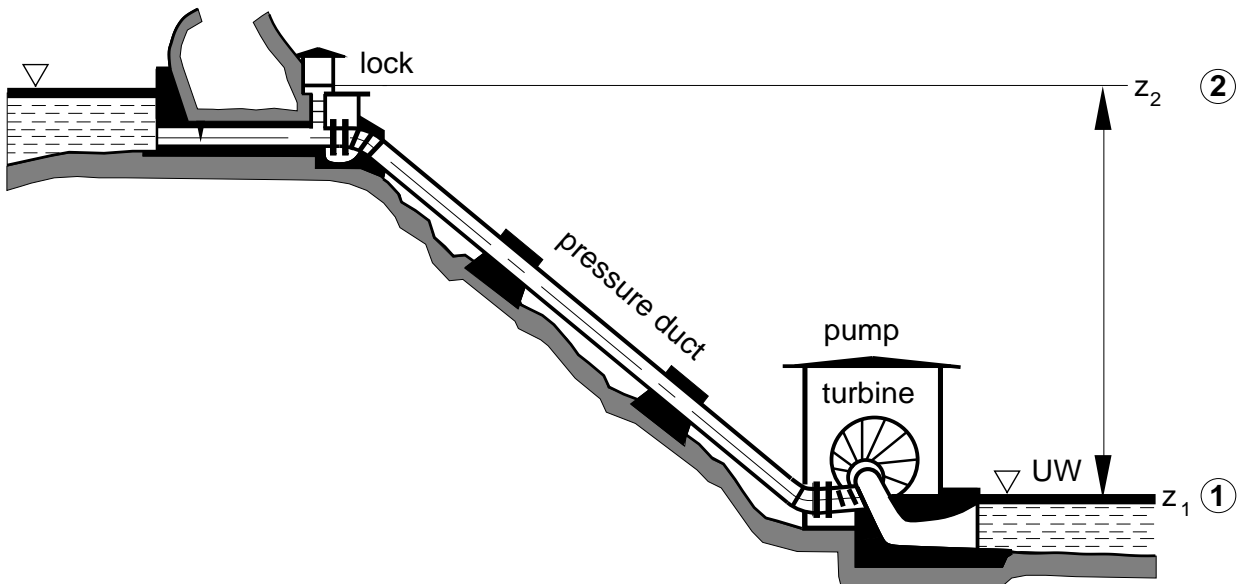


Fig. 2.40 : Storage power station

Using the specific work of the pump $\Delta l_P > 0$, the Bernoulli equation (flow direction from 1 → 2) reads

$$\boxed{p_2 + \frac{1}{2} \cdot \rho \cdot c_2^2 + \rho \cdot g \cdot z_2 = p_1 + \frac{1}{2} \cdot \rho \cdot c_1^2 + \rho \cdot g \cdot z_1 + \Delta l_P} . \quad (2.53)$$

If the fluid flows from 2 to 1, thereby driving the turbine, energy is removed from the fluid on the way from 2 to 1, and so the energy content of the fluid is lower at 1 than at 2

$$p_1 + \frac{1}{2} \cdot \rho \cdot c_1^2 + \rho \cdot g \cdot z_1 < p_2 + \frac{1}{2} \cdot \rho \cdot c_2^2 + \rho \cdot g \cdot z_2 .$$

If we define the specific work transformed by a turbine into electrical energy to be positive too, i.e. $\Delta l_T > 0$, the Bernoulli equation in this case (flow direction from 2 → 1) reads

$$\boxed{p_1 + \frac{1}{2} \cdot \rho \cdot c_1^2 + \rho \cdot g \cdot z_1 = p_2 + \frac{1}{2} \cdot \rho \cdot c_2^2 + \rho \cdot g \cdot z_2 - \Delta l_T} . \quad (2.54)$$

Note that the flow direction is different when the pump is used compared to when the turbine is used.

Using the specific work Δl for the pump or the turbine, we can obtain their power in $\{W\} = \{J/s\}$ by multiplication with the volume flux $\dot{V} = A \cdot c$ as

$$L = \Delta l \cdot \dot{V} .$$

Summary of the Fundamental Inviscid Equations of Stream Filament Theory

The fundamental equations of one-dimensional stream filament theory for incompressible and inviscid flows can be summarized as follows:

Conservation of mass	$\rho \cdot c \cdot A = const.$	(2.55)
Conservation of momentum Integral of Euler equation ⇒ Bernoulli equation	$\int^s \frac{\partial c}{\partial t} \cdot ds + \frac{p}{\rho} + \frac{1}{2} \cdot c^2 + g \cdot z = const.$	(2.56)
Conservation of energy	$h + \frac{1}{2} \cdot c^2 + g \cdot z + q + \Delta l = const.$	(2.57)

These are 3 algebraic equations to determine the flow variables c, p, h . They are supplemented by the thermodynamic relations

$$h = c_p \cdot T , \quad q = -\lambda \cdot \frac{\partial T}{\partial s} .$$

The work done by flow machinery Δl in general has to be measured. The solution of the algebraic equations (2.55) to (2.57) is found using either known algebraic methods, or,

if possible, analytically. The numerical solution will be presented in Chapter 3.1 in the form of the software package **KAPPA** (Karlsruhe Parallel Program for Aerodynamics) **Stromfaden** (stream filament). Examples of analytic solutions are found in the book of solved problems in Chapter 2.3.

Navier-Stokes Equation

Now at the end of this chapter on incompressible flows, we will consider two-dimensional conservation of momentum, that is the equation of motion, of **viscous** flows at fixed walls.

Again we set out the stream surface and the stream filament as in Figure 2.27 in the boundary layer flow regime or the viscous wake of the flow past an automobile. Once more we select a cylindrical volume element along the stream filament and consider the streamtube of Figure 2.41 for the viscous flow. Here a cylindrical ring element of length ds and base area $dA = 2 \cdot \pi \cdot r \cdot dr$ is considered. The velocity c is no longer only a function of s and possibly of t , but is now also dependent on the radial coordinate r . Since $\partial c / \partial r \neq 0$ holds for $r \neq 0$ there are shear stress contributions to the balance of forces. For the equation of motion

$$dm \cdot b = \sum_i F_i$$

and mass $dm = \rho \cdot dA \cdot ds = \rho \cdot 2 \cdot \pi \cdot r \cdot dr \cdot ds$, acceleration $b = \partial c / \partial t + c \cdot (\partial c / \partial s)$ and forces acting F_i : pressure forces, shear stresses and the component of gravity along s , we have

$$\begin{aligned} dm \cdot \left(\frac{\partial c}{\partial t} + c \cdot \frac{\partial c}{\partial s} \right) &= \rho \cdot 2 \cdot \pi \cdot r \cdot dr \cdot ds \cdot \left(\frac{\partial c}{\partial t} + c \cdot \frac{\partial c}{\partial s} \right) = p \cdot 2 \cdot \pi \cdot r \cdot dr - \\ \left(p + \frac{\partial p}{\partial s} \cdot ds \right) \cdot 2\pi \cdot r \cdot dr - \rho \cdot g \cdot 2\pi \cdot r \cdot dr \cdot ds \cdot \cos(\varphi) - \tau \cdot 2 \cdot \pi \cdot r \cdot ds + \\ \left(\tau + \frac{\partial \tau}{\partial r} \cdot dr \right) \cdot 2 \cdot \pi \cdot (r + dr) \cdot ds \quad . \end{aligned}$$

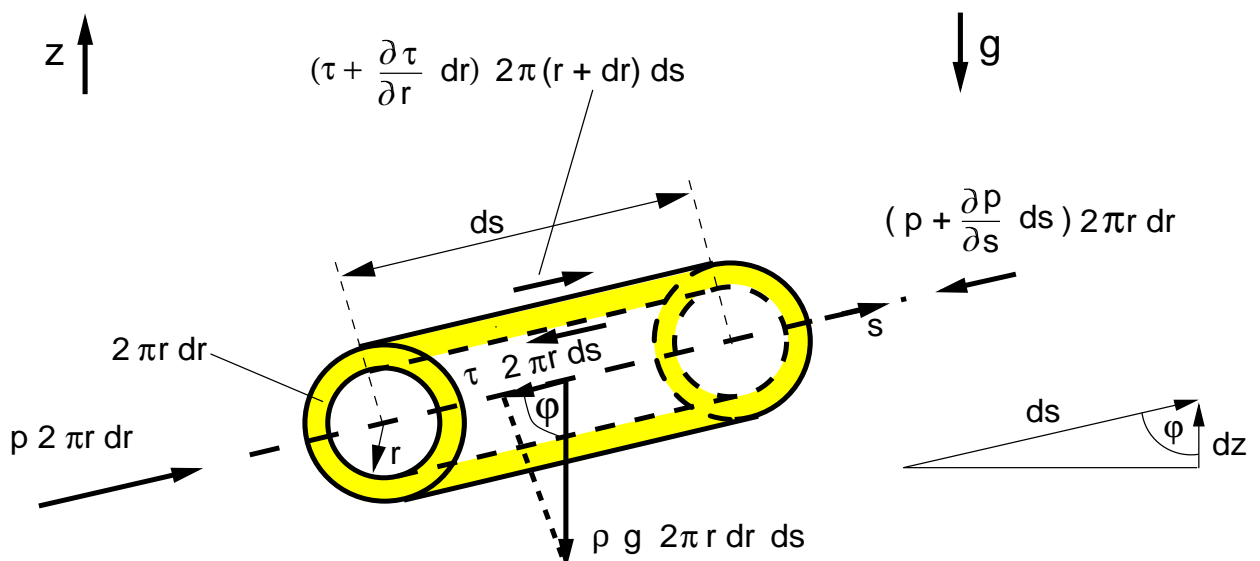


Fig. 2.41 : Balance of forces at a stream filament element dV for viscous flow

With $\cos(\varphi) = dz/ds$ and dividing by $(\rho \cdot 2 \cdot \pi \cdot r \cdot dr \cdot ds)$, while neglecting terms of the order $(dr)^2$, the ansatz $\tau = \mu \cdot (\partial c / \partial r)$ with $\nu = \mu/\rho$ yields the **Navier-Stokes equation** in cylindrical coordinates

$$\boxed{\frac{\partial c}{\partial t} + c \cdot \frac{\partial c}{\partial s} = -\frac{1}{\rho} \cdot \frac{\partial p}{\partial s} + \nu \cdot \left(\frac{1}{r} \cdot \frac{\partial c}{\partial r} + \frac{\partial^2 c}{\partial r^2} \right) - g \cdot \frac{dz}{ds}} \quad . \quad (2.58)$$

This is a second order partial differential equation. In contrast to the Euler equation (2.40), the Navier-Stokes equation also takes the effect of friction into account, by means of changes in the shear stresses which give rise to the second derivative of the velocities. The left-hand side of the Navier-Stokes equation again characterizes the fundamental equation of kinematics (2.36) for one-dimensional flows, but is now supplemented by the pressure, friction and gravitation forces.

The Navier-Stokes equation in stream filament coordinates s and n reads

$$\boxed{\frac{\partial c}{\partial t} + c \cdot \frac{\partial c}{\partial s} = -\frac{1}{\rho} \cdot \frac{\partial p}{\partial s} + \nu \cdot \frac{\partial^2 c}{\partial n^2} - g \cdot \frac{dz}{ds}} \quad . \quad (2.59)$$

The individual terms mean:

$$\frac{\partial c}{\partial t} + c \cdot \frac{\partial c}{\partial s} \quad \text{inertial forces per unit mass,}$$

$$\frac{1}{\rho} \cdot \frac{\partial p}{\partial s} \quad \text{pressure force per unit mass,}$$

$$\nu \cdot \frac{\partial^2 c}{\partial n^2} \quad \text{friction force per unit mass,}$$

$$g \cdot \frac{dz}{ds} \quad \text{gravity per unit mass.}$$

The Navier-Stokes equation can be made **dimensionless** with suitable characteristic quantities. The dimensionless quantities are denoted by a star. All position coordinates appearing s , n and z are referred to a characteristic length L and the velocity c to a characteristic velocity c_∞ . The ratio L/c_∞ represents a characteristic time, used to make the time t dimensionless. The pressure p is made dimensionless with twice the value of the dynamic pressure, i.e. with $\rho \cdot c_\infty^2$.

$$s^* = \frac{s}{L} \quad , \quad n^* = \frac{n}{L} \quad , \quad z^* = \frac{z}{L} \quad , \quad c^* = \frac{c}{c_\infty} \quad , \quad t^* = \frac{t \cdot c_\infty}{L} \quad , \quad p^* = \frac{p}{\rho \cdot c_\infty^2} \quad .$$

If we set these quantities into the dimensional Navier-Stokes equation (2.59), we obtain

$$\frac{c_\infty^2}{L} \cdot \frac{\partial c^*}{\partial t^*} + \frac{c_\infty^2}{L} \cdot c^* \cdot \frac{\partial c^*}{\partial s^*} = -\frac{1}{\rho} \cdot \frac{\rho \cdot c_\infty^2}{L} \cdot \frac{\partial p^*}{\partial s^*} + \nu \cdot \frac{c_\infty}{L^2} \cdot \frac{\partial^2 c^*}{\partial n^{*2}} - g \cdot \frac{L}{L} \cdot \frac{dz^*}{ds^*} \quad .$$

Multiplication by the factor $\frac{L}{c_\infty^2}$ leads to

$$\frac{\partial c^*}{\partial t^*} + c^* \cdot \frac{\partial c^*}{\partial s^*} = -\frac{\partial p^*}{\partial s^*} + \frac{\nu}{c_\infty \cdot L} \cdot \frac{\partial^2 c^*}{\partial n^{*2}} - \frac{g \cdot L}{c_\infty^2} \cdot \frac{dz^*}{ds^*} \quad .$$

The combinations of characteristic quantities in front of each of the last two terms are the Reynolds number $Re_L = (c_\infty \cdot L)/\nu$ and the Froude number $Fr_L = c_\infty^2/(g \cdot L)$, each formed with the characteristic length L , which we already used in the introductory chapters. The dimensionless Navier-Stokes equation reads

$$\boxed{\frac{\partial c^*}{\partial t^*} + c^* \cdot \frac{\partial c^*}{\partial s^*} = -\frac{\partial p^*}{\partial s^*} + \frac{1}{Re_L} \cdot \frac{\partial^2 c^*}{\partial n^{*2}} - \frac{1}{Fr_L} \cdot \frac{dz^*}{ds^*}} , \quad (2.60)$$

with the dimensionless characteristic numbers

$$\text{Froude number: } Fr_L = \frac{\text{inertial force}}{\text{gravity}} = \frac{c \cdot \frac{\partial c}{\partial s}}{g \cdot \frac{dz}{ds}} = \frac{c_\infty^2}{g \cdot L} ,$$

$$\text{Reynolds number: } Re_L = \frac{\text{inertial force}}{\text{viscous force}} = \frac{c \cdot \frac{\partial c}{\partial s}}{\nu \cdot \frac{\partial^2 c}{\partial n^2}} = \frac{c_\infty \cdot L}{\nu} .$$

For $Fr \gg 1$, the inertial force of the flow dominates and gravity may be neglected. For $Re \gg 1$ the inertial force also dominates. The effect of viscosity is restricted to a thin viscous layer **close to the wall**, which we recognize as the **boundary layer**. For the boundary layer thickness δ referred to the length L and shown in Figure 2.42, we have the relation

$$\boxed{\frac{\delta}{L} \sim \frac{1}{\sqrt{Re_L}}} . \quad (2.61)$$

The static pressure inside this boundary layer corresponds to the static pressure of the inviscid outer flow, imprinted onto the boundary layer. For $Re \ll 1$, the viscous force dominates in the entire flow field. Flows in this regime are called **creeping flows** (Figure 2.42), and a division into an inviscid outer flow and a viscous flow layer close to the wall is no longer possible.

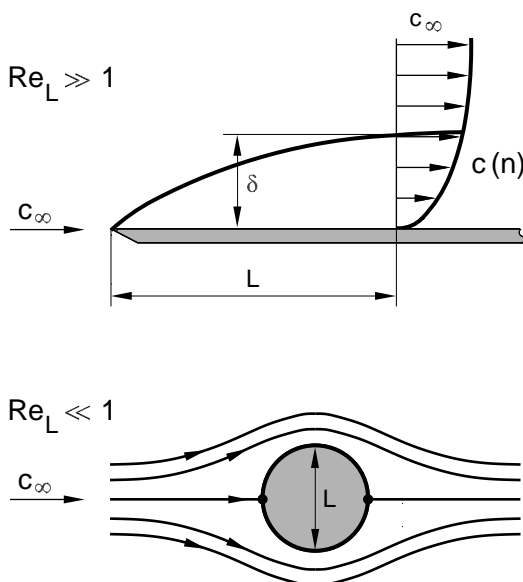


Fig. 2.42 : Plate boundary layer flow and creeping flow past a cylinder

The orders of magnitude of Reynolds numbers which occur for living organisms and in technology are summarized in the following table.

Nature	Re_L	motion
bacteria	10^{-6}	friction dominates motion \Rightarrow ciliary
amoeba (flagella)	10^{-3}	
tadpoles	10^2	inertial force dominates jet propulsion
eel	10^5	wave-like motion
human	10^6	large Re_L numbers motion by means of vortex separation
blue whale	10^8	\Rightarrow tail fin
Technology		
automobile airplane	10^7	combustion engine
submarine	10^9	propeller

If we integrate the dimensionless Navier-Stokes equation (2.60) at a fixed time t along the stream filament coordinate, we obtain

$$\int \frac{\partial c^*}{\partial t^*} \cdot ds^* + \int \frac{\partial}{\partial s^*} \left(\frac{c^{*2}}{2} \right) \cdot ds^* = - \int \frac{\partial p^*}{\partial s^*} \cdot ds^* - \frac{1}{Fr_L} \cdot \int \frac{dz^*}{ds^*} \cdot ds^* + \frac{1}{Re_L} \cdot \int \frac{\partial^2 c^*}{\partial n^{*2}} \cdot ds^* + const. ,$$

$$\boxed{\int \frac{\partial c^*}{\partial t^*} \cdot ds^* + \frac{1}{2} \cdot c^{*2} + p^* + \frac{1}{Fr_L} \cdot z^* - \frac{1}{Re_L} \cdot \int \frac{\partial^2 c^*}{\partial n^{*2}} \cdot ds^* = const.} . \quad (2.62)$$

In the KAPPA software, equation (2.62) supplements the Bernoulli equation (2.56) by the viscous term $(1/Re_L) \cdot \int (\partial^2 c^* / \partial n^{*2}) \cdot ds^*$. In the software package KAPPA-Stromfaden

(Chapter 3.1), this is taken into account to compute the viscous layers. We are then no longer dealing with one-dimensional stream filament theory, rather with the general formulation of the fluid mechanical fundamental equations for three-dimensional flows.

Analytical Solutions of the Navier-Stokes Equation

We consider three **analytical solutions** of the **Navier-Stokes equation**. In a pipe with circular cross-section of radius R , a parabolic velocity profile $c(r)$ is formed (Figure 2.43). This is a steady ($\partial c / \partial t = 0$), fully formed ($\partial c / \partial s = 0$) **pipe flow**. The velocity profile does not change along the coordinate s , so that $(1/\rho) \cdot \partial p / \partial s = \text{const}$. This is a horizontal shear flow with $dz = 0$, and so the gravitational force $g \cdot (dz/ds) = 0$ is eliminated. Under these assumptions, the Navier-Stokes equation in cylindrical coordinates (2.58) reads

$$\frac{1}{r} \cdot \frac{dc}{dr} + \frac{d^2c}{dr^2} = \text{const.} \quad , \quad (2.63)$$

where the constant viscosity ν has been added on to the constant pressure gradient $(1/\rho) \cdot \partial p / \partial s$. Since the velocity $c(r)$ is a function only of the radial coordinate r , we obtain a second order differential equation. With the two boundary conditions

$$r = \pm R \quad \Rightarrow \quad c(R) = 0$$

and the supplementary condition

$$\left. \frac{dc}{dr} \right|_{r=0} = 0 \quad ,$$

the differential equation (2.63) can be solved using a power law ansatz for $c(r)$:

$$c(r) = -\frac{R^2}{4 \cdot \nu \cdot \rho} \cdot \frac{dp}{ds} \cdot \left(1 - \frac{r^2}{R^2} \right) \quad .$$

With the maximum velocity $c_{max} = -(R^2/(4 \cdot \nu \cdot \rho)) \cdot (dp/ds)$ it is found for the pipe flow that

$$c(r) = c_{max} \left(1 - \frac{r^2}{R^2} \right) \quad . \quad (2.64)$$

A parabolic velocity profile $c(n)$ is also found for the plane steady channel flow, called the **Poiseuille flow** (Figure 2.44). The Navier-Stokes equation to be solved (2.59), with $\partial p / \partial s = \text{const.}$ and $dz = 0$ for the fully-formed channel flow $\partial c / \partial s = 0$ can be written as

$$\nu \cdot \frac{\partial^2 c}{\partial n^2} = \text{const.} \quad . \quad (2.65)$$

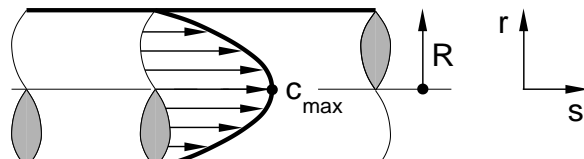


Fig. 2.43 : Hagen-Poiseuille pipe flow

After integrating twice and using the boundary conditions

$$n = \pm H \Rightarrow c(h) = 0$$

we find the parabolic velocity profile

$$c(n) = -\frac{h^2}{2 \cdot \nu \cdot \rho} \cdot \frac{dp}{ds} \cdot \left(1 - \frac{n^2}{h^2}\right) = c_{max} \cdot \left(1 - \frac{n^2}{h^2}\right) . \quad (2.66)$$

The shear stress of this viscous channel flow can be computed with (2.1)

$$\tau(n) = \mu \cdot \frac{dc}{dn} = -\frac{2 \cdot \mu \cdot c_{max}}{h^2} \cdot n .$$

The linear distribution of the magnitudes of the shear stresses shown in Figure 2.44 is therefore found.

In the case of **Couette flow**, shown in Figure 2.45, in a channel with a lower wall at rest and an upper wall moving with constant velocity U , and the additional assumption $\partial p / \partial s = 0$ the Navier-Stokes equation (2.59) is

$$\frac{d^2c}{dn^2} = 0 . \quad (2.67)$$

After integrating twice and using the boundary conditions

$$n = \pm h \Rightarrow c(-h) = 0, \quad c(+h) = U$$

we obtain the linear velocity profile

$$c(n) = \frac{U}{2} \cdot \left(1 + \frac{n}{h}\right) . \quad (2.68)$$

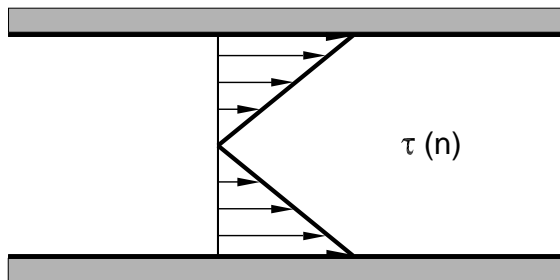
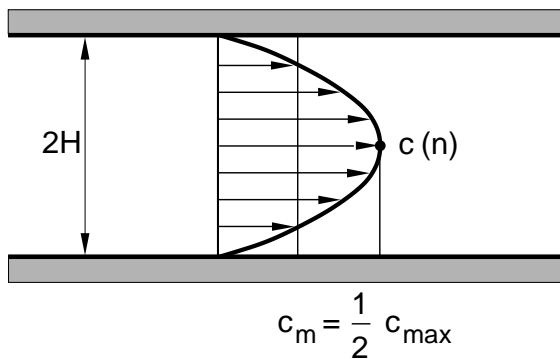


Fig. 2.44 : Poiseuille channel flow

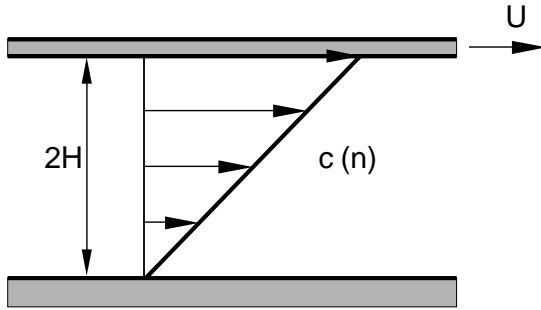


Fig. 2.45 : Couette flow

Drag Coefficients

Now that we have looked at the basics of inviscid and viscous flow regimes, we can go back to the introductory examples in Chapter 1.2 and treat the drag of bodies in a flow more precisely.

The **total drag coefficient** c_w (1.2)

$$c_w = \frac{W}{\frac{1}{2} \cdot \rho_\infty \cdot c_\infty^2 \cdot A} ,$$

with drag W on the body, free stream velocity c_∞ and a characteristic cross-sectional area A , consists of terms corresponding to the inviscid and viscous regions in the flow field:

$$c_w = c_d + c_f , \quad (2.69)$$

the part due to the pressure distribution c_p called **pressure drag** c_d and the **friction drag** c_f . The drag coefficients are written as

$$c_d = \frac{P}{\frac{1}{2} \cdot \rho_\infty \cdot c_\infty^2 \cdot A} , \quad c_f = \frac{\tau_w}{\frac{1}{2} \cdot \rho_\infty \cdot c_\infty^2} ,$$

with the shear stress τ_w at the wall. The pressure force P is computed from the pressure coefficient c_p (1.1)

$$c_p = \frac{p - p_\infty}{\frac{1}{2} \cdot \rho_\infty \cdot c_\infty^2}$$

by integration along the wall streamline s , and the magnitude of the total wall shear stress τ_w by integration of the local value of τ_w on the surface of the body. This yields the total drag W of a body of length L to be

$$W = \left(\int_0^L c_{p,u} \sin \alpha \cdot ds - \int_0^L c_{p,l} \sin \alpha \cdot ds \right. \\ \left. + \int_0^L c_{f,u} \cos \alpha \cdot ds + \int_0^L c_{f,l} \cos \alpha \cdot ds \right) \cdot \frac{1}{2} \cdot \rho_\infty \cdot c_\infty^2 \cdot B , \quad (2.70)$$

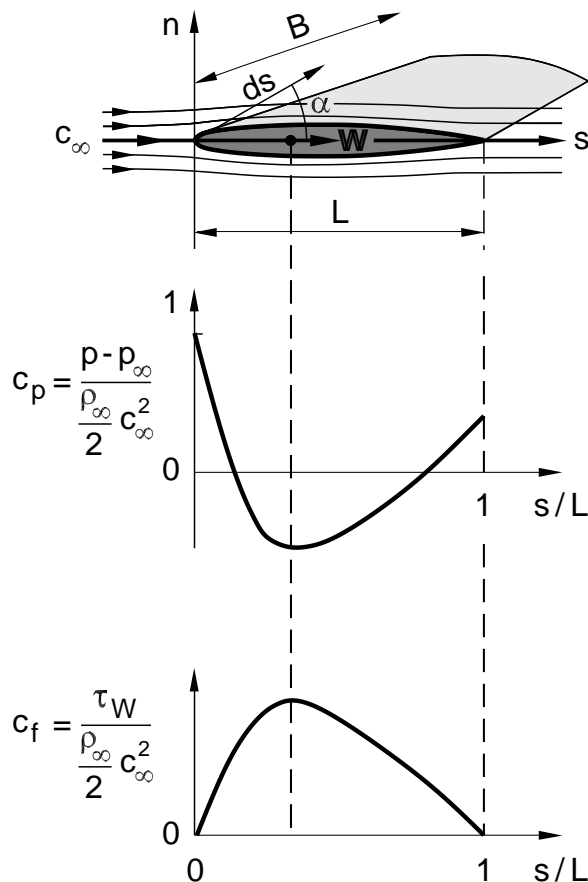


Fig. 2.46 : Pressure coefficient c_p and drag coefficient c_f of symmetric flow past a foil

where u and l are the upper and lower sides of the body respectively, and B is a characteristic depth, with $A = L \cdot B$. The integration is carried out along the two surfaces. In splitting the drag up into the pressure drag and the viscous drag, it was assumed that, although the pressure drag depends on the shape of the body, the friction drag essentially only depends of the size of the surface of the body and not on the shape of this surface.

Figure 2.46 shows the pressure drag coefficient c_d and the friction drag coefficient c_f for a symmetric foil in a flow with c_∞ . Here we note that, in contrast to the example in Chapter 1, we now assume an incompressible flow with low Mach number, such as is found in the case of gliders. Figure 2.47 summarizes the drag contributions of bodies in flows.

body	c_d	c_f
	0 %	100 %
	10 %	90 %
	90 %	10 %
	100 %	0 %

Fig. 2.47 : Contributions due to the pressure drag c_d and the friction drag c_f of a body in a flow

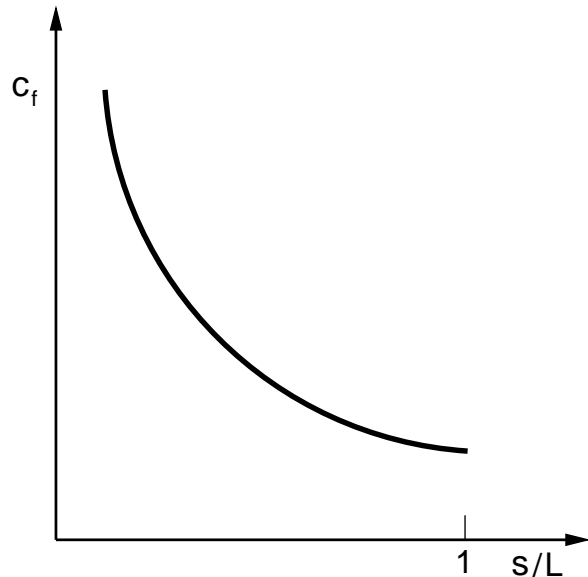


Fig. 2.48 : Friction coefficient c_f of the plate boundary layer

The pressure is imprinted onto the boundary layer of a plate placed longitudinally in a flow. Here the pressure drag c_d is equal to zero and the total drag c_w consists only of the friction drag c_f , whose local value along the plate is shown in Figure 2.48.

Because of its small cross-sectional area A , a slender foil only has a small pressure drag (Figure 2.47), and it is the friction drag which dominates. In the case of a cylinder in a flow, the relationship of the different drag terms is the opposite, and it is the pressure drag which dominates. A plate placed transversely in a flow has essentially only pressure drag, and the friction drag is vanishingly small.

Let us return to the question of the body with the smallest total drag c_w . The racing car build in 1938 and shown in Figure 1.3 with a c_w value of 0.17 is an example of the ideal geometry. It is **streamline bodies**, as shown in Figure 2.49, which have the smallest drag. However, in Chapter 2.4.5 we will see that even these small drag coefficients can be decreased even further by suitable influencing of the wall shear stress τ_w .

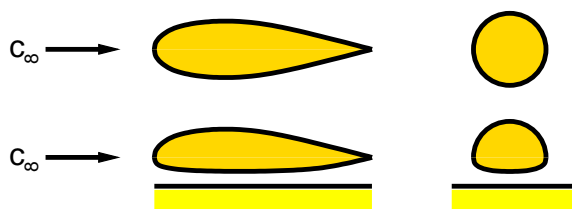


Fig. 2.49 : Streamlined bodies in a free stream (Zeppelin) and close to the ground (automobile)

2.3.3 Compressible Flows

Compressible flow is characterized by a quantity called the compressibility K

$$K = \frac{\text{relative change in volume}}{\text{change in pressure required}} = -\frac{dV}{V} \cdot \frac{1}{dp} . \quad (2.71)$$

Since the pressure change $dp > 0$ for a volume change $dV < 0$, the definition for K gets an additional minus sign, so that K itself is positive. Its value for water, for example, is $K_{H_2O} = 5 \cdot 10^{-5} \text{ 1/bar}$. For gases at constant temperature, the Boyle-Mariotte law holds:

$$p = \text{const.} \cdot \frac{m}{V} , \quad (2.72)$$

$$V = \text{const.} \cdot \frac{m}{p} \Rightarrow \frac{dV}{dp} = -\text{const.} \cdot \frac{m}{p^2} ,$$

with $(1/V) = (p/(m \cdot \text{const.})$ it follows that K is

$$K = -\frac{dV}{dp} \cdot \frac{1}{V} = \text{const.} \cdot \frac{m}{p^2} \cdot \frac{p}{m \cdot \text{const.}} \Rightarrow K = \frac{1}{p} .$$

The value for air at $p = 1 \text{ bar}$ is $K_{air} = (1/p) = 1 \text{ (1/bar)}$. A comparison between air and water yields

$$\frac{K_{air}}{K_{H_2O}} = 20000 .$$

Therefore air is about 20000 times more compressible than water. We have already used this fact by treating water flows generally as incompressible flows, and gas flows at higher flow speeds as compressible flows. As well as the characteristic numbers of the previous chapter, we now also introduce the **Mach number M**

$$M = \frac{c}{a} = \frac{\text{flow velocity}}{\text{speed of sound}} \quad (2.73)$$

as an additional dimensionless characteristic number. The **speed of sound a** corresponds to the velocity of expansion of small disturbances in the variables of state (e.g. pressure disturbances dp) in a compressible medium at rest (Figure 2.50). The velocity of sound is a signal velocity with which disturbances in the flow field are transmitted. The gas through which the sound wave has passed has a pressure perturbation dp , a density perturbation $d\rho$ and a perturbation in the velocity dc .

For an observer moving with $-a$, the sound wave is at rest and behind the sound wave he sees the velocity $dc - a$. If we restrict ourselves to **inviscid** outer flows, we can write down the continuity equation for the sound wave at rest

$$\dot{m} = \rho \cdot c \cdot A = \text{const.} \Rightarrow (\rho + d\rho) \cdot (-a + dc) \cdot A = -\rho \cdot a \cdot A \Rightarrow \frac{d\rho}{\rho} = \frac{dc}{a} ,$$

and the Bernoulli equation becomes

$$\frac{c^2}{2} + \int_0^p \frac{dp}{\rho} = \text{const.} \Rightarrow \frac{(-a + dc)^2}{2} + \int_0^{p+dp} \frac{dp}{\rho} = \frac{(-a)^2}{2} + \int_0^p \frac{dp}{\rho}$$

$$\Rightarrow a \cdot dc = \frac{dp}{\rho} .$$

The speed of sound a is therefore coupled with pressure and density changes in the medium. Small disturbances expand without losses, i.e. isentropically, and so for the square of the speed of sound we can write

$$a^2 = \left(\frac{\partial p}{\partial \rho} \right)_s .$$

This corresponds to the equation of definition (2.9). Using the equation of isentropic change of state

$$\frac{p}{p_1} = \left(\frac{\rho}{\rho_1} \right)^\kappa \quad (2.74)$$

it follows that

$$\frac{\partial p}{\partial \rho} = p_1 \cdot \kappa \cdot \left(\frac{\rho}{\rho_1} \right)^{(\kappa-1)} \cdot \frac{1}{\rho_1} = \kappa \cdot \frac{p_1}{\rho_1} \cdot \frac{\left(\frac{\rho}{\rho_1} \right)^\kappa}{\left(\frac{\rho}{\rho_1} \right)} = \kappa \cdot \frac{p_1}{\rho} \cdot \frac{p}{p_1} = \kappa \cdot \frac{p}{\rho} ,$$

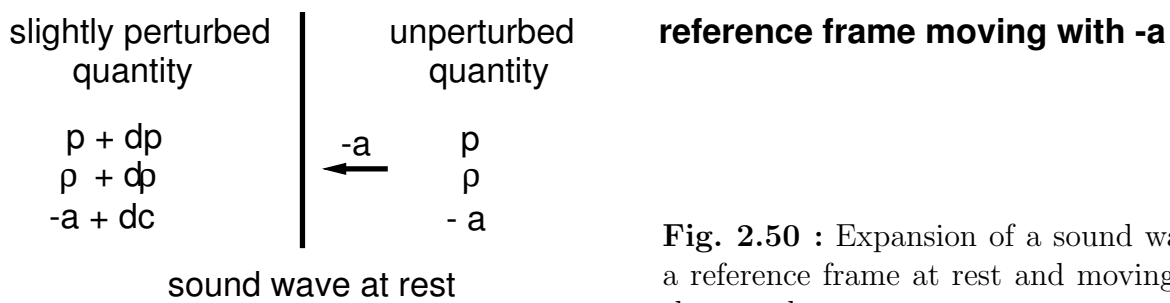
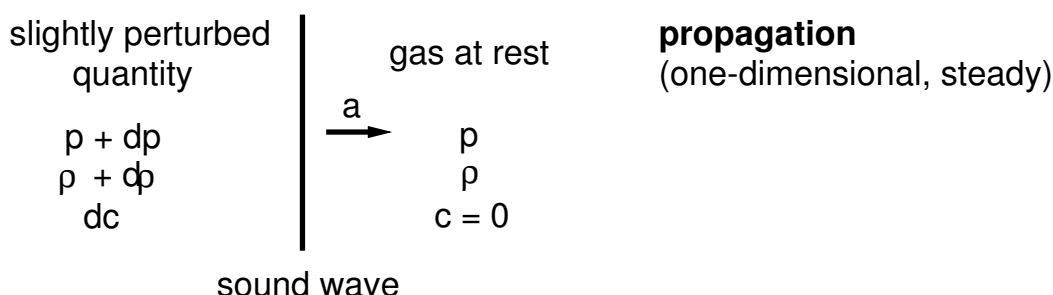


Fig. 2.50 : Expansion of a sound wave in a reference frame at rest and moving with the sound wave

and with the ideal gas equation (2.8)

$$\boxed{a^2 = \kappa \cdot \frac{p}{\rho} , \quad a^2 = \kappa \cdot R \cdot T , \quad a^2 = \kappa \cdot \frac{\mathcal{R}}{\mathcal{M}} \cdot T} , \quad (2.75)$$

with the general gas constant $\mathcal{R} = 8.314 \text{ J/(mol} \cdot \text{K)}$ and the molar mass \mathcal{M} { $\frac{\text{g}}{\text{mol}}$ }. We can write down the following important relations for the speed of sound a

$$\boxed{a \sim \sqrt{T} , \quad a \sim \sqrt{\frac{1}{\mathcal{M}}} .} \quad (2.76)$$

The numerical values for air are

$$\kappa = 1.4 , \quad R = 287 \frac{\text{J}}{\text{kg} \cdot \text{K}} , \quad T = 293.15 \text{ K} \Rightarrow a = 343.20 \frac{\text{m}}{\text{s}} = 1235.5 \frac{\text{km}}{\text{h}} .$$

Sound waves are all around us in both natural and technical areas. One impressive example is that of the crack of a whip. Figure 2.51 shows four snapshots of the end of a whip. In 1 the end of the whip is just about to snap around. In 2, the whip opens up and the crack wave S is formed. This can no longer be considered to be a small disturbance. The sound

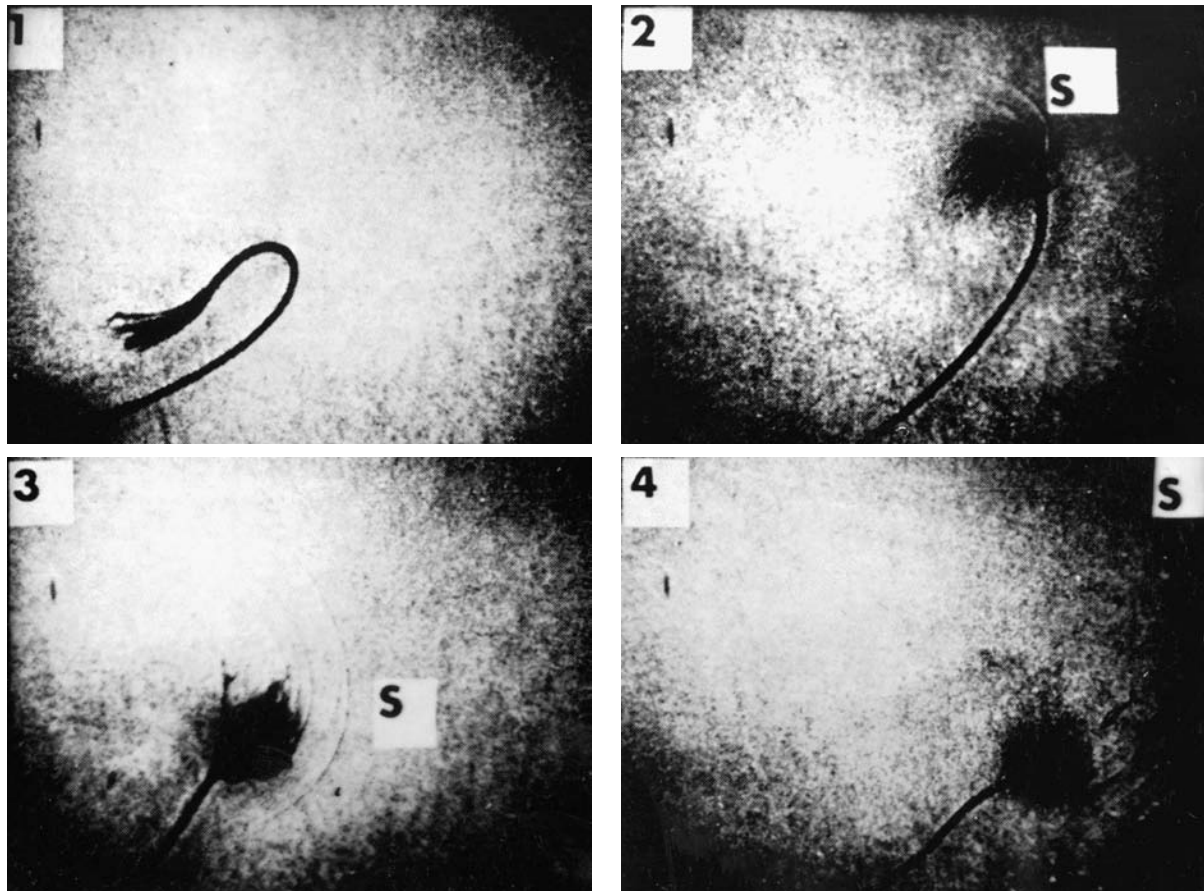


Fig. 2.51 : Crack of a whip

wave is built up to a **shock wave**, which we hear as the loud crack. In the third and fourth pictures the wave spreads out into the compressible surrounding air.

Consider the sound waves in Figure 2.52 which spread out from a source at rest or a moving source (such as the crack of a whip). In the case of the source which is at rest, the sound waves expand as concentric spherical waves. If the sound source is moving with a velocity U_∞ smaller than the speed of sound a_∞ ($M_\infty < 1$), the spherical waves are denser upstream. An external observer first hears a higher frequency (higher tone) and then, after the sound source has moved past, a lower frequency (lower tone). If the sound source moves with a velocity U_∞ which is greater than the speed of sound a_∞ ($M_\infty > 1$), the sound waves remain inside a characteristic cone, known as the Mach cone, with a cone angle of $\sin(\alpha) = a_\infty/U_\infty$. If the source of the sound is a supersonic airplane, this Mach cone is built up to a shock wave (head shock wave), whose pressure distribution on the ground is sketched in Figure 2.53. The shock wave generates a pressure jump Δp on the ground, which we hear as a sonic boom. In order to be able to attain the unperturbed thermodynamic state of the air p_∞ behind the airplane again, a further shock is needed, the tail wave. This reverses the pressure increase due to the head wave. This explains the double sonic boom heard on the ground when a supersonic airplane flies past.

Mach Number Regimes

As well as characterizing viscous flows with the Reynolds number Re_L ; flows with heat transport with the Prandtl number Pr_∞ ; and the effect of gravity with the Froude number Fr_L , the Mach number M_∞ allows us to differentiate between regions of incompressible and compressible flow. An incompressible subsonic flow with $\partial\rho/\partial s \ll \partial c/\partial s$ is present when

$M_\infty \ll 1$ subsonic flow, incompressible (flow past an automobile)

,

compressible subsonic flows are found in the regime

$0.2 < M_\infty < 1$ compressible subsonic flow (ICE or TGV trains)

,

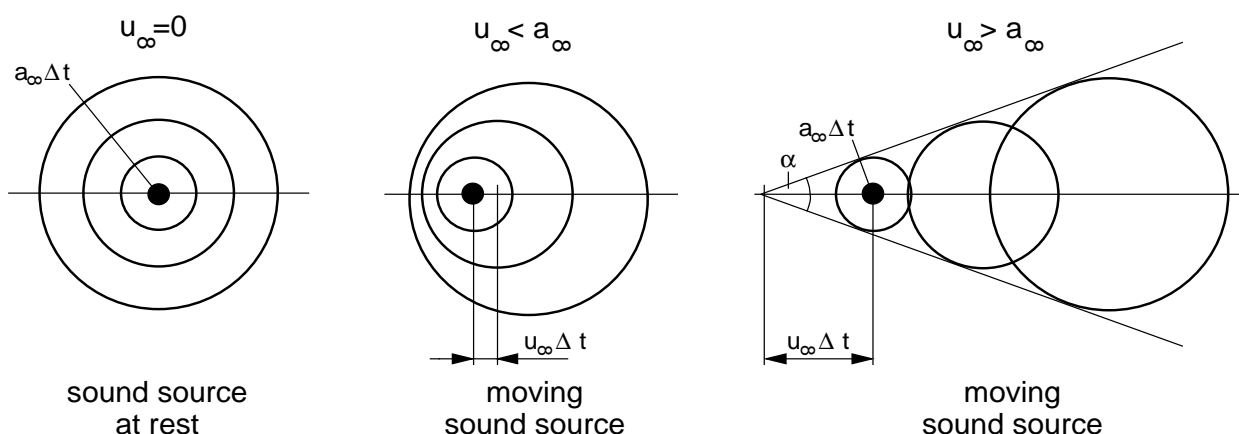


Fig. 2.52 : Wave propagation from a source

transonic flows with $\partial\rho/\partial s \approx \partial c/\partial s$ are found for

$$M_\infty \leq 1 \text{ transonic flow (civil airplane)}$$

and supersonic flows with $\partial\rho/\partial s \gg \partial c/\partial s$ for

$$M_\infty > 1 \text{ supersonic flow (supersonic airplane Concorde)}$$

Hypersonic flows occur for

$$M_\infty \gg 1 \text{ hypersonic flow (re-entry vehicle, Space Shuttle)}$$

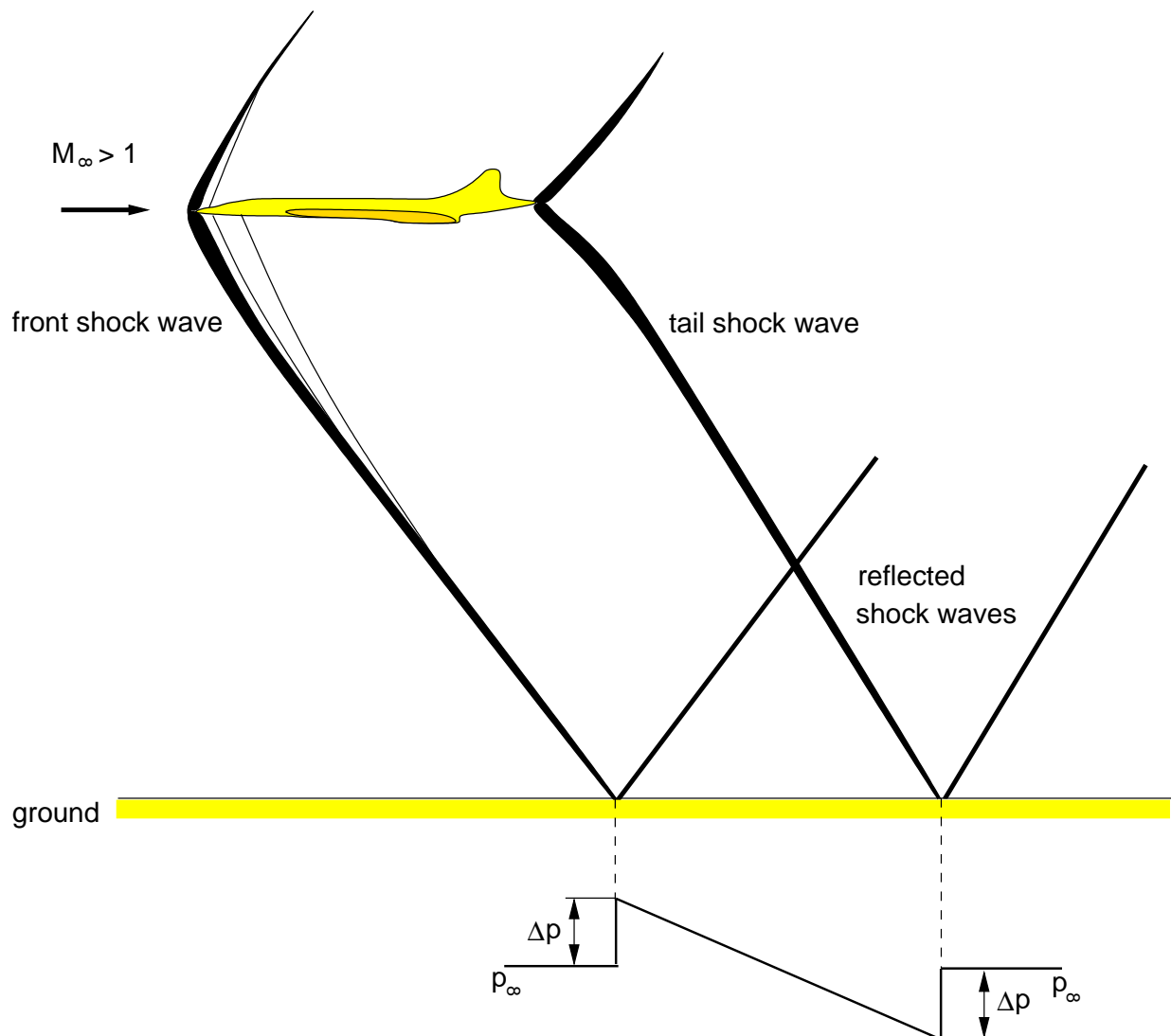


Fig. 2.53 : Supersonic flight and pressure distribution at ground

The thermodynamic equations of state for ideal gases are no longer valid in the hypersonic flow regime. In this Mach number regime, the chemical reactions of hot air have to be taken into account. These are treated in the textbook *Aerothermodynamik*, OERTEL 1994. For example, for the Mach number $M_\infty = 10$, the effect of compressibility dominates and

$$\frac{1}{\rho} \frac{\partial \rho}{\partial s} \sim 100 \frac{1}{c} \frac{\partial c}{\partial s}$$

Stream Filament Theory of Compressible Flows

The derivation of one-dimensional stream filament theory for compressible flows is based on the Euler equation (2.40). In what follows, we consider a steady shear flow, such as inviscid outer flow or inviscid core flow of a nozzle. For the shear flow $dz = 0$, and the Euler equation is written in the stream filament coordinate s as

$$\begin{aligned} c \cdot \frac{dc}{ds} &= -\frac{1}{\rho} \cdot \frac{dp}{ds} = -\frac{1}{\rho} \cdot \frac{d\rho}{dp} \cdot \frac{dp}{ds} = -a^2 \frac{1}{\rho} \cdot \frac{d\rho}{ds} \quad | : c^2 \quad , \\ \frac{1}{c} \cdot \frac{dc}{ds} &= -\frac{1}{M_\infty^2} \cdot \frac{1}{\rho} \cdot \frac{d\rho}{ds} \quad , \\ \boxed{\frac{1}{\rho} \cdot \frac{d\rho}{ds}} &= -M_\infty^2 \cdot \frac{1}{c} \cdot \frac{dc}{ds} \quad , \end{aligned} \quad (2.77)$$

with $(1/\rho) \cdot (d\rho/ds)$ the relative change in density and $(1/c) \cdot (dc/ds)$ the relative change in velocity.

In the subsonic regime $M_\infty^2 \ll 1$, and so, as already mentioned, the relative change in density in subsonic flows is much smaller than the relative change in velocity, and for small Mach number can frequently be completely neglected.

In the supersonic region the opposite is true. Because $M_\infty^2 \gg 1$, the relative change in density is very much larger than the relative change in velocity. If a supersonic flow is accelerated, $dc/ds > 0$, then, because of the factor $-M_\infty^2$, this acceleration leads to a considerable reduction in the density of the medium, $d\rho/ds < 0$. Therefore supersonic flows need space. Because of the continuity equation, the strong relative reduction in density in an accelerated supersonic flow means that the cross-section A increases along s .

In transonic flows $M_\infty^2 \approx 1$, and all changes, both density changes and relative velocity changes, are of the same order of magnitude. Again the integral of the Euler equation leads to the **Bernoulli equation** for compressible flow. If we consider the integral along the stream filament s from the position 1 to the position 2, neglecting gravity with $z_1 = z_2$, we obtain

$$\frac{1}{2} \cdot (c_2^2 - c_1^2) + \int_{p_1}^{p_2} \frac{dp}{\rho} = 0 \quad .$$

The equations of isentropic change of state (2.74) hold for the change in the variables of state (but not for shock waves!),

$$\frac{p}{p_1} = \left(\frac{\rho}{\rho_1} \right)^\kappa \Rightarrow \frac{1}{\rho} = \left(\frac{p_1}{p} \right)^{\frac{1}{\kappa}} \cdot \frac{1}{\rho_1} = \frac{p_1^{\frac{1}{\kappa}}}{\rho_1} \cdot p^{-\frac{1}{\kappa}} \Rightarrow$$

$$\int_{p_1}^{p_2} \frac{dp}{\rho} = \frac{p_1^{\frac{1}{\kappa}}}{\rho_1} \cdot \int_{p_1}^{p_2} p^{-\frac{1}{\kappa}} \cdot dp = \frac{p_1^{\frac{1}{\kappa}}}{\rho_1} \cdot \left[\frac{\kappa}{\kappa-1} \cdot p^{\frac{\kappa-1}{\kappa}} \right]_{p_1}^{p_2} = \frac{p_1^{\frac{1}{\kappa}}}{\rho_1} \cdot \frac{\kappa}{\kappa-1} \cdot \left[p_2^{\frac{\kappa-1}{\kappa}} - p_1^{\frac{\kappa-1}{\kappa}} \right] \Rightarrow$$

$$\int_{p_1}^{p_2} \frac{dp}{\rho} = \frac{\kappa}{\kappa-1} \cdot \left(\frac{p_2}{\rho_2} - \frac{p_1}{\rho_1} \right) .$$

So the Bernoulli equation for compressible flows reads

$$\boxed{\frac{1}{2} \cdot c_2^2 + \frac{\kappa}{\kappa-1} \cdot \frac{p_2}{\rho_2} = \frac{1}{2} \cdot c_1^2 + \frac{\kappa}{\kappa-1} \cdot \frac{p_1}{\rho_1} \Rightarrow \frac{1}{2} \cdot c^2 + \frac{\kappa}{\kappa-1} \cdot \frac{p}{\rho} = const.} . \quad (2.78)$$

With $a^2 = \kappa \cdot (p/\rho)$ it follows that

$$\boxed{\frac{1}{2} \cdot c_2^2 + \frac{a_2^2}{\kappa-1} = \frac{1}{2} \cdot c_1^2 + \frac{a_1^2}{\kappa-1} \Rightarrow \frac{1}{2} \cdot c^2 + \frac{a^2}{\kappa-1} = const.} . \quad (2.79)$$

Using the equation of state for the ideal gas $(p/\rho) = R \cdot T = (c_p - c_v) \cdot T$ and the isentrop exponent $\kappa = (c_p/c_v)$ it follows that

$$\frac{\kappa}{\kappa-1} \cdot \frac{p}{\rho} = \frac{c_p}{c_v} \cdot \frac{1}{\frac{c_p}{c_v} - 1} \cdot (c_p - c_v) \cdot T = c_p \cdot T = h ,$$

$$\boxed{c_p \cdot T_2 + \frac{1}{2} \cdot c_2^2 = c_p \cdot T_1 + \frac{1}{2} \cdot c_1^2 \Rightarrow c_p \cdot T + \frac{1}{2} \cdot c^2 = const.} , \quad (2.80)$$

$$\boxed{h_2 + \frac{1}{2} \cdot c_2^2 = h_1 + \frac{1}{2} \cdot c_1^2 \Rightarrow h + \frac{1}{2} \cdot c^2 = const.} . \quad (2.81)$$

This corresponds to the energy equation (2.52), without taking the heat flux and gravity into account.

Determining the constants of the Bernoulli equation is carried out using the **reservoir values**, or the so-called **critical values**.

The reservoir values p_0, ρ_0, a_0, T_0 with $c = 0$ satisfy equation (2.79)

$$\frac{1}{2} \cdot c^2 + \frac{a^2}{\kappa-1} = \frac{a_0^2}{\kappa-1} \Rightarrow a^2 \left(\frac{1}{2} \cdot M^2 + \frac{1}{\kappa-1} \right) = \frac{a_0^2}{\kappa-1}$$

$$\Rightarrow \frac{a^2}{a_0^2} = \frac{1}{1 + \frac{\kappa-1}{2} \cdot M^2} ,$$

with $a^2 = \kappa \cdot R \cdot T$ and $a_0^2 = \kappa \cdot R \cdot T_0$ it follows that

$$\frac{T}{T_0} = \frac{1}{1 + \frac{\kappa-1}{2} \cdot M^2} , \quad (2.82)$$

T is always smaller than T_0 , since $M_\infty^2 > 0$ holds at all times. The isentropic relation

$$\frac{\rho}{\rho_0} = \left(\frac{T}{T_0} \right)^{\frac{1}{\kappa-1}}$$

leads to an expression for the reservoir pressure ρ_0

$$\frac{\rho}{\rho_0} = \frac{1}{\left(1 + \frac{\kappa-1}{2} \cdot M^2 \right)^{\frac{1}{\kappa-1}}} . \quad (2.83)$$

Since $M_\infty^2 > 0$, ρ is smaller than ρ_0 . Using the isentropic relation

$$\frac{p}{p_0} = \left(\frac{T}{T_0} \right)^{\frac{\kappa}{\kappa-1}}$$

it follows that the reservoir pressure p_0 satisfies

$$\frac{p}{p_0} = \frac{1}{\left(1 + \frac{\kappa-1}{2} \cdot M^2 \right)^{\frac{\kappa}{\kappa-1}}} . \quad (2.84)$$

Equation (2.82) can also be used to determine the reservoir temperature T_0 at the stagnation point of a projectile. If we assume a flow temperature of $T = 300 \text{ K}$, in the stagnation point ($c = 0$), for a Mach number of $M_\infty = 2$, we find the stagnation point temperature $T_0 = 540 \text{ K}$. The stagnation point of the supersonic airplane Concorde therefore heats up during the flights. For $M_\infty = 5$, the stagnation point temperature is already $T_0 = 1,800 \text{ K}$. At such high temperatures, however, the assumption of isentropic change of state and the ideal gas law are not longer guaranteed.

In order to determine the constants in the Bernoulli equation, the critical values can also be used (index *). Critical values are those values found in a flow when the velocity of sound $M = 1$ has just been reached:

$$p(M = 1) = p^* , \quad T(M = 1) = T^* , \quad \rho(M = 1) = \rho^* ,$$

$$a(M = 1) = a^* , \quad c(M = 1) = c^* = a^* .$$

Therefore

$$\frac{1}{2} \cdot c^2 + \frac{a^2}{\kappa - 1} = \frac{1}{2} \cdot c^{*2} + \frac{a^{*2}}{\kappa - 1} = a^{*2} \cdot \left(\frac{1}{2} + \frac{1}{\kappa - 1} \right) = a^{*2} \cdot \frac{\kappa + 1}{2 \cdot (\kappa - 1)}$$

or

$$\frac{1}{2} \cdot c^2 + c_p \cdot T = \frac{1}{2} \cdot a^{*2} + c_p \cdot T^* ,$$

with

$$a^{*2} = \kappa \cdot R \cdot T^* = \frac{c_p}{c_v} \cdot (c_p - c_v) \cdot T^* = c_p \cdot (\kappa - 1) \cdot T^* \Rightarrow$$

$$\begin{aligned}\frac{1}{2} \cdot c^2 + c_p \cdot T &= \frac{1}{2} \cdot c_p \cdot (\kappa - 1) \cdot T^* + c_p \cdot T^* = \\ &= \frac{1}{2} \cdot c_p \cdot (\kappa - 1) \cdot T^* + \frac{2}{2} \cdot c_p \cdot T^* = c_p \cdot \frac{\kappa + 1}{2} \cdot T^* .\end{aligned}$$

Therefore there is a relation between the reservoir values (index 0) and the critical values (index *). To find this relation, we set the Mach number in equations (2.82) and (2.84) to $M = 1$, give variable quantities the index *, and leave the reservoir values as they are. We obtain

$$\boxed{\frac{T^*}{T_0} = \frac{2}{\kappa + 1} , \quad \frac{\rho^*}{\rho_0} = \left(\frac{2}{\kappa + 1}\right)^{\frac{1}{\kappa-1}} , \quad \frac{p^*}{p_0} = \left(\frac{2}{\kappa + 1}\right)^{\frac{\kappa}{\kappa-1}}} . \quad (2.85)$$

In particular, for air with the value $\kappa = 1.4$ we find

$$\frac{T^*}{T_0} = 0.833 , \quad \frac{\rho^*}{\rho_0} = 0.634 , \quad \frac{p^*}{p_0} = 0.528 .$$

Stream Filament Theory with Variable Cross-Section A(s)

For a variable cross-section $A(s)$ the continuity equation reads

$$\dot{m} = \rho(s) \cdot c(s) \cdot A(s) = const. .$$

Taking the logarithm of the continuity equation we find

$$\ln(\rho(s) \cdot c(s) \cdot A(s)) = \ln(\rho(s)) + \ln(c(s)) + \ln(A(s)) = \ln(const.) ,$$

and differentiation d/ds leads to

$$\frac{1}{\rho} \cdot \frac{d\rho}{ds} + \frac{1}{c} \cdot \frac{dc}{ds} + \frac{1}{A} \cdot \frac{dA}{ds} = 0 .$$

Using the Euler equation (2.77), the density term can be eliminated from the continuity equation and we obtain

$$\frac{1}{c} \cdot \frac{dc}{ds} \cdot (-M^2 + 1) + \frac{1}{A} \cdot \frac{dA}{ds} = 0 ,$$

$$\boxed{\frac{1}{c} \cdot \frac{dc}{ds} = \frac{1}{M^2 - 1} \cdot \frac{1}{A} \cdot \frac{dA}{ds}} . \quad (2.86)$$

Equation (2.86) allows one to determine how the cross-section $A(s)$ of a nozzle must be shaped to accelerate a gas continuously from subsonic Mach numbers $M < 1$ to supersonic Mach numbers $M > 1$ (Figure 2.54). Continuous acceleration requires that $dc/ds > 0$. If the Mach number is less than one, $M < 1$, a narrowing of the cross-section is needed: $dA/ds < 0$. If the Mach number is greater than one $M < 1$, a widening of the cross-section is required: $dA/ds > 0$, in order to accelerate the gas. For the Mach number $M = 1$, the differential equation (2.86) has a singularity. In order to ensure that $dc/ds > 0$, $dA/ds = 0$ has to hold.

If one wishes to accelerate a flow continuously from the subsonic region to the supersonic region, the nozzle required must first have a narrowing in the cross-section, and then, downstream from the narrowest cross-section, a further widening of the cross section. Such a nozzle is shown in Figure 2.54. It is called a **Laval nozzle**.

At the narrowest point in the cross-section, the critical values (index *) introduced in equation (2.85) are found at Mach number $M = 1$. The divergent part of the nozzle in the supersonic region can be explained by considering that the relative decrease in density in the supersonic region is much greater than the relative increase in velocity. For this reason, conservation of the constant mass flux $\dot{m} = \rho \cdot c \cdot A = \text{const.}$ requires that the cross-section $A(s)$ increases along s .

In what follows we will derive the differential equation which relates the relative change in cross-section, $(1/A) \cdot (dA/ds)$, to the relative change in Mach number $(1/M) \cdot (dM \cdot ds)$. The logarithm of the defining equation for the Mach number $c = M \cdot a$ yields

$$\ln(c) = \ln(M) + \ln(a) \quad .$$

Differentiation d/ds leads to

$$\frac{1}{c} \cdot \frac{dc}{ds} = \frac{1}{M} \cdot \frac{dM}{ds} + \frac{1}{a} \cdot \frac{da}{ds} \quad . \quad (2.87)$$

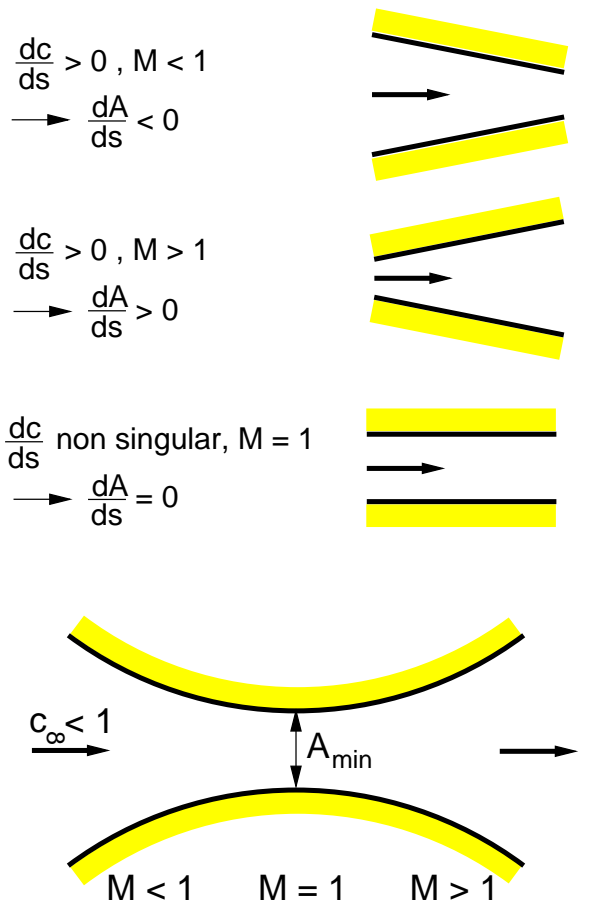


Fig. 2.54 : Laval nozzle

Taking the logarithm of $a^2 = \kappa \cdot (p/\rho)$ yields $2 \cdot \ln(a) = \ln(\kappa) + \ln(p) - \ln(\rho)$. Differentiation d/ds leads to

$$\frac{2}{a} \cdot \frac{da}{ds} = \frac{1}{p} \cdot \frac{dp}{ds} - \frac{1}{\rho} \cdot \frac{d\rho}{ds} .$$

In the next step, the expression dp/ds has to be related to $d\rho/ds$:

$$a^2 = \frac{dp}{d\rho} \Rightarrow dp = a^2 \cdot d\rho \Rightarrow \frac{dp}{ds} = a^2 \cdot \frac{d\rho}{ds} = \kappa \cdot \frac{p}{\rho} \cdot \frac{d\rho}{ds} \Rightarrow$$

$$\frac{1}{p} \cdot \frac{dp}{ds} = \frac{\kappa}{\rho} \cdot \frac{d\rho}{ds} .$$

We find that

$$\frac{2}{a} \cdot \frac{da}{ds} = (\kappa - 1) \cdot \frac{1}{\rho} \cdot \frac{d\rho}{ds} ,$$

and with the Euler equation it follows that

$$\frac{1}{a} \cdot \frac{da}{ds} = \frac{\kappa - 1}{2} \cdot \frac{-M^2}{c} \cdot \frac{dc}{ds} .$$

Inserting this equation into equation (2.87), taking equation (2.86) into account delivers

$$\frac{1}{M^2 - 1} \cdot \frac{1}{A} \cdot \frac{dA}{ds} = \frac{1}{M} \cdot \frac{dM}{ds} + \frac{(\kappa - 1)(-M^2)}{2} \cdot \frac{1}{M^2 - 1} \cdot \frac{1}{A} \cdot \frac{dA}{ds} ,$$

$$\boxed{\frac{1}{A} \cdot \frac{dA}{ds} \cdot \left(\frac{1 + \frac{\kappa-1}{2} \cdot M^2}{M^2 - 1} \right) = \frac{1}{M} \cdot \frac{dM}{ds}} .$$

(2.88)

This is a first order ordinary differential equation to determine $M(s)$ for a given cross-section $A(s)$. Using the boundary condition $M = M^* = 1$ for $A = A_{min} = A^*$ with $M^* = 1$ the solution reads

$$\boxed{\frac{A}{A^*} = \frac{1}{M} \cdot \left(1 + \frac{\kappa - 1}{\kappa + 1} \cdot (M^2 - 1) \right)^{\frac{\kappa+1}{2 \cdot (\kappa-1)}}} .$$

(2.89)

Equation (2.89) gives the Mach number as an implicit function of a given cross-section $A(s)$, if the velocity is the velocity of sound at the narrowest point A^* . In this case, the mass flux \dot{m} through the nozzle can be determined as a function of the critical values

$$\dot{m} = \rho \cdot c \cdot A = \rho^* \cdot c^* \cdot A^* = \rho^* \cdot a^* \cdot A^* = const. .$$

For the solution curve discussion of equation (2.89), we consider the direction field of the ordinary differential equation (2.88). First of all we solve equation (2.88) for dM/ds

$$\frac{dM}{ds} = M \cdot \frac{1}{A} \cdot \frac{dA}{ds} \cdot \left(\frac{1 + \frac{\kappa-1}{2} \cdot M^2}{M^2 - 1} \right) \Rightarrow \frac{dM}{ds} = M'(s) = f(M, A, s) .$$

The derivative of the Mach number $M'(s)$ is therefore a function f of the Mach number $M(s)$, of the given cross-section $A(s)$ and of the coordinate s . The relation $M'(s) = f(M, A, s)$ assigns a direction in the (s, M) plane to every point (s, M) .

A direction element to be specially defined is found at the narrowest cross-section A_{min} of Figure 2.55. For $M \neq 1$, with $dA/ds = 0$, we find

$$\frac{dM}{ds} = 0 \quad ,$$

i.e. horizontal tangents. For $M = 1$, as long as $dA/ds \neq 0$, vertical tangents are found, with

$$\frac{dM}{ds} = \infty \quad .$$

The singular point at the narrowest cross-section A_{min} with $dA/ds = 0$ and with Mach number 1 is a saddle point. The singular point has no uniquely defined direction assigned to it. There are two possible directions of propagation. These three limiting cases can be used to draw the mathematically possible solution curves to equation (2.89) in Figure 2.55.

Not all the solution curves are physically relevant for the (assumed) continuous acceleration in the Laval nozzle. The region where backflow occurs, for example, is not physically relevant, leaving those relevant solution curves as shown in Figure 2.56. The solution curve that ultimately is found in the Laval nozzle depends on ratio of the pressure p at the end of the nozzle to the reservoir pressure p_0 . Depending on the application of either high back pressure p_A or low back pressure p_E , we obtain different flow forms, to be treated in what follows.

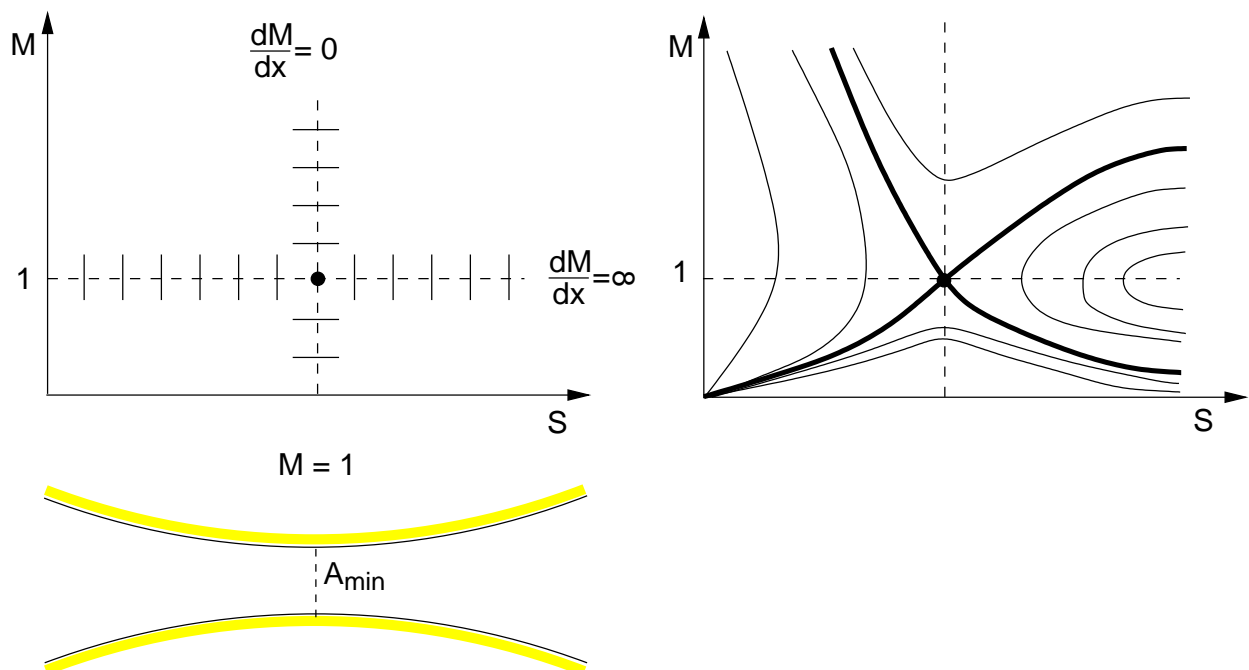


Fig. 2.55 : Direction field of the Laval nozzle differential equation

For a high back pressure p_A , we obtain pure subsonic flow $M < 1$ through the Laval nozzle. In the region where the cross-section narrows, the flow is accelerated (nozzle). Where the cross-section widens, the flow is then decelerated for $M < 1$. In this case the Laval nozzle acts as a diffusor.

If the back pressure is p_B , the Mach number 1 is just reached at the narrowest cross-section, and the critical values are obtained (index *). In the region where the cross-section of the Laval nozzle widens, a subsonic flow is again found, and the flow is decelerated.

If the back pressure exceeds this critical value p_B , as for the value p_D , acceleration occurs for supersonic values $M > 1$, but continual flow through the Laval nozzle is no longer possible. A **shock** occurs in the subsonic region, leading to a discontinuity in the flow quantities. At the position s , the solution curve jumps from supersonic $M > 1$ to subsonic $M < 1$ behavior.

If the back pressure at the end of the nozzle is lowered to the value p_D , the shock moves to the end of the nozzle.

It is only for the back pressure p_E that we can speak of an ideal Laval nozzle. The continuous acceleration of the flow follows the upper solution curve in Figure 2.56 from the subsonic regime $M < 1$ to the supersonic regime $M > 1$. At the end of the nozzle, as sketched in Figure 2.57, a free jet without a shock is found, and the pressure is the surrounding pressure p_∞ .

For back pressures between p_D and p_E , oblique shocks are found at the end of the nozzle, followed by so-called expansion fans. This flow form of oblique shocks followed by expansion fans is then to be found periodically in the free jet, so that a characteristic node-structure appears. Such a supersonic free jet is used in a blowtorch to cut through metal.

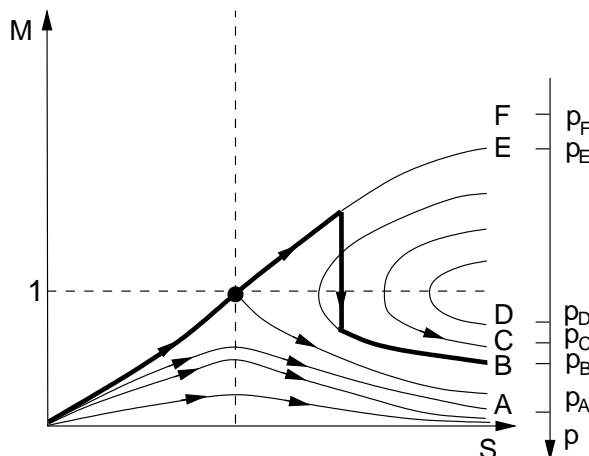


Fig. 2.56 : Dependence of Mach number in the Laval nozzle on the back pressure p at the outlet of the nozzle

If the back pressure at the end of the nozzle is further reduced to p_F , the oblique shocks vanish, and pure expansion flow occurs at the end of the nozzle, seen as a free jet bell. This can be seen at high altitudes after a rocket starts.

Figure 2.58 shows the mass flux density in the Laval nozzle. The mass flux density is the ratio between the mass flux \dot{m} and the cross-sectional area of the flow A

$$\frac{\dot{m}}{A} = \rho \cdot c \quad .$$

In the supersonic case, for the Laval nozzle with critical values at the narrowest cross-section $A^* = A_{min}$ we have

$$\dot{m} = const. \Rightarrow \rho \cdot c \cdot A = \rho^* \cdot c^* \cdot A^* \Rightarrow \frac{\rho \cdot c}{\rho^* \cdot c^*} = \frac{A^*}{A} \quad .$$

Since the cross-section A in a Laval nozzle is larger than A^* everywhere except at the narrowest point, where $A_{min} = A^*$, we have

$$\frac{A^*}{A} = \frac{\rho \cdot c}{\rho^* \cdot c^*} \leq 1 \quad .$$

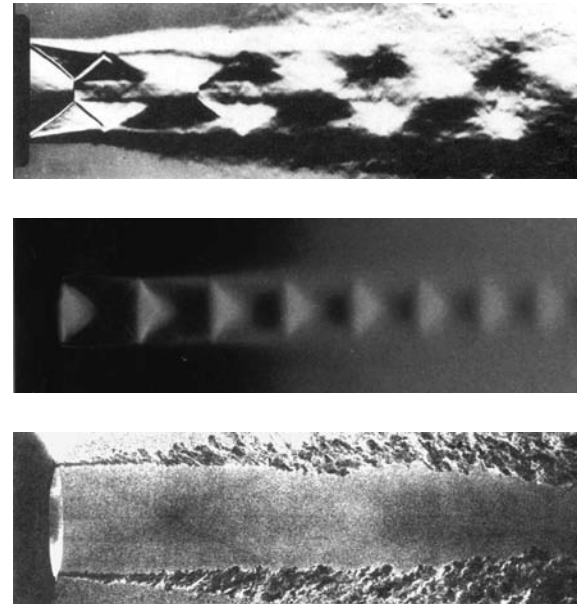
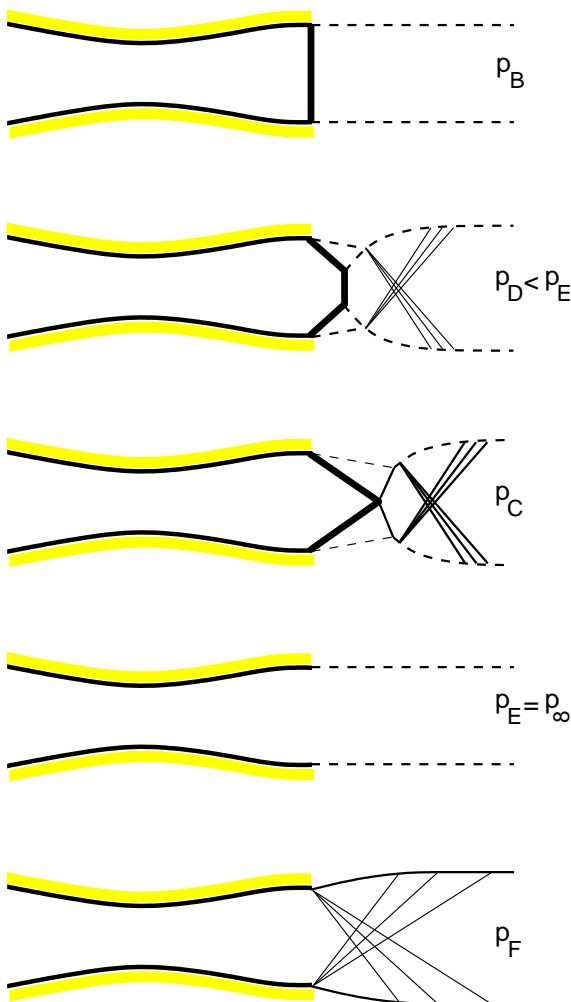


Fig. 2.57 : Dependence of the flow structures at the end of the Laval nozzle on the back pressure p

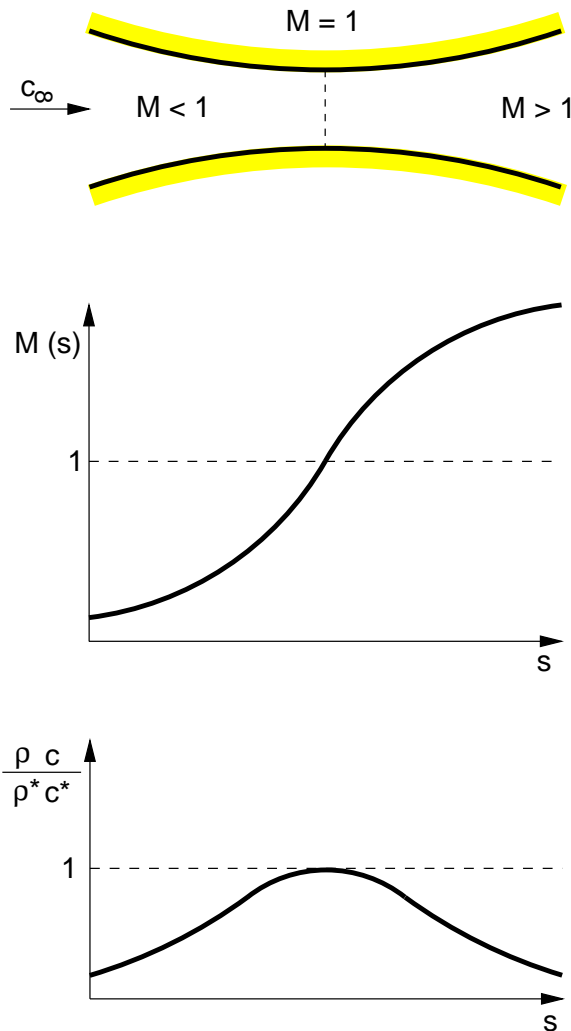


Fig. 2.58 : Mach number and mass flux density in a Laval nozzle

Therefore at the narrowest point in the Laval nozzle where $A_{min} = A^*$, the dimensionless mass flux density $(\rho \cdot c) / (\rho^* \cdot c^*)$ has its maximum value $(\rho \cdot c) / (\rho^* \cdot c^*) = 1$.

Shock Wave

A shock wave is quite generally a sharp change in the flow variables velocity \vec{v} , pressure p , density ρ and temperature T . These changes occur in an extremely thin layer of the gas with a size of the order of magnitude of several mean free paths. The mean free path is the mean distance which a molecule or atom moves between two collisions with other molecules. For air, the mean free path $\bar{\lambda}$ in normal conditions is $\bar{\lambda} = 10^{-7} \text{ m}$. In regions of this order of magnitude very large gradients of the variables of state occur, so that it is permitted to model the shock wave by a discontinuous change within the framework of continuum mechanics. A compression shock wave, which the expression shock wave generally refers to, is a discontinuous increase in the density ρ in the shock region. As well as the density, the temperature T and the pressure p also increase, while the magnitude of the velocity $| \vec{v} |$ decreases.

A shock wave can in principle only occur in a supersonic flow region. In the special case of a normal shock wave, where the free stream direction and the shock front form a right angle,

the flow progresses from a supersonic region to a subsonic region. In the case of an oblique shock wave, seen for example in the Mach cone of the flow past the supersonic airplane Concorde, the free stream and the shock wave front form the Mach angle α , already met at the start of this chapter. In this case the flow can also progress from supersonic to supersonic flow, whereby the supersonic velocity after the shock wave must be smaller than that before the shock wave.

The left-hand side of Figure 2.59 shows the velocity ratios on a schematic cross-section through a wing. The supersonic regime on the wing is denoted by the Mach number $M > 1$. This region ends downstream with the shock wave, and here the flow is subsonic, with $M < 1$. This shock wave is slightly curved, and is almost perpendicular at the point where it touches the boundary layer. We will now write down the shock wave equations for such a shock wave. The same equations hold for the shock wave in the Laval nozzle.

We assume, quite generally, a steady, inviscid supersonic flow. This is characterized by the values given for c_1 , ρ_1 , p_1 and T_1 . Using the speed of sound (2.75), $a_1 = \sqrt{\kappa \cdot p_1 / \rho_1}$, we determine the Mach number of the free stream $M_1 = c_1 / a_1$. Here κ denotes the ratio of the specific heats c_p / c_v . On passing through the shock wave these values undergo discontinuous changes in the direction of the normal to the shock wave surface. We consider the flow variables c_2 , ρ_2 , p_2 and T_2 downstream from the shock wave surface. The velocity c_2 is then smaller than the free stream velocity c_1 , while the other variables of state increase. On the right-hand side of Figure 2.59 this is shown by a smaller vector for c_2 after the shock wave. The change of state through the normal shock wave can be described using the conservation of mass, momentum and energy equations for a one-dimensional, steady, inviscid flow before and after the shock wave. We start with the equations from the one-dimensional theory:

$$\text{Mass:} \quad \rho_1 \cdot c_1 = \rho_2 \cdot c_2 \quad (2.90)$$

$$\text{Momentum:} \quad p_1 + \rho_1 \cdot c_1^2 = p_2 + \rho_2 \cdot c_2^2 \quad (2.91)$$

$$\text{Energy:} \quad h_1 + \frac{1}{2} \cdot c_1^2 = h_2 + \frac{1}{2} \cdot c_2^2 \quad . \quad (2.92)$$

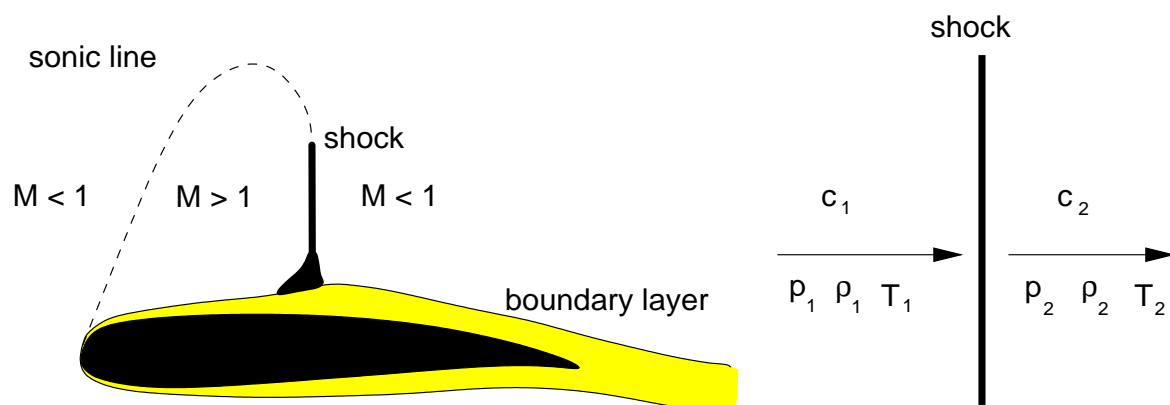


Fig. 2.59 : Shock wave on a transonic foil and change of state through a normal shock wave

For the enthalpy h we have the caloric equation of state:

$$h = c_p \cdot T = e + \frac{p}{\rho} = c_v \cdot T + \frac{p}{\rho} .$$

Solving the basic equations (2.90) - (2.92) for the four unknown quantities after the shock wave c_2 , p_2 , ρ_2 and T_2 , we obtain the **shock wave equations**.

Taking the thermal equation of state for ideal gases $p/\rho = R \cdot T$ into account, we can write the dependence of the enthalpy on the following quantities:

$$h = c_v \cdot \frac{1}{R} \cdot \frac{p}{\rho} + \frac{p}{\rho} = \left(\frac{c_v}{c_p - c_v} + 1 \right) \cdot \frac{p}{\rho} = \frac{\kappa}{\kappa - 1} \cdot \frac{p}{\rho} = \frac{a^2}{\kappa - 1} .$$

Thus the balance of energy (2.92) reads:

$$\frac{\kappa}{\kappa - 1} \cdot \frac{p_1}{\rho_1} + \frac{1}{2} \cdot u_1^2 = \frac{\kappa}{\kappa - 1} \cdot \frac{p_2}{\rho_2} + \frac{1}{2} \cdot u_2^2 .$$

Together with the conservation equations for mass (2.90) and momentum (2.91), we obtain a system of three algebraic equations to determine the three desired quantities c_2 , p_2 and ρ_2 after the shock wave. The temperature T_2 can then be computed with the thermal equation of state using p_2 and ρ_2 . Assuming the initial values c_1 , p_1 and ρ_1 are given, the system of equations can then be solved for the desired variables. We obtain

$$\begin{aligned} \frac{c_2}{c_1} &= \frac{\rho_1}{\rho_2} = \begin{cases} 1 \\ 1 - \frac{2}{\kappa+1} \cdot \left(1 - \frac{\kappa \cdot p_1}{\rho_1 \cdot c_1^2} \right) \end{cases} , \\ \frac{p_2}{p_1} &= \begin{cases} 1 \\ 1 + \frac{2 \cdot \kappa}{\kappa+1} \cdot \left(\frac{c_1^2 \cdot \rho_1}{\kappa \cdot p_1} - 1 \right) \end{cases} . \end{aligned}$$

For given initial values in front of the shock wave, the system of equations yields two solutions. The upper solution with the value 1 is the identity solution, for the case where no shock wave occurs. The lower solution is the desired shock wave solution. Using the velocity of sound $a_1 = \sqrt{\kappa \cdot p_1 / \rho_1}$ and the Mach number $M_1 = c_1 / a_1$ we can bring the shock wave equations to a form where the only parameter on the right-hand side is the Mach number $M_1 > 1$

$$\frac{c_2}{c_1} = \frac{\rho_1}{\rho_2} = 1 - \frac{2}{\kappa + 1} \cdot \left(1 - \frac{1}{M_1^2} \right) = \frac{1}{M_1^2} \cdot \left[1 + \frac{\kappa - 1}{\kappa + 1} \cdot (M_1^2 - 1) \right] , \quad (2.93)$$

$$\frac{p_2}{p_1} = 1 + \frac{2 \cdot \kappa}{\kappa + 1} \cdot (M_1^2 - 1) , \quad (2.94)$$

$$\frac{T_2}{T_1} = \frac{a_2^2}{a_1^2} = \left[1 + \frac{2 \cdot \kappa}{\kappa + 1} (M_1^2 - 1) \right] \cdot \left[1 - \frac{2}{\kappa + 1} \left(1 - \frac{1}{M_1^2} \right) \right] , \quad (2.95)$$

$$M_2^2 = \frac{1 + \frac{\kappa - 1}{\kappa + 1} \cdot (M_1^2 - 1)}{1 + \frac{2 \cdot \kappa}{\kappa + 1} \cdot (M_1^2 - 1)} . \quad (2.96)$$

The shock wave equations (2.93) - (2.95) yield the dependence of the values after the normal shock wave on the free stream Mach number. Whereas the pressure and the temperature after the shock wave can increase arbitrarily with increasing free stream Mach number, the density ratio ρ_2/ρ_1 for $M_1 \rightarrow \infty$ tends towards the ratio $(\kappa+1)/(\kappa-1)$. For air with $\kappa = 1.4$, the density after the shock wave can reach at most six times the free stream density. However this estimate is reached with the assumption of an ideal gas.

We now determine a relationship between p_2 and ρ_2 after the shock wave and to do this eliminate c_2 from the equations (2.90) - (2.92). After several steps, we obtain a relation which describes a symmetric hyperbola in the $(\rho_1/\rho_2, p_2/p_1)$ plane. This can be used to follow the thermodynamically possible changes in the variables of state p_1 and ρ_1 through the shock wave. This hyperbola is called the **Hugoniot curve** and reads

$$\frac{p_2}{p_1} = \frac{\kappa - 1}{\kappa + 1} \cdot \frac{\frac{\kappa+1}{\kappa-1} - \frac{\rho_1}{\rho_2}}{\frac{\rho_1}{\rho_2} - \frac{\kappa-1}{\kappa+1}} . \quad (2.97)$$

A further relation is obtained when we derive a relation for p_2/p_1 as a function of ρ_1/ρ_2 from only the conservation of mass and momentum equations (2.90) and (2.91), without using the balance of energy. This then leads to the kinematically possible changes of state, described by an equation for a straight line. This line is called the **Rayleigh line** and reads

$$\frac{p_2}{p_1} - 1 = -\kappa \cdot M_1^2 \cdot \left(\frac{\rho_1}{\rho_2} - 1 \right) . \quad (2.98)$$

The Rayleigh line has the slope $-\kappa \cdot M_1^2$, and meets the Hugoniot curve at two points, at the identity with $p_2 = p_1$ and $\rho_2 = \rho_1$ and at the shock wave solution after the shock wave (Figure 2.60).

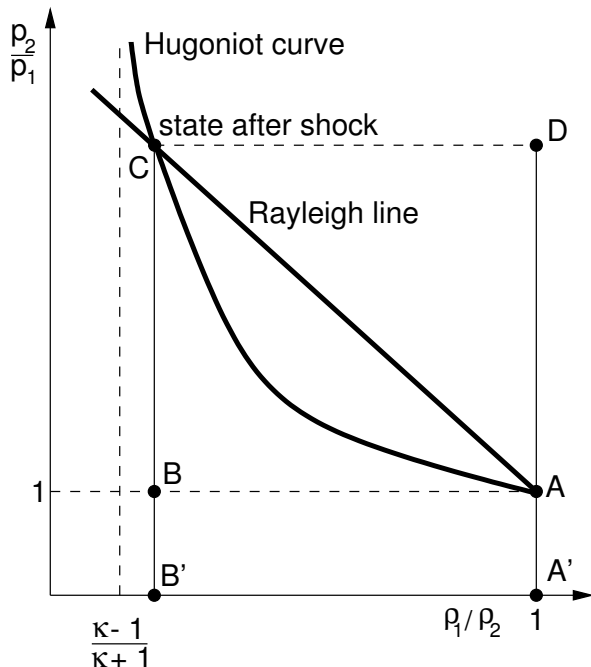


Fig. 2.60 : Hugoniot diagram

The areas in the Hugoniot diagram can be interpreted as energies. The area below the Rayleigh line $A'B'CD$ is the internal energy e of the shock wave

$$\frac{e_2 - e_1}{\frac{p_1}{\rho_1}} = \underbrace{\frac{1}{2} \cdot \left(\frac{p_2}{p_1} - 1 \right) \cdot \left(1 - \frac{\rho_1}{\rho_2} \right)}_{ABCD} + \underbrace{1 \cdot \left(1 - \frac{\rho_1}{\rho_2} \right)}_{A'B'CD} .$$

The triangular area ACD above the Rayleigh line represents the kinetic energy $c_2^2/2$

$$\frac{\frac{c_2^2}{2}}{\frac{p_1}{\rho_1}} = \underbrace{\frac{1}{2} \cdot \left(\frac{p_2}{p_1} - 1 \right) \cdot \left(1 - \frac{\rho_1}{\rho_2} \right)}_{ACD} ,$$

so that the total area $A'B'CD$ represents the increase of the total energy in the shock wave.

In front of a blunt body in a supersonic flow $M_1 > 1$, a head shock wave as shown in Figure 2.61 occurs. Around the stagnation streamline, the head shock wave can be approximately

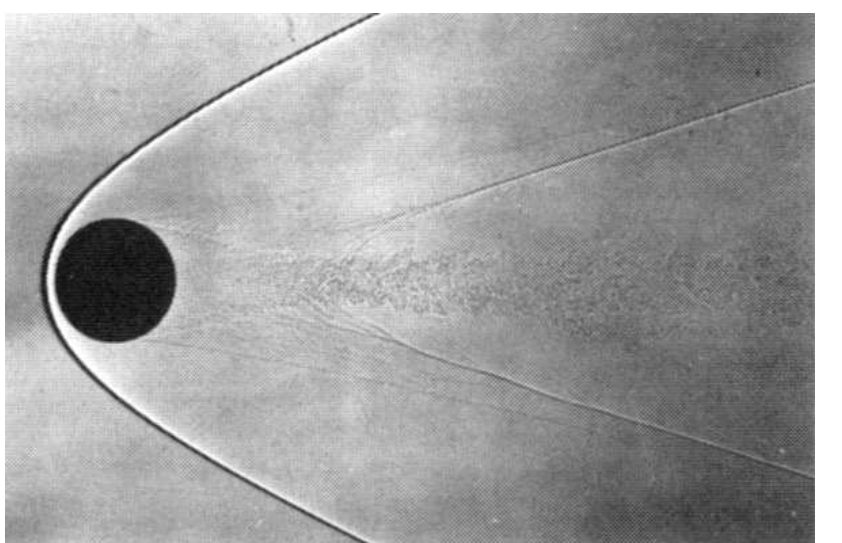
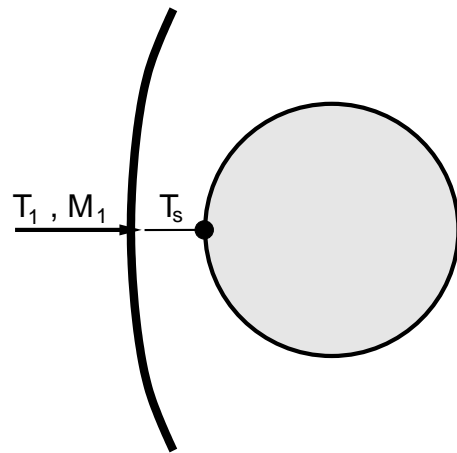


Fig. 2.61 : Leading shock wave of a sphere

considered as a normal shock wave. The temperature in the stagnation point T_2 can be computed with the energy equation (2.92) and the caloric equation of state $h = c_p \cdot T$

$$c_p \cdot T_S = c_p \cdot T_1 + \frac{c_1^2}{2} \quad .$$

With $M_1 = c_1/a_1$, $a_1^2 = \kappa \cdot R \cdot T$, $c_p - c_v = R$ and $\kappa = c_p/c_v$ the stagnation point temperature T_S is

$$\frac{T_S}{T_1} = 1 + \frac{\kappa - 1}{2} \cdot M_1^2 \quad . \quad (2.99)$$

We have already computed $T_S = 540 \text{ K}$ for a supersonic flight with $M_1 = 2$. For a hypersonic flight with $M_1 = 10$, a stagnation point temperature of $T_S = 6,300 \text{ K}$ occurs, meaning that heat-shielding materials such as ceramic tiles are necessary for heat protection. Since the heat transfer depends on the radius of curvature, and is relatively low for large radii, i.e. for blunt bodies, re-entry vehicles, such as those used for the space shuttle, we designed to be blunt. Figure 2.62 shows the space shuttle in a supersonic wind tunnel. The head shock wave is an almost normal shock wave close to the stagnation streamline, which passes over to the oblique shock wave of the head shock wave. We have already mentioned that the downstream Mach number after the oblique shock wave can be $M > 1$. Therefore the wing of the space shuttle may also be in a supersonic free stream, leading to a second head shock wave in front of the wing.

Figure 2.63 summarizes the possible flow forms from subsonic to supersonic free stream past a wing profile. In a subsonic free stream, with a Mach number smaller than $M_\infty = 0.75$, the acceleration does not reach supersonic Mach numbers $M > 1$ at any point on the profile, and the flow is purely subsonic. In the case of the transonic Mach number $M_\infty = 0.81$ we obtain the supersonic region on the profile already discussed in Chapter 1.1 (Figure 1.18). At the end of the profile here is an almost normal shock wave. For subsonic Mach numbers larger than 0.85, a shock wave forms on the lower side of the profile, and for Mach numbers close to 1, this, together with the upper shock wave, passes over to an oblique shock wave of the tail wave. For supersonic Mach numbers $M_\infty > 1$, a separated head shock wave first appears in front of the profile. For the supersonic flight Mach number $M_\infty = 2$, an attached oblique shock wave appears as the head shock wave, which, together with the tail wave, leads to the double sonic boom of the supersonic airplane discussed in Figure 2.53.

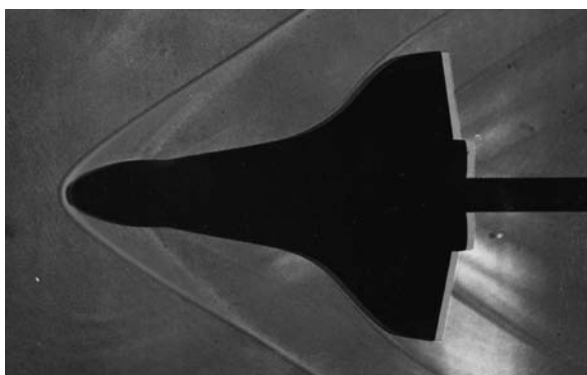


Fig. 2.62 : Head shock waves in front of the re-entry vehicle Space Shuttle, $M_1 = 3$

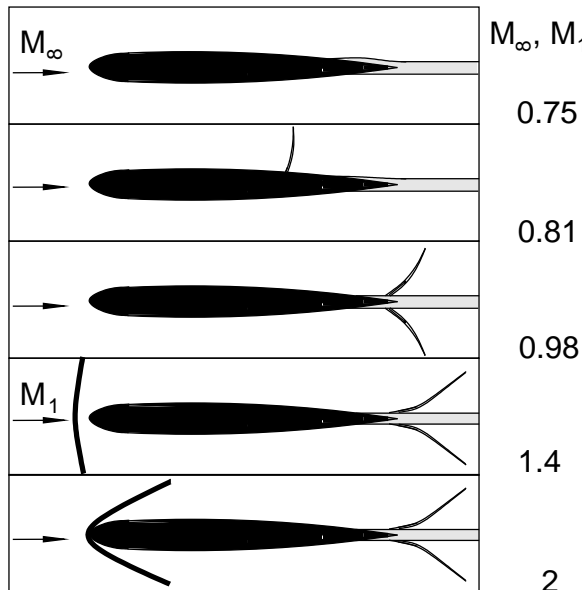


Fig. 2.63 : Flow forms past a wing profile from subsonic to supersonic free stream

Oblique shock waves can be computed using the fundamental equations of the normal shock wave (2.90) - (2.92) and (2.93) - (2.96), as long as these are applied to the normal components of the velocities. Figure 2.64 shows the change of direction of the velocity vector $\vec{c} = (c_n, c_t)$ through an oblique shock wave with normal component c_n and tangential component c_t . With

$$c_{n,1} = c_1 \cdot \sin(\alpha) \quad , \quad c_{t,1} = c_1 \cdot \cos(\alpha) \quad ,$$

$$c_{n,2} = c_2 \cdot \sin(\alpha - \beta) \quad , \quad c_{t,2} = c_2 \cdot \cos(\alpha - \beta) \quad ,$$

the fundamental equations of the oblique shock wave (2.90) - (2.92) can be written

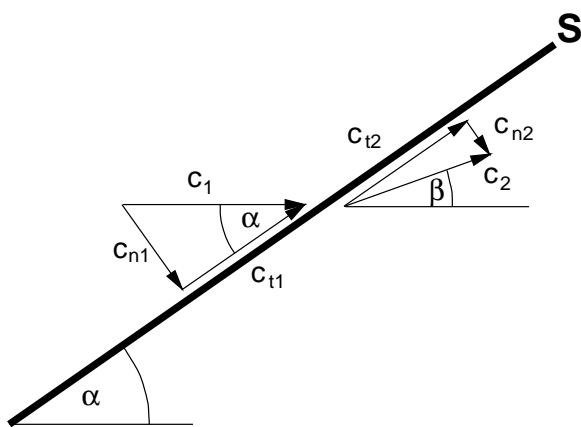


Fig. 2.64 : Oblique shock wave

$$\text{Mass:} \quad \rho_1 \cdot c_{n,1} = \rho_2 \cdot c_{n,2} \quad , \quad (2.100)$$

$$\text{Momentum:} \quad p_1 + \rho_1 \cdot c_{n,1}^2 = p_2 + \rho_2 \cdot c_{n,2}^2 \quad , \quad (2.101)$$

$$\begin{aligned} \text{Energy:} \quad h_1 + \frac{1}{2} \cdot c_1^2 &= h_2 + \frac{1}{2} \cdot c_2^2 \quad . \\ &\rho_1 \cdot c_{n,1} \cdot c_{t,1} = p_2 + \rho_2 \cdot c_{n,2} \cdot c_{t,2} \quad , \end{aligned} \quad (2.102)$$

Equations (2.100) and (2.101) yield the tangential component

$$c_{t,1} = c_{t,2} \quad . \quad (2.103)$$

Equation (2.102), with $c^2 = c_n^2 + c_t^2$ delivers

$$h_1 + \frac{1}{2} \cdot c_{n,1}^2 = h_2 + \frac{1}{2} \cdot c_{n,2}^2 \quad . \quad (2.104)$$

Therefore, the shock wave equations for the normal shock wave hold for the normal components of the velocity in front of and behind the shock wave, with the additional condition that the tangential components $c_{t,1}$ and $c_{t,2}$ must be the same. Figure 2.65 shows the possible shock wave angles α for different free stream Mach numbers M_1 , and it is seen that beyond a certain limiting value β_G of the downstream flow angle β , an oblique shock wave is no longer possible. For $\beta > \beta_G$ the separated head shock wave already discussed occurs.

Unsteady shock waves are generated by a **shock tube**. A shock tube consists of a high-pressure section and a low-pressure section, separated by a membrane. If the high-pressure section is filled with propellant gas at over-pressure until the membrane bursts, an unsteady shock wave in the low-pressure section of the shock tube, filled with the test gas, moves

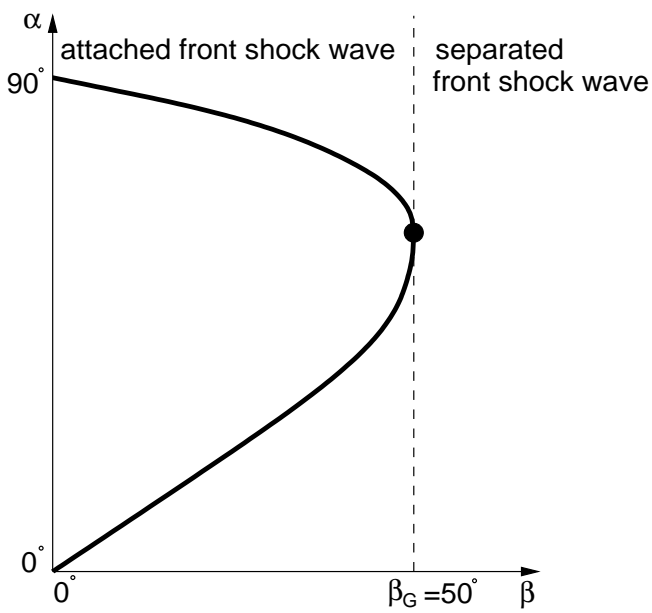


Fig. 2.65 : Shock wave angle α of oblique shock waves

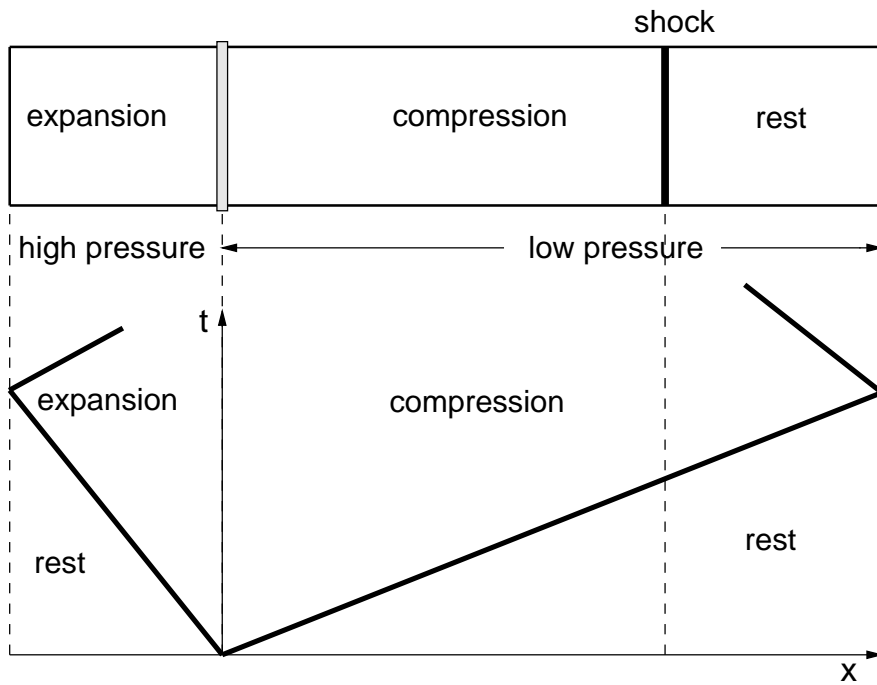


Fig. 2.66 : Shock tube, position-time diagram of a shock wave and an expansion wave

with constant velocity c_s (see the diagram in Figure 2.66). In the high-pressure section the corresponding expansion wave moves. If we move with constant shock wave velocity c_s with the shock wave, we can compute the change of state through the unsteady shock wave with the fundamental equations (2.90) - (2.92) and (2.93) - (2.96) of the normal shock wave.

$$c_1 = -c_s \quad , \quad c_2 = c_2 - c_1 h_2 + \frac{1}{2} \cdot c_{n,2}^2 \quad .$$

2.4 Technical Flows

2.4.1 Turbulent Flows

Most flows which occur in nature and in technology are turbulent at high enough Reynolds numbers. In contrast to the laminar flows which we have discussed until now, turbulent flows are characterized by fluctuations in the flow variables, leading to an additional transverse exchange of momentum and energy. This results in more full time-averaged velocity profiles compared to the laminar profiles found in boundary layers, channels and pipes.

Figure 2.67 shows the laminar velocity profile already discussed compared with the profiles of turbulent boundary layer and pipe flows which occur when a so-called critical Reynolds number Re_c is exceeded. If a colored filament is added to a steady laminar flow, as in Figure 2.68, a straight streakline will be seen, as already seen in Chapter 2.3.1. In the turbulent flow the colored filament breaks up because of the fluctuations superimposed on the flow and the consequent transverse exchange of momentum.

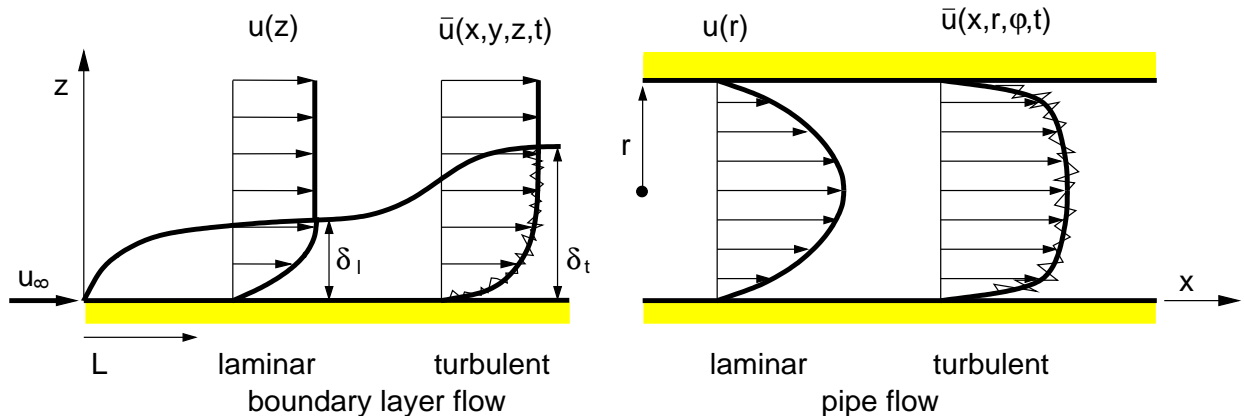


Fig. 2.67 : Laminar and turbulent velocity profiles in boundary layer and pipe flow

Turbulent flows are fundamentally three-dimensional and time dependent. We now leave the area of one-dimensional stream filament theory and return to denoting the flow variables as $\vec{v}(x, y, z, t)$, $p(x, y, z, t)$, $\rho(x, y, z, t)$.

The **mathematical description** of turbulent flows is derived from the experimental results in Figure 2.68. Reynolds was able to conclude from his experiments that the flow variables, such as the u component of the velocity, can be represented as a superposition of the time-averaged velocities $\bar{u}(x, y, z)$ and the additional fluctuations $u'(x, y, z, t)$. The **Reynolds ansatz** for turbulent flows is written (see Figure 2.69)

$$\vec{v}(x, y, z, t) = \bar{\vec{v}}(x, y, z) + \vec{v}'(x, y, z, t) \quad . \quad (2.105)$$

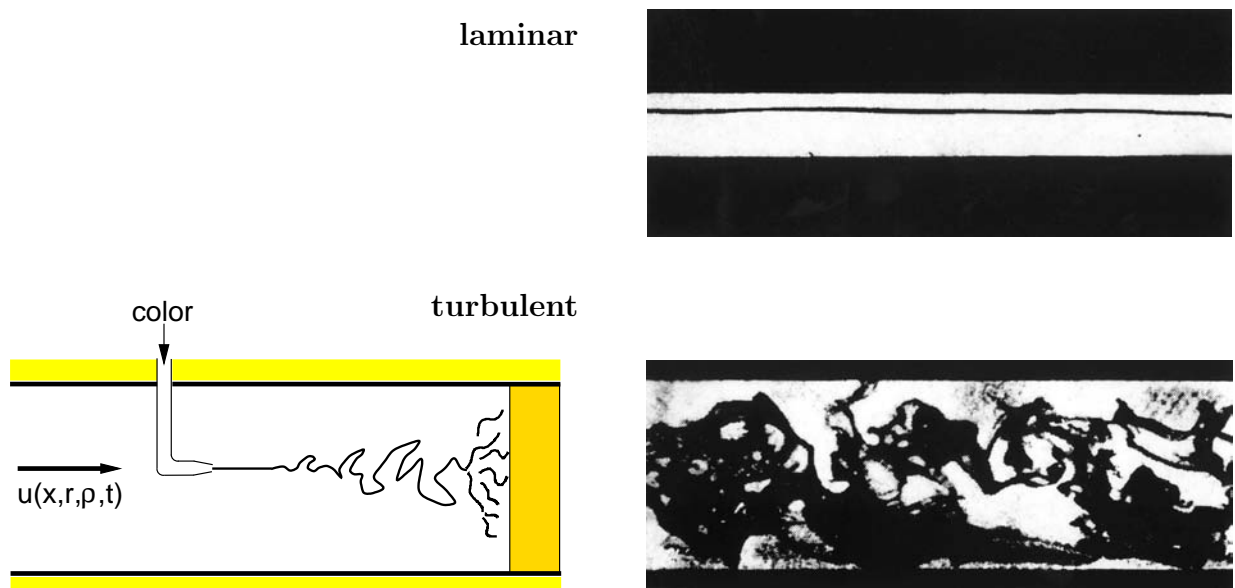


Fig. 2.68 : Reynolds experiment: laminar and turbulent pipe flow , REYNOLDS 1883

The definition of the time-average at a fixed position for the example of the velocity component u reads

$$\bar{u} = \frac{1}{T} \cdot \int_0^T u(x, y, z, t) \cdot dt \quad . \quad (2.106)$$

T is a time interval large enough that any increase in T does not lead to a further change in the time-averaged value \bar{u} . From the definition of the time-average, we can see that the time-average of the fluctuating quantities must vanish, i.e. the velocity fluctuations satisfy

$$\bar{u}' = 0 \quad , \quad \bar{v}' = 0 \quad , \quad \bar{w}' = 0 \quad .$$

The proof of this for the u component of the velocity reads:

$$\begin{aligned} \bar{u} &= \frac{1}{T} \cdot \int_0^T u(x, y, z, t) \cdot dt = \frac{1}{T} \cdot \int_0^T (\bar{u} + u') \cdot dt = \frac{1}{T} \cdot \int_0^T \bar{u} \cdot dt + \frac{1}{T} \cdot \int_0^T u' \cdot dt \\ &\quad \frac{1}{T} \cdot \int_0^T \bar{u} \cdot dt = \frac{1}{T} \cdot \bar{u} \cdot \int_0^T dt = \bar{u} \quad , \\ \Rightarrow \quad \bar{u} &= \bar{u} + \bar{u}' \quad \Rightarrow \quad \bar{u}' = 0 = \frac{1}{T} \cdot \int_0^T u' \cdot dt \quad . \end{aligned}$$

The dimensionless **turbulence intensity** Tu is used to characterize turbulent flows. In the numerator of this quantity is the square root of the time-averaged square of the fluctuating variables, and in the denominator the time-averaged flow velocity at a certain position. The turbulence intensity for the velocity component u in the main direction of flow x is

$$Tu = \frac{\sqrt{\overline{(u')^2}}}{\bar{u}} \quad .$$

Since turbulent flows are three-dimensional, the three-dimensional generalization of the turbulence intensity at a certain position in the flow field follows as

$$Tu = \frac{\sqrt{\frac{1}{3} \cdot (\overline{(u')^2} + \overline{(v')^2} + \overline{(w')^2})}}{|\vec{v}|} = \frac{\sqrt{\frac{1}{3} (\overline{(u')^2} + \overline{(v')^2} + \overline{(w')^2})}}{\sqrt{\bar{u}^2 + \bar{v}^2 + \bar{w}^2}} \quad . \quad (2.107)$$

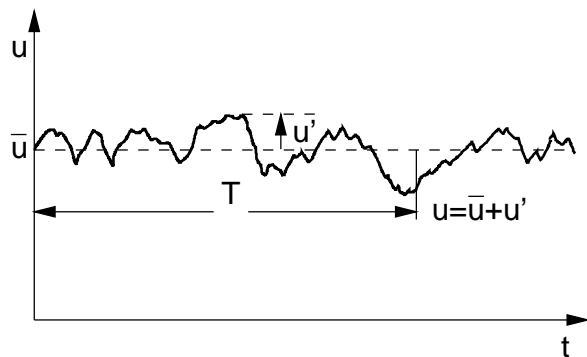


Fig. 2.69 : Reynolds ansatz for the u component of the velocity

Because of the fluctuating motions u' , v' and w' in a turbulent flow, there is an **additional contribution to the flow drag**. However, this additional contribution has nothing to do with the molecular viscosity μ , but rather is due to the additional transverse and longitudinal exchange processes which occur in a turbulent flow. In what follows we will look at the mathematical treatment of these processes.

Our starting point is the Navier-Stokes equation (2.59). In passing from the stream filament coordinate system, s and n , to a Cartesian coordinate system (x, y, z) , the velocity c along the stream filament is replaced by the variable u , s by x and n by z . We obtain

$$\frac{\partial u}{\partial t} + u \cdot \frac{\partial u}{\partial x} = -\frac{1}{\rho} \cdot \frac{\partial p}{\partial x} + \nu \cdot \frac{\partial^2 u}{\partial z^2} - g \cdot \frac{dz}{dx} . \quad (2.108)$$

This equation is also valid in principle for turbulent flows but has to be supplemented by the second and third Navier-Stokes equations for the u and v components respectively. For an incompressible flow with $\rho = \text{const.}$, the turbulent flow quantities appearing in equation (2.108) are the velocity component u and the pressure p . Using the Reynolds ansatz (2.105) for u and p we find

$$\overline{\frac{\partial(\bar{u} + u')}{\partial t}} + (\bar{u} + u') \cdot \overline{\frac{\partial(\bar{u} + u')}{\partial x}} = -\frac{1}{\rho} \cdot \overline{\frac{\partial(\bar{p} + p')}{\partial x}} + \nu \cdot \overline{\frac{\partial^2(\bar{u} + u')}{\partial z^2}} - \overline{-g \cdot \frac{dz}{dx}} .$$

Taking the computation rules for the time-average into account, this leads to

$$\overline{(\bar{u} + u') \cdot \frac{\partial(\bar{u} + u')}{\partial x}} = -\frac{1}{\rho} \cdot \overline{\frac{\partial \bar{p}}{\partial x}} + \nu \cdot \overline{\frac{\partial^2 \bar{u}}{\partial z^2}} - \overline{g \cdot \frac{dz}{dx}} .$$

Note here that $\partial(\bar{u} + u')/\partial t = 0$ is only valid for flows whose time-average is steady. Such flows are called quasi-steady turbulent flows. The time-average of the non-linear inertia terms on the left-hand side of the equation is considered separately. We have

$$\overline{(\bar{u} + u') \cdot \frac{\partial(\bar{u} + u')}{\partial x}} = \overline{\bar{u} \cdot \frac{\partial \bar{u}}{\partial x}} + \overline{\bar{u} \cdot \frac{\partial u'}{\partial x}} + \overline{u' \cdot \frac{\partial \bar{u}}{\partial x}} + \overline{u' \cdot \frac{\partial u'}{\partial x}} = \bar{u} \cdot \overline{\frac{\partial \bar{u}}{\partial x}} + \overline{u' \cdot \frac{\partial u'}{\partial x}} .$$

In particular for the term $\overline{u' \cdot (\partial u'/\partial x)}$:

$$\begin{aligned} \overline{u' \cdot \frac{\partial u'}{\partial x}} &= \frac{1}{T} \cdot \int_0^T u' \cdot \frac{\partial u'}{\partial x} \cdot dt = \frac{1}{T} \cdot \int_0^T \frac{\partial}{\partial x} \left(\frac{(u')^2}{2} \right) \cdot dt = \frac{\partial}{\partial x} \left(\frac{1}{T} \cdot \int_0^T \frac{(u')^2}{2} \cdot dt \right) \\ &= \frac{\partial}{\partial x} \left(\overline{\frac{(u')^2}{2}} \right) . \end{aligned}$$

Therefore the time-averaged Navier-Stokes equation reads

$$\bar{u} \cdot \overline{\frac{\partial \bar{u}}{\partial x}} + \frac{\partial}{\partial x} \left(\overline{\frac{(u')^2}{2}} \right) = -\frac{1}{\rho} \cdot \overline{\frac{\partial \bar{p}}{\partial x}} + \nu \cdot \overline{\frac{\partial^2 \bar{u}}{\partial z^2}} - \overline{g \cdot \frac{dz}{dx}} . \quad (2.109)$$

If we multiply this equation with the constant density ρ and write the pressure and gravity terms on the left-hand side, we find

$$\rho \cdot \bar{u} \cdot \overline{\frac{\partial \bar{u}}{\partial x}} + \overline{\frac{\partial \bar{p}}{\partial x}} + \rho \cdot \overline{g \cdot \frac{dz}{dx}} = \frac{\partial}{\partial z} \underbrace{\left(\mu \cdot \overline{\frac{\partial \bar{u}}{\partial z}} \right)}_{\bar{\tau}_{zx}} - \frac{\partial}{\partial x} \underbrace{\left(\rho \cdot \overline{\frac{(u')^2}{2}} \right)}_{\frac{1}{2} \cdot \bar{\tau}'_{xx}}$$

On the right-hand side of the equation are the terms responsible for the drag in the flow. As well as the shear stress $\bar{\tau}_{zx}$ due to the viscosity, a turbulent flow also has an additional drag term due to the velocity fluctuations, denoted here by the index ' as τ'_{xx} . In general, the additionally appearing parts of the stress τ' in turbulent flows are called **Reynolds apparent normal and shear stresses**, since they are caused by the turbulent longitudinal and transverse exchange and not by the molecular viscosity μ .

The lower double indices in the stress variable τ follow the same conventions used in solid state physics. The first index denotes the normal to cross-section and the second index denotes the direction in which the force on this cross-section acts.

In the general three-dimensional case, τ' is a stress tensor with 9 components, consisting of 6 apparent shear stresses and 3 apparent normal stresses (trace of the shear stress tensor).

$$\tau' = \begin{pmatrix} \tau'_{xx} & \tau'_{xy} & \tau'_{xz} \\ \tau'_{yx} & \tau'_{yy} & \tau'_{yz} \\ \tau'_{zx} & \tau'_{zy} & \tau'_{zz} \end{pmatrix} = \begin{pmatrix} -\rho \cdot \overline{u' \cdot u'} & -\rho \cdot \overline{v' \cdot u'} & -\rho \cdot \overline{w' \cdot u'} \\ -\rho \cdot \overline{u' \cdot v'} & -\rho \cdot \overline{v' \cdot v'} & -\rho \cdot \overline{w' \cdot v'} \\ -\rho \cdot \overline{u' \cdot w'} & -\rho \cdot \overline{v' \cdot w'} & -\rho \cdot \overline{w' \cdot w'} \end{pmatrix} . \quad (2.110)$$

Because of the balance of moments, equivalent components of the stress tensor are equal, i.e. we have $\tau'_{xy} = \tau'_{yx}$ or $-\rho \cdot \overline{u' \cdot w'} = -\rho \cdot \overline{w' \cdot u'}$ etc. The time-averaged products of the fluctuation variables and thus the components of the stress tensor τ' are unknown and have to be described using model equations.

Starting out from the Newtonian ansatz of laminar flows, Boussinesq made the assumption that the unknown fluctuation terms can be reduced to the known time-averaged quantities of the basic flow by introducing an unknown proportionality factor μ_t , called the turbulent viscosity. Using the **Boussinesq assumption** the following relations are found

$$\begin{aligned} \tau'_{xx} &= -\rho \cdot \overline{u' \cdot u'} = \mu_t \cdot \left(\frac{\partial \bar{u}}{\partial x} + \frac{\partial \bar{u}}{\partial x} \right) = \mu_t \cdot 2 \cdot \frac{\partial \bar{u}}{\partial x} , \\ \tau'_{zx} &= -\rho \cdot \overline{u' \cdot w'} = \mu_t \cdot \left(\frac{\partial \bar{u}}{\partial z} + \frac{\partial \bar{w}}{\partial x} \right) . \end{aligned} \quad (2.111)$$

Here μ_t is a function which has to be determined, and is not, like the molecular viscosity μ , a material constant.

One possible ansatz to determine μ_t is the **Prandtl mixing length ansatz**. Figure 2.70 shows a turbulent two-dimensional boundary layer flow in the (x, z) plane. The Reynolds ansatz yields

$$\begin{aligned} u &= \bar{u}(z) + u' \\ w &= w' . \end{aligned}$$

If we move a fluid element with fluctuation velocity from the height z_0 to the height $z_0 + l$, the change in \bar{u} with $\bar{u}(z_0 + l) > \bar{u}(z_0)$ is found writing out the Taylor expansion:

$$\bar{u}(z_0) - \bar{u}(z_0 + l) = \bar{u}(z_0) - \left(\bar{u}(z_0) + \left. \frac{d\bar{u}}{dz} \right|_{z_0} \cdot l + \left. \frac{d^2 \bar{u}}{dz^2} \right|_{z_0} \cdot \frac{l^2}{2} + \dots \right) .$$

Neglecting higher order terms it follows that

$$\bar{u}(z_0) - \bar{u}(z_0 + l) = -l \cdot \frac{d\bar{u}}{dz} \Big|_{z_0} .$$

This lower velocity $-l \cdot (d\bar{u}/dz|_{z_0})$ at the height $z_0 + l$ was considered by Prandtl to be the velocity fluctuation

$$u'(z_0 + l) = -l \cdot \frac{d\bar{u}}{dz} \Big|_{z_0}$$

at $z_0 + l$. For continuity reasons, it follows for w' that:

$$w' = l \cdot \frac{d\bar{u}}{dz} .$$

The mixing length l is therefore the distance a fluid element will travel before it is completely mixed with its surroundings and loses its identity. This allows us to consider the velocity fluctuations u' and w' in terms of the mixing length l and the time-averaged velocity profile $\bar{u}(z)$. The apparent shear stress $\tau'_{zx} = -\rho \cdot \overline{u' \cdot w'}$ can then be computed as

$$\tau'_{zx} = -\rho \cdot \overline{u' \cdot w'} = -\rho \cdot \overline{\left(-l \cdot \frac{d\bar{u}}{dz} \right) \cdot l \cdot \frac{d\bar{u}}{dz}} = \rho \cdot l^2 \cdot \left(\frac{d\bar{u}}{dz} \right)^2 .$$

Since we assumed a two-dimensional turbulent boundary layer flow with $\bar{w} = 0$, we also have $(\partial \bar{w} / \partial x) = 0$, and it follows for the Boussinesq assumption (2.111) that

$$\tau'_{zx} = \mu_t \cdot \frac{d\bar{u}}{dz} . \quad (2.112)$$

This yields an equation to determine the desired quantity μ_t , since we have

$$\tau'_{zx} = -\rho \cdot \overline{u' \cdot w'} = \rho \cdot l^2 \cdot \left(\frac{d\bar{u}}{dz} \right)^2 = \mu_t \cdot \frac{d\bar{u}}{dz}$$

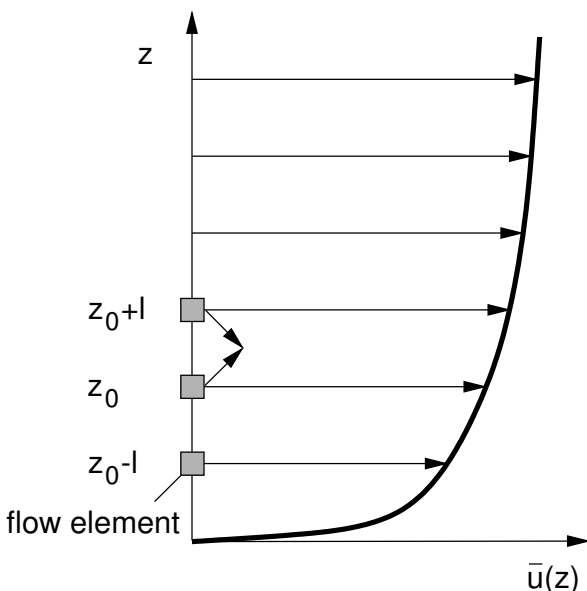


Fig. 2.70 : Prandtl mixing length ansatz

and therefore

$$\boxed{\mu_t = \rho \cdot l^2 \cdot \left(\frac{d\bar{u}}{dz} \right)} . \quad (2.113)$$

The mixing length l is still unknown. It has to be determined from experiments, leading to empirical approximation formulae for the computation of l .

Following these fundamental considerations of turbulent flows, let us return to the turbulent plate boundary layer flow in Figure 2.67. The order of magnitude of the turbulent apparent viscosity μ_t permits the turbulent plate boundary layer to be divided up into regimes (Figure 2.71). Directly at the wall $\mu_t \ll \mu$. This is the **viscous sublayer** and is of particular technical importance in reducing drag with so-called riblets. These will be discussed at the end of this chapter.

In the viscous sublayer the velocity fluctuations u' and w' are very small, and for the mixing length we have $l \rightarrow 0$. The total shear stress $\bar{\tau}_{tot}$ in the turbulent flow under consideration reads

$$\bar{\tau}_{tot} = \mu \cdot \frac{d\bar{u}}{dz} - \rho \cdot \overline{u' \cdot w'} .$$

Because of $\overline{u' \cdot w'} \approx 0$, it follows that the wall shear stress $\bar{\tau}_w$ in the viscous sublayer satisfies

$$\bar{\tau}_w = \mu \cdot \left(\frac{d\bar{u}}{dz} \right)_w .$$

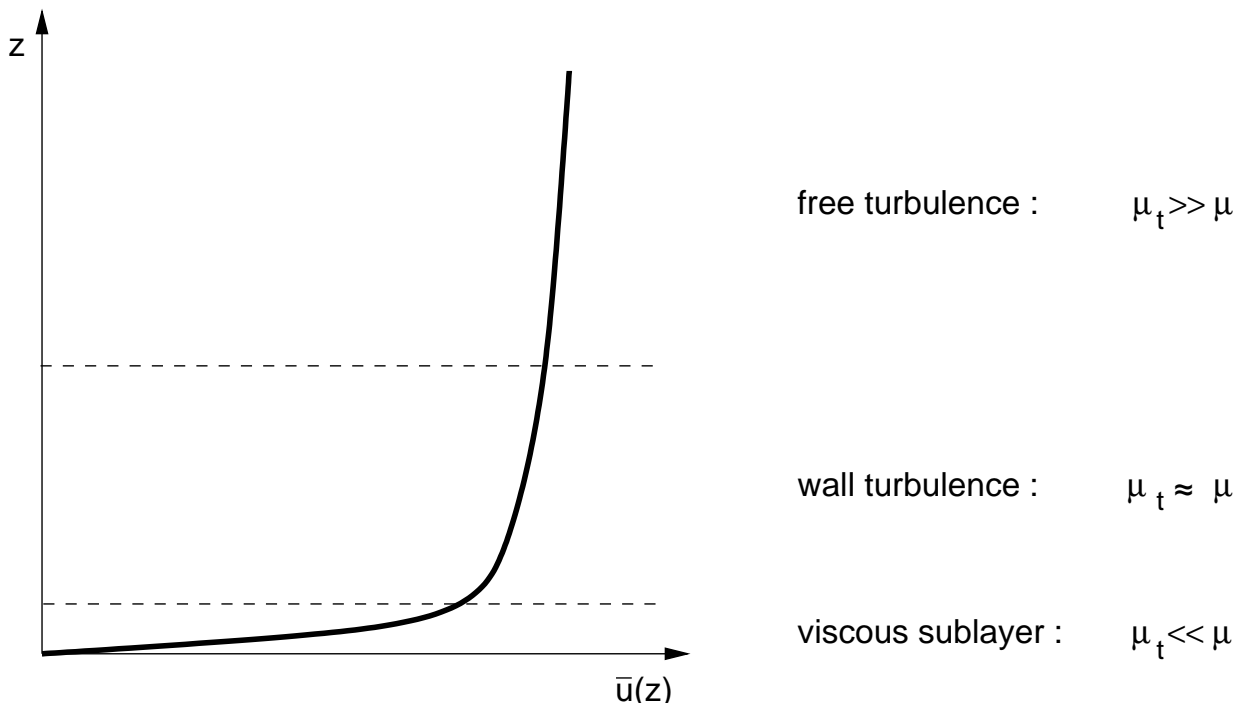


Fig. 2.71 : Division of the turbulent boundary layer flow

Separation of variables leads to an ordinary differential equation for the desired velocity profile

$$d\bar{u} = \frac{1}{\mu} \cdot \bar{\tau}_w \cdot dz \quad .$$

Integration yields

$$\int_0^{\bar{u}} d\bar{u} = \frac{1}{\mu} \cdot \int_0^z \bar{\tau}_w \cdot dz \quad ,$$

that is, a linear velocity distribution $\bar{u}(z)$ for a constant shear stress $\bar{\tau}_w$

$$\boxed{\bar{u}(z) = \frac{\bar{\tau}_w}{\mu} \cdot z} \quad .$$

(2.114)

Extending this expression with the constant density ρ delivers

$$\bar{u}(z) = \frac{\bar{\tau}_w}{\rho} \cdot \frac{\rho}{\mu} \cdot z = \frac{\bar{\tau}_w}{\rho} \cdot \frac{z}{\nu} \quad .$$

Defining the so-called wall shear stress velocity u_τ as a new quantity, with $u_\tau = \sqrt{(\bar{\tau}_w/\rho)}$, we obtain

$$\boxed{\frac{\bar{u}(z)}{u_\tau} = \frac{u_\tau \cdot z}{\nu} = z^+} \quad ,$$

(2.115)

with the new dimensionless coordinate $z^+ = (u_\tau \cdot z)/\nu$.

In the region of wall turbulence, outside the viscous sublayer but still close to the wall, the wall shear stress is still constant: $\bar{\tau}_w = const.$. Prandtl assumed that the wall shear stress can be written as follows, with the mixing length $l = k \cdot z$ as a linear function of z (k is a constant)

$$\bar{\tau}_w = \rho \cdot l^2 \cdot \left(\frac{d\bar{u}}{dz} \right)^2 = \rho \cdot k^2 \cdot z^2 \cdot \left(\frac{d\bar{u}}{dz} \right)^2 \quad .$$

This leads to a differential equation to determine $\bar{u}(z)$:

$$\frac{\bar{\tau}_w}{\rho} = u_\tau^2 = k^2 \cdot z^2 \cdot \left(\frac{d\bar{u}}{dz} \right)^2 \Rightarrow \frac{d\bar{u}}{dz} = u_\tau \cdot \frac{1}{k \cdot z} \Rightarrow d\bar{u} = \frac{u_\tau}{k} \cdot \frac{1}{z} \cdot dz \quad .$$

Indefinite integration yields

$$\bar{u}(z) = \frac{u_\tau}{k} \cdot \ln(z) + C_1 \Rightarrow$$

$$\frac{\bar{u}(z)}{u_\tau} = \frac{1}{k} \cdot \ln \left(\frac{z^+ \cdot \nu}{u_\tau} \right) + C_1 = \frac{1}{k} \cdot \ln(z^+) + \frac{1}{k} \cdot \ln \left(\frac{\nu}{u_\tau} \right) + C_1 \quad .$$

Summarizing the last two terms to a new constant of integration C , we obtain a logarithmic velocity profile in the region of wall turbulence

$$\boxed{\frac{\bar{u}(z)}{u_\tau} = \frac{1}{k} \cdot \ln(z^+) + C} \quad . \quad (2.116)$$

The time-averaged velocity profiles (2.114) - (2.116) close to the wall are shown in Figure 2.72. The viscous sublayer exists in the region $0 < z^+ < 5$. After this comes the transition region $5 < z^+ < 30$ and then the logarithmic region, with $30 < z^+ < 350$.

The laminar-turbulent transition for the plate boundary layer flow takes place at the critical Reynolds number

$$Re_c = 5 \cdot 10^5 \quad .$$

For a pipe flow, the critical Reynolds number is $Re_c = 2300$.

The laminar-turbulent transition leads to an increase of the friction drag c_f , shown in Figure 2.73 as dependent on the Reynolds number Re_L , formed with the length of the plate L . The local friction coefficient $c_f(x)$ at the position $x = L$ is

$$\boxed{c_f(L) = \frac{\tau_w(L)}{\frac{1}{2} \cdot \rho \cdot u_\infty^2} = \begin{cases} \frac{0.664}{\sqrt{Re_L}} & \text{laminar boundary layer flow} \\ \frac{0.0609}{(Re_L)^{\frac{1}{5}}} & \text{turbulent boundary layer flow} \end{cases} .} \quad (2.117)$$

The transition from the laminar to the turbulent boundary layer flow does not take place suddenly, but rather over a transition region. The dimensionless integral friction drag coefficient ζ can be calculated from the local drag coefficient $c_f(x)$. The integral friction drag

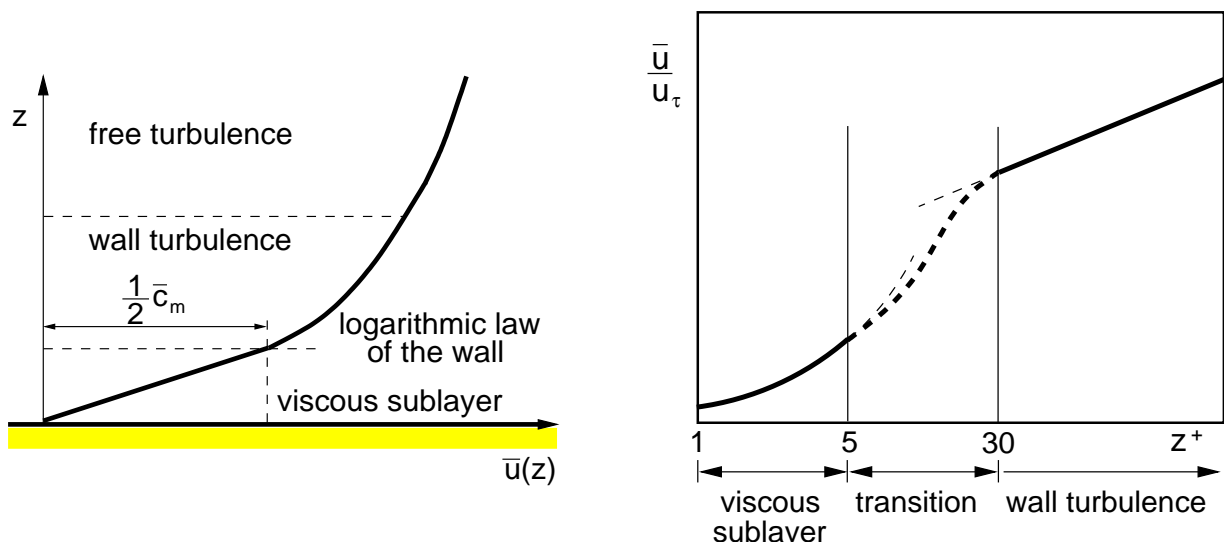


Fig. 2.72 : Turbulent boundary layer profile

coefficients are defined as the ratio of the wall friction force \vec{F}_R to the product of the dynamic pressure and the plate surface area $A = L \cdot b$. Here b denotes the breadth of the plate perpendicular to the plane sketched and L the length along the plate.

$$\tau_w(x) = \mu \cdot \left(\frac{\partial u}{\partial z} \right)_w , \quad c_f(x) = \frac{\tau_w(x)}{\frac{1}{2} \cdot \rho \cdot u_\infty^2} , \quad F_R = b \int_0^L \tau_w(x) \cdot dx \Rightarrow$$

$$F_R = b \cdot \frac{1}{2} \cdot \rho \cdot u_\infty^2 \cdot \int_0^L c_f(x) \cdot dx \Rightarrow \zeta = \frac{F_R}{\frac{1}{2} \cdot \rho \cdot u_\infty^2 \cdot L \cdot b} = \frac{1}{L} \cdot \int_0^L c_f(x) \cdot dx .$$

For the integral friction drag coefficient ζ at a distance L from the leading edge of the plate we have

$$\zeta = \frac{F_R}{\frac{1}{2} \cdot \rho \cdot u_\infty^2 \cdot b \cdot L} = \frac{1}{L} \cdot \int_0^L c_f(x) \cdot dx$$

$$= \begin{cases} \frac{1.328}{\sqrt{Re_L}} & \text{laminar boundary layer flow} \\ \frac{0.074}{(Re_L)^{\frac{1}{5}}} & \text{turbulent boundary layer flow} \end{cases} \quad (2.118)$$

Therefore the friction drag of a plate in a laminar flow is smaller than the friction drag of a plate in a completely turbulent flow under otherwise identical conditions. Therefore

$$\zeta_t > \zeta_l .$$

The different thickening behavior of the boundary layer thickness δ of laminar and turbulent boundary layer flows can be seen in Figure 2.74. The starting point is the relation (2.61) for a laminar boundary layer flow:

$$\boxed{\frac{\delta}{l} \sim \frac{1}{\sqrt{Re_L}}} .$$

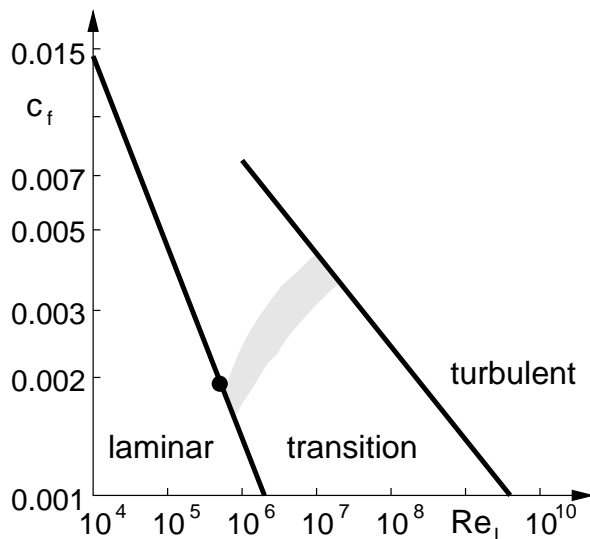


Fig. 2.73 : Friction drag c_f of the laminar and turbulent plate boundary layers

In the case of the laminar Blasius boundary layer, the proportionality factor is 5:

$$\frac{\delta}{L} = \frac{5}{\sqrt{Re_L}} .$$

Multiplication with $\sqrt{Re_L}$ yields

$$\frac{\delta}{L} \cdot \sqrt{Re_L} = 5 \Rightarrow \frac{\delta}{L} \cdot \sqrt{\frac{U_\infty \cot L}{\nu}} = 5 \Rightarrow \delta \cdot \sqrt{\frac{U_\infty}{\nu \cdot L}} = 5 .$$

For a turbulent boundary layer flow we have

$$\boxed{\frac{\delta}{l} \sim \frac{1}{(Re_L)^{\frac{1}{5}}} .} \quad (2.119)$$

Multiplication with $\sqrt{Re_L}$ delivers

$$\frac{\delta}{L} \cdot \sqrt{Re_L} \sim \frac{(Re_L)^{\frac{1}{2}}}{(Re_L)^{\frac{1}{5}}} \Rightarrow \delta \cdot \sqrt{\frac{U_\infty}{\nu \cdot L}} \sim Re_L^{\frac{1}{2} - \frac{1}{5}} \Rightarrow \delta \cdot \sqrt{\frac{U_\infty}{\nu \cdot L}} \sim Re_L^{0.3} .$$

By manipulating the turbulent wall shear stress τ'_w , the friction coefficient c_f of the turbulent boundary layer flow can be reduced. The idea for this comes from nature. Fast-swimming sharks (up to 45 km/h) have microscopically thin grooves on their scales in the direction of flow. Figure 2.75 shows a close-up of the longitudinal and transverse grooves on a single scale of a blue shark.

It can be assumed that less friction occurs on surfaces with longitudinal grooves than on smooth surfaces. This knowledge is applied in technology in the production of foils with longitudinal grooves, so-called riblets, with a height $z^+ = 500$ and a separation of $y^+ = 100$. Such foils are applied to smooth surfaces to reduce their friction drag.

As a result, the fluctuations in the transverse flow v' and therefore the transverse exchange in the viscous sublayer of the boundary layer are prevented. The outcome is a reduction

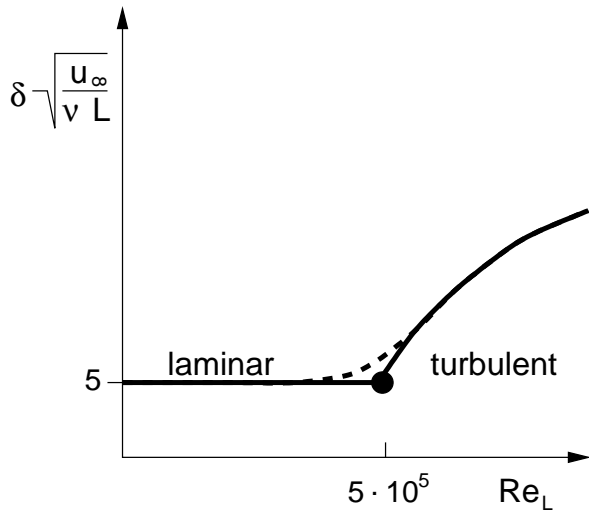


Fig. 2.74 : Boundary-layer thickness δ of laminar and turbulent plate boundary layers

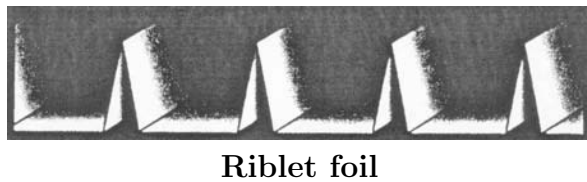
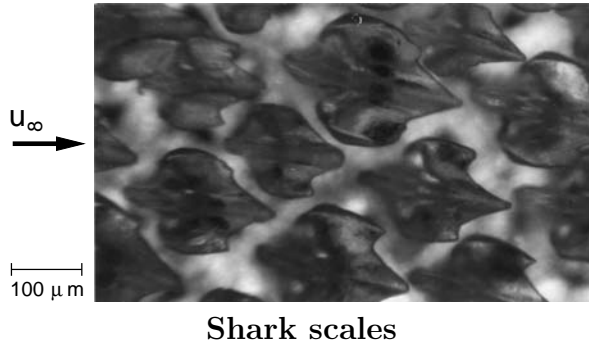


Fig. 2.75 : Shark scales and riblet foil

in the friction drag c_f of 8 %. In the case of an airplane, the friction drag c_f is more than 50 %. Since riblet foil cannot be applied to all parts of the aircraft, the real potential of drag reduction is 3 %. It has been seen that a 1 % reduction in fuel used by an Airbus A340 is made when 30 % of its surface is covered with riblet foil. The drag reducing foil can also be used in next-generation high-speed trains, as well as to reduce losses in pipe flows.

2.4.2 Balance of Momentum

The balance of momentum is carried out on a control volume V to determine directly the **integral forces** for given flow variables at the edge of the control volume V . The momentum $d\vec{I}$ of a mass element $dm = \rho \cdot dV$ is defined as the product of the mass element and the velocity vector \vec{v}

$$d\vec{I} = dm \cdot \vec{v} = \rho \cdot \vec{v} \cdot dV \quad \Rightarrow \quad d\vec{I} = \begin{pmatrix} dI_x \\ dI_y \\ dI_z \end{pmatrix} = dm \cdot \begin{pmatrix} u \\ v \\ w \end{pmatrix} = \rho \cdot \begin{pmatrix} u \\ v \\ w \end{pmatrix} \cdot dV .$$

Since the density ρ can be time dependent in compressible flows, $\rho = \rho(t)$, conservation of mass $m = \rho(t) \cdot V(t) = const.$ requires that the volume V must also be taken to be time dependent, i.e. $V = V(t)$. The momentum of the total mass m , or of the total volume under consideration, is calculated by integrating the differential momentum $d\vec{I}$ of the mass element over the volume $V(t)$:

$$\vec{I} = \int_{V(t)} \rho \cdot \vec{v} \cdot dV \quad \Rightarrow \quad \vec{I} = \begin{pmatrix} I_x \\ I_y \\ I_z \end{pmatrix} = \int_{V(t)} \rho \cdot \begin{pmatrix} u \\ v \\ w \end{pmatrix} \cdot dV .$$

The balance of momentum states that the total time derivative d/dt of the momentum is equal to the sum of all external forces. External forces may be mass

forces $\vec{\mathbf{F}}_M$ and surface forces $\vec{\mathbf{F}}_A$.

$$\frac{d\vec{\mathbf{I}}}{dt} = \frac{d}{dt} \int_{V(t)} \rho \cdot \vec{\mathbf{v}} \cdot dV = \sum \vec{\mathbf{F}}_M + \sum \vec{\mathbf{F}}_A ,$$

$$\Rightarrow \begin{pmatrix} \frac{dI_x}{dt} \\ \frac{dI_y}{dt} \\ \frac{dI_z}{dt} \end{pmatrix} = \sum \begin{pmatrix} F_{M,x} \\ F_{M,y} \\ F_{M,z} \end{pmatrix} + \sum \begin{pmatrix} F_{A,x} \\ F_{A,y} \\ F_{A,z} \end{pmatrix} .$$

In what follows we will consider the time derivative of the integral more closely. Since both the region of integration V and the integrand $\rho \cdot \vec{\mathbf{v}}$ depend on the time, the simplest manner of procedure is to form the derivative d/dt as the limiting value of the difference quotients:

$$\begin{aligned} \frac{d}{dt} \int_{V(t)} \rho \cdot \vec{\mathbf{v}} \cdot dV = \\ \lim_{\Delta t \rightarrow 0} \frac{1}{\Delta t} \left(\int_0^{V(t+\Delta t)} \rho(t + \Delta t) \cdot \vec{\mathbf{v}}(t + \Delta t) \cdot dV - \int_0^{V(t)} \rho(t) \cdot \vec{\mathbf{v}}(t) \cdot dV \right) . \end{aligned}$$

The first term is dealt with using the additivity of the integral

$$\begin{aligned} \int_0^{V(t+\Delta t)} \rho(t + \Delta t) \cdot \vec{\mathbf{v}}(t + \Delta t) \cdot dV = \\ \int_0^{V(t)} \rho(t + \Delta t) \cdot \vec{\mathbf{v}}(t + \Delta t) \cdot dV + \int_{V(t)}^{V(t+\Delta t)} \rho(t + \Delta t) \cdot \vec{\mathbf{v}}(t + \Delta t) \cdot dV . \end{aligned}$$

Taylor expanding the integrand up to the linear terms yields

$$\rho(t + \Delta t) \cdot \vec{\mathbf{v}}(t + \Delta t) = \rho(t) \cdot \vec{\mathbf{v}}(t) + \frac{\partial(\rho \cdot \vec{\mathbf{v}})}{\partial t} \cdot \Delta t + \dots .$$

We now insert the final two equations into the difference quotients, and find

$$\begin{aligned} \frac{d}{dt} \int_{V(t)} \rho \cdot \vec{\mathbf{v}} \cdot dV = \\ \lim_{\Delta t \rightarrow 0} \frac{1}{\Delta t} \left(\int_0^{V(t)} \frac{\partial(\rho \cdot \vec{\mathbf{v}})}{\partial t} \cdot \Delta t \cdot dV + \int_{V(t)}^{V(t+\Delta t)} \rho(t + \Delta t) \cdot \vec{\mathbf{v}}(t + \Delta t) \cdot dV \right) . \end{aligned}$$

In the next step we reduce the volume integral over the difference $V(t + \Delta t) - V(t)$ to an integral over the surface $A(t)$ of the volume $V(t)$. Using one-dimensional stream filament theory for the mass flux \dot{m} we obtain the relation

$$\dot{m} = \rho \cdot c \cdot A \Rightarrow \frac{\dot{m}}{\rho} = \dot{V} = c \cdot A .$$

Generalizing this to three-dimensional flows, we compute the volume flux \dot{V} as a surface integral over the scalar product $(\vec{\mathbf{v}} \cdot \vec{\mathbf{n}})$ of the velocity vector $\vec{\mathbf{v}} = (u, v, w)$ with the unit vector normal to the external surface $\vec{\mathbf{n}} = (n_x, n_y, n_z)$

$$\dot{V} = \int_A (\vec{\mathbf{v}} \cdot \vec{\mathbf{n}}) \cdot dA .$$

The volume flux satisfies

$$\dot{V} = \lim_{\Delta t \rightarrow 0} \frac{V(t + \Delta t) - V(t)}{\Delta t} = \lim_{\Delta t \rightarrow 0} \frac{1}{\Delta t} \cdot \int_{V(t)}^{V(t+\Delta t)} \cdot dV = \int_{A(t)} (\vec{v} \cdot \vec{n}) \cdot dA .$$

The total time derivative of the momentum yields

$$\begin{aligned} \frac{d}{dt} \int_{V(t)} \rho \cdot \vec{v} \cdot dV = \\ \lim_{\Delta t \rightarrow 0} \left(\frac{\Delta t}{\Delta t} \cdot \int_{V(t)} \frac{\partial(\rho \cdot \vec{v})}{\partial t} \cdot dV + \int_{A(t)} \rho(t + \Delta t) \cdot \vec{v}(t + \Delta t) \cdot (\vec{v} \cdot \vec{n}) \cdot dA \right) . \end{aligned}$$

After taking the limit, we find the **balance of momentum**

$$\boxed{\frac{d \vec{I}}{dt} = \frac{d}{dt} \int_V \rho \cdot \vec{v} \cdot dV = \int_V \frac{\partial(\rho \cdot \vec{v})}{\partial t} \cdot dV + \int_A \rho \cdot \vec{v} \cdot (\vec{v} \cdot \vec{n}) \cdot dA} . \quad (2.120)$$

The first term describes the local time change of the momentum inside the control volume under consideration. In order to evaluate this integral, knowledge of the flow quantities inside the control volume is necessary. For steady flows ($\partial/\partial t = 0$). The second term describes the convective momentum flux through the surface of the control volume. In order to compute this integral, only flow data on the edge of the control volume are needed.

For steady flows, the balance of momentum reads

$$\boxed{\frac{d \vec{I}}{dt} = \frac{d}{dt} \int_V \rho \cdot \vec{v} \cdot dV = \int_A \rho \cdot \vec{v} \cdot (\vec{v} \cdot \vec{n}) \cdot dA = \sum \vec{F}_M + \sum \vec{F}_A} . \quad (2.121)$$

With

$$\vec{F}_I = - \int_A \rho \cdot \vec{v} \cdot (\vec{v} \cdot \vec{n}) \cdot dA \Rightarrow \begin{pmatrix} F_{I,x} \\ F_{I,y} \\ F_{I,z} \end{pmatrix} = - \int_A \rho \cdot \begin{pmatrix} u \\ v \\ w \end{pmatrix} (\vec{v} \cdot \vec{n}) \cdot dA$$

we find

$$\boxed{\vec{F}_I + \sum \vec{F}_M + \sum \vec{F}_A = 0} , \quad (2.122)$$

$$\Rightarrow \begin{pmatrix} F_{I,x} \\ F_{I,y} \\ F_{I,z} \end{pmatrix} + \sum \begin{pmatrix} F_{M,x} \\ F_{M,y} \\ F_{M,z} \end{pmatrix} + \sum \begin{pmatrix} F_{A,x} \\ F_{A,y} \\ F_{A,z} \end{pmatrix} = \begin{pmatrix} 0 \\ 0 \\ 0 \end{pmatrix} .$$

The momentum force vector \vec{F}_I is parallel to the velocity vector \vec{v} , and the direction of \vec{F}_I is always towards the inside of the control volume. The pressure force \vec{F}_D , which is one of the surface forces \vec{F}_A , is defined as

$$\vec{F}_D = - \int_A p \cdot \vec{n} \cdot dA \Rightarrow \begin{pmatrix} F_{D,x} \\ F_{D,y} \\ F_{D,z} \end{pmatrix} = - \int_A p \begin{pmatrix} n_x \\ n_y \\ n_z \end{pmatrix} \cdot dA .$$

Since the pressure p is a positive scalar quantity, and \vec{n} is the external unit vector normal to the surface, the direction of the pressure force \vec{F}_D , is, because of the minus sign, also towards the inside of the control volume.

Let us now apply the balance of momentum (2.122) to laminar **boundary layer flow**. The function f which connects the boundary layer thickness with the Reynolds number Re_L (2.61) can now be determined

$$\frac{\delta}{L} = f(Re_L) \quad .$$

The control volume used in Figure 2.76 is a rectangular block of length L , height $\delta(L)$ and depth b in the y direction. The pressure p is imprinted onto the boundary layer from the outer flow $(\partial p / \partial z) = 0$, and, in the case of the plate boundary layer, is constant in the outer flow. Therefore it follows that the pressure must also be constant in the boundary layer, and so all pressure forces appearing must cancel out each other. At position 3, for reasons of simplicity, we assume a linear velocity profile $u(z)$, since, compared to the Blasius boundary layer profile, this can be integrated analytically. For $u(z)$ we then have

$$u(z) = \frac{u_\infty}{\delta(L)} \cdot z \quad .$$

At the left edge, at position 1, the flow passes through the cross-section $A_1 = b \cdot \delta(L)$ with the constant velocity u_∞ . The momentum force F_{I,x_1} therefore reads

$$\begin{aligned} F_{I,x_1} &= - \int_{A_1} \rho \cdot u_\infty \cdot (\vec{v} \cdot \vec{n}) \cdot dA_1 \\ &= - \rho \cdot u_\infty \begin{pmatrix} u_\infty \\ 0 \\ 0 \end{pmatrix} \cdot \begin{pmatrix} -1 \\ 0 \\ 0 \end{pmatrix} \cdot A_1 = \rho \cdot u_\infty^2 \cdot A_1 = \rho \cdot u_\infty^2 \cdot b \cdot \delta(L) \quad . \end{aligned}$$

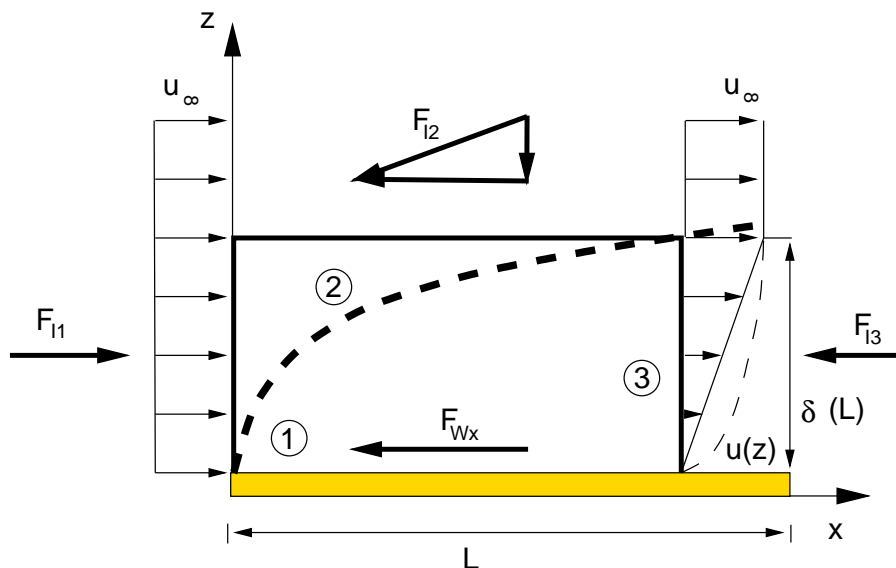


Fig. 2.76 : Forces on the control volume V for the laminar plate boundary layer

For the momentum force F_{I,x_3} , with $dA_3 = b \cdot dz$, it follows that

$$\begin{aligned} F_{I,x_3} &= - \int_{A_3} \rho \cdot u(z) \cdot (\vec{v} \cdot \vec{n}) \cdot dA_3 \\ &= - \int_{A_3} \rho \cdot u(z) \cdot \begin{pmatrix} uz \\ 0 \\ 0 \end{pmatrix} \cdot \begin{pmatrix} 1 \\ 0 \\ 0 \end{pmatrix} \cdot dA_3 = -\rho \cdot b \cdot \int_0^{\delta(L)} u^2(z) \cdot dz \quad . \end{aligned}$$

Therefore the momentum force F_{I,x_1} points in the $+x$ direction and F_{I,x_3} in the $-x$ direction. Computing the integral yields

$$\begin{aligned} F_{I,x_3} &= -\rho \cdot b \cdot \int_0^{\delta(L)} u^2(z) \cdot dz = -\rho \cdot b \cdot \int_0^{\delta(L)} \frac{u_\infty^2}{\delta^2(L)} \cdot z^2 \cdot dz \\ &= -\rho \cdot b \cdot \frac{u_\infty^2}{\delta^2(L)} \cdot \left[\frac{1}{3} \cdot z^3 \right]_0^{\delta(L)} = -\frac{1}{3} \cdot \rho \cdot b \cdot u_\infty^2 \cdot \delta(L) \quad . \end{aligned}$$

Before we compute the momentum force vector \vec{F}_{I_2} , we will first use the conservation of mass. The mass flux \dot{m}_1 entering through the surface $A_1 = b \cdot \delta(L)$ is

$$\dot{m}_1 = \rho \cdot U_\infty \cdot A_1 = \rho \cdot U_\infty \cdot b \cdot \delta(L) \quad .$$

The mass flux \dot{m}_3 exiting through the surface A_3 is

$$\begin{aligned} \dot{m}_3 &= \rho \cdot \int_0^{A_3} u(z) \cdot dA_3 = \rho \cdot b \cdot \int_0^{\delta(L)} u(z) \cdot dz = \rho \cdot b \cdot \frac{u_\infty}{\delta(L)} \cdot \int_0^{\delta(L)} z \cdot dz \\ &= \rho \cdot b \cdot \frac{u_\infty}{\delta(L)} \cdot \left[\frac{1}{2} \cdot z^2 \right]_0^{\delta(L)} = \frac{1}{2} \cdot \rho \cdot u_\infty \cdot b \cdot \delta(L) \quad . \end{aligned}$$

Since $\dot{m}_3 < \dot{m}_1$ and the plate is impermeable to the flow, the difference in mass fluxes $\dot{m}_2 = \dot{m}_1 - \dot{m}_3$ must pass out through the surface $A_2 = b \cdot L$.

$$\dot{m}_2 = \dot{m}_1 - \dot{m}_3 = \rho \cdot u_\infty \cdot b \cdot \delta(L) - \frac{1}{2} \cdot \rho \cdot u_\infty \cdot b \cdot \delta(L) = \frac{1}{2} \cdot \rho \cdot u_\infty \cdot b \cdot \delta(L) \quad .$$

Therefore the boundary layer has a displacement action, and the flow through the surface A_2 produces a momentum force vector \vec{F}_{I_2} . For the velocity component with which the mass flux \dot{m}_2 passes vertically out through the surface A_2 , we first assume an unknown component $w_2(x) > 0$ in the $+z$ direction. Further, $w_2(x)$ must satisfy the supplementary condition $w_2 \ll u_\infty$. The velocity of the fluid in the x direction along the surface A_2 is of magnitude u_∞ . By definition, the momentum force vector \vec{F}_{I_2} is first of all computed quite generally to

$$\vec{F}_{I_2} = - \int_{A_2} \rho \cdot \vec{v} \cdot (\vec{v} \cdot \vec{n}) \cdot dA_2 = - \int_{A_2} \rho \cdot \begin{pmatrix} u_\infty \\ 0 \\ w_2(x) \end{pmatrix} \cdot \left[\begin{pmatrix} u_\infty \\ 0 \\ w_2(x) \end{pmatrix} \cdot \begin{pmatrix} 0 \\ 0 \\ 1 \end{pmatrix} \right] \cdot dA_2 \quad ,$$

$$\vec{F}_{I_2} = \begin{pmatrix} F_{I,x_2} \\ F_{I,y_2} \\ F_{I,z_2} \end{pmatrix} = - \int_{A_2} \rho \cdot \begin{pmatrix} u_\infty \\ 0 \\ w_2(x) \end{pmatrix} \cdot w_2(x) \cdot dA_2 \quad .$$

For the x component F_{I,x_2} of the momentum force vector $\vec{\mathbf{F}}_{\mathbf{I}_2}$ we therefore obtain

$$F_{I,x_2} = -u_\infty \cdot \int_{A_2} \rho \cdot w_2(x) \cdot dA_2 = -u_\infty \cdot \dot{m}_2 = -\frac{1}{2} \cdot \rho \cdot u_\infty^2 \cdot b \cdot \delta(L) .$$

The z component F_{I,z_2} has, because of $w_2(x)$ a very small magnitude, points in the z direction and is of no importance for the following considerations.

The wall friction force $F_{W,x}$ is the force which decelerates the free stream velocity u_∞ to the value zero at the surface of the plate. Therefore it points in the negative x direction, and because $du/dz > 0$, we have

$$F_{W,x} = -b \cdot \int_0^L |\tau_w| \cdot dx = -b \cdot \int_0^L \mu \cdot \left. \frac{du}{dz} \right|_{z=0} \cdot dx = -b \cdot \mu \cdot u_\infty \cdot \int_0^L \frac{1}{\delta(x)} \cdot dx .$$

The balance of momentum in the x direction yields

$$|F_{I,x_1}| - |F_{I,x_2}| - |F_{I,x_3}| - |F_{W,x}| = 0 ,$$

$$\begin{aligned} \rho \cdot u_\infty^2 \cdot b \cdot \delta(L) - \frac{1}{2} \cdot \rho \cdot u_\infty^2 \cdot b \cdot \delta(L) - \frac{1}{3} \cdot \rho \cdot u_\infty^2 \cdot b \cdot \delta(L) \\ - \mu \cdot b \cdot u_\infty \cdot \int_0^L \frac{1}{\delta(x)} \cdot dx = 0 , \end{aligned}$$

$$\frac{1}{6} \cdot \rho \cdot u_\infty \cdot \delta(L) = \mu \cdot \int_0^L \frac{1}{\delta(x)} \cdot dx \Rightarrow \frac{\rho \cdot u_\infty}{6 \cdot \mu} \cdot \delta(L) = \int_0^L \frac{1}{\delta(x)} \cdot dx .$$

If we differentiate the last equation on both sides by s and take the relation $\nu = \mu/\rho$ into account, we obtain

$$\frac{u_\infty}{6 \cdot \nu} \cdot \frac{d\delta(x)}{dx} = \frac{1}{\delta(x)} \Rightarrow \delta(x) \cdot d\delta = \frac{6 \cdot \nu}{u_\infty} \cdot dx .$$

Integration yields

$$\int_0^{\delta(L)} \delta \cdot d\delta = \frac{6 \cdot \nu}{u_\infty} \cdot \int_0^L dx \Rightarrow \left[\frac{1}{2} \cdot \delta^2 \right]_0^{\delta(L)} = \frac{6 \cdot \nu}{u_\infty} \cdot [x]_0^L ,$$

$$\Rightarrow \delta^2(L) = \frac{12 \cdot \nu \cdot L}{u_\infty} \Rightarrow \frac{\delta^2}{L^2} = \frac{12 \cdot \nu}{u_\infty \cdot L} = \frac{12}{\frac{u_\infty \cdot L}{\nu}} = \frac{12}{Re_L} .$$

The originally desired function $\delta/L = f(Re_L)$ is thus found to be

$$\frac{\delta}{L} = \sqrt{\frac{12}{Re_L}} \approx \frac{3.464}{\sqrt{Re_L}} .$$

The factor 3.464 is a consequence of the simplifying assumption of a linear velocity profile $u(z)$. The exact value, found by using the real Blasius profile for the boundary layer, is 5, so that

$$\frac{\delta}{L} = \frac{5.0}{\sqrt{Re_L}} .$$

The **lift A** and the **drag W** of a wing can also be determined directly with the balance of momentum (2.122) if the time-averaged wake profile $\bar{u}(z)$, $\bar{p}(z)$ is known. The time-averaged velocity and pressure distributions are measured on a fixed control volume V in a wind tunnel and numerical integration is used to determine the momentum and pressure forces. The balance of momentum in the x direction is written, using the notation of Figure 2.77, as follows

$$F_{I_\infty} - F_{I,N} - F_{I,x} + F_{D_\infty} - F_{D,N} + F_{D,x} - W = 0 . \quad (2.123)$$

Here the index N denotes the time-averaged profiles in the wake, ∞ the unperturbed free stream, and F_I , F_D the momentum and pressure forces due to the displacement action of the wing. The minus sign in front of the drag force is because the drag enters into the balance law as a reaction force. The balance of momentum in the z direction yields

$$F_{I,z} + F_{D,z} - A = 0 . \quad (2.124)$$

Application of equations (2.123) and (2.124) is one of the usual methods to determine the drag and lift forces of bodies in a flow from the measured velocity and pressure profiles, without solving the fundamental fluid mechanical equations directly. The weight G has to be taken into account in a separate balance of the mass forces.

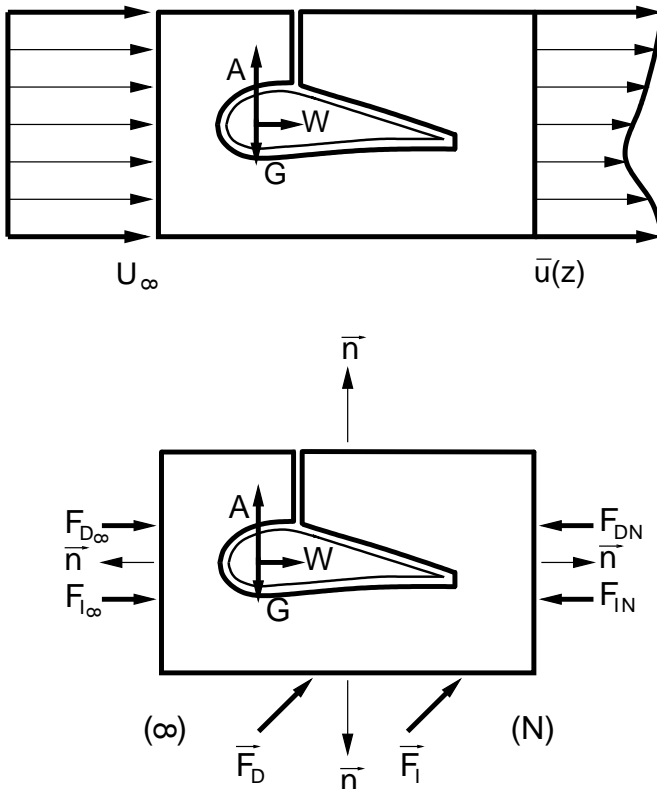


Fig. 2.77 : Forces on the control volume V for the flow past a foil

2.4.3 Balance of Angular Momentum

For many applications, particularly in the area of flow machinery, a statement analogous to the balance of momentum is important for the **moments**. The balance of angular momentum can be used to determine the points of action of the momentum forces, or the work done or energy gained in the flow through a rotor.

The angular momentum \vec{L} is a vector lying in the plane spanned by a displacement vector \vec{r} and the momentum vector $\vec{I} = m \cdot \vec{v}$. The angular momentum is

$$\vec{L} = \vec{r} \times \vec{I} = (\vec{r} \times \vec{v}) \cdot m \quad ,$$

$$\begin{pmatrix} L_x \\ L_y \\ L_z \end{pmatrix} = \left[\begin{pmatrix} r_x \\ r_y \\ r_z \end{pmatrix} \times \begin{pmatrix} u \\ v \\ w \end{pmatrix} \right] \cdot m = \begin{pmatrix} r_y \cdot w - r_z \cdot v \\ r_z \cdot u - r_x \cdot w \\ r_x \cdot v - r_y \cdot u \end{pmatrix} \cdot m \quad .$$

The differential angular momentum $d\vec{L}$ of a mass element $dm = \rho \cdot dV$ yields

$$d\vec{L} = (\vec{r} \times \vec{v}) \cdot dm = \rho \cdot (\vec{r} \times \vec{v}) \cdot dV \quad .$$

Therefore the angular momentum of a volume $V(t)$ is

$$\vec{L} = \int_0^{V(t)} \rho \cdot (\vec{r} \times \vec{v}) \cdot dV \quad .$$

The balance of angular momentum states that **the total rate of change d/dt of the angular momentum \vec{L} is equal to the sum of all the external moments acting $\sum \vec{M}_a$** .

These external moments $\sum \vec{M}_a$ are due to the mass and surface forces $\sum \vec{F}_M + \sum \vec{F}_A$, already discussed in connection with the balance of momentum. Here they act on a lever \vec{r} and we have

$$\sum \vec{M}_a = \sum (\vec{r} \times \vec{F}_M) + \sum (\vec{r} \times \vec{F}_A) \quad .$$

The balance of angular momentum reads

$$\frac{d\vec{L}}{dt} = \frac{d}{dt} \int_0^{V(t)} \rho \cdot (\vec{r} \times \vec{v}) \cdot dV = \sum \vec{M}_a \quad . \quad (2.125)$$

The formation of the total time derivative is carried out completely analogously to the process described in connection with the balance of momentum. We obtain

$$\begin{aligned} \frac{d\vec{L}}{dt} &= \frac{d}{dt} \int_V \rho \cdot (\vec{r} \times \vec{v}) \cdot dV \\ &= \int_V \frac{\partial(\rho \cdot (\vec{r} \times \vec{v}))}{\partial t} \cdot dV + \int_A \rho \cdot (\vec{r} \times \vec{v}) \cdot (\vec{v} \cdot \vec{n}) \cdot dA = \sum \vec{M}_a \quad . \end{aligned}$$

Just as in the case of the balance of momentum, for steady flows ($\partial/\partial t = 0$) the volume integral drops away and we only require the surface integral and the flow data on the edge of the control region

$$\int_A \rho \cdot (\vec{r} \times \vec{v}) \cdot (\vec{v} \cdot \vec{n}) \cdot dA = \sum \vec{M}_a .$$

A control volume at rest in a steady flow will of course satisfy the steady flow condition as long as the coordinate system is at rest too.

Now a flow machine with a rotor in a coordinate system at rest generates an unsteady flow. Here we first carry out a transformation of reference frame to a coordinate system rotating with the rotor, in order to generate a steady flow. If we define the moment of momentum \vec{M}_I , in analogy to the definition of the momentum force, as an inertial moment:

$$\vec{M}_I = - \int_A \rho \cdot (\vec{r} \times \vec{v}) \cdot (\vec{v} \cdot \vec{n}) \cdot dA ,$$

we obtain the **balance of angular momentum**

$$\vec{M}_I + \sum \vec{M}_a = 0 \Rightarrow \begin{pmatrix} M_{I,x} \\ M_{I,y} \\ M_{I,z} \end{pmatrix} + \sum \begin{pmatrix} M_{a,x} \\ M_{a,y} \\ M_{a,z} \end{pmatrix} = \begin{pmatrix} 0 \\ 0 \\ 0 \end{pmatrix} . \quad (2.126)$$

The moment of momentum vector \vec{M}_I is locally parallel to the vector product $(\vec{r} \times \vec{v})$, because the scalar product $(\vec{v} \cdot \vec{n})$ only makes a contribution to the sign and the magnitude of the moment of momentum, and not to its direction.

In order to illustrate the balance of angular momentum we will now consider an example of its application. Figure 2.78 shows an **elbow bend**, flanged onto a pipe. The elbow bend steers the flow from the vertical flow direction to the horizontal flow direction. The flow exits into free surroundings at the right end of the elbow bend.

We want to consider how large is the moment \vec{M}_k which the elbow bend causes to act on the flange junction. Here we assume that the dimension l (Figure 2.78), the flow velocity c , the density ρ of the fluid and the cross-sectional area A_1 are known.

Evaluating the integral

$$\vec{M}_I = - \int_A \rho \cdot (\vec{r} \times \vec{v}) \cdot (\vec{v} \cdot \vec{n}) \cdot dA \quad (2.127)$$

for the control surface shown in Figure 2.78, we obtain the scalar magnitude of the vector \vec{M}_I as

$$| \vec{M}_I | = \rho \cdot l \cdot c^2 \cdot A_1 . \quad (2.128)$$

In evaluating equation (2.127), the following points should be noted. At position 1, the fluid flows over the edge of the control space. The expression beneath the integral in equation (2.127) is equal to the zero vector for this section of the control surface, since $\vec{r} \times \vec{v} = \vec{0}$.

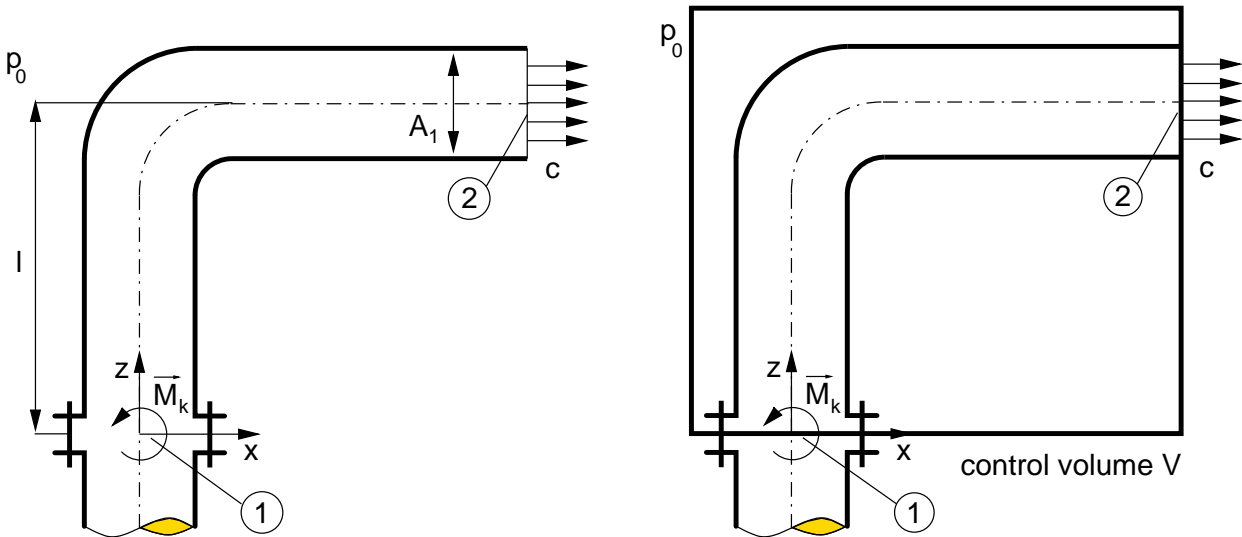


Fig. 2.78 : Elbow bend

At position 2, on the other hand, the cross product delivers a vector in the negative axial direction. It points into the plane of the sketch, and therefore its magnitude acquires a minus sign. The scalar product $\vec{v} \cdot \vec{n}$ is positive at the position 2 and evaluates as $c \cdot A_1$. Taking these details into account, the scalar value for \vec{M}_I as formulated in equation (2.128) is obtained .

Other than this, no other resulting forces which produce a moment act on the control surface. The elbow bend induces the moment $-\vec{M}_k$ on the fluid. The direction of rotation of \vec{M}_k is initially assumed to be positive. The actual rotation direction is then calculated using the equation

$$\vec{M}_I + \sum \vec{M}_a = 0 \quad .$$

The following equation for $-\vec{M}_k = \sum \vec{M}_a$ is obtained

$$\rho \cdot l \cdot c^2 \cdot A_1 - | \vec{M}_k | = 0 \quad \Rightarrow \quad | \vec{M}_k | = \rho \cdot l \cdot c^2 \cdot A_1 \quad .$$

Therefore the fluid imposes a moment on the elbow bend which acts in the positive direction.

2.4.4 Pipe Hydraulics

The objective in this section is to determine the velocity distribution $u(r)$ and, as a supplement to Chapter 2.3.2, the pressure loss Δp and friction loss c_f for laminar and turbulent flows through circular pipes.

We start out from the steady laminar **Hagen-Poiseuille pipe flow** in Figure 2.43. The flow is fully formed, i.e. the velocity profile $u(r)$ depends only on the radial coordinate r and does not vary with x , $(\partial u / \partial x) = 0$. The flow is driven by a constant pressure difference in the flow direction x , i.e. $(dp/dx) = \text{const.} < 0$.

We have already met the parabolic velocity profile $u(r)$ (2.63) which is the analytic solution of the Navier-Stokes equation (2.62). Our first step in this chapter on pipe dynamics will be

to determine the same result again with the force balance on a cylindrical volume element $dV = \pi \cdot r^2 \cdot dx$ as sketched in Figure 2.79. In a fully formed pipe flow, no resulting momentum forces act, so that the only forces are pressure forces.

The pressure force at position 1 ($p_1 > p_2$) reads

$$|\vec{F}_{D,1}| = p_1 \cdot \pi \cdot r^2 = p \cdot \pi \cdot r^2 .$$

The pressure force at position 2 is

$$|\vec{F}_{D,2}| = p_2 \cdot \pi \cdot r^2 = \left(p + \frac{dp}{dx} \cdot dx \right) \cdot \pi \cdot r^2 .$$

The friction is

$$|\vec{F}_R| = |\tau| \cdot 2 \cdot \pi \cdot r \cdot dx .$$

Since the velocity distribution $u(r)$ decreases from a maximum value in the center of the pipe u_{max} to the value zero at the wall of the pipe, for $r \neq 0$ we have $(du/dr) < 0$. Therefore the magnitude of the shear stress is

$$|\tau| = -\mu \cdot \frac{du}{dr} .$$

The balance of forces follows as

$$\begin{aligned} |\vec{F}_{D,1}| - |\vec{F}_{D,2}| - |\vec{F}_R| &= 0 , \\ \Rightarrow p \cdot \pi \cdot r^2 - \left(p + \frac{dp}{dx} \cdot dx \right) \cdot \pi \cdot r^2 - |\tau| \cdot 2 \cdot \pi \cdot r \cdot dx &= 0 , \\ -\frac{dp}{dx} \cdot \pi \cdot r^2 = |\tau| \cdot 2 \cdot \pi \cdot r &\Rightarrow |\tau(r)| = -\frac{dp}{dx} \cdot \frac{r}{2} \Rightarrow \frac{du}{dr} = \frac{1}{\mu} \cdot \frac{dp}{dx} \cdot \frac{r}{2} . \end{aligned}$$

This equation corresponds to the first order ordinary differential equation (2.62) to determine the desired velocity distribution $u(r)$. After separating the variables and integrating indefinitely, we first of all obtain

$$u(r) = \frac{1}{4 \cdot \mu} \cdot \frac{dp}{dx} \cdot r^2 + C .$$

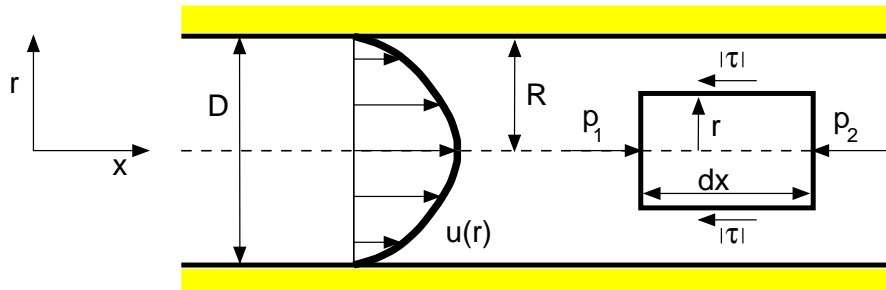


Fig. 2.79 : Balance of forces for Hagen-Poiseuille pipe flow

The constant of integration C is determined using the boundary condition $u(r = R) = 0$ as

$$C = -\frac{1}{4 \cdot \mu} \cdot \frac{dp}{dx} \cdot R^2 \quad .$$

The velocity profile $u(r)$ is therefore

$$u(r) = \frac{1}{4 \cdot \mu} \cdot \frac{dp}{dx} \cdot r^2 - \frac{1}{4 \cdot \mu} \cdot \frac{dp}{dx} \cdot R^2 = -\frac{1}{4 \cdot \mu} \cdot \frac{dp}{dx} \cdot (-r^2 + R^2) \quad ,$$

$$u(r) = -\frac{1}{4 \cdot \mu} \cdot \frac{dp}{dx} \cdot R^2 \cdot \left(1 - \frac{r^2}{R^2}\right) \quad .$$

(2.129)

We therefore obtain a parabolic velocity distribution for $u(r)$ with the maximum velocity

$$u_{max} = -\frac{1}{4 \cdot \mu} \cdot \frac{dp}{dx} \cdot R^2 \quad .$$

The volume flux in the pipe \dot{V} is then

$$\begin{aligned} \dot{V} &= \int_A u(r) \cdot dA = \int_0^R u(r) \cdot 2 \cdot \pi \cdot r \cdot dr = \int_0^R u_{max} \cdot \left(1 - \frac{r^2}{R^2}\right) \cdot 2 \cdot \pi \cdot r \cdot dr \\ &= 2 \cdot \pi \cdot u_{max} \cdot \int_0^R \left(r - \frac{r^3}{R^2}\right) \cdot dr \end{aligned}$$

$$\begin{aligned} \dot{V} &= 2 \cdot \pi \cdot u_{max} \left[\frac{1}{2} \cdot r^2 - \frac{1}{4} \cdot \frac{r^4}{R^2} \right]_0^R = 2 \cdot \pi \cdot u_{max} \cdot \frac{1}{4} \cdot R^2 \\ &= \frac{u_{max}}{2} \cdot \pi \cdot R^2 = \frac{u_{max}}{2} \cdot A = u_m \cdot A \quad . \end{aligned}$$

The volumetric average of the pipe velocity u_m follows as

$$u_m = \frac{1}{2} \cdot u_{max} = -\frac{1}{8 \cdot \mu} \cdot \frac{dp}{dx} \cdot R^2 \quad .$$

The volume flux can then be determined as follows:

$$\dot{V} = u_m \cdot A = \frac{1}{2} \cdot u_{max} \cdot A = -\frac{\pi}{8 \cdot \mu} \cdot \frac{dp}{dx} \cdot R^4 \quad .$$

(2.130)

Therefore, for laminar Hagen-Poiseuille pipe flow we obtain the following proportionality relation at the position $x = L$:

$$\dot{V} \sim \Delta p = L \cdot \frac{dp}{dx} \quad , \quad \dot{V} \sim R^4 \quad .$$

Equation (2.130) clarifies the characteristic form of the volume flux. It is proportional to the pressure loss $\Delta p = p_1 - p_2$ and to the fourth power of the radius R .

We now consider the size of the pressure loss Δp for a given volume flux. This pressure loss is a consequence of the effect of friction. From (2.130)

$$\dot{V} = \frac{\pi}{8 \cdot \mu} \cdot \frac{\Delta p}{L} \cdot R^4 \quad , \quad \Delta p = p_1 - p_2$$

it follows that

$$\Delta p = \dot{V} \cdot \frac{8 \cdot \mu \cdot L}{\pi \cdot R^4} = u_m \cdot \pi \cdot R^2 \cdot \frac{8 \cdot \mu \cdot L}{\pi \cdot R^4} = u_m \cdot \frac{8 \cdot \mu \cdot L}{R^2} = \frac{u_m \cdot 8 \cdot \rho \cdot \nu \cdot L}{R^2} \quad .$$

In what follows we expand the term on the right-hand side of Δp so that characteristic quantities of the flow can be summarized:

$$\Delta p = \frac{1}{2} \cdot \rho \cdot u_m^2 \cdot \frac{16 \cdot \nu \cdot L}{u_m \cdot R^2} = \frac{1}{2} \cdot \rho \cdot u_m^2 \cdot \frac{16 \cdot \nu \cdot L}{u_m \cdot (\frac{D}{2})^2} = \frac{1}{2} \cdot \rho \cdot u_m^2 \cdot \frac{L}{D} \cdot \frac{64}{\frac{u_m \cdot D}{\nu}} \quad .$$

Defining the Reynolds number formed with the diameter of the pipe D as $Re_D = (u_m \cdot D)/\nu$ and writing the factor $64/Re_D$ as a loss coefficient λ_{lam} , we obtain the following equations to determine the pressure loss

$$\boxed{\Delta p = \frac{1}{2} \cdot \rho \cdot u_m^2 \cdot \frac{L}{D} \cdot \lambda_{lam} \quad , \quad \lambda_{lam} = \frac{64}{Re_D}} \quad . \quad (2.131)$$

These equations hold for laminar pipe flows, i.e. for Reynolds numbers smaller than the critical Reynolds number Re_c

$$\boxed{Re_D = \frac{u_m \cdot D}{\nu} < Re_c = 2300} \quad .$$

For fully formed **turbulent pipe flow** the time-averaged velocity satisfies $(\partial \bar{u}/\partial x) = 0$, so that again momentum forces occur in the time average. In Figure 2.80 we apply the balance of momentum to a control volume $V = \pi \cdot R^2 \cdot L$ with pipe radius R , and determine the pressure force at position 1 ($\bar{p}_1 > \bar{p}_2$) as

$$|\vec{F}_{D,1}| = \bar{p}_1 \cdot \pi \cdot R^2 \quad .$$

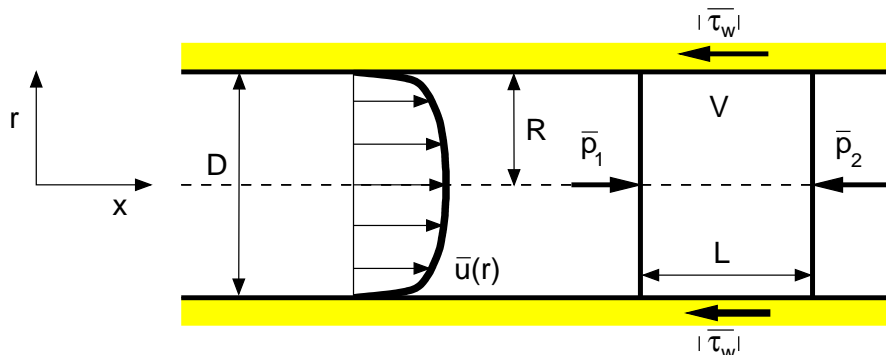


Fig. 2.80 : Balance of forces on a control volume V for turbulent pipe flow

The pressure force at position 2 is

$$|\vec{\mathbf{F}}_{\mathbf{D},2}| = \bar{p}_2 \cdot \pi \cdot R^2 \quad .$$

The wall friction force is

$$|\vec{\mathbf{F}}_{\mathbf{R},w}| = |\bar{\tau}_w| \cdot 2 \cdot \pi \cdot R \cdot L \quad ,$$

and the balance of forces follows as

$$|\vec{\mathbf{F}}_{\mathbf{D},1}| - |\vec{\mathbf{F}}_{\mathbf{D},2}| - |\vec{\mathbf{F}}_{\mathbf{R},w}| = 0 \quad ,$$

$$\bar{p}_1 \cdot \pi \cdot R^2 - \bar{p}_2 \cdot \pi \cdot R^2 - |\bar{\tau}_w| \cdot 2 \cdot \pi \cdot R \cdot L = 0 \quad ,$$

$$(\bar{p}_1 - \bar{p}_2) \cdot \pi \cdot R^2 = \Delta \bar{p} \cdot \pi \cdot R^2 = |\bar{\tau}_w| \cdot 2 \cdot \pi \cdot R \cdot L \Rightarrow \Delta \bar{p} = |\bar{\tau}_w| \cdot \frac{2 \cdot L}{R} \quad .$$

There is no theoretical ansatz for the wall shear stress $|\bar{\tau}_w|$, and so we use an empirical ansatz, which determines the pressure loss equation $\Delta \bar{p}$ in analogy to the laminar case:

$$|\bar{\tau}_w| = \frac{1}{2} \cdot \rho \cdot \bar{u}_m^2 \cdot \frac{\lambda_t}{4} \Rightarrow \Delta \bar{p} = \frac{1}{2} \cdot \rho \cdot \bar{u}_m^2 \cdot \frac{\lambda_t}{4} \cdot \frac{2 \cdot L}{R} = \frac{1}{2} \cdot \rho \cdot \bar{u}_m^2 \cdot \frac{L}{2 \cdot R} \cdot \lambda_t \quad ,$$

$$\Delta \bar{p} = \frac{1}{2} \cdot \rho \cdot \bar{u}_m^2 \cdot \frac{L}{D} \cdot \lambda_t \quad , \quad \lambda_t = \lambda_t(Re_D) \text{ from experiment,} \quad Re_D = \frac{\bar{u}_m \cdot D}{\nu} \quad (2.132)$$

From experimental results, we obtain the pressure loss coefficient λ_t in the form of the **Blasius law**

$$\lambda_t = \frac{0.3164}{(Re_D)^{\frac{1}{4}}} \quad , \quad \text{valid for } 3 \cdot 10^3 \leq Re_D \leq 10^5 \quad , \quad (2.133)$$

and the implicit **Prandtl representation**

$$\frac{1}{\sqrt{\lambda_t}} = 2 \cdot \log_{10} \left(Re_D \cdot \sqrt{\lambda_t} \right) - 0.8 \quad , \quad \text{valid for } Re_D \leq 10^6 \quad . \quad (2.134)$$

If the pipe is rough, values of λ_t can be read off from the **Nikuradse diagram** in Figure 2.81. The roughness K_s here is the spatial average of the surface roughness of the pipe walls. Some values for different materials are listed in Figure 2.82.

The extension to the implicit equation (2.134) for rough pipes, determined from experiment, yields

$$\frac{1}{\sqrt{\lambda_t}} = 2 \cdot \log_{10} \left(\frac{2.51}{Re_D \cdot \sqrt{\lambda_t}} + \frac{K_s}{3.71 \cdot D} \right) \quad . \quad (2.135)$$

For Reynolds numbers $Re_D > 10^6$ the loss coefficient λ_t becomes independent of the Reynolds number, since then the viscous sublayer of the turbulent pipe boundary layer

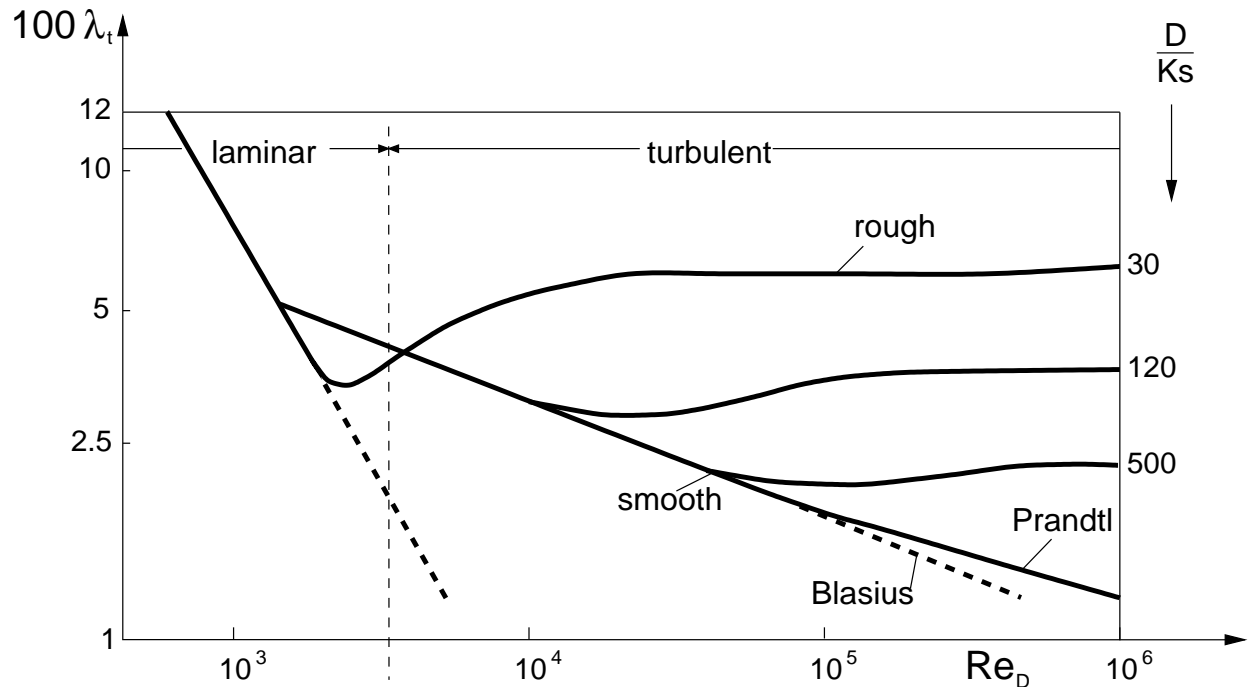


Fig. 2.81 : Nikuradse diagram

covers the roughness of the pipe. Figure 2.83 shows λ_t for different pipe cross-sections.

In order to compute the time-averaged turbulent velocity profile $\bar{u}(r)$ we start out from the ansatz for the wall shear stress $\bar{\tau}_w$

$$|\bar{\tau}_w| = \frac{1}{2} \cdot \rho \cdot \bar{u}_m^2 \cdot \frac{\lambda_t}{4}$$

Using the Blasius equation (2.133)

$$\lambda_t = \frac{0.3164}{(Re_D)^{\frac{1}{4}}} = \frac{0.3164}{\left(\frac{\bar{u}_m \cdot D}{\nu}\right)^{\frac{1}{4}}}$$

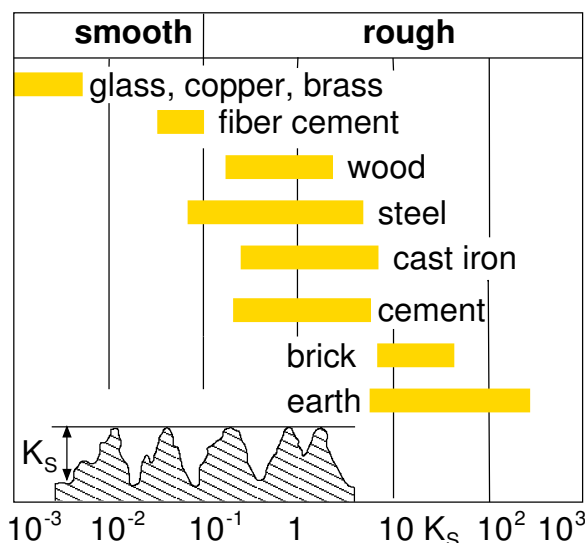


Fig. 2.82 : Roughness of different materials

and taking the proportionality $R \sim D$ and $\bar{u}_m \sim \bar{u}_{max}$ into account, we obtain the relation

$$|\bar{\tau}_w| \sim \rho \cdot \bar{u}_{max}^2 \cdot (\bar{u}_{max})^{-\frac{1}{4}} \cdot R^{-\frac{1}{4}} \cdot \nu^{\frac{1}{4}} = \rho \cdot (\bar{u}_{max})^{\frac{7}{4}} \cdot R^{-\frac{1}{4}} \cdot \nu^{\frac{1}{4}} .$$

Initially we restrict ourselves to determining $\bar{u}(r)$ close to the wall for $r \rightarrow R$ and introduce the substitution $z = R - r$. A power ansatz with unknown exponent m can then be written down for the velocity profile $\bar{u}(r)$ close to the wall as follows:

$$\begin{aligned} \bar{u}(r) &= \bar{u}_{max} \cdot \left(\frac{z}{R}\right)^m , \\ \Rightarrow \quad \bar{u}_{max} &= \bar{u}(r) \cdot \frac{R^m}{z^m} \quad \Rightarrow \quad (\bar{u}_{max})^{\frac{7}{4}} = \bar{u}^{\frac{7}{4}}(z) \cdot R^{\frac{7 \cdot m}{4}} \cdot z^{-\frac{7 \cdot m}{4}} . \end{aligned}$$

Therefore the wall shear stress follows as

$$|\bar{\tau}_w| \sim \rho \cdot \bar{u}^{\frac{7 \cdot m}{4}}(z) \cdot R^{\frac{7 \cdot m}{4} - \frac{1}{4}} \cdot z^{-\frac{7 \cdot m}{4}} \cdot \nu^{\frac{1}{4}} .$$

Prandtl and von Kármán introduced the hypothesis that $|\bar{\tau}_w|$ should be independent of the pipe radius R for a turbulent pipe flow, i.e. the exponent of R should vanish

$$\Rightarrow \quad \frac{7 \cdot m}{4} - \frac{1}{4} = 0 \quad \Rightarrow \quad m = \frac{1}{7} .$$

Substituting r back into the expression for the time-averaged velocity profile, we obtain the $(1/7)$ power law for turbulent pipe flow

$$\boxed{\bar{u}(r) = \bar{u}_{max} \cdot \left(1 - \frac{r}{R}\right)^{\frac{1}{7}}} . \quad (2.136)$$

For $m = (1/7)$ the average velocity \bar{u}_m is

$$\bar{u}_m = 0.816 \cdot \bar{u}_{max} .$$

The region of validity of this law is the same as that for the Blasius equation (2.133), $Re_D \leq 10^5$.

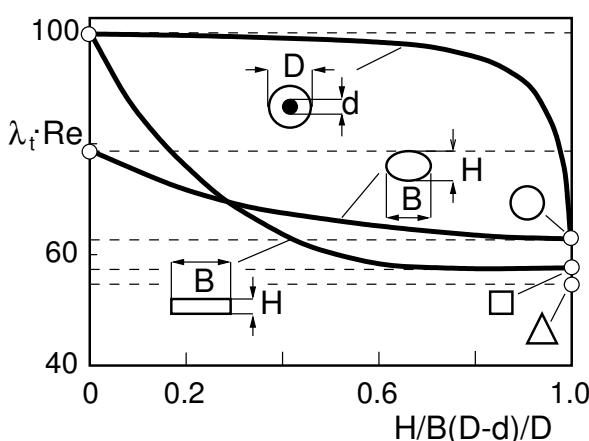


Fig. 2.83 : Pressure loss λ_t at different pipe cross-sections

Let us mention two unphysical disadvantages of this profile. At the pipe wall we obtain an infinitely steep increase in the velocity

$$\left. \frac{d\bar{u}}{dr} \right|_{r=R} \longrightarrow \infty .$$

However this is unimportant, since the law is not valid in the viscous sublayer.

At the center of the pipe there is a bend in the velocity profile and $(d\bar{u}/dr)(r = 0)$ is not defined.

The parabolic velocity profile of laminar pipe flows (2.129), as well as the time-averaged velocity profile of turbulent pipe flows (2.136) are compared in Figure 2.84 for equal volume fluxes \dot{V} .

All that remains to do is determine the thickness of the viscous sublayer Δ . Using the ansatz

$$|\tau_w| = \frac{1}{2} \cdot \rho \cdot \bar{u}_m^2 \cdot \frac{\lambda_t}{4} = \mu \cdot \left(\frac{d\bar{u}}{dz} \right)_w$$

we obtain a linear increase in the velocity from the value zero at the wall to the value $0.5 \cdot \bar{u}_m$ at $z = \Delta$, therefore

$$\left(\frac{d\bar{u}}{dz} \right)_w = \frac{\frac{1}{2} \cdot \bar{u}_m}{\Delta} \Rightarrow \mu \cdot \left(\frac{d\bar{u}}{dz} \right)_w = \nu \cdot \rho \cdot \frac{\frac{1}{2} \cdot \bar{u}_m}{\Delta} = \frac{1}{2} \cdot \rho \cdot \bar{u}_m^2 \cdot \frac{\lambda_t}{4} .$$

The thickness Δ of the viscous sublayer therefore follows as

$$\Delta = \frac{4 \cdot \nu}{\bar{u}_m \cdot \lambda_t} \Rightarrow \frac{\Delta}{D} = \frac{4}{\lambda_t} \cdot \frac{\nu}{\bar{u}_m \cdot D} = \frac{4}{Re_D \cdot \lambda_t} .$$

Taking the Blasius law (2.133) into account

$$\lambda_t = \frac{0.3164}{(Re_D)^{\frac{1}{4}}}$$

it follows that

$$\frac{\Delta}{D} = \frac{12.64}{(Re_D)^{\frac{3}{4}}} .$$

(2.137)

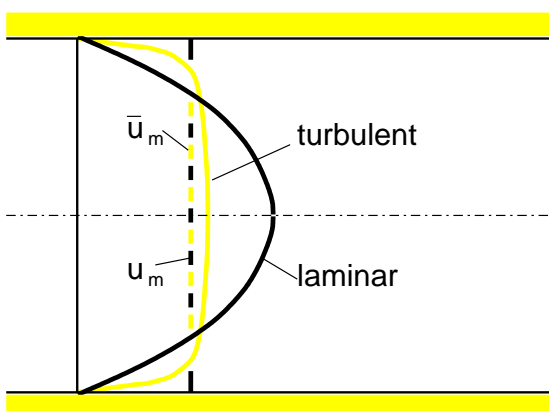


Fig. 2.84 : Velocity profiles for laminar and turbulent pipe flows

2.4.5 Flows Past Bodies

In problems involving flows past bodies, one of the most important phenomena is that of **flow separation**, which we met several times in previous sections. Depending on the size of the Reynolds number, flow separation can take place in a steady or unsteady manner.

Let us consider the flow past a **sphere**. The left-hand picture in Figure 2.85 shows laminar, steady flow separation at low Reynolds numbers. The separation of the boundary layer on a sphere leads to a region of backflow. Because of the acceleration downstream of the stagnation point, the pressure p on the surface of the sphere decreases greatly and takes on a constant value in the backflow region. Separation of a turbulent boundary layer takes place at larger Reynolds numbers much further downstream on the surface of the sphere. Because of the flow deceleration, the pressure p first increases again beyond the widest point of the sphere, to then take on a constant value in the turbulent backflow region.

The flow separation on a sphere can be made plausible with the following considerations. The separation of a flow from a wall occurs when the no-slip condition close to the wall causes the boundary layer fluid to decelerate and to be transported into the main flow region. If the pressure in the outer flow increases downstream, the slower fluid within the boundary layer

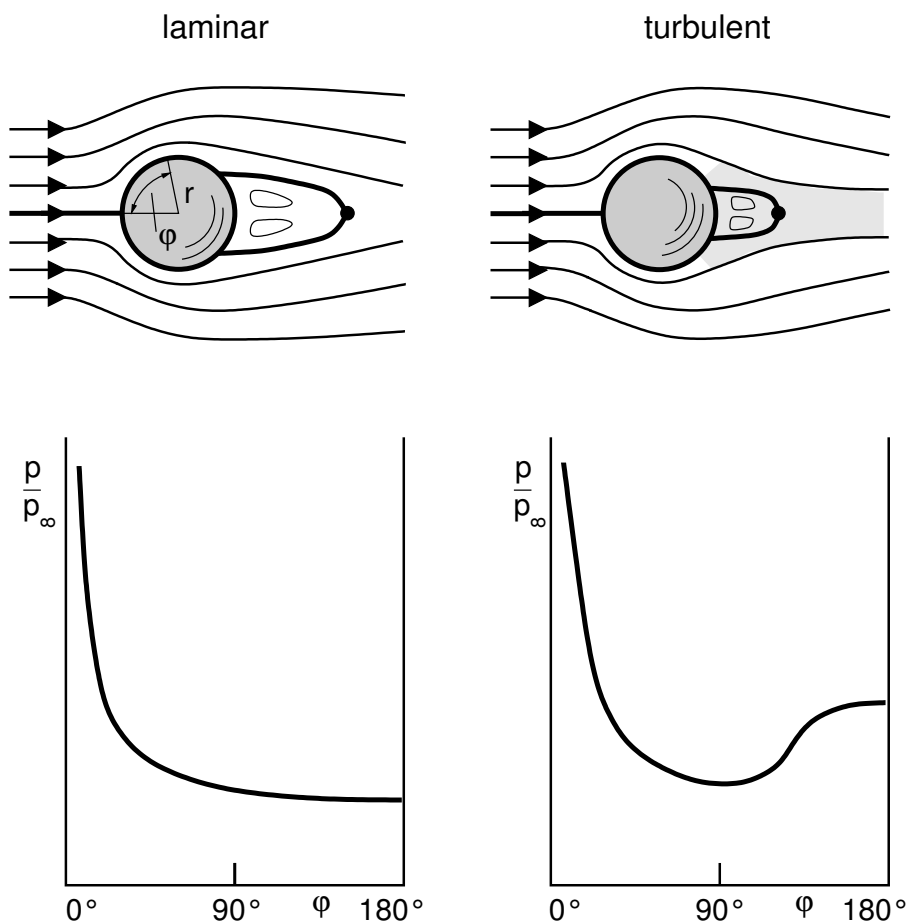


Fig. 2.85 : Separation and pressure distribution in the flow past a sphere

is no longer able, because of its lower kinetic energy, to flow downstream into the higher pressure region. Because the turbulent boundary layer flow has an additional longitudinal and transverse momentum exchange and so a higher kinetic energy, the turbulent boundary layer can remain attached to the surface of the sphere further downstream. The backflow region tapers off, as does the wake flow, so that the total drag c_w is considerably reduced.

In order to achieve a mathematical description of the **separation criterion**, we look at a two-dimensional laminar or turbulent boundary layer on, for example, a cylinder. Because of the no-slip condition at the wall $u = 0$ and $w = 0$ for $r = R$, with the radius of the cylinder R or $z = 0$, it follows from the Navier-Stokes equation in Cartesian coordinates (2.65) that

$$\boxed{\frac{1}{\rho} \cdot \frac{dp}{dx} = \nu \cdot \frac{\partial^2 u}{\partial z^2}} \quad . \quad (2.138)$$

Equation (2.138) and Figure 2.86 can be used to discuss the development of the boundary layer flow with the pressure gradient. If the pressure in the x direction decreases, i.e. if $\partial p / \partial x$ is negative, the flow outside the boundary layer is decelerated downstream. In this case $(\partial^2 u / \partial z^2) < 0$ too, and the curvature of the velocity profile $u(z)$ at the wall is negative. Because of the acceleration of the flow, the velocity at the edge of the boundary layer increases, with the result that $\partial u / \partial z$ increases with increasing x downstream. Because of $\tau_w = \mu \cdot (\partial u / \partial z) z = 0$, the wall shear stress τ_w then also increases with increasing x , so that $(\partial \tau_w / \partial x) > 0$.

If $(\partial p / \partial x) = 0$, equation (2.138) implies that $\partial^2 u / \partial z^2$ will also be zero at the wall, i.e. the velocity profile $u(z)$ has a turning point at the wall. The velocity at the edge of the boundary layer remains constant because there is no pressure gradient present. Inside the boundary layer however, the flow is decelerated by the friction forces present. This means that close to wall, the velocity gradient $\partial u / \partial z$ decreases with increasing x . This leads to a reduction of the wall shear stress τ_w in the x direction, with $(\partial \tau_w / \partial x) < 0$.

The flow separation from the contour of the body begins at the position where the upstream positive wall shear stress τ_w sinks so low that it assumes the value zero for the first time.

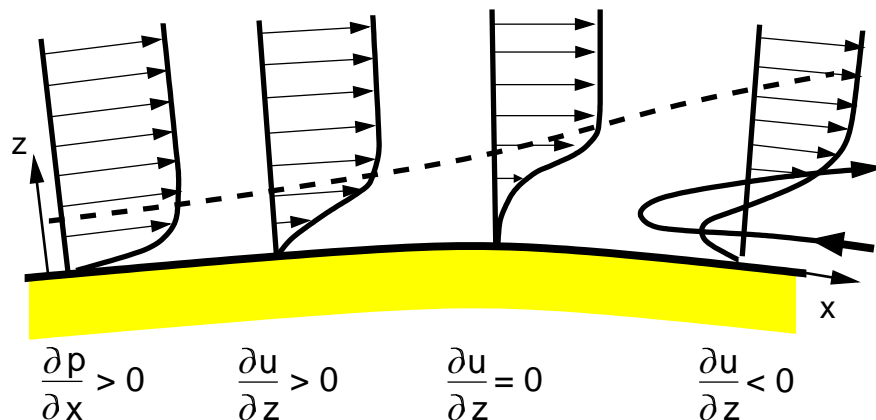


Fig. 2.86 : Boundary-layer separation

This is the criterion for the start of separation.

separation criterion : $\tau_w = 0$

(2.139)

Figure 2.86 shows the boundary layer separation for the case of a positive pressure gradient $(\partial p / \partial x) > 0$. A positive pressure gradient leads first of all to the flow outside the boundary layer being decelerated in the x direction. In the figure this is indicated in the way the velocity arrows at the edge of the boundary layer become ever shorter with increasing x .

Because $(\partial p / \partial x) > 0$, equation (2.138) implies that the curvature of the velocity profile at the wall must satisfy $(\partial^2 u / \partial z^2) > 0$. At greater distances from the wall, the curvature of the velocity profile $u(z)$ is always negative. Therefore, if the curvature at the wall is positive, with $(\partial^2 u / \partial z^2) > 0$, there must be at least one point inside the boundary layer where $(\partial^2 u / \partial z^2) = 0$. This point is a turning point of the velocity profile $u(z)$.

In contrast to the start of separation where the turning point is at the wall, the turning point moves inside the boundary layer downstream of the start of separation. Figure 2.85 demonstrates the consequences of a positive pressure gradient $(\partial p / \partial x) > 0$. In this case the boundary layer flow is not only decelerated by friction forces, but also by pressure forces, and the curvature at the wall is always positive. The wall shear stress τ_w decreases in the x direction, at separation begins at $\tau_w = 0$.

In the two-dimensional case this is equivalent to $(\partial u / \partial z) = 0$. Further downstream, the wall shear stress becomes negative. This implies a reversal of the flow direction close to the wall with $(\partial u / \partial z) < 0$ and hence backflow. The backflow leads to a recirculation region downstream of the separation point.

Now that we have worked out the separation criterion for two-dimensional boundary layer flow, let us return to the case of the flow past a sphere and discuss the Reynolds number dependence of the drag coefficient $c_w = c_w(Re_D)$, where D is the diameter of the sphere.

We start our discussion of the dependence of c_w on the Reynolds number for the case of Reynolds numbers $Re_D \leq 1$. In this case the friction forces are much greater than the inertial forces, and we speak of creeping flows, which can be described analytically. For the case of a **sphere** in a steady flow with $Re_D \leq 1$, the analytic solution of the Navier-Stokes equation

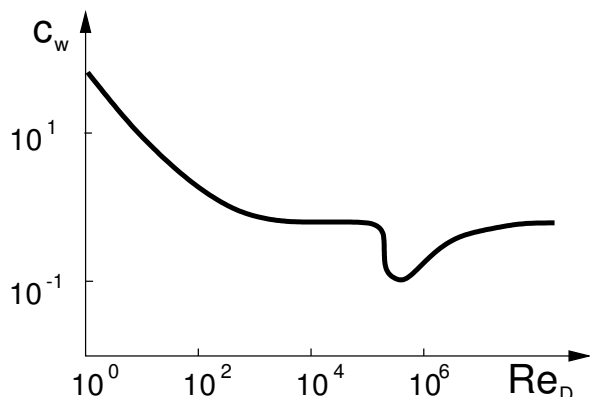


Fig. 2.87 : Dependence of the drag coefficient c_w of the sphere on the Reynolds number $Re_D = (u_\infty \cdot D) / \nu$

leads to a drag force W of

$$W = 6 \cdot \pi \cdot \mu \cdot \frac{D}{2} \cdot u_{\infty} \quad . \quad (2.140)$$

One third of this drag force W is due to the pressure gradient, and two thirds to the friction forces. We also note that for creeping flows, the drag force W is proportional to the first power of the velocity u_{∞} . Taking the definition of the c_w value into account, we can use equation (2.38) to write down a relation for $c_w = c_w(Re_D)$:

$$c_w = \frac{W}{\frac{1}{2} \cdot \rho \cdot u_{\infty}^2 \cdot \frac{\pi}{4} \cdot D^2} = \frac{24 \cdot \mu}{\rho \cdot u_{\infty} \cdot D} = \frac{24}{Re_D} \quad . \quad (2.141)$$

The relation $c_w = (24/Re_D)$ is also known as **Stokes drag law** and is valid in the Reynolds number region $Re_D \leq 1$. If the Reynolds number is increased to a value of $Re_D \approx 300$, steady separation takes place downstream. The fluid particles directly at the wall lose so much kinetic energy through the strong friction forces that they are unable to compensate the pressure increase in the rear half of the sphere. This leads to flow separation close to the equator of the sphere. A steady backflow region is found in the wake directly behind the sphere. In computing the steady wake flow the inertial terms can no longer be ignored, and the Navier-Stokes equations have to be solved.

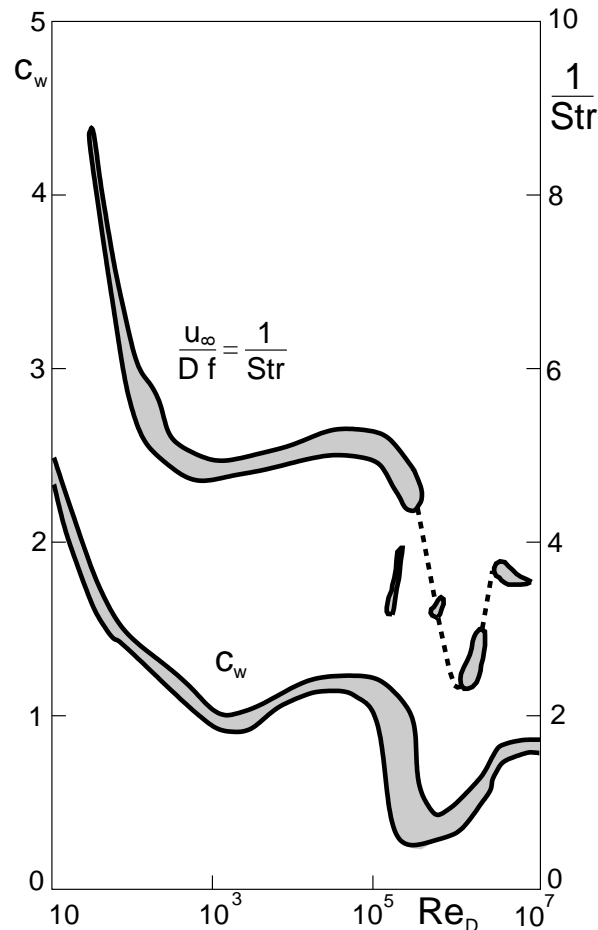
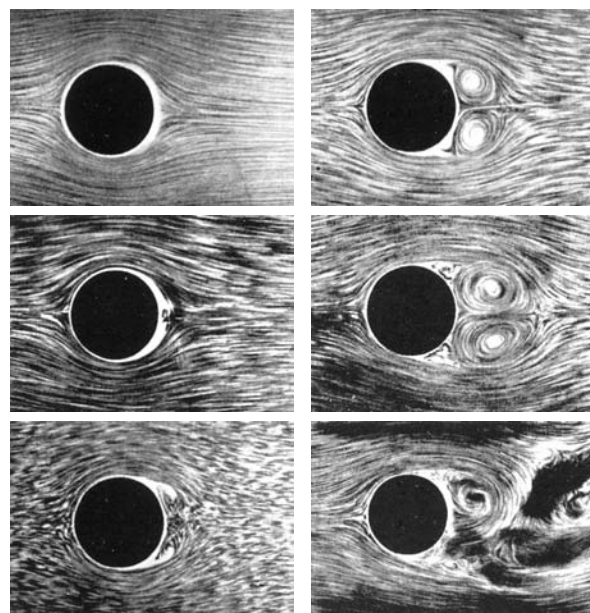


Fig. 2.88 : Drag coefficient c_w and reciprocal values of the dimensionless separation frequency $1/Str$ for the flow past a cylinder

A further increase in the Reynolds number to a value of $Re_D = 2000$ initially leads to the formation of unsteady vortex separation of the laminar boundary layer on the surface of the sphere with a laminar wake.

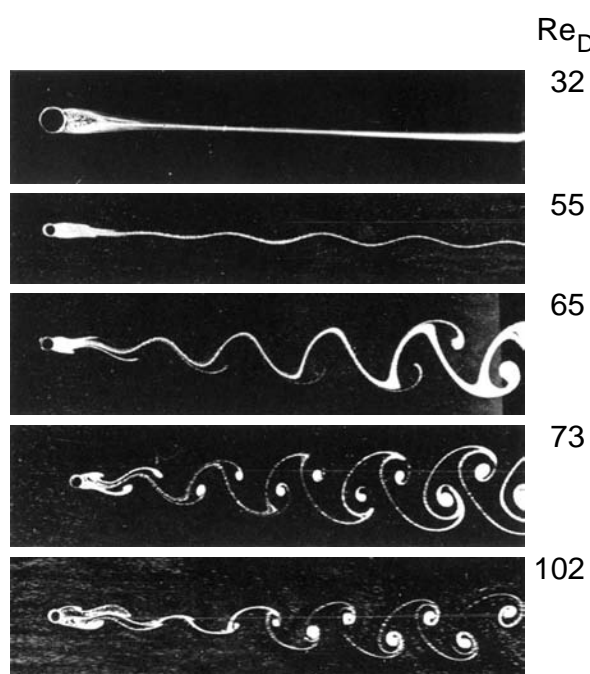
Above $Re_D = 2000$, to about $Re_D = 3 \cdot 10^5$, the transition to a turbulent wake flow takes place. In the Reynolds number region $3 \cdot 10^5 \leq Re_D \leq 4 \cdot 10^5$, the boundary layer flow on the sphere becomes turbulent. The separation region moves downstream on the surface of the sphere and the wake flow tapers off. This leads to a drastic reduction in the c_w value, as shown in Figure 2.87. The friction drag is larger in a turbulent boundary layer, i.e. the drop in the c_w value is due to a reduction in the pressure drag.

In the region $4 \cdot 10^5 \leq Re_D \leq 10^6$ the laminar-turbulent transition region moves forwards



PRANDTL 1927

Start-up of a cylinder from rest, intermediate states in the formation of the Kármán vortex street



HOMANN 1936

Constant flow past a cylinder

Fig. 2.89 : Steady flow past a cylinder and laminar Kármán vortex street

on the surface of the sphere, increasing the friction drag, while the pressure drag essentially remains constant. Again the c_w value increases. In the Reynolds number region $Re_D > 10^6$, the boundary layer on the surface of the sphere is turbulent downstream of the front stagnation point, fixing the separation point. This does not change for any further increase in Re_D , and so the c_w value of the sphere also becomes independent of Re_D .

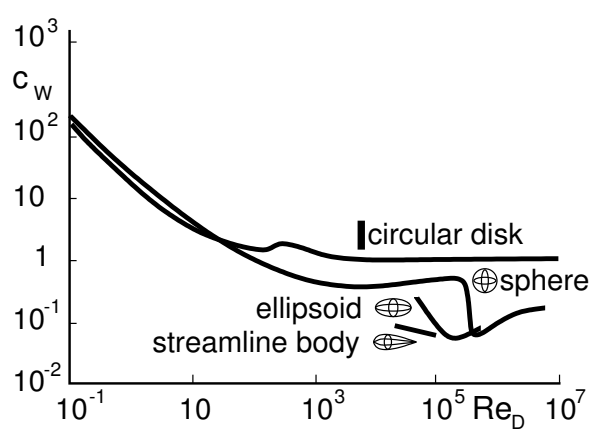
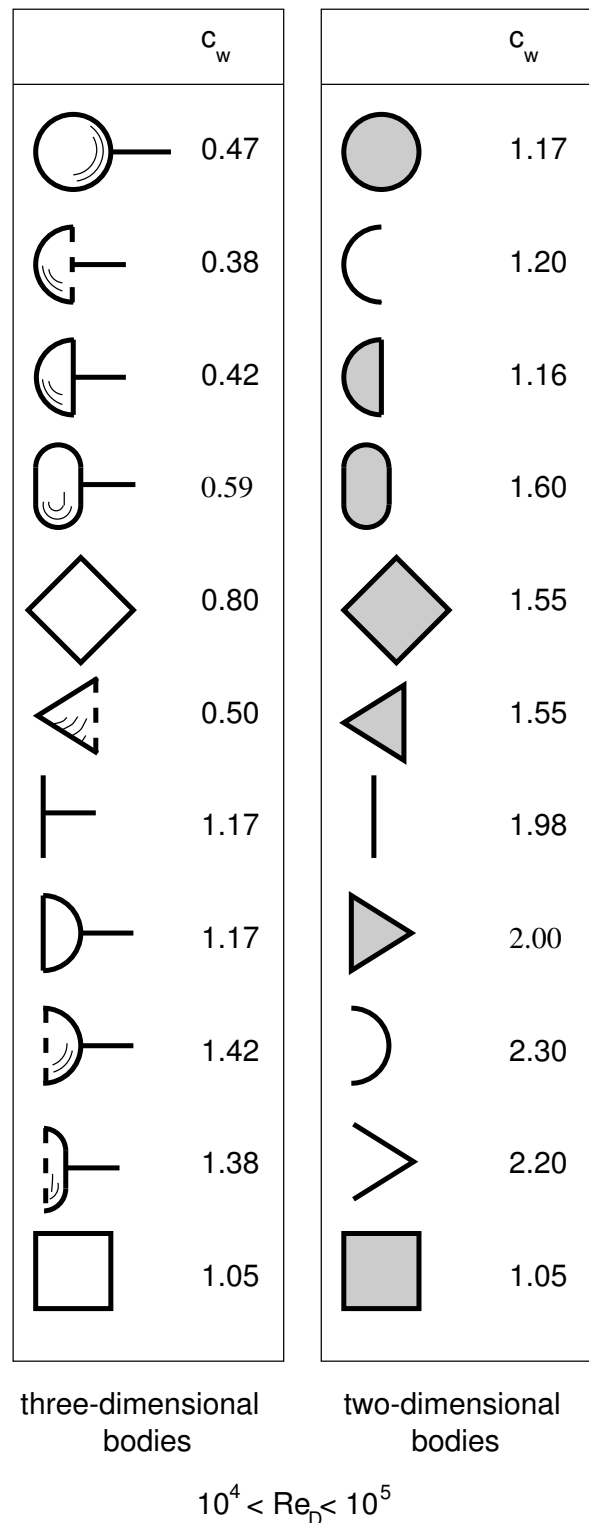


Fig. 2.90 : Drag coefficient c_w of blunt bodies

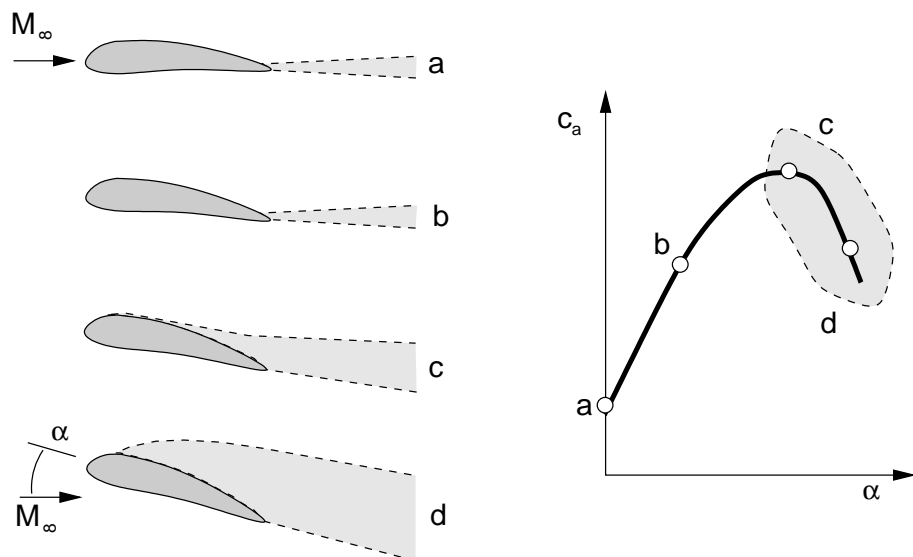


Fig. 2.91 : Flow separation at a wing profile

In the case of the **flow past a cylinder** the dependence of the drag coefficient c_w on the Reynolds number Re_D is equivalent. Figure 2.88 shows all known experimental values c_w with the measured reciprocal values of the dimensionless separation frequency $1/Str$. These are the values for the Kármán vortex street already described in Chapter 1.1. Figure 2.89 shows the flow past a cylinder for the steady flow separation region where $3 \leq Re_D < 40$

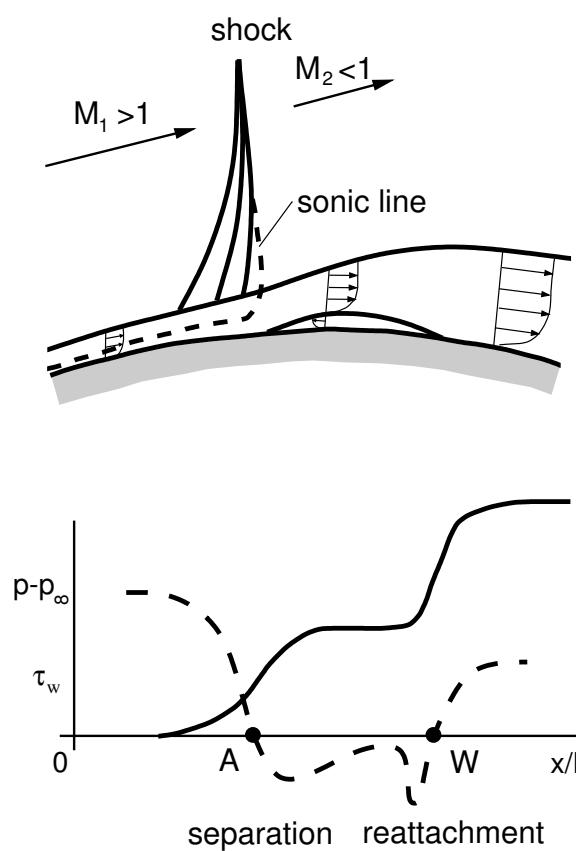


Fig. 2.92 : Shock induced separation on a transonic wing profile; pressure and wall shear stress distribution

and for the laminar Kármán vortex street region where $40 \leq Re_D \leq 200$.

The periodic vortex separation of the Kármán vortex street starts at the Reynolds number $Re_D = 40$. With increasing Reynolds number, $1/Str$ decreases greatly, taking on an almost constant value of $Str = 0.21$ for Reynolds numbers between 10^3 and 10^4 . After the transition to turbulent boundary layer flows on the cylinder, $1/Str$ drops greatly, corresponding to the drop in the drag coefficient c_w . For Reynolds numbers greater than 10^7 a constant separation frequency is found in the turbulent wake flow with constant c_w value.

The drag coefficient c_w in the Reynolds number region from 10^4 to 10^5 are shown in Figure 2.90 for different three-dimensional and two-dimensional body shapes, with the Reynolds number dependence for different axisymmetric bodies also shown.

Flow separation also takes place in the **flow past a wing** upstream of the trailing edge of the wing and in the shock wave region. Let us return to Figure 1.18 of the introductory Chapter 1.2 and discuss the effect of the angle of attack α of the wing. The left-hand side of Figure 2.91 shows a subsonic wing profile at four different angles of attack α for a free stream with Mach number M_∞ . The regions where the friction effect is large are shaded grey. Case (a) shows the wing profile with $\alpha = 0^\circ$. The diagram on the right is the lift coefficient c_a as a function of the angle of attack α . It can be seen that for $\alpha = 0^\circ$ the lift coefficient satisfies $c_a > 0$. As we have already discussed, this is a consequence of the profiling of the wing, which causes the fluid on the upper side of the wing to flow faster than on the lower side and thus generates a pressure difference. The friction effect mainly dominates in the boundary layer and in the wake of the wing. Directly behind the trailing edge of the wing a shear layer of the boundary layer forms above and below the wing, passing over to the wake flow downstream.

A slight increase in the angle of attack α , as in case (b), leads to a considerable increase in the lift coefficient c_a , without there being much effect on the wake, compared to case (a). In case (c), a further increase in the angle of attack leads to a maximum lift coefficient c_a for a certain angle α . However, here separation already occurs on the upper side of the profile, shown here as an extended shaded friction-dominated region downstream. A further increase of the angle of attack α leads to an expansion of the separation region downstream on the upper side of the wing, and thus to an increase of the lift coefficient. In the limiting case, separation will take place at the leading edge of the wing, and there is no lift at all.

In the case of the transonic wing, the supersonic region on the wing, as already seen in Figure 1.18 and Figure 2.58, is ended by a shock wave. This shock wave causes a pressure jump in the wing boundary layer, which again can lead to flow separation if the boundary layer fluid cannot overcome the pressure increase.

The conditions under which shock-boundary-layer interaction will lead to flow separation are shown in Figure 2.92. Velocity profiles in the boundary layer $\bar{u}(x, z)$, the sonic line $M = 1$, the pressure distribution p and the wall shear stress $\bar{\tau}_w$ are shown. In the supersonic region in front of the shock wave, a supersonic flow already occurs inside the turbulent boundary layer. Below the dashed sonic line is a region where perturbations may spread out upstream. It is also shown how the shock wave fans out into different weaker compression regions due to the effect of the boundary layer. Behind the shock, the pressure in the turbulent boundary layer becomes so large that the wall shear stress $\bar{\tau}_w$ tends to zero. At this point separation

on the wing profile begins.

Further downstream both the wall shear stress and velocity take on negative values. Close to the wall backflow occurs, as shown in the middle velocity profile of the three shown in Figure 2.92. In the separation and backflow regions, the pressure is considerably greater than that without separation. This has an effect on the lift and the drag. Whereas the drag increases, the lift decreases. Because of the further acceleration of the flow on the profile and the dying away of the pressure increase in the turbulent boundary layer due to the shock wave, the flow reattaches again after a certain distance. At this point the wall shear stress again becomes zero, and takes on positive values further downstream. Therefore a bounded separation region forms on the wing. Again the expansion of the separation region is of interest, since this affects the global flow field, i.e. the outer flow. Similarity considerations for the length l of the separation region in the flow direction lead to the result that larger Reynolds numbers lower the length l , while higher Mach numbers increase l .

Having now looked at the flow separation on a wing, we now return to the same phenomenon in the incompressible **flow past an automobile**. Whereas flow separation on the wing must be avoided in order to retain the lift, it is an essential component in the reduction of drag in the flow past an automobile. We have already got a first impression of the separation regimes in the flow past a vehicle in the introductory Chapter 1.2 in Figure 1.20.

For the case of an automobile with notchback, let us compute the flow separation on the rear window and on the edge of the trunk cover. We are now immediately able to understand the flow behavior with one look at Figure 1.21. This shows the qualitative pressure distribution on the contour of a notchback vehicle. Positive pressure differences are seen in the regions in danger of separation mentioned above. Those regions, denoted with an \oplus sign, are simply the regions where a positive pressure gradient $\partial p / \partial x$ is present, which, as we now know, leads to flow separation and backflow.

The separated boundary layer on the back of the automobile in Figure 1.22 generates a part of the wake flow of the vehicle as a free shear layer after passing the edge of the trunk cover. In these regions there is a point of departure to influence the flow deliberately in order to reduce the drag. The aim is to remove the shear layer behind the spoiler resulting from separation, and so to restrict the formation of a certain region of the wake flow which contributes greatly to the drag on the vehicle.

Flow separation can also occur in pipes and diffusers. Starting out with the previous Chapter 2.4.4, we consider the flow separation in the supply pipes. The flow separation here also causes additional losses. We consider the **elbow bend** in Figure 2.93, which steers a vertical flow to a horizontal flow. We assume a steady fully-formed pipe flow in the straight vertical piece of the pipe, in which a driving pressure gradient is present in the flow direction, and constant pressure in the radial direction transverse to the flow.

The Bernoulli equation for curved stream filaments leads us to the statement that the pressure increases in the radial direction in order to keep the centrifugal force in equilibrium. A pressure gradient is formed transverse to the flow direction, leading to a pressure increase at the outer wall and a pressure decrease at the inner wall of the elbow bend. This works

against the pressure drop along the streamline coordinate s of the outer wall and boosts it at the inner wall. The streamline coordinate s denotes the arc length of a stream filament and is read positive downstream.

In the previous examples we have already seen many times that a pressure increase in the flow direction leads to flow separation. Therefore separation will first occur at the outer wall at position A . At the exit from the elbow bend, the pressure again levels out transverse to the flow direction. The pressure at the inner wall increases and that at the outer wall drops again. This leads to reattachment of the flow A_w at the outer wall, and to the start of flow separation at the point B at the inner wall. At the inner wall, the flow will again reattach with increasing arc length s some distance after passing the elbow bend in the straight horizontal pipe section B_w . Again a negative pressure gradient $\partial p / \partial s$ is present here, keeping the friction forces in equilibrium. The pressure transverse to the flow direction is again constant in this straight section of the pipe.

It can be seen in Figure 2.93 that, downstream of the separation points A and B at both the outer and inner walls, recirculation regions form, which cause additional energy losses in the flow. The lower picture in Figure 2.93 shows the pressure in the pipe for two streamlines in the outer and inner wall regions along the streamline coordinate s . The inclined straight line shows the linear pressure drop in a straight pipe section. Even if there is no separation, the energy losses in the flow due to the friction yield a pressure loss in the flow direction.

Above the straight line, the thick curve shows the pressure of a streamline at the outer wall which would be found without separation. Below the straight line is the corresponding curve for a streamline at the inner wall. The separation at both point A and point B takes place

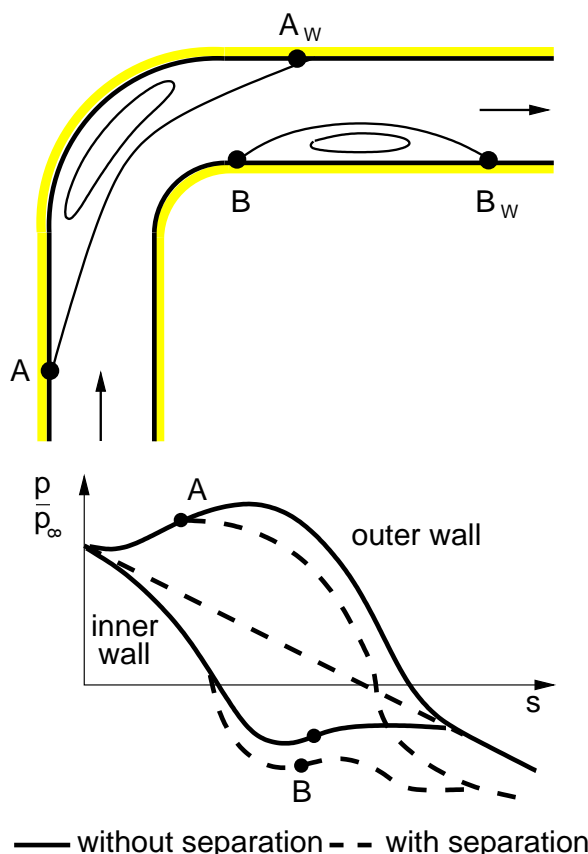


Fig. 2.93 : Flow separation in an elbow bend

in a region of increasing pressure. The additional flow loss caused by separation is seen in the way that the dashed pressure curves at the outer and inner walls of the elbow bend lie below the curves without separation.

As well as the flow separation, a secondary flow also occurs in the elbow bend. This is superimposed onto the main flow in the direction of the streamline coordinate s and causes considerable velocity components perpendicular to the main flow. The origin of this secondary flow is the curvature of the pipe, as well as the deceleration of the flow from friction forces at the wall. The velocity at the inner side of the elbow bend is greater than that at the outer side. The fluid close to the wall has, because of the friction, a lower velocity than that in the center of the bend. The centrifugal forces which are larger in the center of the bend than at the side walls cause an outward motion. However, for reasons of continuity, this is only possible if a motion in the opposite direction takes place at the walls of the bend. Therefore a double vortex forms and is superimposed onto the main flow. The secondary vortices also lead to flow losses, so that we can divide the losses in an elbow bend into the following three components: **friction losses** and **separation losses** due to the curvature, and losses due to **secondary flows**.

3 Software and Applications

It is not only in fluid mechanics that the field of activity of engineers has seen considerable changes due to the increased use of computers and networks. As well as having the analytic abilities needed to solve fluid mechanical problems, the engineer is increasingly required to be able to handle fluid mechanical software in practical applications in industry. In order to promote this development, we have supplied tutorial software in conjunction with this textbook, to ease the introduction to the use of commercial fluid mechanical software. It is essential for future engineers to be able to work with fluid mechanical software comfortably and independently.

Fluid mechanical software accompanying the lectures is available on the internet, via the homepage of the Institute for Fluid Mechanics at the University of Karlsruhe. Interaction between students and teaching assistants is encouraged via email and by means of internet consultation.

<http://www-isl.mach.uni-karlsruhe.de>

3.1 Fluid Mechanical Software

The software accompanying the textbook concerning the **fundamentals of fluid mechanics** discussed in Chapter 2 is available in the software module

KAPPA-Stromfaden http://www-isl.mach.uni-karlsruhe.de/stromfaden.html
--

Here the algebraic equations of the one-dimensional stream filament theory presented in Chapters 2.3.2 and 2.3.3, as well as the two-dimensional Navier-Stokes equation for viscous flow, are solved iteratively for given examples. Examples of application are the flow past an automobile and a wing, as well as the unsteady flow out of a container (incompressible) and the flow through a nozzle (compressible).

After calling up the page <http://www-isl.mach.uni-karlsruhe.de/stromfaden.html> or else clicking on **KAPPA-Stromfaden**, the menu shown on the next page appears:

KAPPA-Stream-Filament

- incompressible compressible
- inviscid viscous
- steady unsteady

automobile: upper side lower side

wing: upper side lower side

nozzle: nozzle flow

exhaust:

free stream velocity in km/h (automobile),

back pressure / reservoir pressure ratio (nozzle):

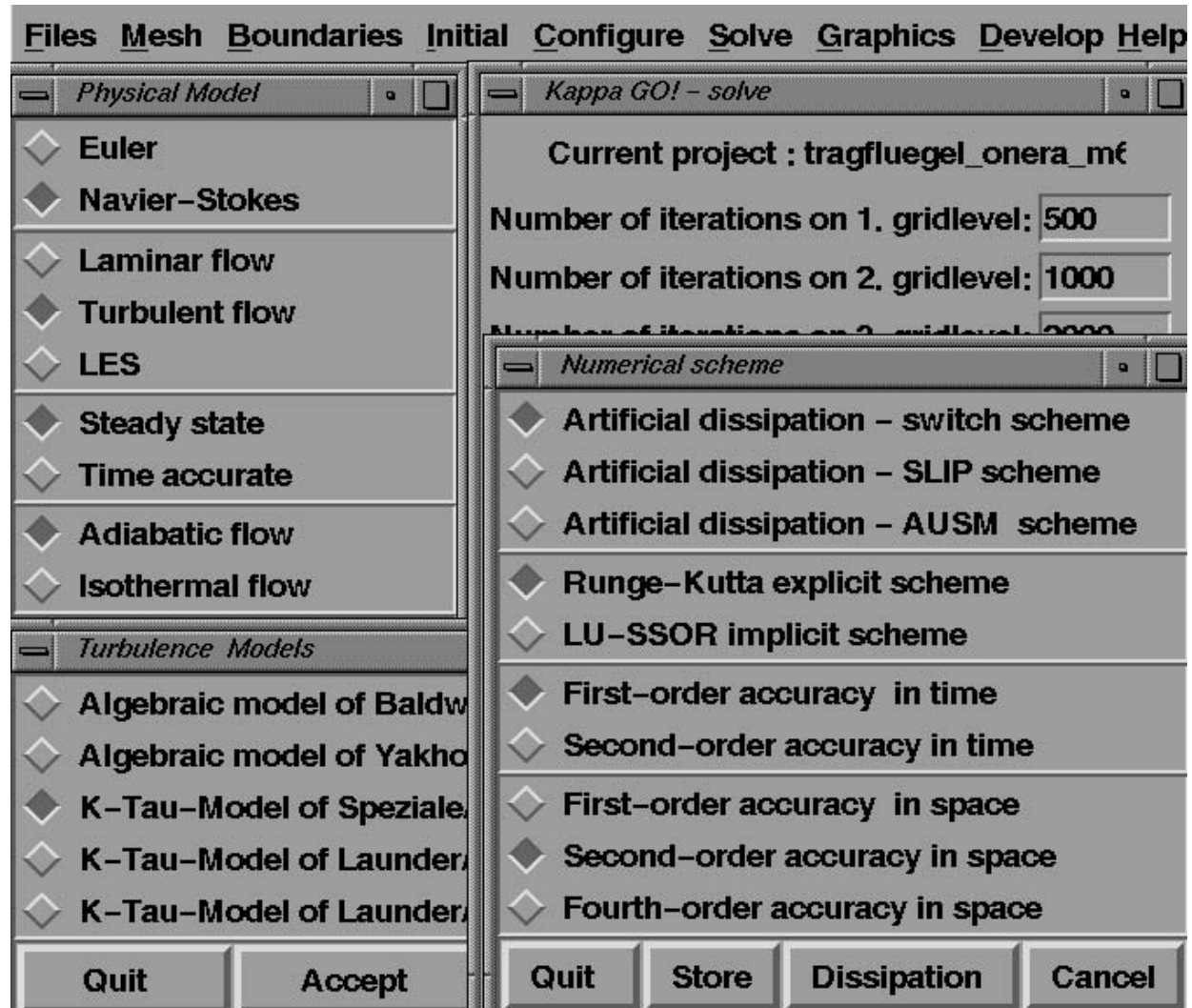
By clicking on the options offered, the steady, compressible, inviscid flow through a Laval nozzle, for example, can be computed. The results are obtained in the form of pressure and Mach number distributions, $p(x)$ and $M(x)$, along the axis of the nozzle for a selected pressure ratio of the pressure p_A at the exit of the nozzle, to the reservoir pressure p_0 in the container to which the nozzle is connected. Therefore KAPPA-Stromfaden permits us to study the effect of the pressure ratio on the characteristic flow form in the nozzle.

For example, it is seen that for a pressure ratio of $(p_A/p_0) = 0.98$ a pure supersonic flow exists everywhere in the nozzle, with a maximum Mach number at the narrowest cross-section of $M_{max} \approx 0.37$. If the pressure ratio is reduced to $(p_A/p_0) = 0.9$, for example, a normal shock wave occurs downstream of the narrowest cross-section. This is seen in a discontinuous drop in the Mach number from $M > 1$ to $M < 1$. For a small pressure ratio of, for example, $(p_A/p_0) = 0.1$, a continuously accelerated flow in the Laval nozzle is ultimately obtained. In this case the Mach number along the axis of the nozzle increases by a factor of 10 from an initial value of $M \approx 0.22$ to about $M \approx 2.2$.

The KAPPA-Stromfaden software can be used to carry out the **preliminary design** in product development, as introduced in Chapter 1.3. Supplementary fluid mechanical software is available for the **calculation** of the preliminary design, whereby the mathematical basics necessary for this are not treated in this textbook. To this end we recommend the more extensive texts: H.OERTEL, M.BÖHLE, Strömungsmechanik, 1999 and H.OERTEL, E.LAURIEN, Numerische Strömungsmechanik, 2002. The university-developed software package **KAPPA** (**K**arlsruhe **P**arallel **A**erodynamics) and the commercial

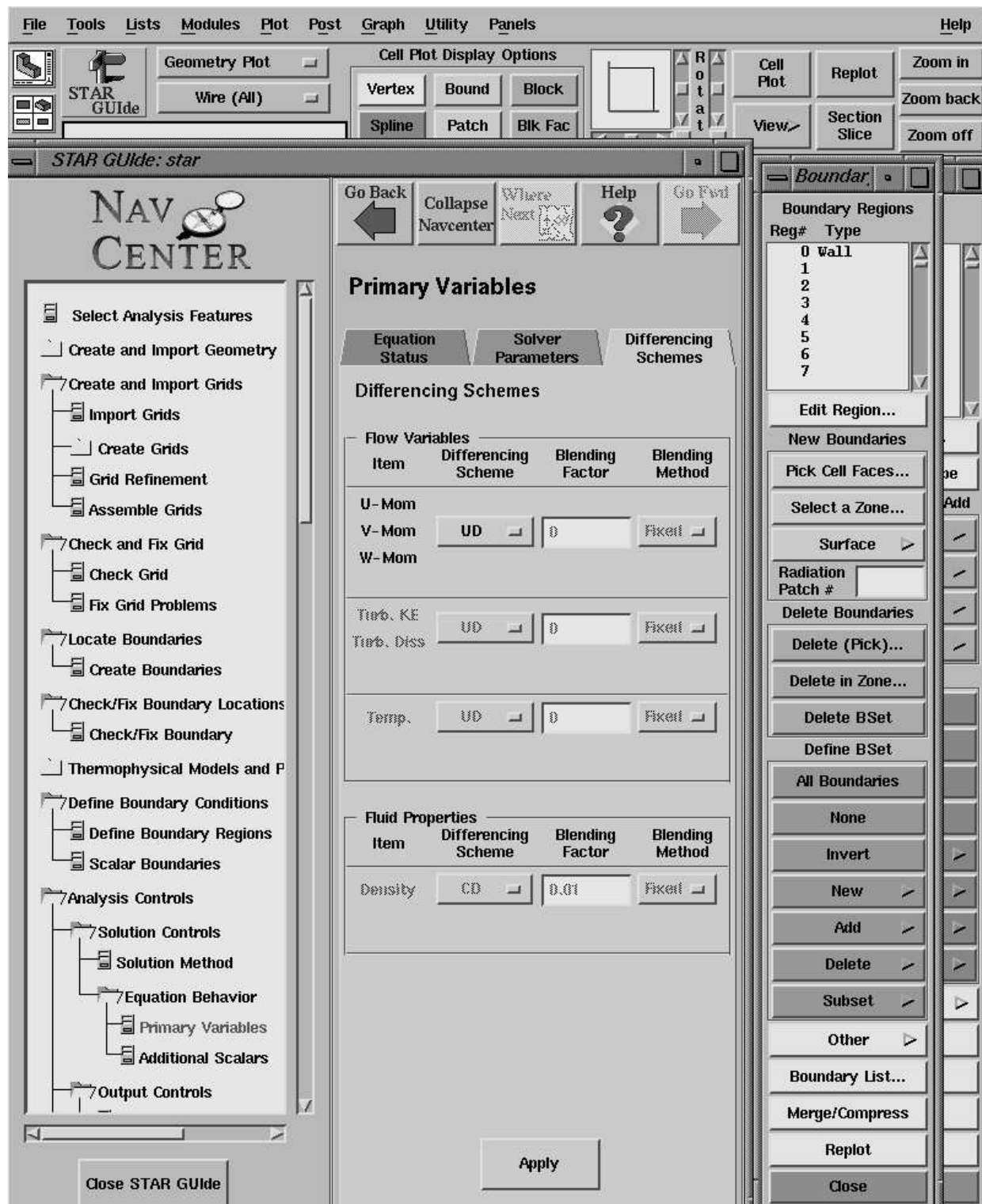
software **STAR-CD** can be used for calculation, and both are available through the Institute of Fluid Mechanics. Within the framework of product development, these packages can be used to compute laminar and turbulent, incompressible and compressible, steady and unsteady, three-dimensional flows for given product geometries.

After calling up <http://www-isl.mach.uni-karlsruhe.de/skappa.html>, and downloading, the following menu appears:



In order to use the software package, more than just the textbook is needed. The internet instructions given by the teaching assistants can also be studied independently with the training course in the following chapter.

Downloading the page <http://www-isl.mach.uni-karlsruhe.de/star-cd.html> causes the following menu from the commercial software package STAR-CD to appear. A license is needed to use this software, and this license also includes training in the use of the software package.



The fluid mechanical software packages mentioned above can be used to compute the flow examples described in Chapters 3.2 and 3.3.

3.2 Training Course

Now that we have already got to know some examples of stream filament theory software, we continue with the introduction to the **software** for the solution of fluid mechanical problems in **industrial projects**. Accompanying the introductory course, taught at the University of Karlsruhe (TH) as a practical training course in numerical fluid mechanics, we recommend our more extensive textbook H.OERTEL, E.LAURIEN 2002. The **introductory course** is structured so that it can also be studied via the internet. At the end of the introductory course, the student will be able to use the **KAPPA** software package independently to compute the flow past a transonic wing.

The introductory course is to be found at the address

<http://www-isl.mach.uni-karlsruhe.de/seinfuehrung.html>

Now that the first numerical computation with the software package KAPPA has been successfully carried out under the guidance of the teaching assistants, the **training course** for higher-semester students follows. This is an introduction to the application to industrial projects. In the practical application of fluid mechanical software, the first thing learned is that the computational grid and the model used (e.g. turbulence model), as well as the boundary conditions for each class of geometries, have to be set up from scratch, or else newly adapted. This first phase of the adaptation of the software is called the **verification**.

steady flows past bodies	steady flows through channels
laminar plate boundary layer	laminar pipe flow
turbulent plate boundary layer (turbulence models)	turbulent pipe flow (turbulence models)
transonic foil (RAE 2822)	backward-facing step (turbulence models)
transonic wing (ONERA M6)	
unsteady flows past bodies	unsteady flows through channels
Rayleigh-Stokes problem	
laminar Kármán vortex street	shock tube
turbulent Kármán vortex street (turbulence models)	

flows past bodies

flows through channels

Fig. 3.1 : Test verification cases for steady and unsteady flows

It requires highly developed engineering skills and is generally only possible under expert guidance. In what follows we present some helpful points in the training course, which is to be found at the address

<http://www-isl.mach.uni-karlsruhe.de/sverifikation.html>

and can be used independently, as long as software licenses are available on the computer used.

Before we start computing an actual industrial project, let us run the software package through the test cases in Figure 3.1. Here it first has to be determined whether the problem concerns a flow past a body or a flow through channels. There are then further subdivisions into steady and unsteady test cases.

Steady Flows Past Bodies

Laminar Plate Boundary Layer

The laminar plate boundary layer is a frequently used test case for spatial discretization in fluid mechanical software. In this case, a plate of length L at room temperature $T_\infty = 293K$ is placed in a flow with Reynolds number $Re_L = 1105$.

We compare the numerical results with the analytical Blasius solution:

$$c_f(x) = \frac{0.664}{\sqrt{Re(x)}} .$$

$Re(x) = \rho \cdot u_\infty \cdot x / \mu$ is the local Reynolds number formed with the length x . Figure 3.2 shows the dimensionless wall shear stress

$$c_f = \frac{\tau_w}{\frac{1}{2} \rho u_\infty} .$$

For all discretization schemes tested, the numerical results agree very well with the analytical Blasius boundary layer solution.

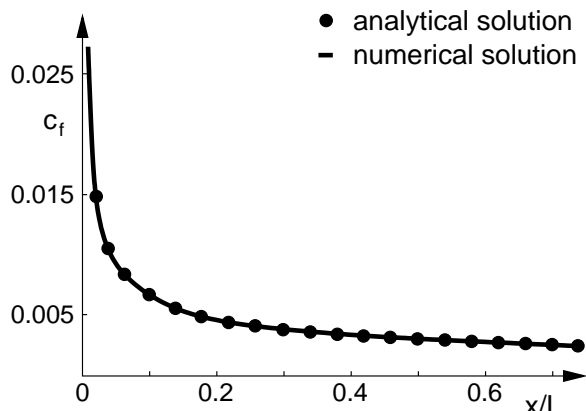


Fig. 3.2 : Local friction coefficient of the laminar plate boundary layer, $Re_L = 1105$

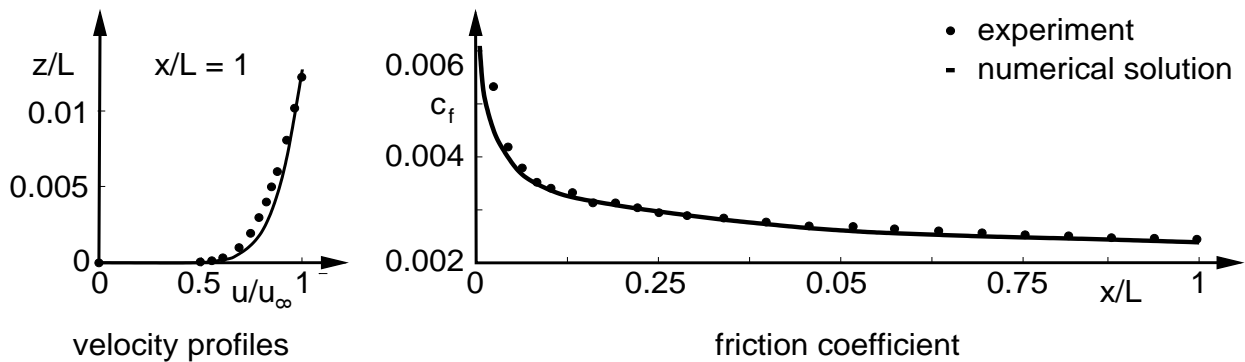


Fig. 3.3 : Turbulent plate boundary layer, $Re_L = 2 \cdot 10^6$

Turbulent Plate Boundary Layer

The two-dimensional, turbulent plate boundary layer without pressure gradient is an important example of adapting turbulence models. A fine enough computational grid can be used to keep the effect of the discretization error on the numerical solution very small. To compute the numerical results an experiment is used. Here the Reynolds number is $Re_L = 2 \cdot 10^6$. The plate with the length L is in a flow with Mach number $M_\infty = 0.1$ and the temperature of the free flow is $T_\infty = 293K$. The intensity of turbulence in the free stream is given as $Tu_\infty = 0.5\%$. The transition is fixed with a Reynolds number formed with the momentum thickness of $Re_\delta = 770$. The mean velocity profile at the position x/L and the total friction coefficient along the plate are compared with experimental data for these parameters.

Figure 3.3 shows the computed and measured time-averaged velocity profile friction coefficients. It can be seen that the given turbulence model computes the boundary layer to be too full. The effect of the friction coefficients however is small, and there is good agreement of the computed total friction coefficients with the experimentally determined values.

Transonic Foil

The transonic foil RAE2822 is a test case for a compressible flow past a body. The foil is in a flow with Mach number $M_\infty = 0.73$, Reynolds number $Re_L = 6.5 \cdot 10^6$ and at an angle of attack $\alpha = 3.19^\circ$, and a temperature of $T_\infty = 300K$. The transition is fixed at $x/L = 0.05$.

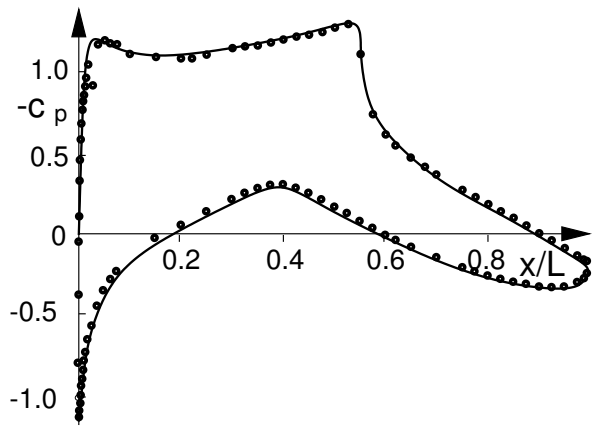


Fig. 3.4 : Pressure coefficient of flow past a foil (RAE 2822), $Re_L = 6.5 \cdot 10^6$, $M_\infty = 0.73$

The intensity of turbulence in the free stream is $Tu_\infty = 0.3\%$. The turbulence length scale is estimated via the molecular viscosity and the Prandtl mixing length ansatz as

$$l_{turb} \sim \frac{\mu}{\rho \sqrt{k_\infty}} \quad \text{with} \quad k_\infty = Tu_\infty \cdot u_\infty .$$

The distribution of the pressure coefficient c_p over the length x/L , as found in the numerical computation, is compared to the experimental data in Figure 3.4. The pressure distribution and the computed shock wave position agree. The lift coefficient is also found to be in agreement with experiment with $c_a = 0.795$, and the drag coefficient is $c_w = 1.7 \cdot 10^{-2}$.

Transonic Wing

The steady, three-dimensional transonic flow past a wing can be used to check the quality of the software package to compute compressible, three-dimensional flows past bodies with shock waves. The test wing used is the ONERA M6 wing.

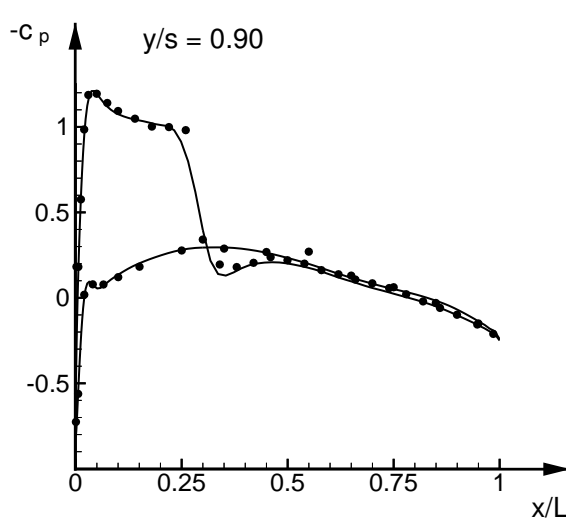
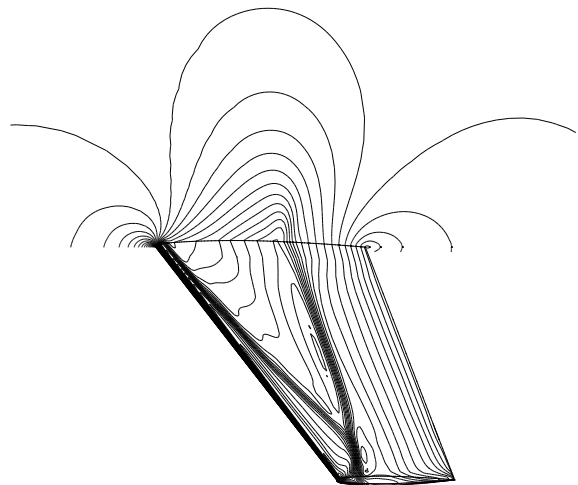
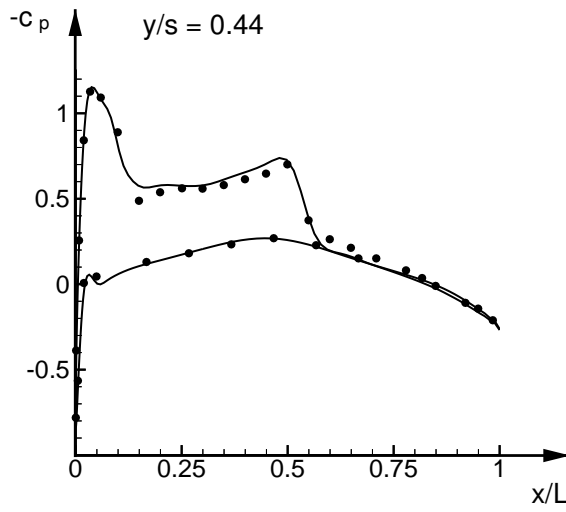


Fig. 3.5 : Pressure coefficient, flow past a wing (ONERA M6), $Re_L = 1.17 \cdot 10^7$, $M_\infty = 0.84$

A double shock wave occurs on the suction side when the wing is placed in a flow with $M_\infty = 0.84$. This moves towards the point of the wing and forms one shock wave. This shock wave branching makes this wing a particularly critical test case. The Reynolds number of the unperturbed free stream is $Re_L = 1.17 \cdot 10^7$ and the temperature of the flow is $T_\infty = 300K$. The wing is placed at an angle $\alpha = 3.06^\circ$ to the flow. The flow is assumed to be adiabatic and turbulent for the computation, i.e. the transition is fixed in the free stream. The turbulent kinetic energy is given by $Tu_\infty = 0.3\%$. The numerical solution is evaluated by comparison with experimental data in various cross-sections of the wing along its span.

Figure 3.5 shows the double shock on the wave as the closely-spaced isobars on the surface. These two shock waves join together towards the point of the wing. The computed pressure distributions along the span s of the wing agree well with the experimental data. The positions of the shock waves on the wing and the branching of the shock, as well as the suction peak along the leading edge, are all in agreement with measurements, in as much as a shock-adapted fine grid can be chosen in the shock wave regime. The computed lift and drag coefficients are $c_a = 0.138$ and $c_w = 7.98 \cdot 10^{-3}$ respectively.

Rayleigh-Stokes Problem

In order to verify the time precision of unsteady laminar flows, we will use the example of the **first Stokes problem** for a flat plate. Consider a flat plate at rest in the (x, y) plane, above which, in the z direction normal to the wall, is a viscous fluid at rest. At the time $t = 0$ the plate is set instantaneously into motion at the constant velocity U_∞ . The effect of friction causes the fluid above the plate to be set into motion, and this fluid forms an unsteady boundary layer. The flow is now computed for the Mach number $M_\infty = 0.1$. The velocity profiles are similar at different times. Figure 3.6 shows the computed velocity profiles drawn against the dimensionless coordinate η . This is the same as the results of the analytical solution for the Rayleigh-Stokes problem, and so is a proof of both the time precision of the numerical solution and the spatial discretization.

Laminar Kármán Vortex Street

A further indication of the time precision of the software is the example of the Kármán vortex street found at the plane flow past a cylinder at super-critical Reynolds numbers. The laminar Kármán vortex street is computed at the Reynolds number $Re_D = 500$. The

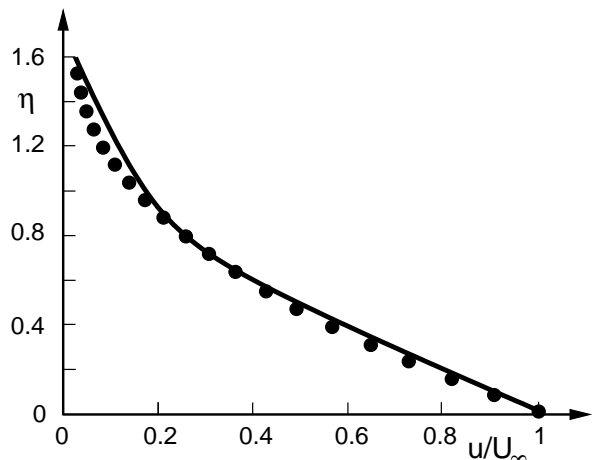


Fig. 3.6 : Velocity profile of the unsteady plate boundary layer

test quantity chosen is the dimensionless frequency of separation, the Strouhal number $Str = fD/u_\infty$. The computed Strouhal number is $Str = 0.209$, compared to that found by experiment $Str = 0.21$. There is also proof of the time precision of the software in this unsteady test case. Figure 3.7 shows the (computed) snapshot of the pressure distribution in the wake of the plane cylinder.

Turbulent Kármán Vortex Street

Another test case is that of the turbulent Kármán vortex street, with which the turbulence model for unsteady flow can be chosen. The numerical calculation is carried out using a Reynolds number of $Re_D = 1.4 \cdot 10^4$ (Fig. 3.8). The computed Strouhal number of $Str = 0.206$ is slightly above the experimental value of $Str = 0.2$. Here again it is seen that the

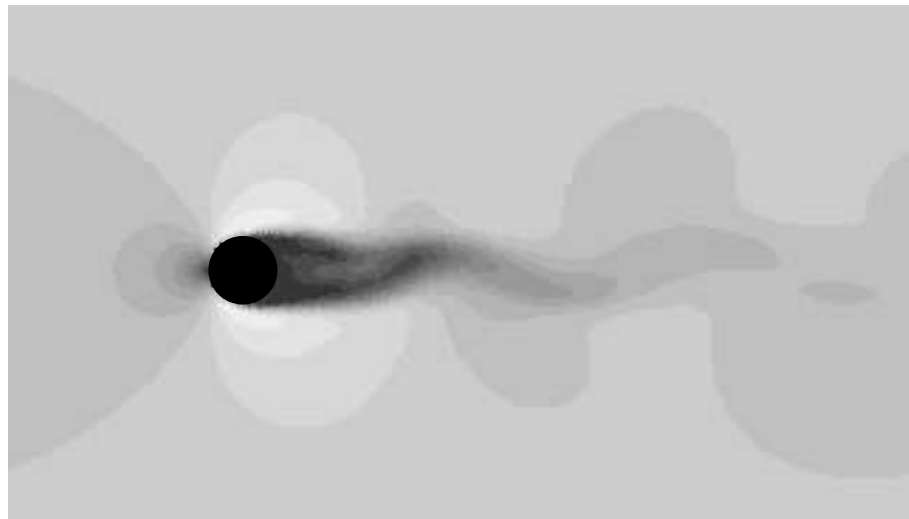


Fig. 3.7 : Snapshot of the velocity distribution of the laminar Kármán vortex street, $Re_D = 500$

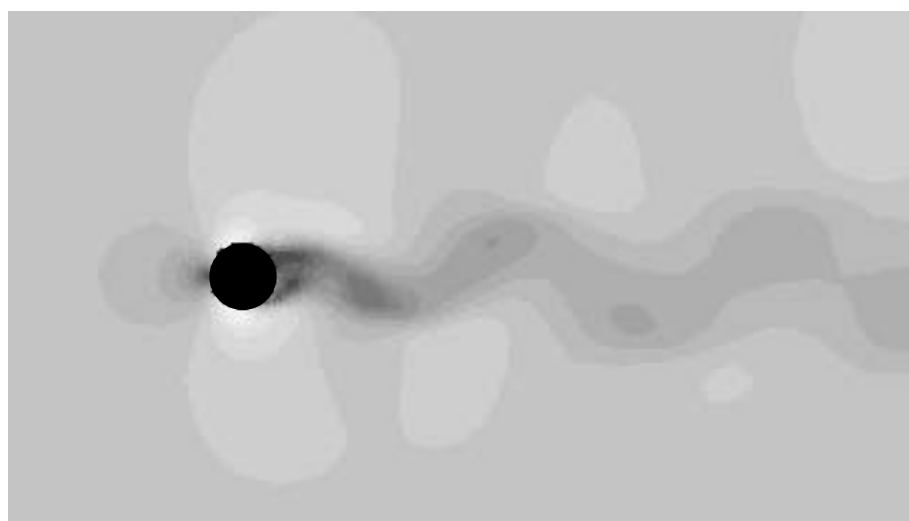


Fig. 3.8 : Snapshot of the velocity distribution of the turbulent Kármán vortex street, $Re_D = 1.4 \cdot 10^4$

turbulence models available in the software are adequate.

Flows Through Channels

Laminar Pipe Flow

Here we consider the laminar flow in a pipe with length $L/D = 50$ and diameter D as a test case. The pipe is hydraulically smooth. For the Reynolds number, formed with the mean velocity and the diameter of the pipe, we choose a value of $Re_D = 660$, while the temperature is $T_\infty = 293 \text{ K}$. The numerical solution is compared with the analytical solution for Hagen-Poiseuille flow. The computed velocity profile shown in Fig. 3.9 fits the parabolic profile of the analytical solution.

Turbulent Pipe Flow

Turbulent pipe flow can again be used to select the turbulence model for flows through channels. As in the case of laminar flow, the hydraulically smooth pipe with a length $L/D = 50$ is computed. The Reynolds number is $Re_D = 1 \cdot 10^5$ and the temperature $T_\infty = 293 \text{ K}$, with an intensity of turbulence of $Tu_\infty = 0.01$ used. Figure 3.10 shows a comparison of the numerical solutions with Prandtl's logarithmic wall law. The variation from the analytical solution is minimal, indicating that turbulence models which use a logarithmic wall law are adequate for pipe flow.

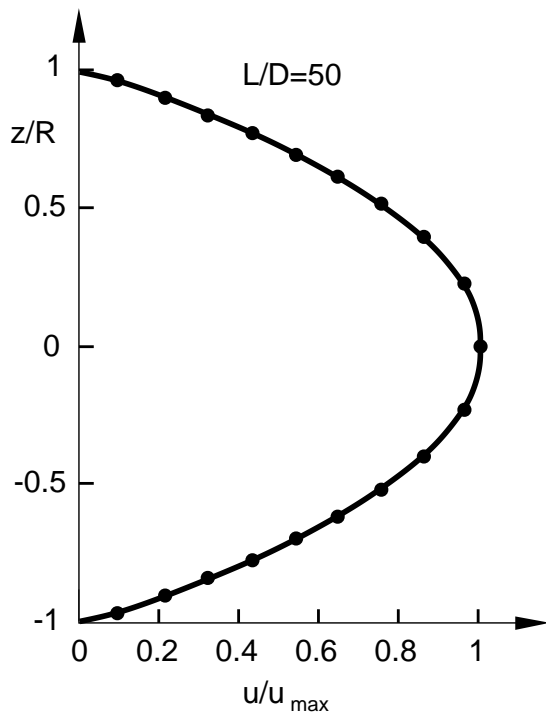


Fig. 3.9 : Velocity profile of laminar pipe flow $Re_D = 660$

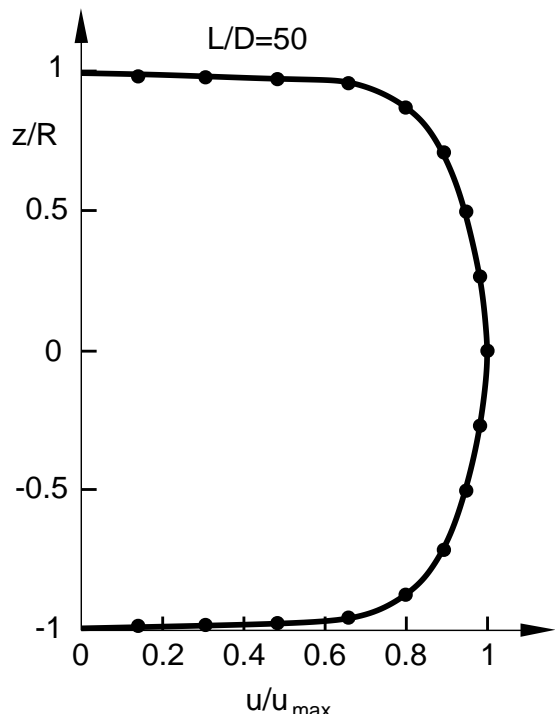


Fig. 3.10 : Velocity profile of turbulent pipe flow $Re_D = 1 \cdot 10^5$

Backward-Facing Step

A critical test case is that of the reattachment of separated turbulent flow in a negative pressure gradient. The backward-facing step is a simple geometry which permits investigation of reattachment of a flow. Again the numerical results are compared with experimental data. The Reynolds number formed with the height of the step H is $Re_H = 3.7 \cdot 10^4$, at a temperature of $T_\infty = 293\text{ K}$. The computed time-averaged velocity profile in the backflow region matches the experimentally determined profile well. However it is seen that the reattachment point varies between $x/H = 5.4$ and 6.1 , depending on the turbulence model used.

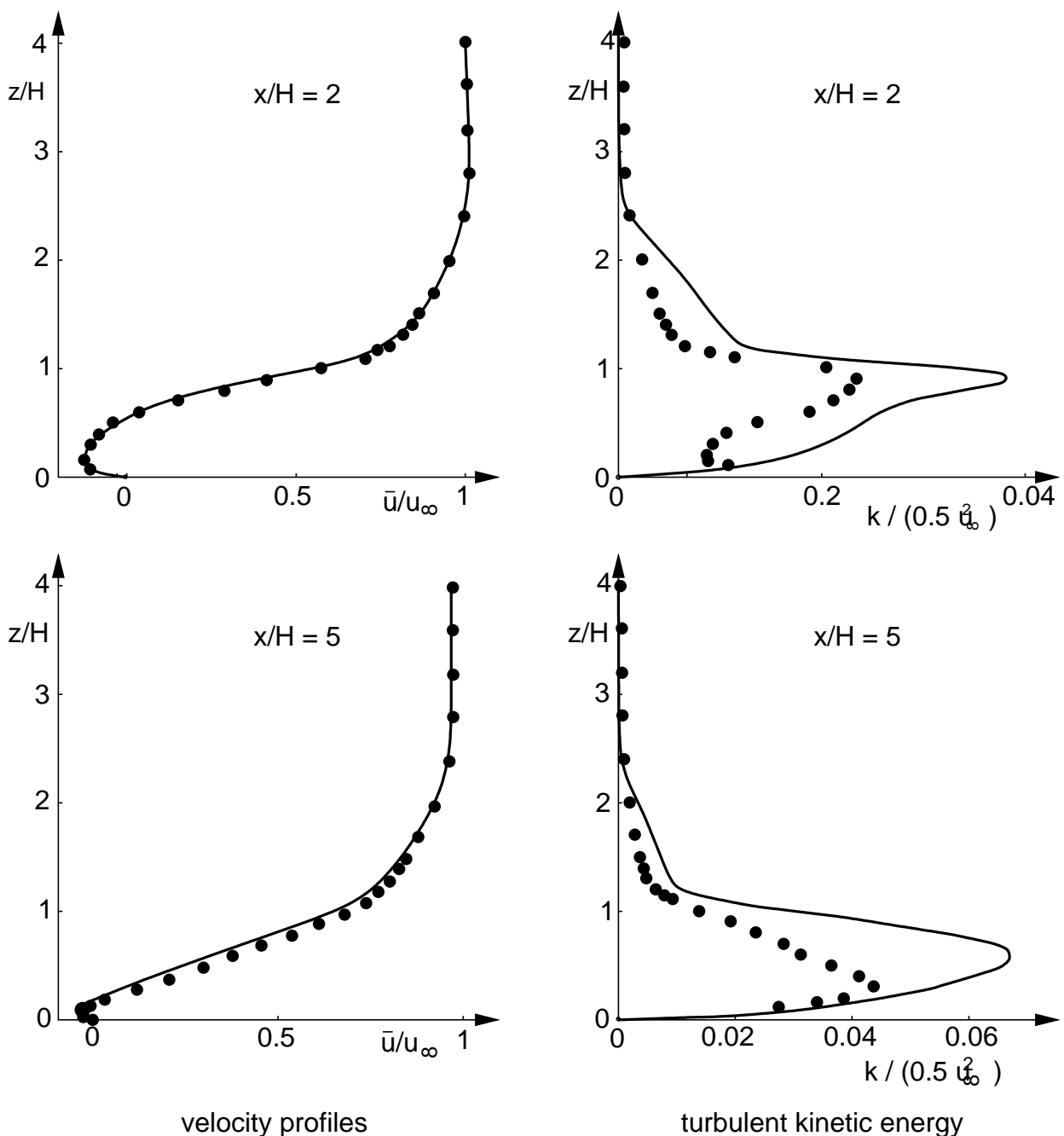


Fig. 3.11 : Turbulent flow separation behind a backward-facing step

In particular, the variations in the turbulent kinetic energy indicate that the isentropy of turbulent viscosity, as assumed in the turbulence model, is not satisfied for separated flows.

Shock Tube

In order to verify the computation of time-dependent, compressible flows through channels, we consider the unsteady shock tube flow. In a shock tube, the high pressure region (driving tube) and the low pressure region (running tube) are separated by a membrane. At the time $t = 0$, the membrane is burst and a flow process takes place. A shock wave moves into the running tube, and a steady expansion fan moves through the driving tube. The aim in this test case is to determine the shock velocity and the analytical Hugoniot values across the shock wave. In addition, it is to be shown that the shock computation is independent of the grid size used. The simulation results are compared to the one-dimensional analytical solution.

Figure 3.12 shows a snapshot of the density, pressure, temperature and velocity behind the shock wave, at the boundary between the driving gas and the gas in the running tube, and in the expansion fan in the driving tube. At the time $t = 0$ the membrane is at the position $x/L = 0.5$. It can be seen that the changes of state from the shock wave (right), to the boundary between the media (center), and on to the expansion fan (left) are represented very well. However the discontinuities across the shock wave and the boundary between the

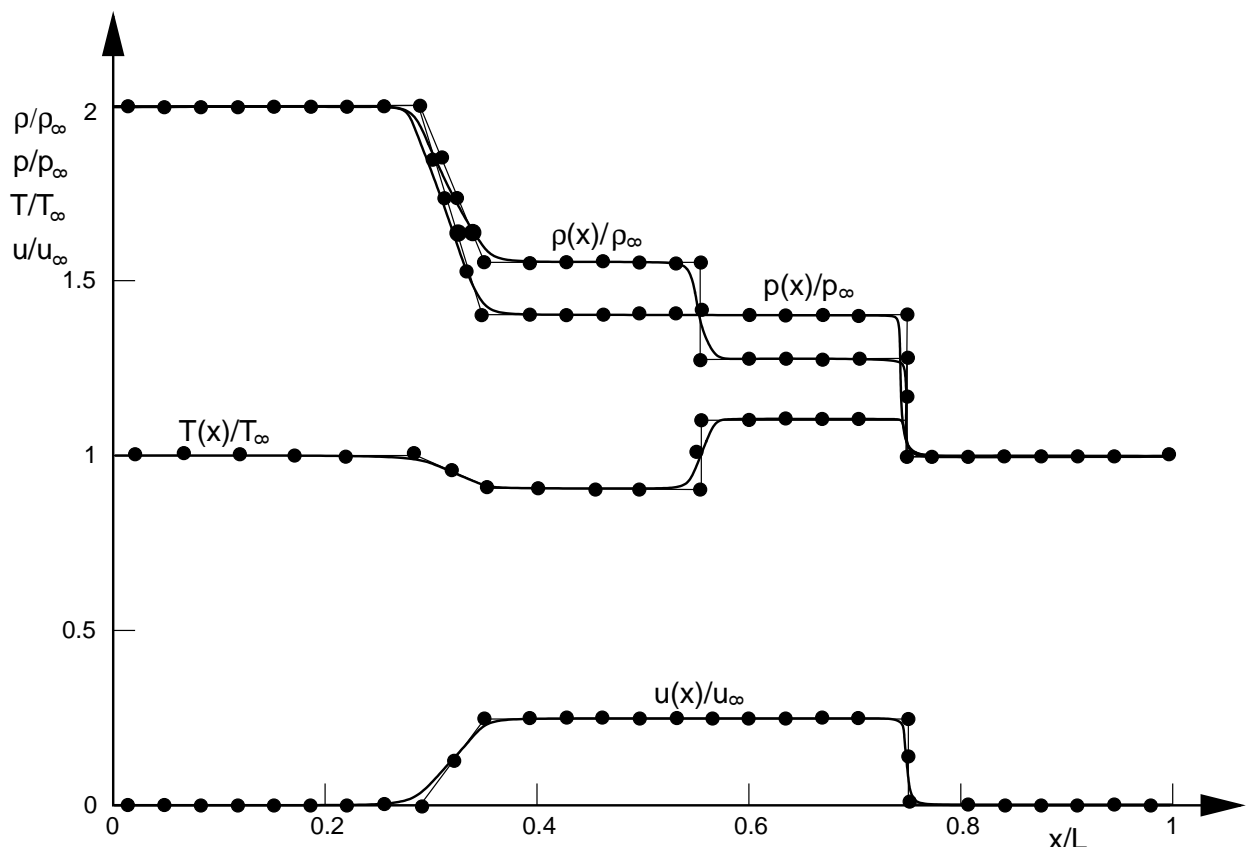


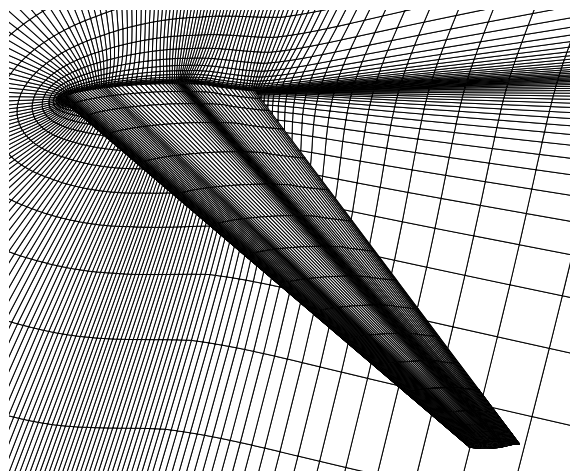
Fig. 3.12 : Shock tube flow

media are no longer sharp.

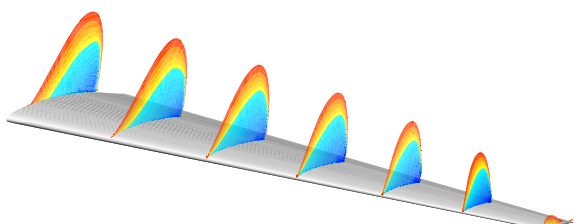
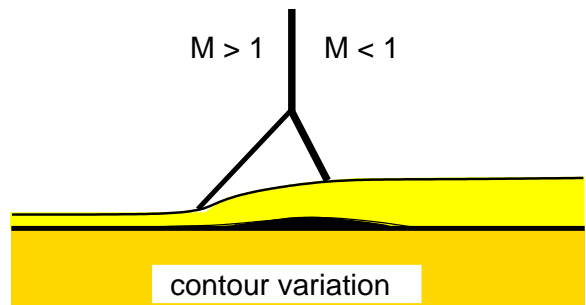
3.3 Industrial Applications

Now that we have successfully tested the software package in the introductory training course, we look at how to approach an **industrial project**. This second part of the training course is to be found at the address

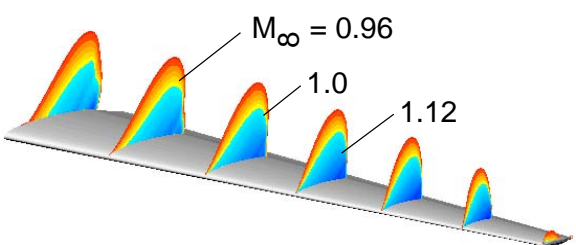
<http://www-isl.mach.uni-karlsruhe.de/sindustrieprojekt.html>



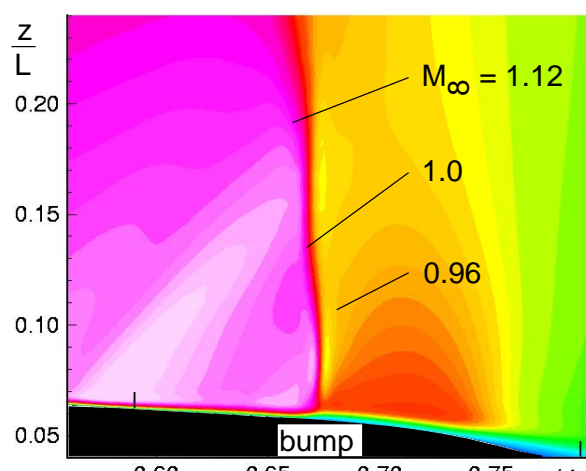
computational grid, $1.2 \cdot 10^6$ mesh points



wing solution without bump



wing solution with bump



section

Fig. 3.13 : Transonic wing with contour variation (bump)

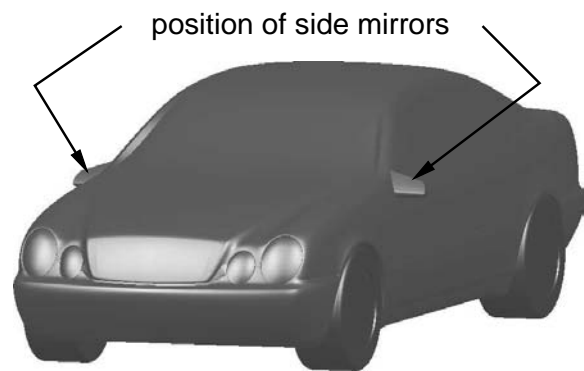
Transonic Wing

As we have already seen in the introductory Chapter 1.2, the development of the wing of an airplane aims to deliver a drag coefficient c_w which is as small as possible for a given lift coefficient c_a . The first step would be to increase the stretch for which the boundary layer on the wing is laminar. This leads to transonic laminar wings with a maximum sweep angle of about $\Phi = 20^\circ$ (see Figure 1.26). However for realistic sweep angles of civil aircraft the laminizing effect is nullified, because of the appearance of so-called transverse flow instabilities in the three-dimensional boundary layer. For this reason other measures are needed to reduce the drag. One possibility is the so-called adaptive wing which adapts itself optimally to the current state of flight. Another possibility is the **bump**, a change in the contour on the surface of the wing in the shock regime which influences the shock-boundary-layer interaction on the wing to such a degree that a drag reduction of up to 9% becomes possible.

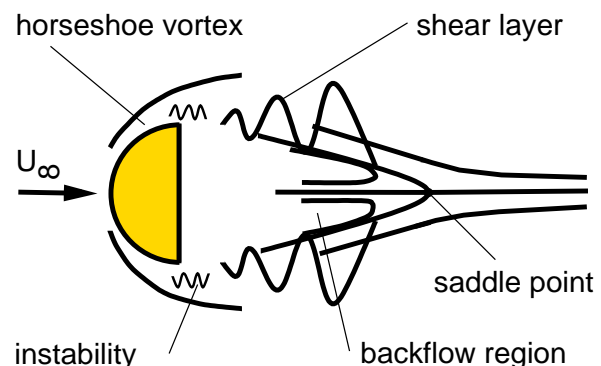
Figure 3.13 shows the effect of such a variation in contour on the wing. First of all the computational grid on an Airbus A320 model wing is shown. The free stream Mach number is $M_\infty = 0.78$, the Reynolds number is $Re_L = 26.6 \cdot 10^6$, the angle of attack $\alpha = 2^\circ$ and the sweep angle $\Phi = 20^\circ$. With the variation in contour, the section of the solution in the shock-boundary-layer interaction region shows that the shock wave fans out and a wake expansion region (shaded in gray) is formed. The change in contour in the shock region and the consequent expansion reduces the tendency towards separation. The boundary layer thickness is reduced and the fanning out of the shock simultaneously leads to a reduction in the drag. These effects both lead towards the desired drag reduction.

Flow Past an Automobile with Mirrors

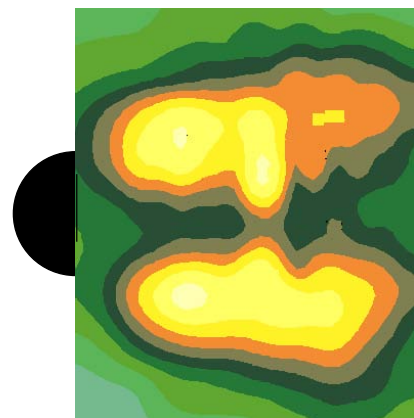
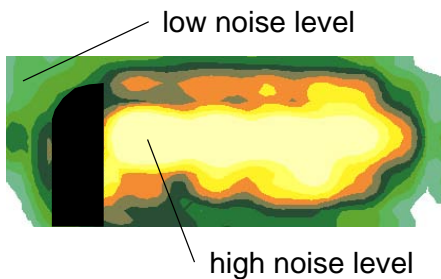
The structure of the wake flow of an automobile has already been introduced in Chapter 1.2. Of particular interest is the effect of the outer mirrors on the aero-acoustics of the automobile. The noise effects due to the flow past the mirrors are locally concentrated on the side windows and are carried on the one hand, into the far field and, on the other hand, through the side windows and the sealing around the doors into the passenger area. Figure 3.14 shows the CAD geometry of the automobile as well as a sketch of the wake flow of the mirror. Close to the surface of the automobile, the no-slip condition at the wall causes a horseshoe vortex to form. Above the horseshoe vortex shear layers are formed at the edge of the mirror and these pass over into the backflow behind the mirror and into the wake flow downstream from the saddle point. A high level of noise is formed in the shear layers of the horseshoe vortex and the wake flow, and this disturbance is heard in the passenger area. The numerical calculation of the flow past the mirrors is carried out with a free stream velocity of 140 km/h and the Reynolds number $Re_D = 5 \cdot 10^5$ of the outer mirror. If we recall the discussion of the flow past a cylinder in Chapter 2.4.5, no dominant separation frequency of the Kármán vortex street, which could cause an additional sound level at the Kármán frequency, occurs at the Reynolds number $5 \cdot 10^5$. The numerical computation and the experiments confirm this fact for the semi-cylindrical shape of the mirror. Figure 3.14 shows the local noise level, computed from the numerical calculation, in two planes vertical and horizontal compared to the mirror. These are compared to experimental results. The



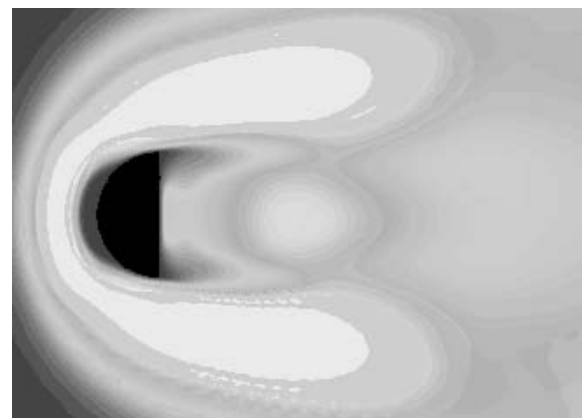
CAD geometry, Mercedes Benz CLK



sketch of mirror wake flow



experimental noise level



numerically computed noise level

Fig. 3.14 : Aero-acoustics of an automobile mirror

measurement of the local sound sources here is carried out using aero-acoustic holography. It can easily be seen that high noise levels occur in the shear layers already discussed and as sources of the change of shape of the mean flow. These can be seen particularly close to the saddle point of the wake flow.

Coriolis Revolution Sensor

In order to be able to control the stability of a vehicle, the Coriolis force is measured using micro-motion sensors in EPS systems. The sensor consists of a closed container of height $240 \mu m$, in which fingers with micrometer dimensions oscillate against each other with frequency f . This gives rise to an unsteady gap flow whose flow losses are kept as small as possible, and so the surrounding pressure of the periodically oscillating fingers is lowered to the gas kinetic region. The Reynolds number Re_H formed with the height of the gap H is so small that the no-slip condition does not hold at the finger wall.

As the motion sensor is used, gas leakage causes the pressure in the enclosed sensor container to increase continually, and the damping characteristics of the motion sensor deteriorates.

Figure 3.15 shows a snapshot of the geometry and the moving finite-volume computational grid for a section of the motion sensor. The gap height H between the oscillating fingers and those at rest is $2.7 \mu m$. At an oscillation frequency of $f = 1450 Hz$, the Reynolds number of the gap flow is $Re_H = 0.01$ at a pressure of $p = 0.01 bar$. Figure 3.15 shows isotachic lines in different sections of the area of computation. Horizontal close-ups around the leading and trailing edges of the central of the three moving fingers are shown at different heights. The different sections are at the lower edge of the finger ($z/H = 0.1$), in the middle ($z/H = 0.5$),

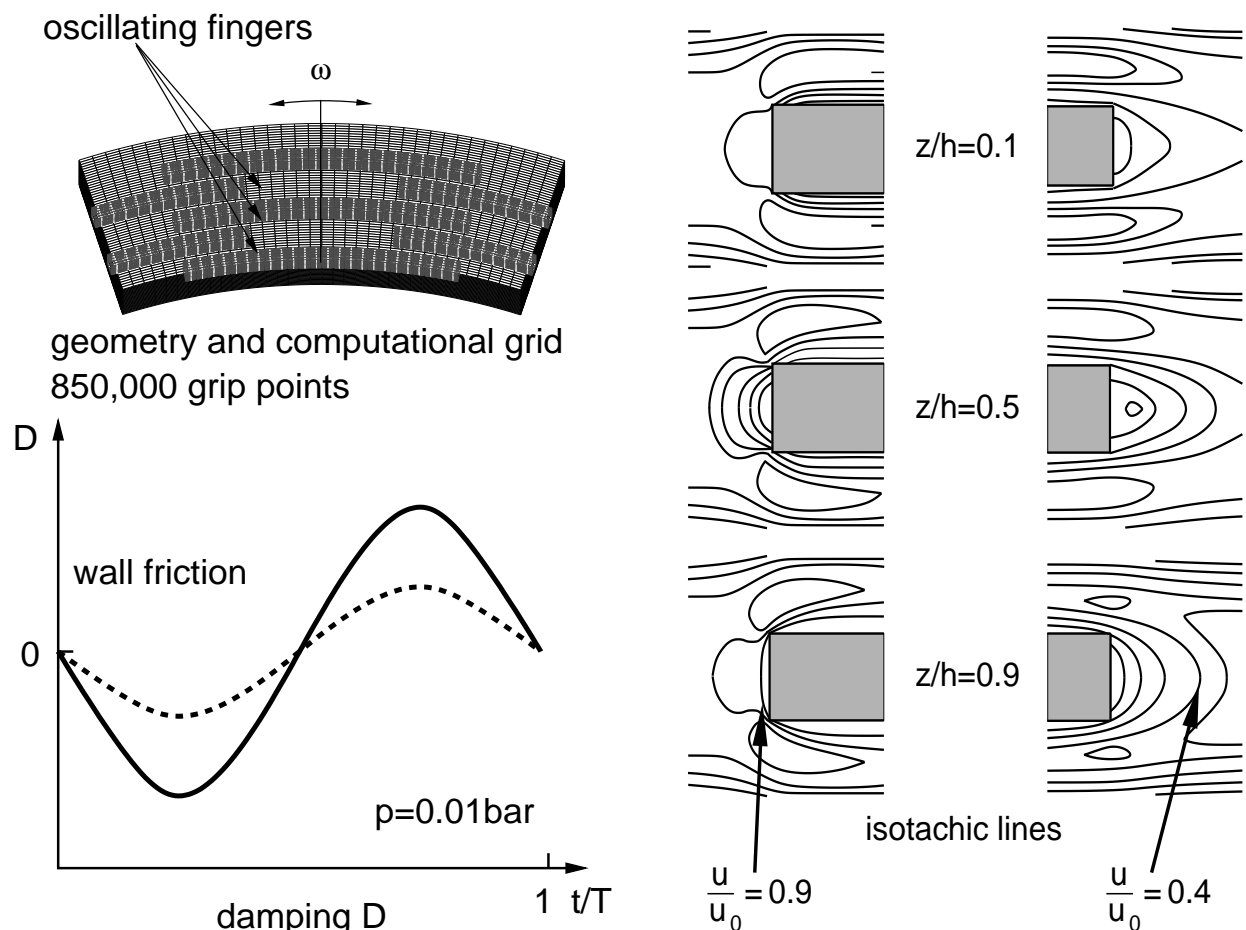


Fig. 3.15 : Gap flow of an oscillating Coriolis revolution sensor

and at the upper edge ($z/H = 0.9$). The three-dimensional flow past the leading edge can be seen. The gap flow met in Chapter 2.4.4 is found in the gaps between the fingers at rest and those moving.

The damping D is made up of the parts due to the pressure and friction forces, shown for one period T .

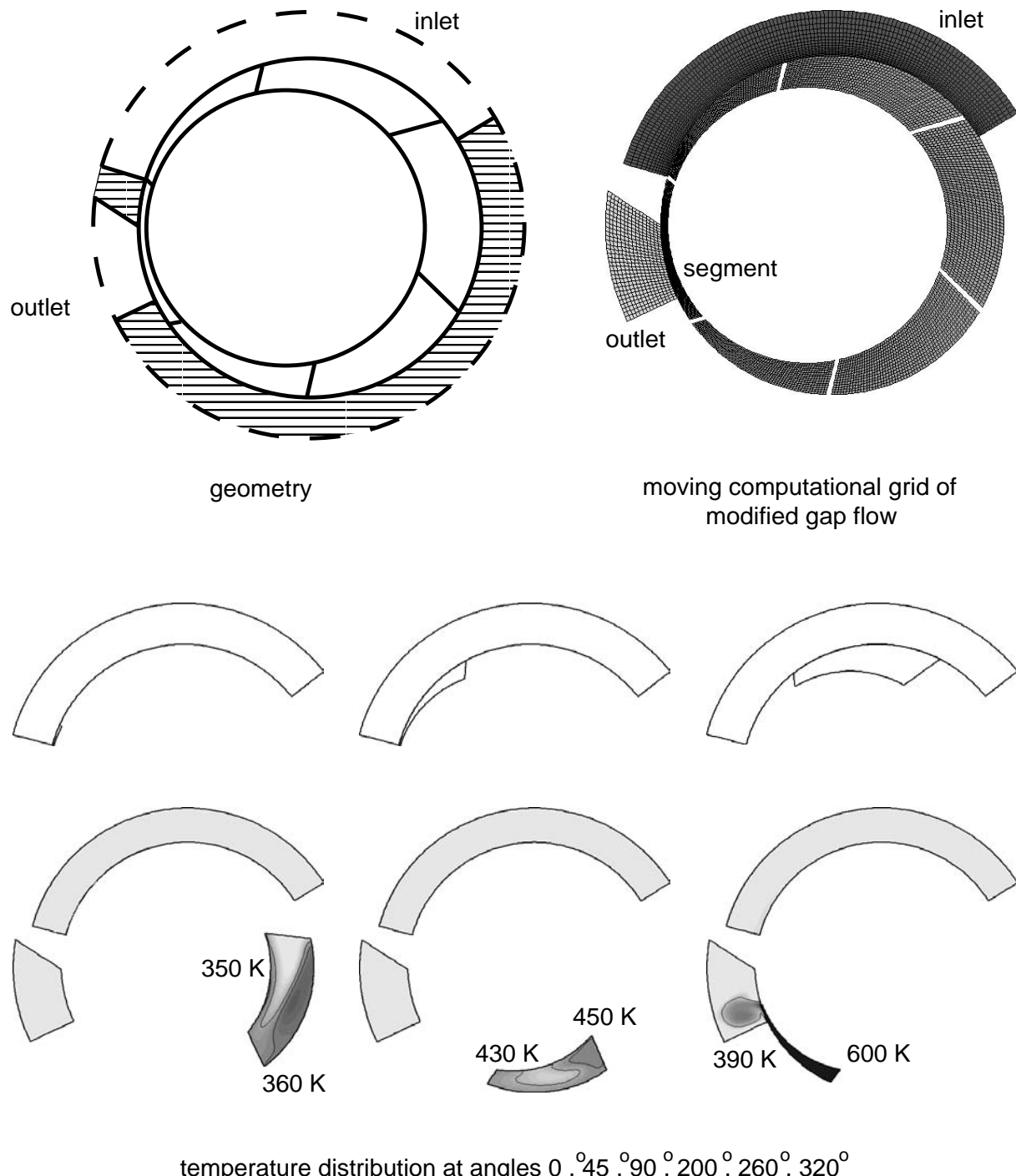


Fig. 3.16 : Gap flow in a rotary valve pump

Rotary Valve Pump

The mode of operation of a rotary valve pump is based on the fact that the position of a sliding piston is changed during rotation, so that the chambers filled with fluid continually increase their volume from 0° to 180° as they coat the inlet slit, and then, after passing through the inlet slit, continually decrease their volume until the compressed medium exits through the outlet slit. As the fluid passes through the compression gap, its pressure and temperature rise.

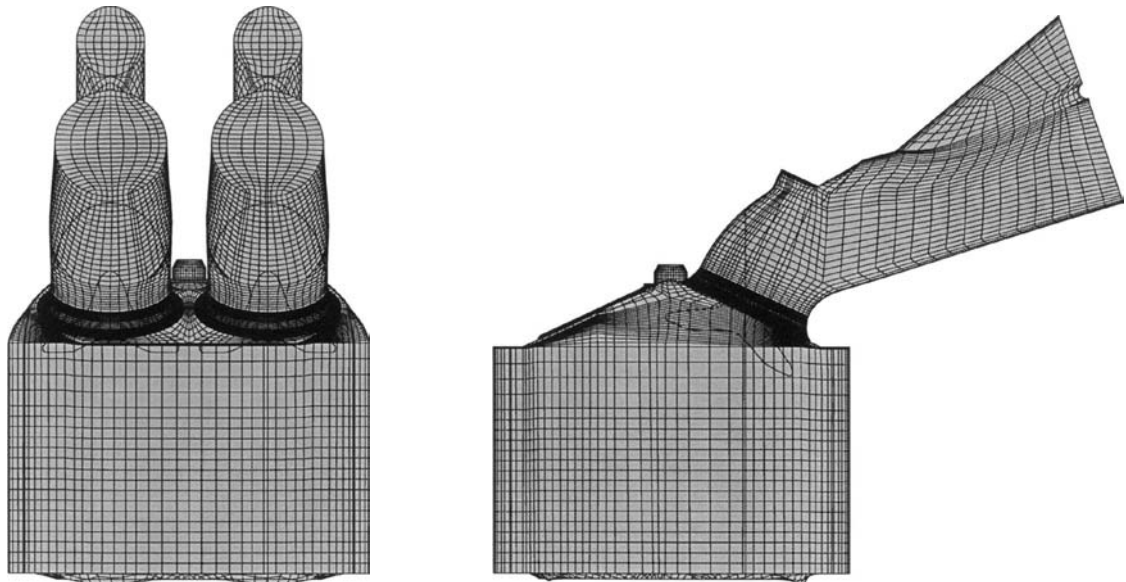
Figure 3.16 shows the simplified geometry of a rotary valve pump as well as the computational grid of the gap flow. It consists of an inlet ring over the entire angular range, and the matching outlet element with corresponding angles. The first segment has the starting position as shown, whereby the cells are initially switched off at the inlet collar, and then successively switched on during rotation. In this type of calculation, the interaction effects between neighboring cells in the suction and expulsion phases are not taken into account. The grid motion is initially fixed, with one row of cells at the inlet, at one degree per time step. In the first steps, the cell layers are successively activated until the entire segment is in contact with the inlet. The segment then moves clockwise until one row of cells reaches the outlet edge. At this point, the cell layers are successively deactivated. Figure 3.16 shows the temperature distributions at six different angular positions of the sliding piston. The inlet temperature of the fluid is 293 K and the wall temperature of the pump 333 K . In the inlet region, vortex formation takes place in the flow past the piston. In the outlet region a jet-like expansion flow is formed in the chamber. The temperature of the compressed flow in the gas increases to values of up to 600 K and then drops again greatly in the expansion area of the outlet chamber.

Flow Through an Engine Cylinder

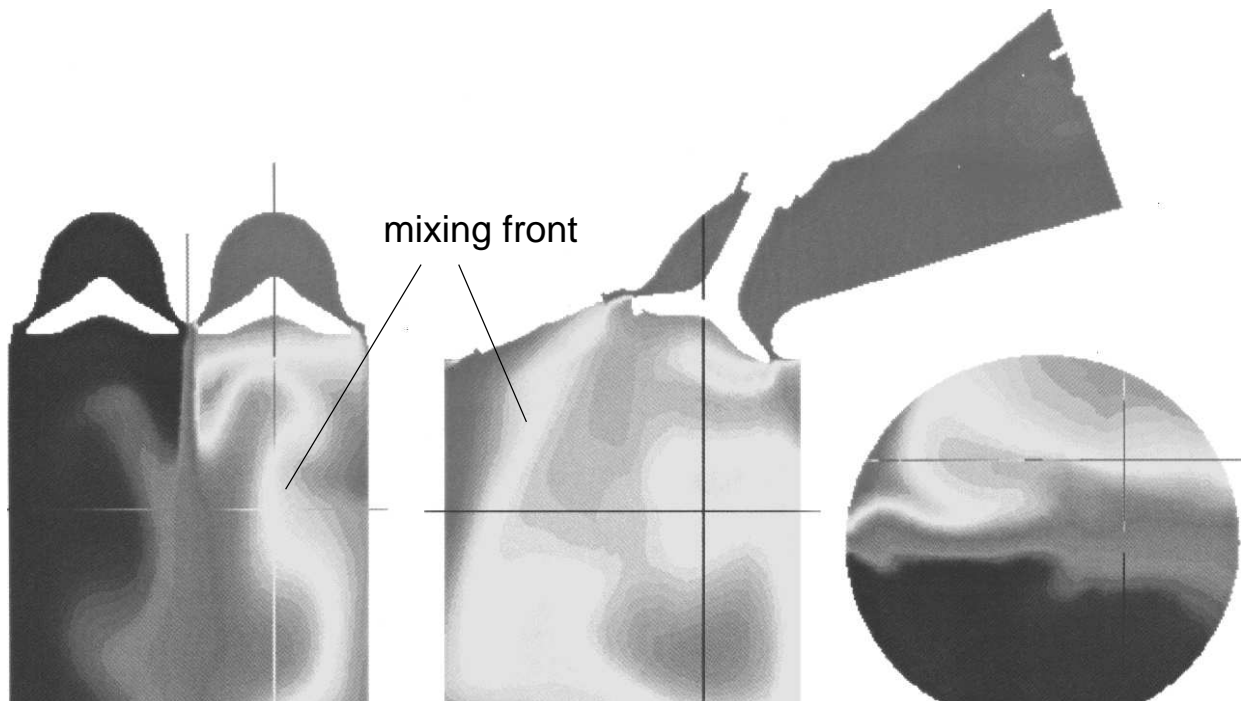
Another example of application in automobile technology is the flow through an engine cylinder. We have already seen the cycle of the moving piston in an Otto engine in Figure 1.7. Therefore in order to compute the flow through an engine, it is necessary to model the following processes physically correctly: the mixing of the air-fuel mixture in the suction phase; the production of the highly turbulent kinetic energy in the compression phase; the combustion after ignition; the expansion phase; and finally the expulsion of the combustion products. The problem in doing this is the turbulence models employed in the software packages.

The suction phase of a 4-valve Otto engine will first be modeled. Here we consider to what degree the turbulence models implemented in the commercial software correctly represent the mixing of the air-fuel mixture. Ultimately this is a requirement for the computation of the compression and combustion in the Otto engine. Figure 3.17 shows a picture of the computational grid at a certain instant of the piston motion in the suction phase of the motor. Here the motor is taken to be mechanically driven with open valves. The computational grid is continuously extended as the piston motion causes the volume of the cylinder to increase. We assume that the engine is symmetric through the middle plane, so that two inlet valves are taken into account. The numerical results show the coherent vortex structures typical to suction pipe injection, such as rotating and tumble flows during the suction phase and well

into the compression phase. The turbulent mixture of the inlet flows of both valves shown in Figure 3.17 (shown dark and light) is, however, not in agreement with experimental results. The drive for the turbulent momentum exchange through the mean velocity gradients of



computational grid with variable mesh points



turbulent mixing

Fig. 3.17 : Turbulent mixing in the suction phases of a four-valve Otto engine

the shear layers is not computed precisely enough. The distribution of the turbulent kinetic energy through turbulent diffusion due to velocity and concentration gradients on the one hand, and of the vortex strength concentration in the main vortices on the other hand, was predicted to be too small. The numerical simulation does not yield much mixing between the fresh gas and the exhaust gas until well into the compression phase. These are effects of the isentropy assumed in the turbulence model, which is not present in the rotational inlet and compression phases. The development of new turbulence models is necessary in order to compute the turbulent mixing more precisely.

Valve Flow

The fluid mechanical elements of an ABS system include hydraulic pipes, and the pumps and control valves which cause the periodic stuttering brake force of an automobile. In what follows we consider the steady three-dimensional flow in a valve in a given state. The numerical computation of the force on the valve head is of interest to predict the size of the reaction force needed.

The geometry and the computational grid of the hydraulic valve are shown in Figure 3.18. The hydraulic fluid flows from the left past a throttle position and through a ring gap which is formed by the moving part of the valve (diaphragm) and the rigid base of the valve. Up until this point, the configuration is rotationally symmetric with respect to the axis of the free stream bore hole. Because the bore hole for the downstream flow is directed upwards, the flow is turned in this direction, so that a three-dimensional separated flow is formed in the valve space.

The computed streamlines show the three-dimensional structure of the valve flow. A vortex forms around the valve head leading into the downstream flow pipe. In the front end of the

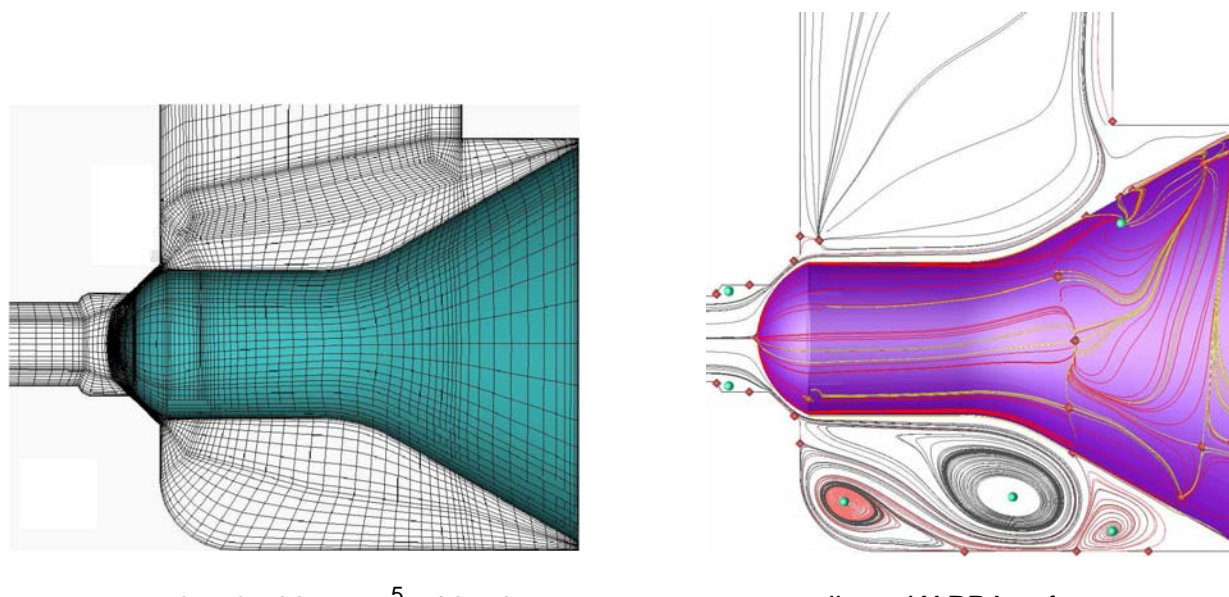


Fig. 3.18 : Structure of the flow in a hydraulic valve

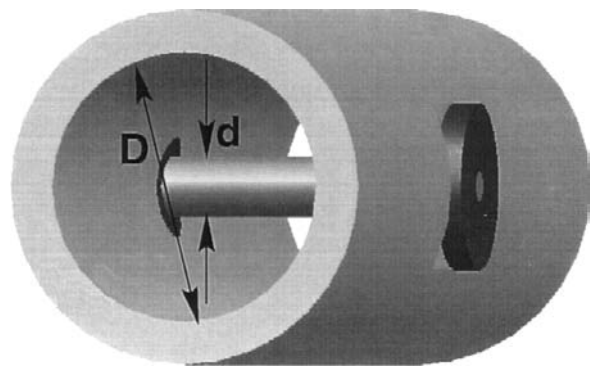
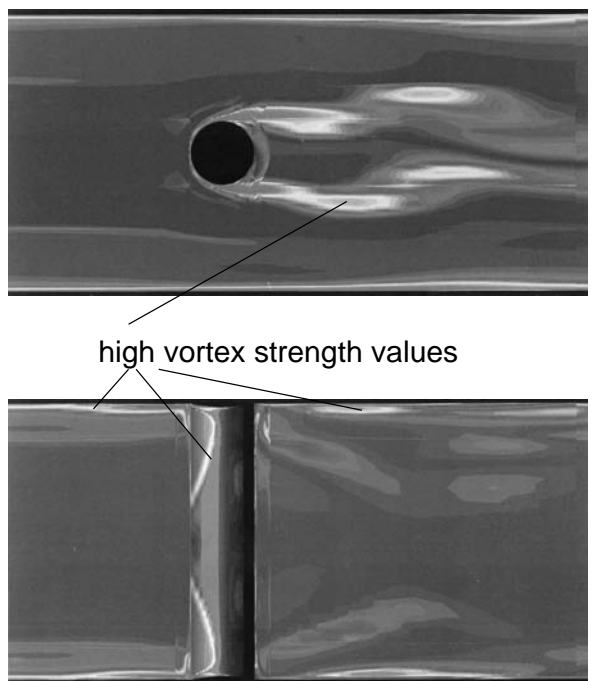
valve space a secondary vortex is formed, and in the rear end, an additional vortex which is connected with a diagonal separation line on the diaphragm. If we begin the computation with a rough grid, a reversal of the orientation of this vortex point takes place as we move to the next finest computational grid. Therefore a system involving a total of three vortex points, with the corresponding saddle points at the fixed edge, forms along the sides of the pipe. The point of separation is in the form of a focus. This can also be represented on the roughest grid, and moves downstream with better resolution of the grid. A system of saddle points and nodes forms above the diagonal separation line in the finest grid shown. This is clearly bounded towards the front and includes the rear part of the diaphragm.

At first we can see that the computed structure of the flow depends on the computational grid chosen. Even for the same grid, different turbulence models lead to different structures of this three-dimensional separated flow. Turbulence models assume isentropy in the turbulent flow, and this is not true in this flow example.

This application example was chosen for this textbook for precisely this reason. Even if the fluid mechanical software is used physically correctly, we see that the skills and experience of an engineer are also required, and these are difficult to teach in a textbook.

Volume Flux Sensor

The separation frequency of the Kármán vortex street behind a blunt body can be used to measure the volume flux of liquids, gases and steam in a pipe flow. The volume flux measurement is based on the proportionality between the flow velocity and the separation



normal component of vortex strength

Fig. 3.19 : Kármán vortex street behind a cylinder in a pipe flow

frequency of the Kármán vortex street behind a blunt body, shaped as a cylinder and set into the pipe. The cylinder with diameter d in the pipe of diameter D is shown in Figure 3.19. The diameter ratio D/d is 4. The Reynolds number of the numerical computation is related to the time-averaged free stream of the turbulent pipe flow and has the value $Re_d = 5300$.

Figure 3.19 shows vertical and horizontal cross-sections of the normal components of the vortex strength vector. In the upper picture we see a snapshot of the Kármán vortex street in the pipe. Large vortex strengths are found in both the periodically separating vortices and the turbulent boundary layer at the edge of the wall. The large vortex strength of the approaching wall boundary layer can also be seen in the horizontal cross-section. Because of the no-slip condition at the wall, this boundary layer becomes a steady horseshoe vortex around the cylinder. The effect of the wall integration into the pipe in the wake of the cylinder is seen in a characteristic expansion region of large vortex strength, downstream from which the turbulent boundary layer forms again, and the Kármán vortex street expands undisturbed. The computed Strouhal number of 0.3 agrees with the experimental values.

Smoke Detector in a Pipe System

For safety reasons, smoke detectors are installed into the pipe system of an air-conditioning system of an airplane. On the one hand they are intended to warn the crew of smoke in the airplane, and on the other hand, they activate an automatic valve which ensures that the smoke is sucked away, particularly in the cockpit and cabin. In order to be able to determine the correct position for such smoke detectors, a steady-state computation of the air-conditioning system was carried out. The aim was to compute the degree of saturation of the air with smoke particles at each detector position which would be necessary to cause the smoke detector to go off.

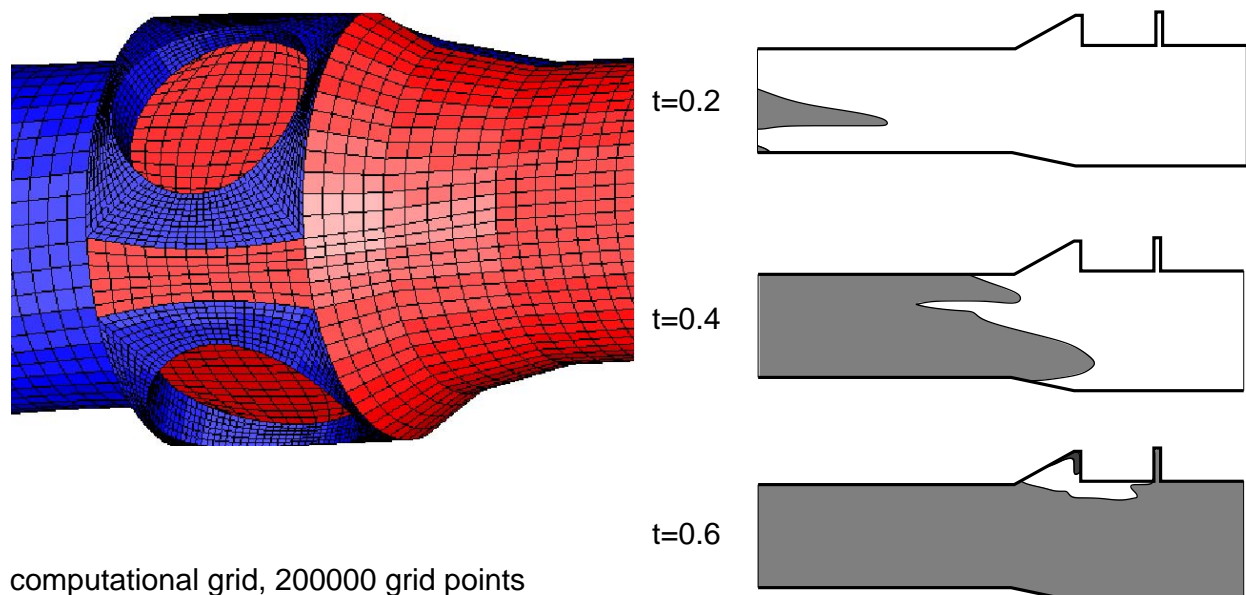


Fig. 3.20 : Concentration fronts in a smoke detector

In order to construct the system safely, two redundant detectors are also integrated into the system. Figure 3.20 shows the positions of installation and the surface network. The pipe system was widened at the detector positions, in order that no obstruction be caused by smoke sensor jutting into the cabin or cockpit. The surface network shows how the detectors are linked together. As well as the detector region, a suction pipe was also included into the computational region.

The flow is turbulent at a Reynolds number $Re_D = 1.9 \cdot 10^5$. The given intensity of turbulence for the medium at the entrance to the simulation region was $Tu_\infty = 5\%$, and the pipe flow was matched to the cabin air at an altitude of 11.2 km. The volume flux was given as $\dot{V} = 118 \text{ l/s}$. Starting out from the steady numerical solution, the smoke distribution is computed with a passive scalar, i.e. the transport of the inert massless smoke is represented based on a steady solution. The particle paths for the massless, frictionless smoke particles are integrated along the steady streamlines. Figure 3.20 shows a snapshot of the smoke dispersion at three different points in time in the smoke detector region. The rate of dispersion of the smoke shows that the smoke sensors will go off within 1 second.

Clean Air Conditioning in an Operating Theater

Pure air covers, such as those used in clean rooms, are used in operating theaters. A laminar vertical flow ensures that germ-free air is constantly blown in from above and dirt removed from the operating table. Cooled clean air is introduced to the operating area and is sucked away below and to the sides. The colder air sinks downwards with a small flow velocity. On the one hand this leads to the formation of a shear layer between the normal air in the room and the germ-free clean air, and on the other hand to the dirt introduced in the operating area being wiped away. The essential quantity considered to determine the effectiveness is the concentration of the clean air on the operating table.

Because the flow is strongly asymmetric, due to the position of the hot operating lights and supports and the air suction, a three-dimensional computational grid is generated to cover the entire operating theater, including operating table, lights and supports.

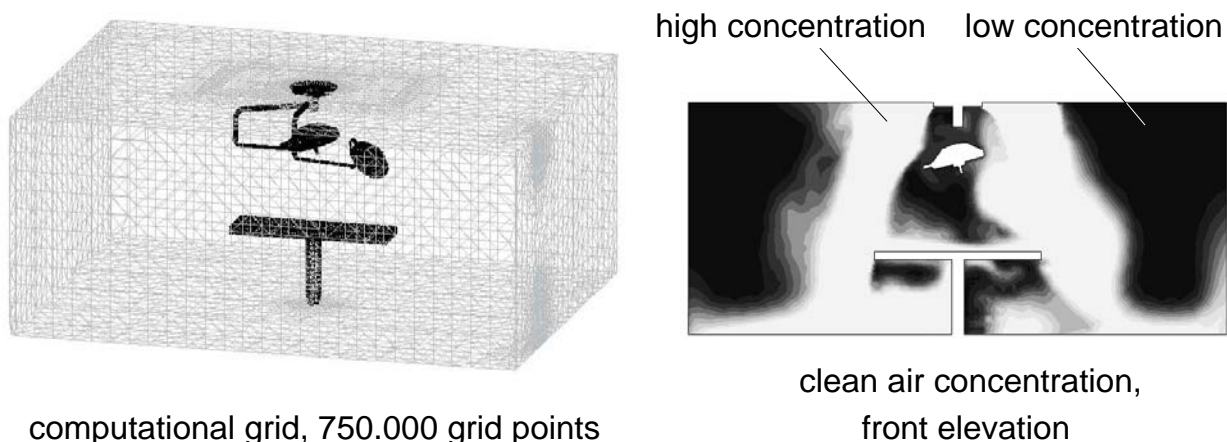


Fig. 3.21 : Clean air conditioning in an operating theater

The clean air is supplied with a Reynolds number of $Re_D = 6100$, where D is the diameter of the operating lights, and at a temperature of 291 K . The temperature of the room is 293 K .

The warm surfaces of the lights are modeled as isothermal walls whose temperature distribution has been determined experimentally. The temperature expansion is computed as convective heat transport.

After the steady numerical solution is computed, a transient expansion calculation is carried out for the concentration of the germ-free air. This corresponds to the particle path integration in the smoke detector example. Figure 3.21 shows a longitudinal cross-section of the clean air concentration in the operating theater, after germ-free air of concentration 1 has been allowed to enter through the inlet. Regions where the clean air concentration is higher are light, and those there the air is dirtier are dark. The result of the computation shows that, although the surface of the operating table is supplied with clean air, the effect on the flow of the operating lights may not be neglected.

Selected Bibliography

G. K. Batchelor:

An Introduction to Fluid Dynamics, Cambridge Univ. Press, 1994

R. B. Bird, W. E. Stewart, E. N. Lightfoot:
Transport Phenomena, Wiley, New York, 1960

T. Cebeci, A. M. O. Smith:

Analysis of Turbulent Boundary Layers, Academic Press, New York, 1974

M. van Dyke,:
An Album of Fluid Motion, The Parabolic Press, Stanford, 1982

J. H. Ferziger, M. Peric:

Computational Methods for Fluid Dynamics, Springer Verlag, Berlin, Heidelberg, 1996

K. Gersten, H. Herwig:

Strömungsmechanik : Grundlagen der Impuls-, Wärme- und Stoffübertragung aus asymptotischer Sicht, Vieweg Verlag, Braunschweig, Wiesbaden, 1992

B. E. Launder, D. B. Spalding:

Lectures in Mathematical Models of Turbulence, Acad. Press, London, 1972

H. J. Lugt:

Vortex Flow in Nature and Technology, John Wiley & Sons, New York, 1983

K. Meyberg, P. Vachenauer:

Höhere Mathematik 1/2, Springer Verlag, Berlin, Heidelberg, 1998/1997

H. Oertel jr., M. Böhle:

Strömungsmechanik, 2. Auflage, Vieweg Verlag, Braunschweig, Wiesbaden, 2002

H. Oertel jr., M. Böhle, U. Dohrmann:

Übungsbuch Strömungsmechanik, 3. Auflage, Vieweg Verlag, Braunschweig, Wiesbaden, 2001

H. Oertel jr.:

Aerothermodynamik, Springer Verlag, Berlin, Heidelberg, 1994

H. Oertel jr.:

Bereiche der reibungsbehafteten Strömung, 37. Ludwig Prandtl Gedächtnisvorlesung, GAMM Jahrestagung 1994, TU Braunschweig, ZFW (1995)

H. Oertel jr., J. Delfs:

Mathematische Analyse der Bereiche reibungsbehafteter Strömungen, Zeitschrift für Angewandte Mathematik und Mechanik, ZAMM, (1995)

H. Oertel jr., E. Laurien:

Numerische Strömungsmechanik, 2. Auflage, Vieweg Verlag, Braunschweig, Wiesbaden, 2002

H. Oertel jr., J. Delfs:

Strömungsmechanische Instabilitäten, Springer Verlag, Berlin, Heidelberg, 1996

-
- R. Peyret, T. D. Taylor:
Computational Methods for Fluid Flow, Springer Series in Computational Physics, Springer Verlag, New York, 1990
- L. Prandtl:
Führer durch die Strömungslehre, Vieweg Verlag, Braunschweig, 1942
- L. Prandtl:
Gesammelte Abhandlungen, Zweiter Teil, Über Flüssigkeitsbewegung bei sehr kleiner Reibung (1904), Springer Verlag, Berlin, Heidelberg, 1961
- H. Oertel jr. (ed.):
Prandtl-Führer durch die Strömungslehre, Vieweg Verlag, Braunschweig, Wiesbaden, 2001
- H. Schlichting:
Grenzschichttheorie, 1. Auflage, Braun Verlag, Karlsruhe, 1951
- H. Schlichting, K. Gersten:
Boundary-Layer Theory, 8th edition, Springer Verlag, Berlin, Heidelberg, New York, 2000
- W. Schneider:
Mathematische Methoden der Strömungsmechanik, Vieweg Verlag, Braunschweig, 1978
- J. H. Spurk:
Fluid Mechanics, Springer Verlag, Berlin, Heidelberg, New York, 1997
- F. M. White (ed.):
Viscous Fluid Flows, McGraw-Hill, 1974

Index

- acceleration, 51, 54, 61, 67
- adhesion force, 34
- aerodynamics, 9, 12, 43
- aerostatics, 12, 35, 39
- airplane, 2, 3
- analytic solution, 71, 128
- angular frequency, 46
- angular velocity, 63
- apparent stress, 102
- Archimedes' principle, 37
- atmosphere, 39
- automobile, 4
- backflow region, 18
- balance of angular momentum, 116, 117
- balance of energy, 65
- balance of forces, 36, 54, 61, 67
- balance of momentum, 109, 111
- Bernoulli equation, 55, 63, 70, 77, 81
- Bingham material, 27
- biological flows, 9
- Blasius boundary layer, 108
- Blasius equation, 123
- Blasius law, 122
- boundary layer, 15, 58, 69, 75
- boundary layer flow, 11, 12, 57, 67
 - laminar, 106, 112
 - turbulent, 106, 107
- boundary layer thickness, 69, 107, 108
- Boussinesq assumption, 102
- Boyle-Mariotte law, 76
- bubble flow, 18, 20
- building aerodynamics, 5
- calculation, 22
- cavitation, 20
- centrifugal force, 38
- centripetal force, 61, 62
- change of state
 - isentropic, 77, 81, 83
- channel flow, 71, 72
 - viscous, 72
- compressibility, 76, 81
- compressible, 12
- compressible flow, 76, 79
- compressor, 19
- concentration, 34
- construction, 23
- contact angle, 34
- continuity equation, 76, 84
- continuum, 10
- convection cells, 8
- Couette flow, 25, 26, 28, 72, 73
- creeping flow, 69
- critical point, 32
- critical value, 82, 84
- density, 10, 12, 30, 32, 39, 40, 42, 77, 84
- design process, 23
- diffusion, 11
- dilatant fluid, 27
- drag, 18, 73, 75
- drag coefficient, 4, 16, 22, 73, 75, 129
- drag force, 16
- drop flow, 18, 20
- dynamic pressure, 56, 58–60
- elbow bend, 134
- energy
 - internal, 30
 - total, 30
- energy conservation, 10, 63, 66
- energy equation, 82
- energy flux, 64
- energy removal, 65
- energy supply, 65
- energy transport, 11, 30
- enthalpy, 19, 30, 32, 65
- entropy, 30
- equation of motion, 54, 61, 67
- equation of state
 - caloric, 92
 - thermal, 31, 92
- Euler equation, 54, 55, 66, 68, 81, 84
- Euler picture, 49, 50
- Fick's law, 30
- first law of thermodynamics, 30
- flow lines, 18
- flow machinery, 9, 63, 66

- flow past a cylinder, 129, 132
flow past a plate, 47
flow past a sphere, 48, 126
flow past a wing, 13, 47, 57, 133
flow past an automobile, 16, 47
flow regimes, 9, 12, 20
flows in technology, 2
flows in the ocean, 9
flows with chemical reactions, 9
flows with heat transfer, 9
flows with material transfer, 9
fluid element, 36
Fourier law, 28
free stream, 21
friction, 11, 25, 70
friction coefficient, 75
friction drag, 73, 75
friction force, 68
Froude number, 69, 79
fully-formed flow, 71
fundamental aerostatic equation, 41
fundamental hydrostatic equation, 36, 41
fundamental inviscid equations, 66

gas constant, 31, 78
gravitation force, 68
gravity, 67–69, 71

Hagen-Poiseuille flow, 71, 119, 120
heat
 supplied, 30
heat conduction, 11, 28
heat flux, 28, 64
heat transport, 31, 63
horseshoe vortex, 18
Hugnoiot curve, 93
hydrodynamics, 12
hydrostatic paradox, 37
hydrostatics, 12, 35
hypersonic flow, 80

ideal gas, 31, 42, 81, 82
ideal gas equation, 78
ideal gas law, 83
incompressible, 12, 16, 66
incompressible flow, 52, 74
inertial force, 68, 70
inertial frame, 46

injection, 7
interaction force, 11, 12, 28, 32, 33
interface tension, 33
internal combustion engine, 5, 7
internal energy, 30, 65
inviscid equation, 15
inviscid flow, 11, 15, 16, 54, 64, 66
inviscid fundamental equation, 66
inviscid outer flow, 66
ionosphere, 40
isentrop exponent, 82
isentropic relation, 83

Kármán vortex street, 5, 48, 51
KAPPA-Stromfaden, 67, 137
kinetic energy, 56, 64

Lagrange picture, 49, 50
Laval nozzle, 85
Lewis number, 30
lift, 18
lift coefficient, 21
lift force, 21
liquid flow, 19, 20
liquid phase, 32
liquid-steam separator, 18

Mach number, 13, 21, 76, 79, 81, 85
mass concentration, 30
mass conservation, 10, 53, 66
mass diffusion, 30
mass element, 61
mass flux, 53, 56
mass transport, 11, 30
material production, 8
mean free path, 90
mesosphere, 39
minimal area, 34
mixing length, 103
molar mass, 78
momentum conservation, 10, 54, 66
momentum transport, 25, 29
multi-phase flow, 32

Navier-Stokes equation, 67, 129
Newtonian fluid, 26, 27
Nikuradse diagram, 122, 123
no-slip condition, 10, 25

- non-Newtonian fluid, 27
 normal stress, 102
 Otto engine, 7
 outer flow, 11
 partial density, 30
 particle path, 43, 45–48, 51
 phase velocity, 46
 pipe flow, 20, 71
 pipe hydraulics, 118
 Pitot tube, 59
 plate boundary layer, 75, 112
 plate boundary layer flow, 69
 potential vortex, 63
 power, 66
 Prandtl mixing length ansatz, 102
 Prandtl number, 29, 79
 Prandtl tube, 56, 59, 61
 preliminary design, 21, 22
 pressure, 19, 28, 30, 35, 39, 40, 42, 56, 62, 76
 dynamic, 56
 static, 56, 69
 pressure coefficient, 14, 15, 73, 74
 pressure drag, 73, 75
 pressure force, 17, 18, 36, 38, 61, 62, 67, 68, 73
 pressure loss, 20
 pressure side, 14, 15
 product development, 20, 21
 production plant, 8, 9
 chemical, 8, 9, 18
 pseudo-elastic fluid, 27
 pump, 20, 65, 66
 ratio of specific heats, 31
 Rayleigh line, 93
 real gas, 33
 recirculation, 128
 reservoir pressure, 57, 59, 83
 reservoir temperature, 83
 reservoir value, 82, 84
 Reynolds ansatz, 99
 Reynolds number, 13, 69, 79
 roughness, 17
 saddle point, 18, 87
 Schmidt number, 30
 separation, 16, 126
 separation criterion, 127, 128
 separation losses, 136
 shear flow, 62, 71
 shear force, 34
 shear stress, 25, 28, 34, 35, 67, 72
 apparent, 102
 shock tube, 97
 shock wave, 15, 30, 79, 90
 normal, 93
 oblique, 96
 unsteady, 97
 shock wave equations, 92
 shock-boundary-layer interaction, 133
 signal velocity, 76
 sound wave, 76, 77, 79
 specific heat
 ratio, 31
 speed of sound, 76–78
 stagnation point, 10, 57, 83
 stagnation streamline, 57
 static pressure, 56, 58–60
 steady flow, 44, 46, 52, 54, 64
 steam flow, 18, 19
 steam phase, 32
 steam pressure, 20, 32
 Stokes drag law, 129
 storage power station, 65
 stratosphere, 39, 41, 42
 streakline, 45–48, 51
 stream filament, 52–55, 61, 64, 67
 element, 67
 stream filament theory, 43, 53, 66, 71, 84
 compressible, 81
 stream surface, 53, 67
 streamline, 44, 46–48, 51
 streamline body, 75
 streamtube, 52, 64
 subsonic flow, 79, 81, 85
 suction side, 14
 supersonic flow, 80, 81, 85
 surface force, 33
 surface tension, 33–35
 sweep angle, 21
 temperature, 10, 28, 30, 35, 39, 40, 76

- critical, 32
- thermal diffusivity, 29
- thermal expansion coefficient, 31
- thermodynamic equilibrium, 30
- thermodynamic properties, 30
- thermodynamics
 - first law of, 30
- throttle valve, 19
- tornado, 62, 63
- total drag coefficient, 73
- total energy, 30
- total pressure, 57–60
- train, 2, 3
- transonic flow, 80, 81
- transport property, 11, 25
- troposphere, 39, 41
- turbine, 65, 66
- turbulence intensity, 100
- turbulent flow, 9, 98
- turbulent pipe flow, 121
- two phase flows, 9
- two-phase flow, 20
- two-phase regime, 19
- U-pipe pressure gauge, 57, 58
- unsteady flow, 46, 52, 55
- upthrust, 37, 38
- US standard atmosphere, 40, 42
- validation, 22, 23
- Van der Waals equation, 32
- velocity, 20, 25, 44, 56, 63, 68, 71
- velocity vector, 10, 12, 44, 45, 49
- Venturi pipe, 56
- verification, 22, 23
- viscosity, 11, 27, 28
 - dynamic, 26, 29
 - kinematic, 13, 29
- viscous flow, 11, 15, 63, 67
- viscous sublayer, 104
- viscous wake flow, 15
- volume, 31
 - specific, 32
- volume element, 64
- volume flux, 53, 66
- vortex flow, 63
- wake flow, 15, 18
- wall shear stress, 73, 75, 124
- wall streamline, 73
- wave
 - plane, 46
- wave number, 46
- wind tunnel, 3–6, 23
 - experiment, 22
- wing, 21
 - pressure side, 14
- wing design, 22
- work, 30, 63, 65, 66
 - specific, 65, 66
- Young's equation, 34
